Finite element modelling of electromagnetic and coupled thermo-electromagnetic devices

Vong, Poh Kheong

Award date:
2001

Awarding institution:
University of Bath

Finite Element Modelling of Electromagnetic and Coupled Thermo-Electromagnetic Devices

Submitted by Poh Kheong Vong

for the Degree of Doctor of Philosophy of the

University of Bath

2001

Copyright

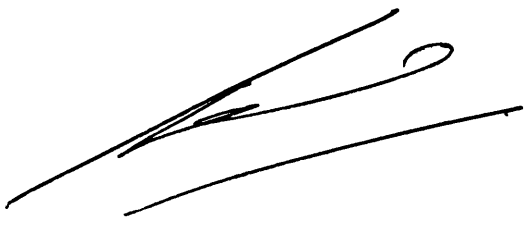

ProQuest LLC
789 East Eisenhower Parkway
P.O. Box 1346
Ann Arbor, MI 48106-1346

Abstract

Several finite element schemes are implemented in this work with the aim of providing accurate modelling of electromagnetic devices and solving coupled thermal-electromagnetic problems. These codes are compared and evaluated using measurements from specially built test rigs and computational finite element models in 2D and 3D.

The first stage involves the modelling of coupled electromagnetic-thermal problems. The mathematical formulation includes a steady-state eddy current equation with time-harmonic magnetic vector potential and Fourier's thermal conduction equation with the appropriate boundary conditions. The final aim is to model heat transfer in electrical machines using finite elements. Accurate thermal modelling is particularly important when optimising the thermal design of machines.

The second stage consists of modelling skew rotating part of electrical machines. Skewing is particularly important for cogging torque reduction in permanent magnet machines. Conventional finite element techniques are expensive for modelling skew since there has to be a radical change of shape in the mesh across the thin air gap. The *Lagrange Multipliers* approach is successfully used for modelling electrical machines in this kind of situation.

Finally, a parameterised template code is design for rapid modelling of electrical devices. The new scheme is convenient for the use of designing electromagnetic devices with complex geometry. The major advantage is once a template of the device is meshed up, a new similar device can be modelled easily by just altering the file which contains the parameterised dimensions of the device. These alterations could be carried out manually or by an optimisation program. Some practical applications of the parameterised codes are demonstrated with measured results compared favourably with the experimental ones.

Acknowledgments

I am eternally grateful to my mother for her love and support over all these years.

Special thanks to the *"MEGA Corps"* especially to three people whom I would like to single out here: Dr. H C Lai, Dr. Philip Coles and Mr. Roger Hill-Cottingham who despite their busy schedules have contributed a generous amount of time in offering helpful suggestions and assistance throughout my Ph.D research.

Above all I would like to express my deepest gratitude to my supervisor, Prof. David Rodger, not only for his invaluable guidance and encouragement but also for making the past few years so memorable with his earthly humour and unique personality.

This manuscript was prepared with LaTeX.

Contents

List of Figures

List of Tables

List of Symbols

$\boldsymbol{A}$	magnetic vector potential
$\boldsymbol{B}$	magnetic flux density
$\boldsymbol{D}$	electric flux density
$\boldsymbol{E}$	electric field intensity
$\boldsymbol{H}$	magnetic field intensity
$\boldsymbol{J}$	current density
N	shape function
V	electric scalar potential
Θ	weighting parameter
W	weighting function
$[\boldsymbol{K}]$	stiffness matrix
$[\boldsymbol{C}]$	capacitance matrix
$\boldsymbol{f}$	load vector
$[\mathfrak{J}]$	Jacobian matrix
Π	an equivalent functional
$\overline{\Pi}$	Lagrange Multipliers functional
$\delta\Pi$	variation of Π
$\delta\overline{\Pi}$	variation of $\overline{\Pi}$
γ	Lagrange Multipliers
ψ	total magnetic scalar potential

ϕ	reduced magnetic scalar potential
μ	permeability
$\hat{\mathbf{n}}$	normal component
$\boldsymbol{u}$	velocity
t	time
σ	electrical conductivity
α	electrical resistivity coefficient
κ	thermal conductivity
κ_f	fluid thermal conductivity
ρ	material density
C_p	specific heat capacity
T	temperature
$\dot{q}$	internal heat generation
q	heat flux
Q_s	heat storage in component volume
Q_e	heat storage in elemental volume
ϵ_r	radiation emissivity
σ_r	Stefan-Boltzmann constant
Nu	Nusselt number
Ra	Rayleigh number
Pr	Prandtl number
Gr	Grasnof number
Re	Reynolds number
ω	angular velocity
$\hbar_c$	convection coefficient
$\hbar_r$	radiation coefficient
$\hbar_\omega$	rotating convection coefficient
ν	kinematic viscosity

μ_v	molecular viscosity
u_∞	free stream velocity
α_k	thermal diffusivity
β	coefficient of volume expansion
g	gravity acceleration
δ	characteristic length
α_w	Peclet number
V_s	component volume
V_e	elemental volume
T_∞	ambient temperature
T_s	surface temperature
T_t	stator surface temperature at air gap
T_d	rotor surface temperature at air gap
P_h	hysteresis power loss
P_e	eddy current power loss
$T(\theta)$	cogging torque
N_s	number of slots
θ_p	angular pole pitch
θ_s	angular slot pitch
N_m	number of magnet poles
τ_p	pole pitch
τ_m	pole arc
N_{sm}	number of slots per magnet pole
$\overline{P}$	periodic parameter
k_r	Russell and Norsworthy coefficient

Chapter 1

General Introduction

1.1 Electromagnetics

The science of electromagnetics was introduced to the world when James Clerk Maxwell, a professor at Cambridge University published his classic unified theory of electricity and magnetism in 1873. But the study on electromagnetics begin much more earlier with important discoveries by the "giants" of the past.

The first systematic experiments on electric and magnetic phenomena was described in the celebrated book *De Magnete* of William Gilbert in 1600 AD. Benjamin Franklin in 1750 established the law of conservation of charge. Later Charles Augustin de Coulomb successfully measured electric and magnetic forces. Alessandro Volta had invented the voltaic cell, which in effect a battery by 1800. Hans Christian Oersted observed the magnetic effects near an electric current in 1819, which demolished the popular belief that electricity and magnetism were independent phenomena. The following year Andre Marie Ampère extended his work and formulated a complete theory. At the same time Georg Simon Ohm of Germany published his famous Ohm's law relating current, voltage and resistance. In 1831, Michael Faraday demonstrated that a changing magnetic field could produce an electric current. Faraday's extensive experimental investigations enabled Maxwell to reveal his classic to the world.

The action of all forms of electromagnetic device is governed by two fundamental

laws postulated by Faraday and Maxwell. Faraday's law states that when relative motion exists between the magnetic field and a coil situated in the field an *e.m.f* will be induced in the coil that is directly proportional to the rate of change of flux with respect to time between the field and the coil. While Maxwell observed that if a current-carrying conductor is placed in a magnetic field, a force will be exerted and relative motion will take place between the structure carrying the conductor and that carrying the field.

From these laws the power of electromagnetic was harnessed to construct electromagnetic devices. Faraday in his experimental research discovered electromagnetic induction. This was followed up by Joule who managed to measured the heat produced in conducting material, thus confirming the presence of induced circulating currents in conductors known as eddy currents today. Further work on eddy currents was presented in 1833 by Lenz whose law gave the direction of the induced currents. All these major contributions led to Nikola Tesla's invention of the induction machine in 1895. Since then many new inventions and new theory has sprung up, we are truly in fact an electromagnetic society. An in depth study of electromagnetics can be found in [1].

1.2 The Finite Element Method as a Numerical Analysis Tool

The label *finite element* was first coined in 1960 by Clough [2] in his paper on plane elasticity problems. But the idea of finite elements date much further back. Its development has occurred along two paths, one in engineering and the other in mathematics. Both of which required the use of *trial functions* to effect a solution.

A trial or approximate function is an assumed mathematical function that is usually based on physical intuition to represent a continuous function in a continuum problem. It is applied globally to the region of interest and approximates the expected behaviour of the region to some external loads.

In a paper by Gauss in 1795, trial functions were used in a form of *weighted residuals.* Later these functions were applied by Rayleigh and Ritz in their variational methods. In the variational approach the undetermined solution is first expressed in terms of the trial functions with unknown parameters. The next step is to find the function that renders the functional stationary subjected to the given boundary conditions of the system. The functional is then differentiated with respect to each parameter, and the resulting equation is set to zero. If there are n unknown parameters, there will be n simultaneous equations to be solved. In this way the approximate solution is chosen from a selection of assumed solutions. See Riley [3] for more details.

Galerkin in 1915 introduced a particular type of weighted residual method where the trial functions are made the weighting functions. The unknown parameters are now chosen such that the trial function becomes 'a best fit' to the exact solution through direct reference to the system partial differential equations and boundary constraints {discussed in Chapter 2 }. Such an approach contrasts quite remarkably from the indirect path of the variational method, where an energy related functional is made stationary.

Early usage of trial functions are done on a global scale, over an entire region and therefore, not suitable for real problems with irregular geometries and unknown solutions. Courant [4] in 1943 introduced *piecewise continuous trial functions.* In his efforts, the piecewise trial functions are not applied globally to the entire region of interest but rather locally to small subregions or elements. In other words, the entire domain is *discretised* into smaller pieces. By doing it this way, Courant greatly extended the applicability of trial functions in obtaining approximate solutions to real-world problems.

In the years since 1960 there has been an extraordinary growth in the finite element method. It has received widespread use in engineering, especially since the advent of digital computers. Discrete problems can generally be solved readily now even if the number of elements is large.

Several areas where the finite element method is popular as a numerical modelling technique are in the field of electromagnetics, stress analysis and thermal heat transfer problems. The major advantages of this method are the relative ease in modelling complex geometries and in assigning higher-order forms of solutions to specialise areas of the modelled problem.

This thesis will not contain a detailed explanation of the finite element method and applications, since an abundance of books and literature already exists on this subject. An excellent general reference on finite element method is by Zienkiewicz [5] and a more specialised one in finite element method for electrical engineers by Silvester [6]. The basic theory for finite elements in electromagnetics will be described in Chapter 2.

1.3 2D and 3D Finite Element Modelling of Electromagnetic Related Problems

Ever since the dawn of the age of digital computer in 1960, the development of computational electromagnetics has been closely linked to its remarkable growth. The availability of high processing speed computer at an economical level and rapid developments in computer graphics systems, which enabled the visualisation of modelled device geometries electromagnetic field are some of the major factors that catalysed this monumental growth. Advancement in the field of numerical techniques in discretising Maxwell's equations added further attraction to the usage of finite element method as a designing tool.

This research is based on using and developing some program codes for the software package *MEGA* in electromagnetic devices optimisation, heat transfer and coupled thermal-electromagnetic problems. *MEGA* is one of the commercially available integrated software packages for solving applied electromagnetics using the finite element method. The software has been developed by the Applied Electromagnetics Research

Group at the University of Bath as part of the ongoing research in the field of modelling electromagnetic devices. The finite element method is applied to numerically solve the differential form of Maxwell's equations.

This comprehensive program is capable of solving a wide range of 2D and 3D problems using a set of formulations, some of them are listed below:

- Magnetostatics 2D and 3D
- Electrostatics 2D and 3D
- Steady-state AC with eddy currents using complex number representation in 2D and 3D
- Transient eddy current problems
- Moving conductor problems for 2D and 3D formulations using *Minkowski transformation*
- Dynamic movement modelling using the *Lagrange Multipliers*
- Thermal diffusion equation strongly coupled to the electromagnetic solution
- Voltage or current forced wound coils.
- Coupled external circuit model

Finite element matrix systems are typically large but sparse. For a large number of problems, especially those with non-moving effects the system matrix is symmetric which represents considerable savings in computation time and computer memory space.

The advantages of finite elements are numerous, particularly in industrial application where there is clear evidence of the advantages of finite element analysis over other methods. Two examples will be that of its inherent ability to calculate accurately

armature effects and small torque variations called cogging torque. The effect of cogging torque on permanent magnet (PM) servo machines will be discussed in Chapter 5.

1.4 Research Aims

Design and optimisation of electromagnetic devices have become increasingly important over the recent decades. In an increasingly globalised world economy, cost cutting, material restrictions, design versatility are just a few possible criteria that clients will demand. That's where computational modelling comes in. Often now the design of a new prototype begins from the computer which serves as the drawing board and finishing up with a real model. Finite element methods are often the preferred choice.

Other methods such as analytical and lumped parameter circuit methods may provide a significant insight and experience into the behaviour of electromagnetic devices. However, both methods are derived from the electromagnetic field theory under certain assumptions and are thus limited to a range of simple geometries and ideal material properties. These simplifications may sometimes lead to an extensive departure from modelling the real problem. In fact, physical realities such as magnetic non-linearity, coupled electromagnetic-thermal, non-linear thermal properties, hysteresis and time-transient solutions are basically difficult if not impossible to solve.

The aim of this work is to develop a number of new modelling techniques for analysing coupled-thermal system and electromagnetic devices. One particular interest is the modelling of heat transfer in conducting material using finite elements. Galerkin's weighted residual method offers the means to formulate the governing heat transfer equations which enabled the non-linear surface heat flow due to convection and radiation to be prescribed. The heat source is derived from the induction heating due to the eddy currents circulating in the material.

When conductors are subjected to transformer or motional induction, eddy currents tend to be induced and flow in closed paths in the material. Eddy currents produce their own magnetic field which tends to oppose the variation of the imposed magnetic field as stated in Lenz's law. These induced currents effectively flow in a surface layer of thickness around the skin depth δ depending on the frequency, material conductivity and relative permeability. Eddy currents result in joule heating in the conducting material. Strongly and weakly coupled electromagnetic-thermal systems are modelled. For induction heating at power frequency 50 Hz, the thermal time constant is enormous and a fully time-transient coupled electromagnetic solution is untenable. Therefore, it is viable to just solve the electromagnetics part of the solution as AC steady-state and then couple the solution to an iterative transient thermal system. However, in a weakly coupled model the inherent weakness is that after a certain temperature rise the changes in the material's resistivity will be substantial and thus lower the temperature rise. To circumvent this problem, the electromagnetic part is resolved again with a new resistivity value whenever the need arises and recoupled again to the thermal solver until the temperature steady-state is reached.

Analysing cogging torque in permanent magnet (PM) machines is another important task. Several well-known techniques in reducing cogging torque are validated with computational predictions and measurements from test rigs. In the mean time, the modelling technique has to be optimised to improve the accuracy of the simulation results and also finding the most economical way in solving problems especially 3D problems. The *Lagrangian Multipliers* technique allows the modelling of dynamic movement of the rotating and ease the task of constructing skew rotor or stator slots for reducing the cogging torque effect.

Parameterised template meshing techniques are another area of interest. It was conceived due to the laborious work that one has to do every time several dimensions of the studied machine needs to be changed. Generally this required a fair amount of time as the machine has to be remodelled again. This is where the parameterised

technique is particularly useful. But the method avoided the trap of generating only triangle elements, as most software with automatic mesh generation do. The users will have the freedom of choosing the type of elements and mesh density. Parameterised template can be coupled to a computer optimiser for optimising industrial designs.

1.5 Thesis Outline

The thesis contains eight chapters, covering two major areas of research. The first part includes the work on heat transfer with non-linear convective and radiation coefficients used to model the heat flow from the surface of conducting domains. The heat generated is provided by the induced eddy currents, otherwise known as induction heating and I^2R losses in the coils. The remaining chapters are focused on electromagnetic design and optimisation.

- **Chapter 1: General Introduction.**

  General overview of the whole thesis plus a brief introduction on finite elements as numerical analysis tools, electromagnetic devices, inductive heating and thermal coupled problems.

- **Chapter 2: Finite Element Theory: An Overview.**

  A general description of the finite element theory and various formulations for modelling conducting and non-conducting regions of electrical devices. The treatment of the boundary conditions between different regions are also discussed together with non-linear transient time-stepping scheme and a brief recourse of the finite element shape functions.

- **Chapter 3: Numerical Techniques in Solving Heat Transfer with Non-Linear Boundary Conditions.**

  This chapter introduces two major numerical methods in modelling thermal heat transfer in conducting material, the lumped parameter circuit method and finite element technique.

  In the lumped parameter method, the various components of the conducting domain are represented by a series of thermal resistances and capacitances. This is equivalent to an electrical circuit in which heat flow is analogous to electric current and temperature to electrical voltage. The concept of lumped parameter thermal modelling is not new. The idea has already been in existence for some time. However, improvements are needed in many areas especially regarding the temperature dependent convection and radiation heat transfers from the surface of the conductor frame. The finite element technique uses the *backward difference* scheme to time march towards the temperature steady-state.

  The lack of measured universal value on the convection and radiation coefficients severely limited the ability of both techniques in predicting an accurate solution, worst the models are heavily dependent on the empirical correlations. This correlation data is only available for certain geometrical surfaces and is not known to be remarkably accurate. Alternatively, the computational fluid dynamics can be used to calculate the velocity of the air and then coupled the solution to the energy equation of moving fluid domain with input of fluid viscosity values. For low frequency induction heating material which has a relatively long thermal time constant as compared with the electromagnetic time constant, the computational cost could be enormous. The following Chapter 4 will be on the discussion of low frequency induction heating in conducting material over a long period of time.

- **Chapter 4: Finite Element Modelling of Thermo-Coupled Electromagnetic Problems.**

  Heating effects due to induced eddy current and copper I^2R losses are topics of discussion in this chapter. The eddy currents equation will be solved as an AC problem. The temperature rise in conducting materials such as aluminium and copper are studied. The surface convection and radiation coefficients are obtained from the empirical correlations for various geometry at different orientations. Several characteristics of the method will be investigated and experimental results will be presented to verify the method. Galerkin's upwinding technique is applied for the velocity term in the moving eddy current and thermal regions. Accurate thermal modelling is particularly important when optimising a machine thermal design.

- **Chapter 5: Finite Element Modelling of Cogging Torque in Permanent Magnet Machines.**

  The effects of cogging torque, an unwanted element due to magnetic interactions in PM machines, are discussed here. Several design techniques are used in the efforts of reducing this unwanted torque. Basically 3D finite element models of PM machines are built and then simulated at very low rotational speed in order to calculate the cogging torque produced in each individual machine.

  The computational results are then validated with the real-time measurements obtained from test machines provided by industries.

- **Chapter 6: Optimisation of Electromagnetic Devices using Parameterised Templates.**

  Parameterised template meshing for rapid remodelling of electrical machines

and various devices are discussed in this chapter. A permanent magnet (PM) machine, synchronous generator and Fluxset sensor are modelled using this technique.

A design optimisation technique based on the Simplex algorithm coupled to the parameterised templates is also discussed. The feasibility of the technique is demonstrated with a case study of harmonics reduction in the generated voltage of a synchronous generator with salient-pole configuration.

- **Chapter 7: Some Practical Applications of Parameterised Templates in Modelling Linear Induction and PM Machines.**

  The parameterised templates technique is applied to assist in the work of designing two linear electrical machines. The design exercise is part of an ongoing research and development of linear permanent magnet (PM) machines and linear induction machines (LIM) for industrial applications.

- **Chapter 8: Conclusions.**

  Concludes the research in this thesis.

Chapter 2

Finite Element Theory: An Overview

2.1 Introduction

Increasingly in today's world, a large part of design work consists of creating numerical models of real objects. These prototypes exist only as computer models which enables the models to be examined more closely for better understandings. This approach is useful in that many designs can be tested and modifications are not expensive.

The finite element method is a numerical technique for obtaining approximate solutions to a wide area of engineering problems. Originally developed for stress analysis in complex airframes structure, it has since found extended use in the broad field of continuum mechanics, and problems of non-linear magnetics with application to transformers, electrical machines and other power devices. It is widely used now by designers to determine the performance and efficiency of a likely successful design.

One particular area where finite elements are widely used is in solving electromagnetic field problems which are too complex to be solved using the analytical method, especially those involving non-linear characteristics. In solving such field problems, it is often necessary to obtain approximate numerical solutions to the problems rather than the exact solutions.

For modelling devices numerically, the device of interest is discretised into subregions called finite element by this technique. The non-linear partial differential equation derived from Maxwell's equation is then invoked to describe the variation of the magnetic scalar or vector potentials throughout the device.

Many finite element packages have recently become commercially available. A good example of a powerful software applying this technique for solving 2D and 3D electromagnetic problems is *MEGA*. It is a fully integrated software package developed by the Applied Electromagnetics Research Group of the University of Bath.

2.2 Maxwell's Equations

The governing equations of electromagnetic field problems can be described very concisely by a single set of equations, namely those of Maxwell [7].

Maxwell's equations are the basic equations which define the field equations solved by *MEGA*. The displacement current term in Ampère's law is found to be insignificant compared with the current density term at power frequencies. Consequently a subset of Maxwell's equations can be used:

$$\nabla \times \boldsymbol{H} = \boldsymbol{J} \tag{2.1}$$

$$\nabla \times \boldsymbol{E} = -\frac{\partial \boldsymbol{B}}{\partial t} \tag{2.2}$$

$$\nabla \cdot \boldsymbol{B} = 0 \tag{2.3}$$

The continuity condition, the relations between $\boldsymbol{J}$ and $\boldsymbol{E}$ as well as $\boldsymbol{B}$ and $\boldsymbol{H}$ are added for the solution of all these equations. The known constitutive conditions:

$$\nabla \cdot \boldsymbol{J} = 0 \tag{2.4}$$

$$\boldsymbol{J} = \sigma \boldsymbol{E} \tag{2.5}$$

$$\boldsymbol{B} = u\boldsymbol{H} \tag{2.6}$$

With the equivalent mathematical integral of Maxwell's equations of the form

$$\oint \boldsymbol{H} \cdot d\ell = \int_s \boldsymbol{J} \cdot \mathrm{d}s \tag{2.7}$$

$$\oint \boldsymbol{E} \cdot d\ell = -\int_s \frac{\partial \boldsymbol{B}}{\partial t} \cdot \mathrm{d}s \tag{2.8}$$

These correspond to Ampère's circuital and Faraday's laws respectively.

And

$$\int_s \boldsymbol{B} \cdot \mathrm{d}s = 0 \tag{2.9}$$

where the magnetic flux of $\boldsymbol{B}$ over any enclosed surface s is zero.

The interface conditions at the boundary for equations (2.1), (2.2), (2.3) and (2.4) are the continuity of $\boldsymbol{H} \times \hat{\mathbf{n}}$, $\boldsymbol{E} \times \hat{\mathbf{n}}$, $\boldsymbol{B} \cdot \hat{\mathbf{n}}$ and $\boldsymbol{J} \cdot \hat{\mathbf{n}}$ respectively, where $\hat{\mathbf{n}}$ is the normal unit vector at the boundary.

Figure 2.1 shows a typical electromagnetic problem which has been divided into three types of region. Region Ω_ϕ contains the source currents and is solved using the reduced scalar potential, ϕ. Region Ω_ψ is the non-conducting regions without source currents and is assigned the full scalar potential ψ. Region $\Omega_{\boldsymbol{A}}$ represents the eddy current regions which the magnetic vector potential $\boldsymbol{A}$ is required for solving.

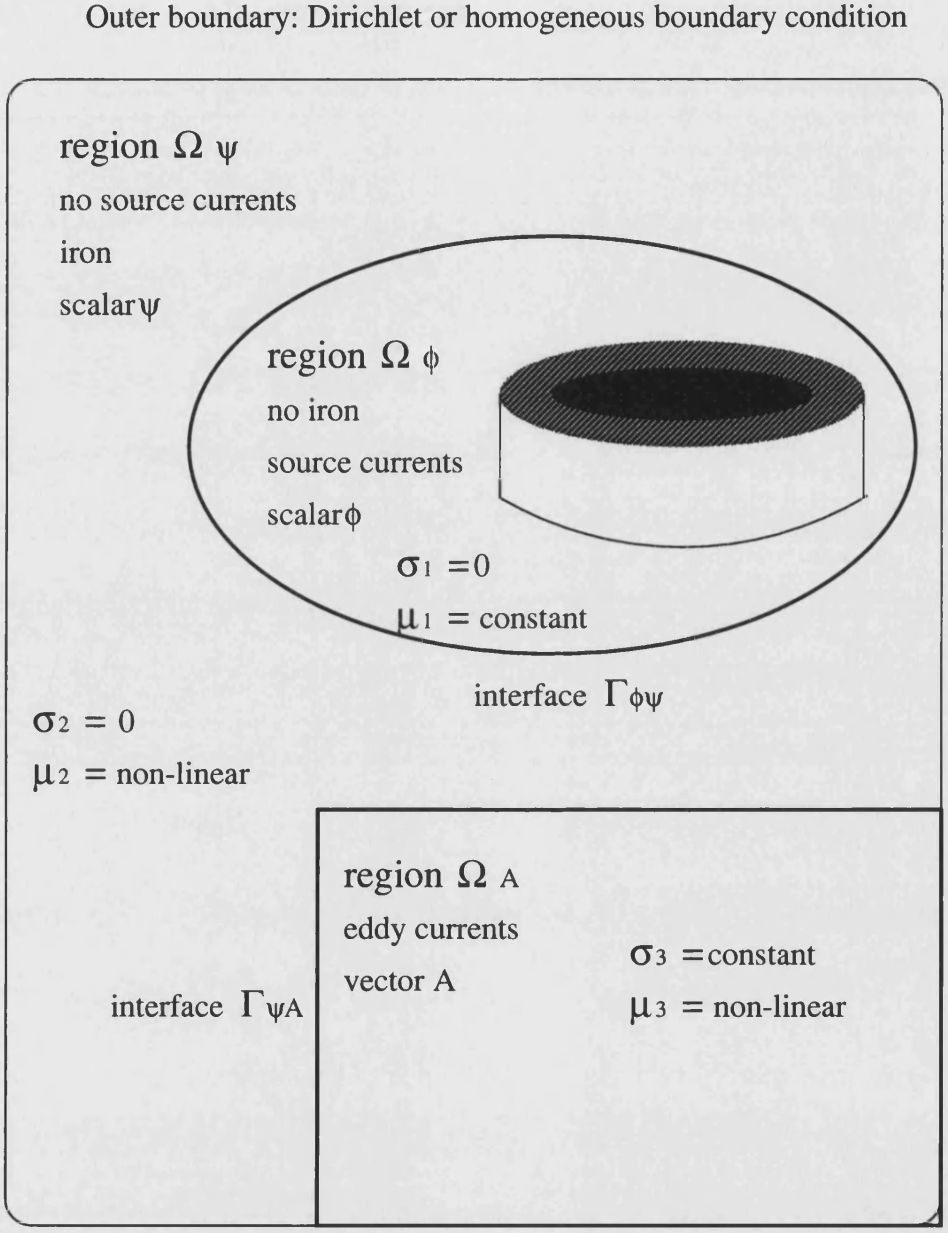

Figure 2.1: Partitioning of a typical electromagnetic problem.

2.3 Governing Equations for 3D Magnetostatic Problems

Solving for magnetic field due to current-carrying conductors near a non-linear magnetic material (e.g iron) in region Ω_ψ of Figure 2.1 often leads to 3D modelling.

The problem can be formulated in terms of magnetic vector potential $\boldsymbol{A}$ but in 3D cases this means that three components of $\boldsymbol{A}$ have to be solved. Other than expensive computation, the difficulties associated with $\nabla \cdot \boldsymbol{A}$ make it more desirable to look for another approach. A more economical approach would to use the magnetic scalar potential ψ [8], [9].

2.3.1 Non-conducting Regions with Source Currents

The magnetic field intensity in region Ω_ϕ containing the source currents can be separated into two parts corresponding to a source field $\boldsymbol{H_S}$ and induced magnetisation $\boldsymbol{H_M}$ in the material

$$\boldsymbol{H} = \boldsymbol{H_S} + \boldsymbol{H_M} \tag{2.10}$$

The Biot-Savart law can be used to solve the equation

$$\nabla \times \boldsymbol{H_S} = \boldsymbol{J} \tag{2.11}$$

Since the Maxwell equation

$$\nabla \times \boldsymbol{H} = \boldsymbol{J} \tag{2.12}$$

applying to time-invariant situations must be satisfied, it follows that the curl of $\boldsymbol{H_M}$ must be zero. This implied that $\boldsymbol{H_M}$ can be defined as the gradient of a scalar

$$\boldsymbol{H} = \boldsymbol{H_S} - \nabla\phi \tag{2.13}$$

where ϕ is known as the reduced scalar potential.

Since $\nabla \cdot \boldsymbol{B} = 0$ and $\boldsymbol{B} = \mu_1 \boldsymbol{H}$, the governing equation can be written as

$$\nabla \cdot \mu_1 \boldsymbol{H}_S - \nabla \cdot \mu_1 \nabla \phi = 0 \tag{2.14}$$

which is further reduced to the simple ϕ expression

$$\nabla \cdot \mu_1 \nabla \phi = 0 \tag{2.15}$$

The reduced scalar method is not applicable in regions where iron is present (region Ω_ψ). Equation (2.14) would lead to numerical difficulties since as the material permeability $\mu \to \infty$, $\boldsymbol{H} \to 0$, which means $\boldsymbol{H}_S$ and $\boldsymbol{H}_M$ are nearly equal and opposite. A full scalar potential ψ would have to be used to remedy the situation.

2.3.2 Non-conducting Regions without Source Currents

In current free regions, the magnetic field can be described entirely in terms of the magnetic scalar potential ψ. This method makes the curl of $\boldsymbol{H}$ free, and so only the divergence of $\boldsymbol{B}$ needs to be enforced.

A typical source free 3D non-conducting region is modelled using full magnetic scalar potential ψ as stated above. The magnetic field strength is derived by taking the gradient of this scalar field

$$\boldsymbol{H} = -\nabla \psi \tag{2.16}$$

Therefore, the magnetic field can be efficiently described by a single scalar variable. Using a scalar potential thus ensured that $\nabla \times \boldsymbol{H} = 0$. The divergence of $\boldsymbol{B}$ must then be made zero.

This leads to the governing equation for the non-conducting regions in terms of ψ

$$\nabla \cdot \mu_2 \nabla \psi = 0 \tag{2.17}$$

The basic full scalar ψ and reduced scalar ϕ methods can be extended to allow multiply connected conditions [10], and to produce cuts for multiply connected problems.

2.4 Governing Equations for 3D Magnetodynamic Problems

The $\boldsymbol{A} - V$ formulation is the classical method of representing electromagnetic fields using magnetic vector potential and electric scalar potential for modelling eddy current regions.

2.4.1 Eddy Current Regions

Again with reference to Figure 2.1, region $\Omega_{\boldsymbol{A}}$ represents a domain in which eddy currents can flow. A 3-component vector provides one of the most economic descriptions of the field behaviour.

An usual method for solving the magnetic field $\boldsymbol{B}$ involves first defining a magnetic vector potential, such that

$$\boldsymbol{B} = \nabla \times \boldsymbol{A} \tag{2.18}$$

The magnetic field $\boldsymbol{B}$ found from $\boldsymbol{A}$ as defined in equation (2.18) will have zero divergence because of the vector identity $\nabla \cdot \nabla \times \boldsymbol{A} = 0$ for any vector potential $\boldsymbol{A}$. Thus, equation (2.3) is satisfied.

Then according to Faraday's law

$$\nabla \times \boldsymbol{E} = -\frac{\partial(\nabla \times \boldsymbol{A})}{\partial t} \tag{2.19}$$

Integrating both sides of the equation (2.19) yields the following expression for $\boldsymbol{E}$

$$\boldsymbol{E} = -\frac{\partial \boldsymbol{A}}{\partial t} - \nabla V \tag{2.20}$$

The $\frac{\partial \boldsymbol{A}}{\partial t}$ term is normally associated with the induced $e.m.f$ due to the varying magnetic field and the V term is to ensure complete generality since the curl of any gradient is equal to zero.

Using equation (2.5) gives

$$\boldsymbol{J} = -\sigma_3\left(\frac{\partial \boldsymbol{A}}{\partial t} + \nabla V\right) \tag{2.21}$$

The total current density $\boldsymbol{J}$ is made up of the time-dependent eddy current density $\boldsymbol{J_E}$ and source current density $\boldsymbol{J_S}$.

It can be seen from equation (2.21) that

$$\boldsymbol{J_E} = -\sigma_3 \frac{\partial \boldsymbol{A}}{\partial t} \tag{2.22}$$

And

$$\boldsymbol{J_S} = -\sigma_3 \nabla V \tag{2.23}$$

Taking the divergence of equation (2.21) gives

$$\nabla \cdot \sigma_3\left(\frac{\partial \boldsymbol{A}}{\partial t} + \nabla V\right) = 0 \tag{2.24}$$

It is known that $\nabla \times \boldsymbol{H} = \boldsymbol{J}$, thus using the $\boldsymbol{A} - V$ potentials in Ampère's law yields

$$\nabla \times \frac{1}{\mu_3}(\nabla \times \boldsymbol{A}) + \sigma_3\left(\frac{\partial \boldsymbol{A}}{\partial t} + \nabla V\right) = 0 \tag{2.25}$$

However, equations (2.24) and (2.25) cannot ensure an unique solution for $\boldsymbol{A} - V$. A penalty term constraining the divergence of $\boldsymbol{A}$ to be zero can be added and together with the additional constraint of $\boldsymbol{A} \cdot \hat{\mathbf{n}}$ on the boundary regions establish the independence between both equations. Thus, ensuring that the solution is unique. This scheme is implemented in *MEGA* with equation (2.25) now rewritten as

$$\nabla \times \frac{1}{\mu_3}(\nabla \times \boldsymbol{A}) - \left\{\frac{1}{\mu_3}\nabla\nabla \cdot \boldsymbol{A}\right\} = -\sigma_3\left(\frac{\partial \boldsymbol{A}}{\partial t} + \nabla V\right) \tag{2.26}$$

The term in { } is the added penalty term constraining the divergence of $\boldsymbol{A}$ to be zero [11]. To ensure the solution is unique the additional constraint

$$\boldsymbol{A} \cdot \hat{\mathbf{n}} = 0 \tag{2.27}$$

is added on the $\boldsymbol{A} - \psi$ interface.

2.4.2 Eddy Current Regions with Constant Conductivity

To model the eddy current regions of $\Omega_{\boldsymbol{A}}$ in Figure 2.1 the V term can be ignored since the conductivity is constant.

$$\nabla \times \frac{1}{\mu_3}(\nabla \times \boldsymbol{A}) + \sigma_3\left(\frac{\partial \boldsymbol{A}}{\partial t}\right) = 0 \tag{2.28}$$

For a complete description of the problem equation (2.28) must be solved together with two other conditions

$$\nabla \cdot \boldsymbol{J} = 0 \tag{2.29}$$

inside the conductors, and

$$\boldsymbol{J} \cdot \hat{\mathbf{n}} = 0 \tag{2.30}$$

at the interface between the conducting regions.

The first condition equation (2.29) is evident when solving equation (2.28), since we know

$$\nabla \cdot \boldsymbol{J} = \nabla \cdot \sigma_3 \frac{\partial \boldsymbol{A}}{\partial t} \tag{2.31}$$

therefore,

$$\nabla \cdot [\nabla \times \frac{1}{\mu_3}(\nabla \times \boldsymbol{A})] = \nabla \cdot \boldsymbol{J} = 0 \tag{2.32}$$

The second condition on the inside surface of the conductors is weakly implied by the surface integral terms of the $\boldsymbol{A}$ equation {described in section 2.6 } on the conducting - non-conducting interface. The surface integral is expressed in terms of non-conducting scalar potential variables and as the consequence the condition that $\boldsymbol{J} \cdot \hat{\mathbf{n}} = 0$ is weakly imposed [12], [13].

2.5 Boundary Conditions

The laws governing the behaviour of the vector fields at discontinuities in the regions interface stem from the necessity that the integral forms of the Maxwell equations must be satisfied for surfaces and lines straddling such boundaries.

The continuity conditions at the interfaces between adjacent elements *interelement* within a same region and those at the boundary between regions *interregion* must be either weakly or strongly enforced [14].

2.5.1 Interelement Boundary Conditions for Magnetic Scalar Potential Regions

The boundary conditions for the two 2D elements shown in Figure 2.2 are that $\boldsymbol{H} \times \hat{\mathbf{n}}$ and $\boldsymbol{B} \cdot \hat{\mathbf{n}}$ are continuous at the interface.

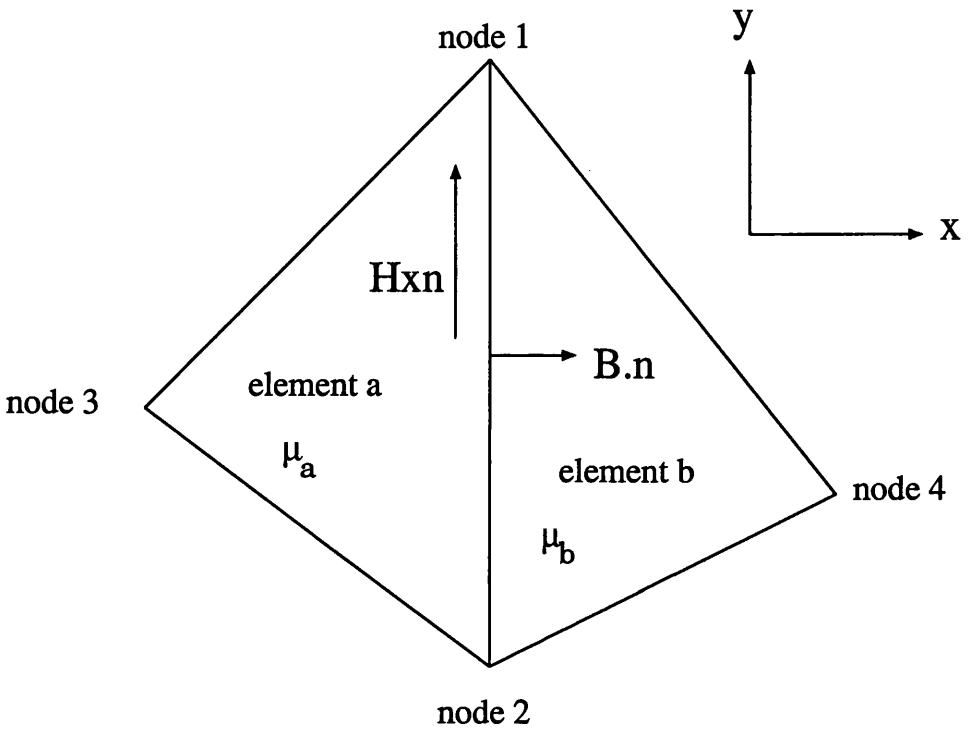

Figure 2.2: 2D elements.

The $\boldsymbol{H} \times \hat{\mathbf{n}}$ boundary condition is automatically satisfied just by making the scalar potential ψ continuous since one of the component of $\boldsymbol{H}$, $H_{y_a} = H_{y_b} = -\dfrac{\partial \psi}{\partial y}$ on the common facet of the two elements along the line adjoining nodes 1 and 2.

The $\boldsymbol{B} \cdot \hat{\mathbf{n}}$ continuous condition means that

$$\mu_a \frac{\partial \psi}{\partial x_a} = \mu_b \frac{\partial \psi}{\partial x_b} \tag{2.33}$$

It is weakly enforced and to solve the equation, the line integral terms of

$$\oint N_i \mu_a \frac{\partial \psi}{\partial n} \mathrm{d}\ell \tag{2.34}$$

is used to combine all the common node equations of the adjacent elements. The result is that the line terms along nodes 1 and 2 naturally cancel each other out and therefore, are not explicitly enforced.

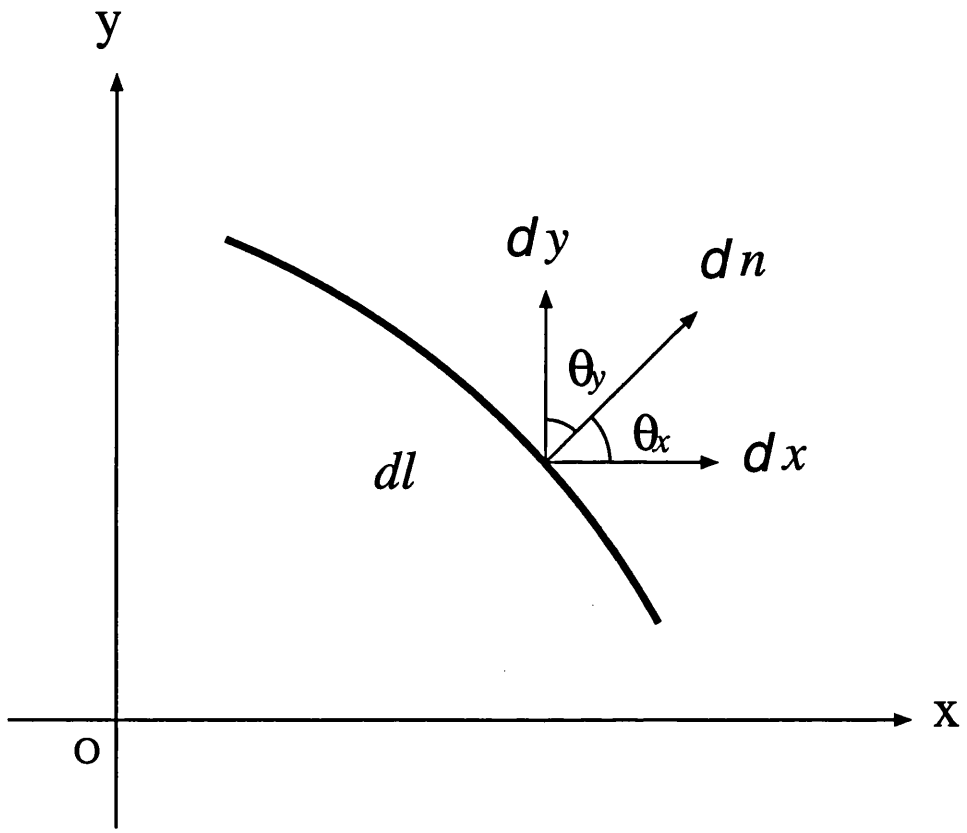

Figure 2.3: Bounding curve.

Notice that, from Figure 2.3,

$$\frac{\partial \psi}{\partial n} = \frac{\partial \psi}{\partial x} n_x + \frac{\partial \psi}{\partial y} n_y$$

where $n_x = \dfrac{\partial x}{\partial n}$ and $n_y = \dfrac{\partial y}{\partial n}$ are the direction cosines of the outward normal vector $\hat{\mathbf{n}}$ to the bounding curve $\mathrm{d}\ell$.

The full expression for equation (2.34) is therefore

$$\oint N_i \mu_a \frac{\partial \psi}{\partial n} \, \mathrm{d}\ell = \oint N_i \mu_a \left[\frac{\partial \psi}{\partial x} n_x + \frac{\partial \psi}{\partial y} n_y \right] \mathrm{d}\ell \tag{2.35}$$

On the outer boundary the interface conditions of $\boldsymbol{B} \cdot \hat{\mathbf{n}} = 0$ and $\boldsymbol{H} \times \hat{\mathbf{n}} = 0$ are easily satisfied just by ignoring the line integral on the boundary in the former case, and setting the scalar potential ψ to the same value along the required boundary in the latter case.

2.5.2 Interelement Boundary Conditions for Magnetic Vector Potential Regions

Similarly, the boundary conditions that $\boldsymbol{H} \times \hat{\mathbf{n}}$ is continuous and $\boldsymbol{B} \cdot \hat{\mathbf{n}}$ is continuous have to be satisfied.

The $\boldsymbol{B} \cdot \hat{\mathbf{n}}$ condition is satisfied since the derivative of the A_z vector potential component is the same in both elements

$$B_x = \frac{\partial A_z}{\partial y} \tag{2.36}$$

The condition $\boldsymbol{H} \times \hat{\mathbf{n}}$ is continuous means that

$$\frac{1}{\mu_a} \frac{\partial A_z}{\partial x_a} = \frac{1}{\mu_b} \frac{\partial A_z}{\partial x_b} \tag{2.37}$$

This interface condition is weakly enforced just like the magnetic scalar potential case by integrating the line integral

$$\oint N_i \left[\frac{1}{\mu_a} \frac{\partial A_z}{\partial x} n_x + \frac{1}{\mu_a} \frac{\partial A_z}{\partial y} n_y \right] \mathrm{d}\ell \tag{2.38}$$

2.5.3 Non-conducting and Source Current Regions Interface

The interface requirements at the boundary between regions Ω_ψ and Ω_ϕ are as usual that the normal component of $\boldsymbol{B}$ and the tangential component of $\boldsymbol{H}$ should be continuous.

The normal component of $\boldsymbol{B}$ implies

$$\mu_1(\boldsymbol{H}_S - \nabla\phi) \cdot \hat{\mathbf{n}} = -\mu_2(\nabla\psi) \cdot \hat{\mathbf{n}} \tag{2.39}$$

The tangential component of $\boldsymbol{H}$ implies

$$(\boldsymbol{H}_S - \nabla\phi) \times \hat{\mathbf{n}} = -(\nabla\psi) \times \hat{\mathbf{n}} \tag{2.40}$$

Equation (2.40) can be integrated along the interface, giving

$$\phi - \int \boldsymbol{H}_{ST} \cdot d\ell = \psi \tag{2.41}$$

which enables one of the scalar unknowns on the interface to be eliminated.

2.5.4 Eddy Current and Non-conducting Regions Interface

At the interface between an eddy current region and a non-conducting region, the continuity conditions are as follows

The normal component of $\boldsymbol{B}$

$$-\mu_2(\nabla\psi) \cdot \hat{\mathbf{n}} = (\nabla \times \boldsymbol{A}) \cdot \hat{\mathbf{n}} \tag{2.42}$$

The tangential component of $\boldsymbol{H}$

$$-(\nabla\psi) \times \hat{\mathbf{n}} = (\frac{1}{\mu_3}\nabla \times \boldsymbol{A}) \times \hat{\mathbf{n}} \tag{2.43}$$

The normal component of $\boldsymbol{J}$

$$(\sigma_3 \frac{\partial \boldsymbol{A}}{\partial t}) \cdot \hat{\mathbf{n}} = 0 \tag{2.44}$$

2.6 Numerical Implementation of $A-\psi-\phi$ Formulations

Before all governing equations in the previous section are solved, each region of the problem is discretised into finite elements and assigned the appropriate approximate functions within each element.

The form of finite element solution is typically written as the summation of the products of the unknown nodal parameters and their corresponding shape functions. The scalar potential solution is then stated as

$$\psi = \sum N_i \psi_i \tag{2.45}$$

where ψ_i is the unknown scalar potential parameter at the i-th node and N_i is the shape function for that particular node. A similar expression can be used to represent the magnetic vector potential $\boldsymbol{A}$ solution.

The shape functions N_i cannot be chosen arbitrarily but rather a certain continuity criteria must be met to ensure that the convergence requirements are satisfied. For example, if at element interfaces the field variable is continuous then it is C_0 continuity, and if in addition, the 1st-order derivatives are also continuous then it is C_1 continuity and so on.

After assigning all the proper trial solutions and shape functions, the following step is to transform the governing equations into appropriate integral form and assembled for solving. One popular method for achieving this is the Galerkin weighted residual method where the weighting functions are chosen to be the same as the element shape functions.

The unknown nodal parameters are now chosen such that the trial function becomes the best approximation to the exact solution through direct references to the region governing equations and boundary constraints.

The basic technique consists of substituting the approximate trial solution with its many unknown nodal parameters into the original governing equations and boundary conditions. This results in an error known as the residual which would have vanished everywhere inside the region or on the boundary had the correct trial function been found. This residual is required to vanish in some average sense over the entire solution domain.

2.6.1 Numerical Model of the Non-conducting Regions

Consider the Galerkin weighted residual treatment of the governing equation (2.15) in region Ω_ϕ and equation (2.17) in region Ω_ψ.

For region Ω_ϕ, applying the Galerkin weighted technique to the Laplacian equation in ϕ results in a set of linear equations of the form

$$\int_{\Omega_\phi} N\,(\mu_1 \nabla^2 \phi)\,\mathrm{d}\Omega = 0 \tag{2.46}$$

where N is the weighting functions.

It is convenient to transform this equation by means of Green's theorem to eliminate the 2nd-order derivatives in the functional:

$$-\int_{\Omega_\phi} \mu_1 (\nabla N \cdot \nabla \phi)\,\mathrm{d}\Omega + \oint_{\Gamma_{\phi\psi}} N \mu_1 \frac{\partial \phi}{\partial n}\,\mathrm{d}\Gamma = 0 \tag{2.47}$$

Similarly, for the non-conducting regions with no source currents Ω_ψ the usual Laplacian equation is reduced to

$$\int_{\Omega_\psi} N\,(\nabla \cdot \mu_2 \nabla \psi)\,\mathrm{d}\Omega = 0 \tag{2.48}$$

Using the Green's theorem to transform equation (2.48) yields

$$-\int_{\Omega_\psi} \mu_2 (\nabla N \cdot \nabla \psi)\,\mathrm{d}\Omega + \oint_{\Gamma_{\psi\phi}} N \mu_2 \frac{\partial \psi}{\partial n}\,\mathrm{d}\Gamma = 0 \tag{2.49}$$

The scalar fields volume is divided into a set of simple subdomains. Within each element, the fields ϕ, ψ are described by a linear combination of nodal values and simple geometric functions of coordinates expressed by equation (2.45).

In the Galerkin method, the weighting functions are the same as the shape functions. In equations (2.47), (2.49) the scalar fields are now expanded according to equation (2.45) for each finite element. Thus, the contribution of the i-th nodes of element e in scalar regions are

$$\int_{\Omega_{\phi e}} \sum_{j=1}^{m} \mu_1 \left(\frac{\partial N_i}{\partial x}\frac{\partial N_j}{\partial x} + \frac{\partial N_i}{\partial y}\frac{\partial N_j}{\partial y} + \frac{\partial N_i}{\partial z}\frac{\partial N_j}{\partial z} \right) \phi_j\,\mathrm{d}\Omega - \oint_{\Gamma_{\phi e}} \mu_1 N_i \frac{\partial \phi}{\partial n}\,\mathrm{d}\Gamma \tag{2.50}$$

$$\int_{\Omega_{\psi e}} \sum_{j=1}^{m} \mu_2 \left(\frac{\partial N_i}{\partial x}\frac{\partial N_j}{\partial x} + \frac{\partial N_i}{\partial y}\frac{\partial N_j}{\partial y} + \frac{\partial N_i}{\partial z}\frac{\partial N_j}{\partial z} \right) \psi_j\,\mathrm{d}\Omega - \oint_{\Gamma_{\psi e}} \mu_2 N_i \frac{\partial \psi}{\partial n}\,\mathrm{d}\Gamma \tag{2.51}$$

If Γ_{ϕ_e} and Γ_{ψ_e} are interior surfaces in their respective regions, ignoring the surface integral will automatically yield the continuity condition of equation (2.33) as the same integral with an opposite sign for the normal $\hat{\mathbf{n}}$ will arise from the other element which shares the same surface. If Γ_{ψ_e} is on the outer periphery then a Neumann condition arises naturally when the surface term is ignored.

When Γ_{ϕ_e} interfaced with Γ_{ψ_e} the sum of the residuals for both regions is

$$-\int_{\Omega_\phi} \mu_1(\nabla N \cdot \nabla\phi)\,\mathrm{d}\Omega - \int_{\Omega_\psi} \mu_2(\nabla N \cdot \nabla\psi)\,\mathrm{d}\Omega + \oint_{\Gamma_{\phi\psi}} N\left(\mu_1\frac{\partial\phi}{\partial n} - \mu_2\frac{\partial\psi}{\partial n}\right)\mathrm{d}\Gamma = 0 \quad (2.52)$$

The surface integral terms located on the $\phi - \psi$ interface are combined to yield the expression $\boldsymbol{H}_S$, equation (2.39). These source terms are moved to the right hand side $(r.h.s)$ of the matrix equations containing all the known terms.

On the interface $\Gamma_{\boldsymbol{A}\psi}$ between regions $\Omega_{\boldsymbol{A}}$ and Ω_ψ, the surface integral term of the reduced scalar ϕ of equation (2.52) is removed and the remaining surface term is used to link the normal component of $\boldsymbol{B}$ between the two regions, that is

$$-\oint_{\Gamma_{\boldsymbol{A}\psi}} N\,\mu_2\frac{\partial\psi}{\partial n}\,\mathrm{d}\Gamma = \oint_{\Gamma_{\boldsymbol{A}\psi}} N\,(\nabla \times \boldsymbol{A}\cdot\hat{\mathbf{n}})\,\mathrm{d}\Gamma \quad (2.53)$$

where $\nabla \times \boldsymbol{A}$ must be expanded in terms of shape functions and nodal parameters of $\boldsymbol{A}$ from the adjacent element in region $\Omega_{\boldsymbol{A}}$.

2.6.2 Numerical Model of the Conducting Regions

The Galerkin method is also used to solve equation (2.28) of the conducting regions $\Omega_{\boldsymbol{A}}$

$$\int_{\Omega_{\boldsymbol{A}}} \boldsymbol{N}\cdot\left[\nabla\times\frac{1}{\mu_3}(\nabla\times\boldsymbol{A}) + \sigma_3\frac{\partial\boldsymbol{A}}{\partial t}\right]\mathrm{d}\Omega = 0 \quad (2.54)$$

If the material permeability μ_3 is constant, the first term of equation (2.54) can be expanded according to the vector identity given by equation (A.16) of Appendix A, as

$$\nabla\times\frac{1}{\mu_3}(\nabla\times\boldsymbol{A}) = -\frac{1}{\mu_3}\left[\nabla\cdot\nabla\boldsymbol{A} - \nabla\nabla\cdot\boldsymbol{A}\right] \quad (2.55)$$

Setting $\nabla \cdot \boldsymbol{A} = 0$ and substituting the above vector identity into equation (2.54) leads to the *diffusion* equation of

$$\int_{\Omega_{\boldsymbol{A}}} N_{xi}\Big(-\nabla \cdot \frac{1}{\mu_3}\nabla A_x + \sigma_3 \frac{\partial A_x}{\partial t}\Big)\, \mathrm{d}\Omega \tag{2.56}$$

with similar equations for the y and z components.

Applying Green's theorem yields

$$\int_{\Omega_{\boldsymbol{A}}} \Big(\frac{1}{\mu_3}\nabla N_{xi} \cdot \nabla A_x + N_{xi}\sigma_3 \frac{\partial A_x}{\partial t}\Big)\, \mathrm{d}\Omega - \oint_{\Gamma_{\boldsymbol{A}_\psi}} N_{xi} \frac{1}{\mu_3}\frac{\partial A_x}{\partial n}\, \mathrm{d}\Gamma = 0 \tag{2.57}$$

for node i with N_{xi} at element e of the conducting regions. The equations for N_{yi} and N_{zi} are of exactly the same form.

If μ_3 is non-linear, applying the Green's theorem on the equation (2.54) results in the expression

$$-\oint_{\Gamma_{\boldsymbol{A}_\psi}} \boldsymbol{N} \cdot \frac{1}{\mu_3}(\nabla \times \boldsymbol{A} \times \hat{\mathbf{n}})\, \mathrm{d}\Gamma + \int_{\Omega_{\boldsymbol{A}}} \Big[\frac{1}{\mu_3}(\nabla \times \boldsymbol{N}) \cdot (\nabla \times \boldsymbol{A}) + \boldsymbol{N} \cdot \sigma_3 \frac{\partial \boldsymbol{A}}{\partial t}\Big]\, \mathrm{d}\Omega = 0 \tag{2.58}$$

Examining the interface conditions at the surface, H_y and H_z must be continuous. Continuity of H_y requires that

$$-\frac{1}{\mu_{3_1}}\frac{\partial A_z}{\partial x_1} + \frac{1}{\mu_{3_1}}\frac{\partial A_x}{\partial z_1} = -\frac{1}{\mu_{3_2}}\frac{\partial A_z}{\partial x_2} + \frac{1}{\mu_{3_2}}\frac{\partial A_x}{\partial z_2} \tag{2.59}$$

Since the transverse derivatives $\dfrac{\partial A_x}{\partial z}$ is continuous, equation (2.59) indicates that there is a discontinuity in the normal derivative of A_z when $\dfrac{1}{\mu_{3_1}} \neq \dfrac{1}{\mu_{3_2}}$, i.e.

$$\frac{\partial A_z}{\partial x_1} = \frac{\mu_{3_1}}{\mu_{3_2}}\frac{\partial A_z}{\partial x_2} + \frac{\mu_{3_2} - \mu_{3_1}}{\mu_{3_2}}\frac{\partial A_x}{\partial z} \tag{2.60}$$

On surface $\Gamma_{A\psi}$

$$H_y: \quad -\frac{\partial \psi}{\partial y} = \frac{1}{\mu_3}\Big(-\frac{\partial A_z}{\partial x} + \frac{\partial A_x}{\partial z}\Big); \qquad H_z: \quad -\frac{\partial \psi}{\partial z} = \frac{1}{\mu_3}\Big(\frac{\partial A_y}{\partial x} - \frac{\partial A_x}{\partial y}\Big) \tag{2.61}$$

The surface integral term of equation (2.57) may then be expanded as

$$\int_{\Gamma_{A\psi}} N_{xi}\Big[-\frac{1}{\mu_3}\Big(\frac{\partial A_y}{\partial y}+\frac{\partial A_z}{\partial z}\Big)n_x+\Big(\frac{\partial \psi}{\partial z}+\frac{1}{\mu_3}\frac{\partial A_y}{\partial x}\Big)n_y-\Big(\frac{\partial \psi}{\partial y}-\frac{1}{\mu_3}\frac{\partial A_z}{\partial x}\Big)n_z\Big]\,\mathrm{d}\Gamma \tag{2.62}$$

in which the first two terms arise from $\nabla \cdot \boldsymbol{A} = 0$ and where n_x, n_y, n_z are direction cosines of the normal $\hat{\mathbf{n}}$ to the surface. The surface integral terms on the $\boldsymbol{A} - \psi$ boundary are expressed in terms of

$$\oint_{\Gamma_{A\psi}} \boldsymbol{N} \cdot \frac{1}{\mu_3}(\nabla \times \boldsymbol{A} \times \hat{\mathbf{n}})\,\mathrm{d}\Gamma = \oint_{\Gamma_{A\psi}} \boldsymbol{N} \cdot (-\nabla\psi \times \hat{\mathbf{n}})\,\mathrm{d}\Gamma \tag{2.63}$$

Simple continuity of the $\boldsymbol{A}$ components ensure the continuity of the $\boldsymbol{B} \cdot \hat{\mathbf{n}}$ throughout the conductor region.

2.7 Standard Shape Functions

Shape functions are well-documented in [15]. As stated earlier, using standard finite elements the scalar and vector fields can be represented by

$$\begin{aligned} a &= N_1\,a_1 + N_2\,a_2 + \cdots + N_n\,a_n \\ &= \sum_{i=1}^{n} N_i\,a_i \end{aligned} \tag{2.64}$$

where N_i are the shape functions and a_i are the field variables at node i in each element.

The lugubrious task of writing and solving equations defined initially in terms of the unknown parameters $a_1 \cdots a_n$ can be avoided by adopting the Lagrangian interpolation concepts:

$$\begin{aligned} L_k(\xi) &= \prod_{m=0, m\neq k}^{n} \frac{\xi - \xi_m}{\xi_k - \xi_m} \\ &= \frac{(\xi - \xi_0)\cdot\cdot(\xi - \xi_{k-1})(\xi - \xi_{k+1})\cdot\cdot(\xi - \xi_n)}{(\xi_k - \xi_0)\cdot\cdot(\xi_k - \xi_{k-1})(\xi_k - \xi_{k+1})\cdot\cdot(\xi_k - \xi_n)} \end{aligned} \tag{2.65}$$

$$\begin{aligned} L_k(\eta) &= \prod_{m=0, m\neq k}^{n} \frac{\eta - \eta_m}{\eta_k - \eta_m} \\ &= \frac{(\eta - \eta_0)\cdot\cdot(\eta - \eta_{k-1})(\eta - \eta_{k+1})\cdot\cdot(\eta - \eta_n)}{(\eta_k - \eta_0)\cdot\cdot(\eta_k - \eta_{k-1})(\eta_k - \eta_{k+1})\cdot\cdot(\eta_k - \eta_n)} \end{aligned} \tag{2.66}$$

Since the Lagrangian polynomials possess the properties of the nodal interpolation functions, the shape functions can be immediately derived as

$$N_i(\xi, \eta) = L_i(\xi)\, L_i(\eta) \tag{2.67}$$

In the quadrilateral element of Figure 2.4, the standard shape functions for this element were derived as a simple product of the appropriate terms in the x and y directions. The C° continuity of all the global shape functions is maintained between such elements as the connection of the two nodal values at each corner ensures a unique straight line variation along any element side. The shape functions for the four nodes in the quadrilateral element using the products of the two Lagrangian interpolation functions for a 2D linear element can be expressed as

$$N_1(\xi, \eta) = \frac{\xi - \xi_2}{\xi_1 - \xi_2} \times \frac{\eta - \eta_4}{\eta_1 - \eta_4} = \frac{\xi - 1}{-1 - 1} \times \frac{\eta - 1}{-1 - 1}$$

$$N_2(\xi, \eta) = \frac{\xi - \xi_1}{\xi_2 - \xi_1} \times \frac{\eta - \eta_3}{\eta_2 - \eta_3} = \frac{\xi + 1}{1 + 1} \times \frac{\eta - 1}{-1 - 1}$$

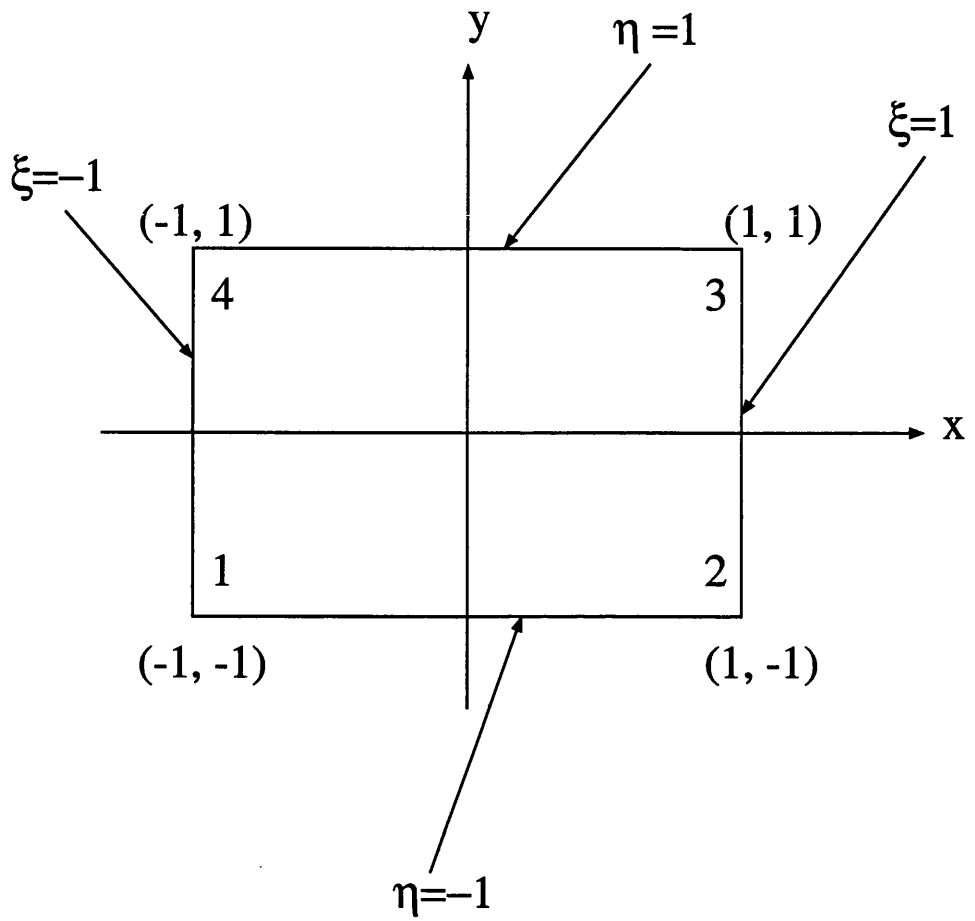

Figure 2.4: Linear quadrilateral element.

$$N_3(\xi,\eta) = \frac{\xi-\xi_4}{\xi_3-\xi_4} \times \frac{\eta-\eta_2}{\eta_3-\eta_2} = \frac{\xi+1}{1+1} \times \frac{\eta+1}{1+1}$$

$$N_4(\xi,\eta) = \frac{\xi-\xi_3}{\xi_4-\xi_3} \times \frac{\eta-\eta_1}{\eta_4-\eta_1} = \frac{\xi-1}{-1-1} \times \frac{\eta+1}{1+1} \tag{2.68}$$

Therefore, the shape functions are found to be:

$$N_1(\xi,\eta) = \frac{1}{4}(1-\xi)(1-\eta)$$

$$N_2(\xi,\eta) = \frac{1}{4}(1+\xi)(1-\eta)$$

$$N_3(\xi,\eta) = \frac{1}{4}(1+\xi)(1+\eta)$$

$$N_4(\xi,\eta) = \frac{1}{4}(1-\xi)(1+\eta) \tag{2.69}$$

Clearly, the shape functions which are formed as the products of the two Lagrangian polynomials would satisfied the requirements of having the value unity at the node for which they are defined and zero at all other nodes. Figure 2.5 shows that if $N_1 = 1.0$, then $N_2 = N_3 = N_4 = 0$, also N_1 varies linearly between nodes 1, 2 and nodes 1, 4. Hence, preserving the C° continuity along the edge 1 - 2 and 1 - 4.

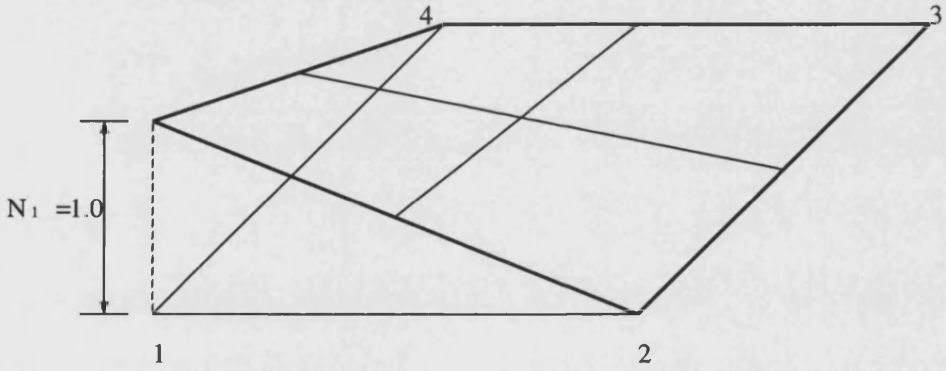

Figure 2.5: Shape functions.

Higher-order shape functions can be formulated in precisely the same way. However, formulating higher-order shape functions using the Lagrangian concept results in the existence of a large number of interior nodes in the elements. This can be avoided by using an alternative series of what is known as the *Serendipity* elements. These elements contains only exterior nodes and their interpolation functions were derived by inspection.

A systematic way of generating derivation of these Serendipity functions are as explained:

- The mid-side shape functions are obtained by taking the appropriate 2nd-order Lagrangian expansion in one direction and then multiply it by a linear function in the other.
- For the corner nodes, the situation is more complex since along the element sides non-zero values for shape functions will be obtained at the mid-side nodes. However, a linear combination of the bilinear shape function type of equation (2.67) and the quadratic shape functions just constructed for the mid-side nodes is suffice to determine the necessary function.

The shape functions are now as follows:

1. Linear element:

$$N_i(\xi,\eta) = \frac{1}{4}(1+\xi\xi_i)(1+\eta\eta_i) \tag{2.70}$$

   which are identical to the 1st-order Lagrangian shape functions.

2. Quadratic element:
   Corner nodes at $\xi_i = \pm 1, \eta_i = \pm 1$

$$N_i(\xi,\eta) = \frac{1}{4}(1+\xi\xi_i)(1+\eta\eta_i)(\xi\xi_i+\eta\eta_i-1) \tag{2.71}$$

   Mid-side nodes at $\xi_i = 0, \eta_i = \pm 1$

$$N_i(\xi,\eta) = \frac{1}{2}(1-\xi^2)(1+\eta\eta_i) \tag{2.72}$$

   Mid-side nodes at $\xi_i = \pm 1, \eta_i = 0$

$$N_i(\xi,\eta) = \frac{1}{2}(1+\xi\xi_i)(1-\eta^2) \tag{2.73}$$

3. Cubic element:

   Corner nodes at $\xi_i = \pm 1, \eta_i = \pm 1$

$$N_i(\xi,\eta) = \frac{1}{32}(1+\xi\xi_i)(1+\eta\eta_i)[9(\xi^2+\eta^2)-10] \tag{2.74}$$

   Mid-side nodes at $\xi_i = \pm 1, \eta_i = \pm\frac{1}{3}$

$$N_i(\xi,\eta) = \frac{9}{32}(1+\xi\xi_i)(1-\eta^2)(1+9\eta\eta_i) \tag{2.75}$$

It is obvious now that mid-side and corner shape functions can be generated by an identical process. For mid-side shape functions a multiplication of the 1st-order and nth-order Lagrangian interpolation is enough to determine N_i. To generate corner shape functions, a combination of the bilinear corner shape functions and the appropriate fractions of the mid-side shape functions to ensure zero at the relevant nodes is necessary.

2.8 Time-Transient Scheme for Non-linear Problems

The application of the Galerkin technique in the $\boldsymbol{A}-\psi-\phi$ finite element formulations results in a system of equations which has the following standard form

$$[\boldsymbol{K}_a]\boldsymbol{x} + [\boldsymbol{C}_a]\dot{\boldsymbol{x}} = \boldsymbol{f}_a \tag{2.76}$$

Time-stepping technique is usually applied for the time-transient problem to solve the finite element matrix system progressively in time. Numerical method such as the **ICCG** scheme can be used to solve at each time-step the finite element matrix.

For non-linear problem, $[\boldsymbol{K}_a]$ matrix is a function of $\boldsymbol{x}$. The non-linear time-transient implementation includes the usage of a time-stepping scheme, which employs the previous solution to determine the solution at the current time-step, together with an embedded non-linear iterative method for correct non-linear field pattern determination to arrest the solution at the current time-step.

If the problem is sinusoidal steady-state, complex representation is used to express the time derivative in equation (2.76) as $j\omega$ and the **ICCG** scheme can be used to solve the $[\boldsymbol{K}_a + jw\boldsymbol{C}_a]$ matrix system.

2.8.1 Time-Stepping Algorithm

The time interval of interest for equation (2.76) is discretised into time-steps. The objective is to obtain an approximation for $\boldsymbol{x}_{n+1}$ given the value of $\boldsymbol{x}_n$ and the forcing vector $\boldsymbol{f}_a$ in the interval of time Δt.

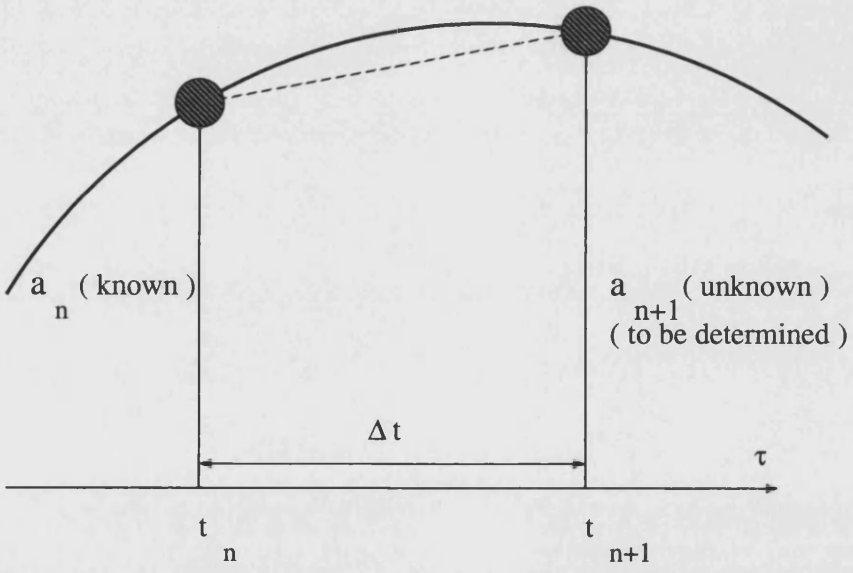

Figure 2.6: Approximation in time domain.

In the interval Δt and assuming a linear expansion in time as shown in Figure 2.6, the solution $\boldsymbol{x}$ is expressed as

$$\boldsymbol{x} \approx \boldsymbol{x}(\tau) = \boldsymbol{x}_n + \frac{\tau}{\Delta t_n}(\boldsymbol{x}_{n+1} - \boldsymbol{x}_n) \tag{2.77}$$

In standard finite element, this equation is translated as

$$\boldsymbol{x}(\tau) = \sum \boldsymbol{N}_i \boldsymbol{x}_i = \left(1 - \frac{\tau}{\Delta t}\right)\boldsymbol{x}_n + \left(\frac{\tau}{\Delta t}\right)\boldsymbol{x}_{n+1} \tag{2.78}$$

in which $\tau = t - t_n$ and $\boldsymbol{x}_n$ is the solution computed at the end of the previous time-step and $\boldsymbol{x}_{n+1}$ is the unknown parameter.

The weighted residual expression is then

$$\int_0^{\Delta t} W([\boldsymbol{K}_a]\boldsymbol{x} + [\boldsymbol{C}_a]\dot{\boldsymbol{x}} - \boldsymbol{f}_a)\,\mathrm{d}\tau = 0 \tag{2.79}$$

Introducing Θ as the weighting parameter defined as

$$\Theta = \frac{1}{\Delta t}\frac{\int_0^{\Delta t} W\tau\,\mathrm{d}\tau}{\int_0^{\Delta t} W\,\mathrm{d}\tau} \tag{2.80}$$

the weighted residual approximation of (2.79) can be solved for all time-steps with the specified Δt using equation (2.78). All potentials are initialised to zero at t = 0 and multiple iterations may be required within each time-step for non-linear problems.

The equation to be solved then can be immediately written as

$$\boldsymbol{K}_a[\boldsymbol{x}_n + \Theta(\boldsymbol{x}_{n+1} - \boldsymbol{x}_n)] + \frac{\boldsymbol{C}_a(\boldsymbol{x}_{n+1} - \boldsymbol{x}_n)}{\Delta t} - \vec{\boldsymbol{f}}_a = 0 \tag{2.81}$$

with $\vec{\boldsymbol{f}}_a$ represented by

$$\vec{\boldsymbol{f}}_a = \frac{\int_0^1 W\boldsymbol{f}_a(t+\tau)\,\mathrm{d}\tau}{\int_0^1 W\,\mathrm{d}\tau} \tag{2.82}$$

A few popular time-stepping schemes exist [16]. The basic difference between them is the choice of the weighting function W. In *MEGA* the unconditional stable *backward*

difference scheme is implemented, where $W = \delta_n(\Delta t)$ with the δ_n representing the Dirac delta function. This form of weighting defined the point collocation technique which ensured that the equation is satisfied at $\tau = \Delta t$.

If the weighting parameter $\Theta = 1$ then the scheme is characterised as *backward difference*. While $\Theta = 0$, $\Theta = 0.5$ and $\Theta = 0.6667$ denote the *forward difference*, *Crank-Nicolson* and *Galerkin* schemes respectively.

2.8.2 Non-linear Iterative Time Schemes

The solution of non-linear problems cannot be approached directly with the time-stepping scheme and some form of iteration is required. In coupled thermo-magnetic situations for example, certain material properties are temperature dependent, which means the matrices are dependent on $\boldsymbol{x}$.

Two well-known iterative techniques are implemented in *MEGA*. They are known as the Simple Iteration method and the Newton-Raphson method.

The Simple Iteration Method

With the Simple Iteration method, the $[\boldsymbol{K}_a]$ matrix remains constant throughout the iteration process. The matrix is solved using the current material properties and updated using the new solution at the following iteration.

The weighted residual approximation is similar to the one expressed for linear matrix:

$$\int_0^{\Delta t} W([\boldsymbol{K}_a]\boldsymbol{x} + [\boldsymbol{C}_a]\boldsymbol{\alpha}_n - \boldsymbol{f}_a)\,\mathrm{d}\tau = 0 \tag{2.83}$$

where $\boldsymbol{\alpha}_n = \frac{\boldsymbol{x}_{n+1} - \boldsymbol{x}_n}{\Delta t}$.

Substituting the Θ expression of equation (2.80), the solution for equation (2.83) becomes

$$\boldsymbol{\alpha}_n = (\Theta \Delta t[\boldsymbol{K}_a] + [\boldsymbol{C}_a])^{-1}(\vec{\boldsymbol{f}}_a - [\boldsymbol{K}_a]\boldsymbol{x}_n) \tag{2.84}$$

The new solution $\boldsymbol{x}_{n+1}$ is obtained by using this rate of change. The $[\boldsymbol{K}_a]$ matrix is updated and the residual computed until the residual tolerance condition is satisfied. The first iteration of the following time-step will then use the final solution of the previous time-step.

Newton-Raphson Method

The Newton-Raphson method is probably the fastest convergent process for solution of non-linear problems, provided we are in the vicinity of the solution. If the $[\boldsymbol{K}_a]$ matrix is itself a function of $\boldsymbol{x}$, then it can be approximated as

$$\boldsymbol{K}_a(\boldsymbol{x}) \approx \boldsymbol{K}_a(\boldsymbol{x}_n^i) + \left(\frac{\partial \boldsymbol{K}_a(\boldsymbol{x})}{\partial \boldsymbol{x}}\right)_n^i (\boldsymbol{x} - \boldsymbol{x}_n) + \frac{1}{2!}\left(\frac{\partial^2 \boldsymbol{K}_a(\boldsymbol{x})}{\partial \boldsymbol{x}^2}\right)_n^i (\boldsymbol{x} - \boldsymbol{x}_n)^2 + ... \tag{2.85}$$

in which the Jacobian matrix is of the form

$$[\mathfrak{J}_n] = \left(\frac{\partial \boldsymbol{K}_a(\boldsymbol{x})}{\partial \boldsymbol{x}}\right)_n^i \tag{2.86}$$

Substituting equation (2.85) into equation (2.79) yields

$$\int_0^{\Delta t} W([\boldsymbol{K}_a(\boldsymbol{x}_n^i)] + [\mathfrak{J}_n]\boldsymbol{\alpha}_n^i \tau + [\boldsymbol{C}_a]\boldsymbol{\alpha}_n^i - \boldsymbol{f}_a)\, \mathrm{d}\tau = 0 \tag{2.87}$$

Using the Θ scheme, the solution for equation (2.87) is

$$\boldsymbol{\alpha}_n^i = ([\boldsymbol{C}_a] + \Theta \Delta t_n[\mathfrak{J}_n])^{-1}[\vec{\boldsymbol{f}}_a - \boldsymbol{K}_a(\boldsymbol{x}_n^i)] \tag{2.88}$$

The *backward difference* scheme is applied when $\Theta = 1$. The computed rate of change $\boldsymbol{\alpha}_n^i$ is then used to obtain $\boldsymbol{x}_{n+1}^i$. The $[\boldsymbol{K}_a]$ matrix is updated according to this solution

and the residual evaluated until the specified tolerance is met. If the tolerance is not met, then a new Jacobian matrix will be formed and equation (2.87) is resolved again and a new α_n^{i+1} is obtained. When the tolerance requirement is satisfied, the solution obtained at the present time-step will be used in the first iteration of the next time-step.

2.9 Summary

The finite element method of analysis is a very powerful computational tool. It has gained wide acceptance in various engineering disciplines such as electromagnetic analysis, thermal and fluid mechanics.

In this chapter the basic finite element method for electromagnetic analysis was introduced. The idea of discretisation and trial functions, which are important to the use of this numerical method were also discussed.

The rapid growth in engineering usage of computer technology will undoubtedly continue to have a significant impact upon the acceptance of the finite element method. Indeed, the finite element technique would not be where it is today if computers had not proliferated and become less expensive.

Chapter 3

Numerical Techniques in Solving Heat Transfer with Non-linear Boundary Conditions

3.1 Introduction

There is an increased tendency to solve thermal formulations using numerical techniques. Methods such as finite-difference, finite-volume, finite element analysis and lumped parameter thermal circuits are used to model heat flow due to conduction within a material domain. The convection boundary condition is usually modelled using some form of curve fit to the known empirical data.

The conductor is modelled using the finite element method as a thermal region with the diffusion governing equation and subjected to time-transient surface convective and radiation heat losses. The heat transfer finite element formulation involves the use of scalar temperature variables T and a *backward* time-difference scheme to model the 2D and 3D time-transient thermal systems.

Special boundary conditions which take into account non-linear convection and radiation are prescribed on the appropriate surfaces as a mean of heat transfer from a domain of interest to the surrounding air at a constant ambient temperature. At this stage empirical methods are employed to model the behaviour of the heat transfer

across the convection and radiation surfaces. Forced and natural convections can be modelled using a set of correlation data. However, the empirical methods are somewhat limited to a few geometries and temperature range. An alternative numerical technique is the Computational Fluid Dynamics (CFD).

The heat generated in the material domain could be due to inductive heating effects, conductive I^2R losses or a known prescribed heat flow rate at the boundary of the domain. Inductive heat loss is generated by the flow of the induced eddy currents in the conducting region. Eddy currents produce their own magnetic field which, in agreement with Lentz's law, tends to oppose the variation of the imposed field. In any case, the circulation of eddy currents leads to unwanted heat dissipation. Inductive heating and winding I^2R losses will be discussed in the following chapter.

This chapter will focused on the modelling of heat flows in conductors with a known constant heat source. The heat transfer is modelled using both the finite element method and lumped parameter thermal circuit technique. Non-linear convective and radiation boundary conditions are prescribed. The characteristic of these boundary conditions are determined by a set of *Churchill-Chu* empirical equations and are strongly temperature dependent.

The analytical or numerical solution of the heat transfer governing equations is often difficult due to non-linearities and coupling terms. In addition, a numerical solution frequently introduces questions of stability and accuracy.

3.2 Mathematical Description of Thermal Transport

3.2.1 Governing Equations

The processes of heat transfer and fluid flow are governed by the fundamental principles from thermodynamics and mechanics. These principles are the conservation of mass, momentum and energy. These conservation principles in turn have local and global forms, respectively leading to differential and integral equations. There are three basic modes by which heat transfer occurs: conduction, convection and radiation.

For heat transfer and fluid flow problems, which arise in the analysis of conduction and convection processes, the most representative differential equation is the general thermal transport equation written in the conservative form as

$$\aleph \frac{\partial \Phi_t}{\partial t} + \Im \nabla \cdot (\boldsymbol{u} \Phi_t) - \nabla \cdot \kappa \nabla \Phi_t - \dot{q} = 0 \tag{3.1}$$

where Φ_t is the unknown single valued function, $\boldsymbol{u}$ is the velocity vector, $\dot{q}$ is the source and $\aleph$, $\Im$ and κ are the specified properties.

In equation (3.1) the term $\Im \nabla \cdot (\boldsymbol{u} \Phi_t)$, which contains the velocity is related to the advection mechanisms while the 2nd-order derivatives term $\nabla \cdot \kappa \nabla \Phi_t$ is the diffusion description.

Transforming the velocity term of transport equation using the appropriate vector identity yields

$$\Im \nabla \cdot (\boldsymbol{u} \Phi_t) = \Im (\boldsymbol{u} \cdot \nabla \Phi_t) + \Im \Phi_t (\nabla \cdot \boldsymbol{u}) \tag{3.2}$$

If the divergence of the velocity field $\nabla \cdot \boldsymbol{u}$ is zero, equation (3.1) is recast as

$$\aleph \frac{\partial \Phi_t}{\partial t} + \Im (\boldsymbol{u} \cdot \nabla \Phi_t) - \nabla \cdot \kappa \nabla \Phi_t - \dot{q} = 0 \tag{3.3}$$

In a *non-moving* conducting region Ω bounded by surface Γ with no flow field, the velocity term can be ignored and the new governing equation is given as

$$\nabla \cdot \kappa \nabla \Phi_t + \dot{q} = \aleph \frac{\partial \Phi_t}{\partial t} \tag{3.4}$$

3.2.2 Boundary Conditions

In addition to the differential equations, the general transport formulation requires the specification of the region geometry and boundary conditions to complete the formulation of a problem.

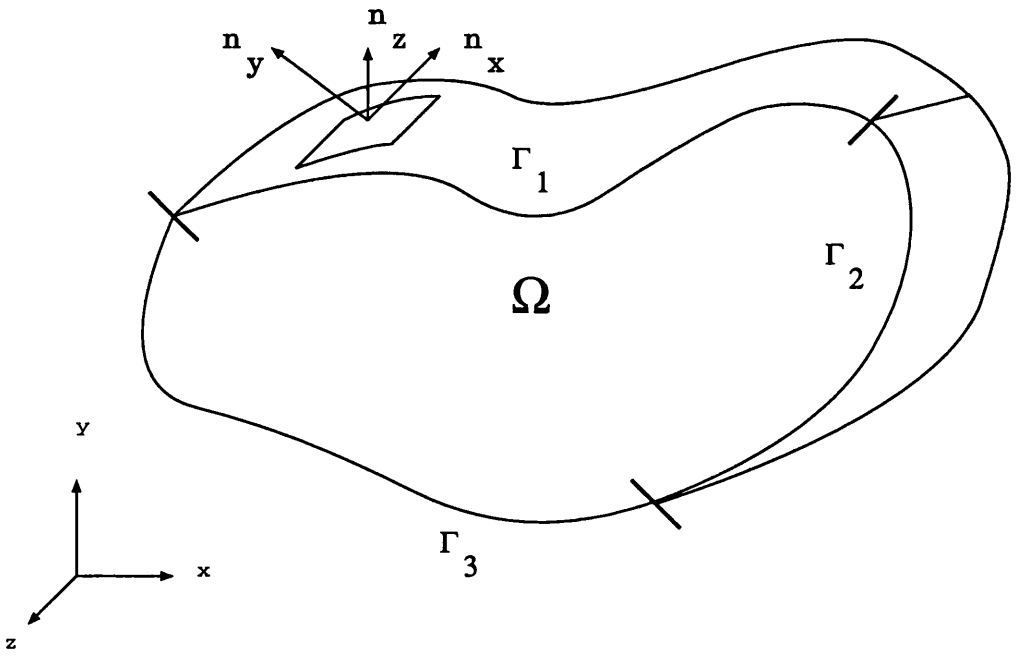

Figure 3.1: A material volume with bounding surfaces.

The most common types of boundary conditions can be illustrated with reference to Figure 3.1 of an arbitrary region Ω bounded by curve Γ:

- The first boundary condition on Γ_1

$$\Phi_t = \boldsymbol{f}_1(x,y,z) \quad \text{on surface } \Gamma_1 \tag{3.5}$$

This type of boundary condition is known as the Dirichlet (function) boundary condition.

- In the second condition, applicable to the boundary Γ_2

$$\frac{\partial \Phi_t}{\partial n} = \boldsymbol{f}_2(x,y,z) \quad \text{on surface } \Gamma_2 \tag{3.6}$$

- The third boundary condition on Γ_3

$$a(x,y,z)\Phi_t + b(x,y,z)\frac{\partial \Phi_t}{\partial n} = \boldsymbol{f}_3(x,y,z) \quad \text{on surface } \Gamma_3 \tag{3.7}$$

Boundaries of this form in Γ_2 and Γ_3 are frequently referred as being the Neumann (gradient) boundary condition.

$\boldsymbol{f}_1(x,y,z)$, $\boldsymbol{f}_2(x,y,z)$ and $\boldsymbol{f}_3(x,y,z)$, a and b are arbitrary functions. The normal derivatives can be expressed as

$$\begin{aligned}
\frac{\partial \Phi}{\partial n} &= \hat{\mathbf{n}} \cdot \nabla \Phi_t \\
&= n_x(\hat{i}) + n_y(\hat{j}) + n_z(\hat{k}) \cdot \left(\frac{\partial \Phi_t}{\partial x}\hat{i} + \frac{\partial \Phi_t}{\partial y}\hat{j} + \frac{\partial \Phi_t}{\partial z}\hat{k} \right) \\
&= \frac{\partial \Phi_t}{\partial x} n_x + \frac{\partial \Phi_t}{\partial y} n_y + \frac{\partial \Phi_t}{\partial z} n_z
\end{aligned} \tag{3.8}$$

where $\hat{\mathbf{n}}$ is the unit vector normal to the boundary and n_x, n_y, n_z denote the direction cosines components of $\hat{\mathbf{n}}$.

3.3 Governing Conduction Differential Equations

When a temperature gradient exists in a material due to the thermal motion of the material microscopic particles then the energy transfer that occurs between two potential difference points in the region is known as *conduction.*

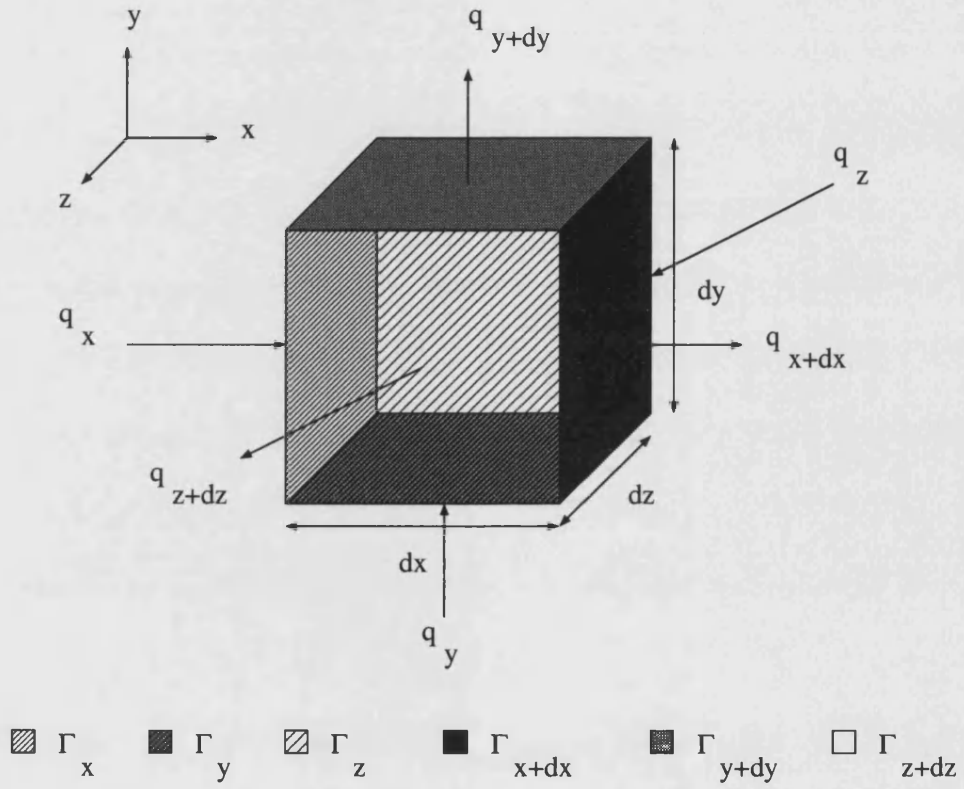

Figure 3.2: Elemental volume for 3D thermal conduction.

The basic governing equation for conductive heat transfer is obtained by applying the principle of conservation of energy to a differential element located at a given position in the conduction region. An example of heat conduction is illustrated in the solid cubic region of Figure 3.2. At a given time, t the 1D heat conduction in the x-direction can be expressed in mathematical form as Fourier's law of conduction:

The heat inflow q_x at surface Γ_x is described as

$$q_x = -\kappa \mathrm{A}_s \frac{\partial T}{\partial x}\bigg]_x \tag{3.9}$$

in which κ is the thermal conductivity and A_s is the area of the surface.

Energy generated within the element for $\mathrm{d}x$:

$$\dot{E}_G = \dot{q}\mathrm{A}_s \Delta x \tag{3.10}$$

where $\dot{q}$ is the internal heat generation.

The time derivatives:

$$\rho C_p \mathrm{A}_s \frac{\partial T}{\partial t} \Delta x \frac{\partial T(x + \Delta x/2, t)}{\partial t} \tag{3.11}$$

where ρ is the material density and C_p is the specific heat capacity.

The heat outflow from surface $\Gamma_{x+\mathrm{d}x}$:

$$q_{x+\mathrm{d}x} = -\kappa \mathrm{A}_s \frac{\partial T}{\partial x}\bigg]_{x+\mathrm{d}x} = -\mathrm{A}_s \left[\kappa \frac{\partial T}{\partial x} + \frac{\partial}{\partial x}\left(\kappa \frac{\partial T}{\partial x}\right)\mathrm{d}x\right] \tag{3.12}$$

Dividing equations (3.9), (3.10), (3.11) and (3.12) with $\mathrm{A}_s \Delta x$, and rearranging gives

$$\kappa \frac{(\partial T/\partial x)_{x+\mathrm{d}x}}{\Delta x} - \kappa \frac{(\partial T/\partial x)_x}{\Delta x} + \dot{q} = \rho C_p \frac{\partial T(x + \Delta x/2, t)}{\partial t} \tag{3.13}$$

In the limit $\Delta x \to 0$, the first term on the left hand side (*l.h.s*) of equation (3.13) is expressed in the form

$$\kappa \frac{\partial T}{\partial x}\bigg]_{x+\mathrm{d}x} = \kappa \frac{\partial T}{\partial x}\bigg]_x + \kappa \frac{\partial}{\partial x}\left(\frac{\partial T}{\partial x}\bigg]_x\right)\mathrm{d}x \tag{3.14}$$

The *r.h.s* of equation (3.13) can be expanded in Taylor series as

$$\rho C_p \frac{\partial T}{\partial t}\left[\left(x + \frac{\Delta x}{2}\right), t\right] = \rho C_p \frac{\partial T}{\partial t}\bigg]_x + \rho C_p \frac{\partial}{\partial x}\left(\frac{\partial T}{\partial t}\bigg]_x\right)\frac{\Delta x}{2} + \ldots\ldots \tag{3.15}$$

To the order of Δx ,the 1D heat conduction equation is written as

$$\kappa \frac{\partial}{\partial x}\left(\frac{\partial T}{\partial x}\right) + \dot{q} = \rho C_p \frac{\partial T}{\partial t} \tag{3.16}$$

For 3D heat transfer, the temperature is assumed to be a function of all three coordinate systems as well as time, $T = T(x, y, z, t)$. The heat conducted in and out of a unit volume in all three x, y, z coordinate directions are considered. The energy balance yields,

$$q_x + q_y + q_z + \dot{q} = q_{x+\mathrm{d}x} + q_{y+\mathrm{d}y} + q_{z+\mathrm{d}z} + \rho C_p \,\mathrm{d}x\,\mathrm{d}y\,\mathrm{d}z \frac{\partial T}{\partial t} \tag{3.17}$$

with the energy quantities in the x, y, z directions expressed as

- At surface Γ_x

$$q_x = -\kappa \,\mathrm{d}y\,\mathrm{d}z \frac{\partial T}{\partial x} \tag{3.18}$$

- At surface $\Gamma_{x+\mathrm{d}x}$

$$q_{x+\mathrm{d}x} = -\left[\kappa \frac{\partial T}{\partial x} + \frac{\partial}{\partial x}\left(\kappa \frac{\partial T}{\partial x}\right)\mathrm{d}x\right]\mathrm{d}y\,\mathrm{d}z \tag{3.19}$$

- At surface Γ_y

$$q_y = -\kappa \,\mathrm{d}x\,\mathrm{d}z \frac{\partial T}{\partial y} \tag{3.20}$$

- At surface $\Gamma_{y+\mathrm{d}y}$

$$q_{y+\mathrm{d}y} = -\left[\kappa \frac{\partial T}{\partial y} + \frac{\partial}{\partial y}\left(\kappa \frac{\partial T}{\partial y}\right)\mathrm{d}y\right]\mathrm{d}x\,\mathrm{d}z \tag{3.21}$$

- At surface Γ_z

$$q_z = -\kappa \,\mathrm{d}x\,\mathrm{d}y \frac{\partial T}{\partial z} \tag{3.22}$$

- At surface $\Gamma_{z+\mathrm{d}z}$

$$q_{z+\mathrm{d}z} = -\left[\kappa \frac{\partial T}{\partial z} + \frac{\partial}{\partial z}\left(\kappa \frac{\partial T}{\partial z}\right)\mathrm{d}z\right]\mathrm{d}x\,\mathrm{d}y \tag{3.23}$$

- Energy generated

$$\dot{E}_G = \dot{q}\,\mathrm{d}x\,\mathrm{d}y\,\mathrm{d}z \tag{3.24}$$

Combining all the relations above, the 3D form of the governing conduction equation with constant thermal conductivity κ then becomes

$$\frac{\partial}{\partial x}\left(\frac{\partial T}{\partial x}\right) + \frac{\partial}{\partial y}\left(\frac{\partial T}{\partial y}\right) + \frac{\partial}{\partial z}\left(\frac{\partial T}{\partial z}\right) + \frac{\dot{q}}{\kappa} = \frac{1}{\alpha_k}\frac{\partial T}{\partial t} \tag{3.25}$$

in which α_k is the *thermal diffusivity*, a group of material properties defined as

$$\alpha_k = \frac{\kappa}{\rho C_p} \tag{3.26}$$

The larger the value of α_k, the quicker the heat will diffuse through the cubic region. A large value of α_k, which indicates a rapid heat transfer rate, could be due to either a high value of thermal conductivity κ or to a low thermal heat capacity ρC_p. A low heat capacity means that less energy would be absorbed and used to raise the temperature of the cubic region. Thermal diffusivity has units of $(\mathrm{m}^2/\mathrm{s})$ in the SI system.

3.4 Governing Equations for Fourier's Law of Heat Transfer

The local 3D differential conduction equation with zero velocity and the source term $\dot{q}$, which is defined as

$$\rho C_p \frac{\partial T}{\partial t} - \nabla \cdot \kappa \nabla T - \dot{q} = 0 \tag{3.27}$$

is applied at every point of the specified time-space continuum. The global form is obtained by numerically integrating the differential equation over the region of space and time together with a weighting function N {discussed in the following section}.

At the boundary of the thermal region, the heat transfer coefficient $\hbar$ may for some simple geometrical surfaces be obtained from available empirical correlation data and research studies. But, frequently it has to be determined from a solution of the coupled fluid flow problem, which is governed by the principle of mass conservation, momentum and energy conservation.

The heat transfer at the surface Γ is then given as

$$q = -\kappa_f \left(\frac{\partial T}{\partial n} \right) \Big]_\Gamma \tag{3.28}$$

where q is the surface heat lost of the region, $\dfrac{\partial T}{\partial n}\Big]_\Gamma$ is the temperature gradient in the fluid evaluated at the boundary between the solid region and fluid region together with the fluid thermal conductivity κ_f.

Alternatively, if the convection coefficient $\hbar_c$ is somehow obtained for the surface then the heat loss from the boundary could be solved without solving the coupled fluid problem with

$$q = \hbar_c (T_s - T_\infty) \tag{3.29}$$

specified as the boundary condition of the conduction region Ω where T_s is the unknown surface temperature and T_∞ is the known ambient temperature of the fluid.

In the thermal conduction region Ω, the thermal conductivity κ could be *anisotropic*, meaning the material has an orthotropic conductivity such that $\kappa_{11} \neq \kappa_{22} \neq \kappa_{33}$ and $\kappa_{ij} = \kappa_{ji} = 0$ when written in terms of region axes.

If the heat conduction is in an anisotropic region, the Fourier's law becomes

$$\begin{aligned} q_x &= \kappa_{11} \frac{\partial T}{\partial x} + \kappa_{12} \frac{\partial T}{\partial x} + \kappa_{13} \frac{\partial T}{\partial x} \\ q_y &= \kappa_{21} \frac{\partial T}{\partial y} + \kappa_{22} \frac{\partial T}{\partial y} + \kappa_{23} \frac{\partial T}{\partial y} \end{aligned}$$

$$q_z = \kappa_{31}\frac{\partial T}{\partial z} + \kappa_{32}\frac{\partial T}{\partial z} + \kappa_{33}\frac{\partial T}{\partial z} \tag{3.30}$$

where κ_{ij} is the symmetric conductivity tensor.

3.5 Galerkin Weighted Residual Technique

The differential equation of the diffusion problem with T as the only unknown nodal value is satisfied in a weighted-integral sense over the entire region Ω. This 2nd-order heat conduction equation is transformed into a weaker form containing only the 1st-order derivatives by the use of Green's theorem, and thereby requires only the C° continuity.

The weak form of the differential equation is a weighted-integral expression that is equivalent to both the governing differential equation as well as the associated natural boundary conditions. To obtain the weak form expression, the heat conduction equation is multiplied by a weighting function N and then integrated over the entire domain Ω. The weighting function used here is the Galerkin weighted residual.

The Galerkin weighted residual equation describing the conduction region is given by

$$\int_\Omega N\left[\nabla\cdot\kappa\nabla T + \dot{q} - \rho C_p\frac{\partial T}{\partial t}\right]\mathrm{d}\Omega = 0 \tag{3.31}$$

Equation (3.31) describes the averaging of the error or residual within the element boundaries, but it does not address the effect of the boundary conditions. The Green-Gauss theorem is used to reduce the order of the equation derivatives and to introduce the influence of the natural boundary condition. After integrating by parts, the equation takes the form

$$\int_\Omega \left(\kappa_x\frac{\partial T}{\partial x}\frac{\partial N_i}{\partial x} + \kappa_y\frac{\partial T}{\partial y}\frac{\partial N_i}{\partial y} + \kappa_z\frac{\partial T}{\partial z}\frac{\partial N_i}{\partial z}\right)\mathrm{d}\Omega - \oint_\Gamma N_i\,\kappa\frac{\partial T}{\partial n}\,\mathrm{d}\Gamma$$

$$+\int_{\Omega} N_i \rho C_p \frac{\partial T}{\partial t} \, d\Omega = \int_{\Omega} N_i \dot{q} \, d\Omega \tag{3.32}$$

By inspecting the surface term in equation (3.32), the specification of the coefficient of the Galerkin weight function in the boundary expression

$$\kappa \frac{\partial T}{\partial n} = \kappa_x \frac{\partial T}{\partial x} n_x + \kappa_y \frac{\partial T}{\partial y} n_y + \kappa_z \frac{\partial T}{\partial z} n_z \tag{3.33}$$

constitutes the natural boundary condition. By definition $\kappa \dfrac{\partial T}{\partial n}$ or in vector form $\hat{\mathbf{n}} \cdot \kappa \nabla T$ is projected positive outward from the surface along the unit normal vector $\hat{\mathbf{n}}$. If the region is isotropic then $\kappa_x = \kappa_y = \kappa_z = \kappa$.

The surface integral terms naturally cancel when combining adjacent elements within the region. On the outer surface, boundary conditions for convective and radiation heat flows can be prescribed.

3.6 Boundary Conditions for Surface Heat Flow

The boundary conditions prescribed at the edges or surfaces of the conduction region, may consist of various types. For isothermal surfaces, the temperatures at the surface nodal points are simply specified at the given value. However, in many cases convection, radiation or the combination of both types of heat transfer are specified at the exposed surfaces to surrounding air.

All the typical surface boundary conditions encountered in finite element formulations are as follow:

1. *Prescribed temperature.* The surface temperature of a boundary are specified to be a constant or a function of the boundary coordinates. Prescribed temperature is an example of a Dirichlet boundary condition.

2. *Adiabatic boundary.* The rate of heat flow across a surface is zero, the Fourier's law gives

$$\kappa \nabla T \cdot \hat{\mathbf{n}} = \kappa \frac{\partial T}{\partial n} = 0 \tag{3.34}$$

3. *Prescribed heat flux.* The rate of heat flow across the surface is specified. According to Fourier's law the surface heat flow is expressed as

$$\kappa \nabla T \cdot \hat{\mathbf{n}} = \kappa \frac{\partial T}{\partial n} = -q_n \tag{3.35}$$

where $\hat{\mathbf{n}}$ is the normal to the boundary and q_n is the rate of heat flow across the surface.

4. *Convective boundary.* Convection occurs when there is a temperature difference between the region surface and adjacent fluid. The Fourier's law governing this condition is given as

$$\kappa \nabla T \cdot \hat{\mathbf{n}} = \kappa \frac{\partial T}{\partial n} = -\hbar_c (T_s - T_\infty) \tag{3.36}$$

where $\hbar_c$ is the convection heat transfer coefficient, T_s is the surface temperature and T_∞ is the ambient temperature.

5. *Radiation.* The rate of heat flow across a boundary is specified in terms of emitted energy from the surface. The boundary condition is

$$\kappa \nabla T \cdot \hat{\mathbf{n}} = \kappa \frac{\partial T}{\partial n} = -\epsilon_r \sigma_r (T_s^4 - T_\infty^4) \tag{3.37}$$

where ϵ_r is the surface emissivity and σ_r is the Stefan-Boltzmann constant.

These conditions give rise to equations connecting the temperature gradient at the surface with other variables governing heat flow and the surface temperature at the exposed surface.

If the convection and radiation boundaries are prescribed, the surface integral term in equation (3.32) enables the natural boundary of equations (3.36) and (3.37) to be inserted

$$\kappa \nabla T \cdot \hat{\mathbf{n}} = \kappa \frac{\partial T}{\partial n} = -[\hbar_c (T_s - T_\infty) + \epsilon_r \sigma_r (T_s^4 - T_\infty^4)] \tag{3.38}$$

3.7 Finite Element Discretisation

In the usual finite element approach, the entire thermal region Ω is divided into non-overlapping subdomains Ω^e and then the approximation T is constructed in a piecewise manner over each subdomains. The shape functions are also defined in a piecewise manner.

In such cases, the temperature function T is written in the standard form by associating with each node j a piecewise constant, discontinuous global shape or basis function N_j, where N_j is defined to have a value unity only on node j and zero on all other nodes,

$$T = \sum_{j=1}^{m} N_j T_j \quad \text{in } \Omega^e \tag{3.39}$$

T_j is the nodal value of T at the j-th node with coordinates (x_j, y_j, z_j) of the element Ω^e.

The governing equation to be solved for each 3D linear element with the shape functions {see Appendix B} to depict the spatial variation of the nodal temperature T is then written as

$$\begin{aligned} &\int_{\Omega^e} \kappa \left(\frac{\partial N_i}{\partial x} \sum_{j=1}^{m} \frac{\partial N_j}{\partial x}[T_j] + \frac{\partial N_i}{\partial y} \sum_{j=1}^{m} \frac{\partial N_j}{\partial y}[T_j] + \frac{\partial N_i}{\partial z} \sum_{j=1}^{m} \frac{\partial N_j}{\partial z}[T_j] \right) \mathrm{d}\Omega^e \\ &- \oint_{\Gamma^e} \kappa N_i \sum_{j=1}^{m} N_j \frac{\partial T_j}{\partial n} \mathrm{d}\Gamma^e + \int_{\Omega^e} \rho C_p N_i \sum_{j=1}^{m} N_j \left[\frac{\partial T_j}{\partial t} \right] \mathrm{d}\Omega^e = \int_{\Omega^e} N_i \dot{q} \, \mathrm{d}\Omega^e \end{aligned} \tag{3.40}$$

Without loss of generality the surface integral term in equation (3.40) can be ignored since the boundary integral cancels at the element interfaces. If the interface is on the outer layer then surface convection and radiation boundary conditions can be enforced.

The application of the Galerkin's technique results in a system of equations which has the global matrix notation of

$$[\boldsymbol{K}]\boldsymbol{T}^{\theta} + [\boldsymbol{C}]\dot{\boldsymbol{T}}^{\theta} = \boldsymbol{f}^{\theta} \tag{3.41}$$

If steady-state conditions are assumed i.e., the problem is invariant with time and so $\frac{\partial}{\partial t} = 0$, then the matrix equation (3.41) is simplified by ignoring the $[\boldsymbol{C}]$ matrix.

3.8 Time-transient Formulations

Time-stepping schemes have been implemented to solve the differential heat transfer equations. The most commonly used is the Θ-family of approximation, which enables many single time-step algorithms to be implemented by changing the parameter Θ. The value of Θ ranges between, $0 \leq \Theta \leq 1.0$.

In the preceding section, it has been shown that the solution matrix has the form

$$[\boldsymbol{C}]\dot{\boldsymbol{T}}^{\theta} + [\boldsymbol{K}]\boldsymbol{T}^{\theta} = \boldsymbol{f}^{\theta} \tag{3.42}$$

Evaluating the equation (3.42) for $\boldsymbol{T}^{\theta}$ at time $t = t_n + \Theta\Delta t_n$, $0 \leq \Theta \leq 1$ by using Taylor series expansions gives

$$\boldsymbol{T}^{n} = \boldsymbol{T}^{\theta} - \Theta\Delta t_n \frac{\partial \boldsymbol{T}}{\partial t}\Big]^{\theta} + \frac{\Theta^2 \Delta t_n^2}{2}\frac{\partial^2 \boldsymbol{T}}{\partial t^2}\Big]^{\theta} - \frac{\Theta^3 \Delta t_n^3}{6}\frac{\partial^3 \boldsymbol{T}}{\partial t^3}\Big]^{\theta} \tag{3.43}$$

$$\boldsymbol{T}^{n+1} = \boldsymbol{T}^{\theta} + (1-\Theta)\Delta t_n \frac{\partial \boldsymbol{T}}{\partial t}\Big]^{\theta} + \frac{(1-\Theta)^2 \Delta t_n^2}{2}\frac{\partial^2 \boldsymbol{T}}{\partial t^2}\Big]^{\theta} + \frac{(1-\Theta)^3 \Delta t_n^3}{6}\frac{\partial^3 \boldsymbol{T}}{\partial t^3}\Big]^{\theta} \tag{3.44}$$

Subtracting these two equations (3.43) and (3.44) yields the approximation

$$\dot{\boldsymbol{T}}^{\theta} \approx \frac{(\boldsymbol{T}^{n+1} - \boldsymbol{T}^{n})}{\Delta t_n} \tag{3.45}$$

Then multiplying equation (3.43) by $(1 - \Theta)$, equation (3.44) by Θ, and adding the resulting equations gives

$$\boldsymbol{T}^{\theta} \approx (1 - \Theta)\boldsymbol{T}^{n} + \Theta\boldsymbol{T}^{n+1} \tag{3.46}$$

When the approximations of equations (3.45) and (3.46) are employed in equation (3.42) using the same representation for $\boldsymbol{f}^{\theta}$ as that adopted by $\boldsymbol{T}^{\theta}$ in equation (3.46), the resulting algorithm is

$$\Big(\frac{[\boldsymbol{C}]}{\Delta t_n} + \Theta[\boldsymbol{K}]\Big)\boldsymbol{T}^{n+1} + \Big(-\frac{[\boldsymbol{C}]}{\Delta t_n} + (1 - \Theta)[\boldsymbol{K}]\Big)\boldsymbol{T}^{n} = (1 - \Theta)\boldsymbol{f}^{n} + \Theta\boldsymbol{f}^{n+1} \tag{3.47}$$

Some of the well-known time-stepping schemes implemented in this program:

1. The choice of $\Theta = 0.0$ implies *Euler's forward difference* scheme, which is an explicit method. It requires an iterative solution at each time-step Δt. In this case $\boldsymbol{T}_i = \boldsymbol{T}_i^n$, the equation (3.47) is rearranged as

$$\Big(\frac{[\boldsymbol{C}]}{\Delta t_n}\Big)\boldsymbol{T}^{n+1} + \Big(-\frac{[\boldsymbol{C}]}{\Delta t_n} + [\boldsymbol{K}]\Big)\boldsymbol{T}^{n} = \boldsymbol{f}^{n} \tag{3.48}$$

   If the capacitance matrix $[\boldsymbol{C}]$ is diagonal, so that its inverse $[\boldsymbol{C}]^{-1}$ can be obtained trivially, the scheme's explicit nature is shown, as $\boldsymbol{T}^{n+1}$ is given in terms of $\boldsymbol{T}^{n}$ by

$$\boldsymbol{T}^{n+1} = \Delta t_n[\boldsymbol{C}]^{-1}\Big[\Big(\frac{[\boldsymbol{C}]}{\Delta t_n} - [\boldsymbol{K}]\Big)\boldsymbol{T}^{n} + \boldsymbol{f}^{n}\Big] \tag{3.49}$$

If finite difference discretisation of the space domain is used, the capacitance matrix $[\boldsymbol{C}]$ will be diagonal but with finite element method the explicit nature of the scheme is lost as the matrix $[\boldsymbol{C}]$ will not be normally diagonal. However, diagonalising or lumping the matrix $[\boldsymbol{C}]$ can be easily accomplished by using the row-sum technique.

The explicit scheme is known to be conditionally stable. Its explicit nature implies a stability condition in terms of maximum allowable time-step Δt_n.

2. If $\Theta = 0.5$, then it is the *Crank-Nicolson* scheme. The global matrix is evaluated as average between time level n and $n+1$, resulting in $\boldsymbol{T}^{\theta} = 0.5(\boldsymbol{T}^n + \boldsymbol{T}^{n+1})$. Equation (3.47) is reduced to

$$\left(\frac{[\boldsymbol{C}]}{\Delta t_n} + \frac{1}{2}[\boldsymbol{K}]\right)\boldsymbol{T}^{n+1} + \left(-\frac{[\boldsymbol{C}]}{\Delta t_n} + \frac{1}{2}[\boldsymbol{K}]\right)\boldsymbol{T}^{n} = \frac{1}{2}\left(\boldsymbol{f}^n + \boldsymbol{f}^{n+1}\right) \tag{3.50}$$

This scheme is known to be implicit as it requires the solution of non-diagonal system of equations to determine $\boldsymbol{T}^{n+1}$.

3. *Backward difference scheme.* This implicit scheme is the result of $\Theta = 1.0$

$$\left(\frac{[\boldsymbol{C}]}{\Delta t_n} + [\boldsymbol{K}]\right)\boldsymbol{T}^{n+1} - \left(\frac{[\boldsymbol{C}]}{\Delta t_n}\right)\boldsymbol{T}^{n} = \boldsymbol{f}^{n+1} \tag{3.51}$$

Implicit schemes such as *backward difference* and *Crank-Nicolson* are unconditionally stable with no time-step restriction. For non-linear cases, the modified matrices of (3.50) and (3.51) require an iterative solution at each time-step for $\boldsymbol{T}^{n+1}$. The linear case can be solved without non-linear iteration but a matrix solution is still required.

3.9 Empirical Correlations for Convection

It is not always possible to find analytical solutions to convection problems. Experimental methods are often used to obtain design information and to secure the more elusive data which increase the understanding of the heat transfer processes. Experimental data are usually expressed in the form of empirical formulas or graphical charts.

In most situations the transient heat conduction problem is coupled with a convection heat transfer at the surface of a solid. Convection is the mode of energy transfer between a solid surface and the adjacent liquid or gas that is in motion. It involves the combined effects of conduction and fluid motion. The faster the fluid motion, the greater the convection heat transfer. The presence of bulk motion of the fluid enhances the heat transfer between the solid surface and the fluid, but it also complicates the determination of heat transfer rates.

Convection is called *Forced Convection* if the fluid is forced to flow over the surface by external means. On the contrary convection is known as *Natural Convection* if the fluid motion is caused by buoyancy forces induced by density differences due to the variation of the temperature in the fluid.

In this chapter, the results of some experimental studies on natural and forced convections are presented for two geometrical shapes, that of the vertical plate and the horizontal cylinder.

3.9.1 Natural Convection

Natural convection is considered where any fluid motion occurs by natural means such as buoyancy. The fluid motion in forced convection is quite noticeable since a fan or a pump can transfer enough momentum to the fluid to move it in a certain direction. The fluid motion in natural convection however, is often not noticeable because of the low velocities involved.

Natural convection heat transfer on a surface depends on the geometry of the surface as well as its orientation. It also depends on the variation of the temperature on the surface and thermophysical properties of the fluid involved.

According to the Newton's law of cooling, convection is expressed as

$$q = \oint_{\Gamma} \hbar_c (T_s - T_\infty)\, d\Gamma \tag{3.52}$$

where $\hbar_c$ is the convection heat transfer coefficient (W/m^2 K), T_s is the surface temperature (°C) and T_∞ is the ambient temperature (°C).

The heat transfer from the thermal region surface to the ambient air is by convection and radiation. These parameters are most sensitive to the accuracy of the predictions made on heat transfer processes in the region. To determine the convection coefficient $\hbar_c$, the *Nusselt number* Nu would have to be determined first.

The natural convection coefficient $\hbar_c$ is related to the *Nusselt number* by the expression

$$\hbar_c = \frac{\kappa\, Nu}{\delta} \tag{3.53}$$

where δ is the characteristics length of geometry (m) and κ is the thermal conductivity of air (W/m K).

The *Nusselt number* for natural convection is a function of the surface temperature of the thermal region, which results in the governing heat flow equation being non-linear. In this research, flat vertical plate and smooth cylindrical frame are studied with the non-linearity of the surface temperature taken into account by using an iterative procedure. A huge amount of work is required in order to ensure that the heat flow over the two geometrical surfaces are modelled accurately.

The empirical correlations for average *Nusselt number* can be represented by the following functional form for a variety of convection problems

$$Nu = C\,(Gr\,Pr)^n \tag{3.54}$$

in which Gr and Pr are known as the *Grasnof number* and *Prandtl number* respectively.

The *Grasnof number* is the ratio of buoyancy to viscous forces and is defined as

$$Gr = \frac{g\beta(T_s - T_\infty)\delta^3}{\nu^2} \tag{3.55}$$

where g is the known gravitational acceleration of 9.81 m/s^2, β is the coefficient of volume expansion, $\frac{1}{K(Kelvin)}$ for ideal gas, δ is the characteristic length and ν is kinematic viscosity of the fluid.

The *Prandtl number* is a function of fluid properties alone. It is defined as the ratio of kinematic viscosity of fluid to the thermal diffusivity of the fluid,

$$Pr = \frac{\nu}{\alpha_k} = \left[\frac{\mu_v}{\rho} \cdot \frac{\rho C_p}{\kappa_f}\right] \tag{3.56}$$

The kinematic viscosity ν, or the ratio of molecular viscosity to fluid density μ_v/ρ, is the measure of the rate of momentum transfer between the fluid molecular, while the thermal diffusivity α_k of the fluid is the measure of heat transfer and energy storage capacities of the molecules. Hence, the *Prandtl number* relates the temperature distribution to the velocity distribution for fluid flow.

The product of the *Grasnof number* and *Prandtl number* will yield a new definition known as the *Rayleigh number*:

$$Ra = GrPr = \frac{g\beta(T_s - T_\infty)\delta^3}{\nu^2}Pr \tag{3.57}$$

The temperature difference ΔT in the *Grasnof number* represents the absolute difference between the surface temperature T_s and the ambient temperature T_∞.

The coefficient of volume expansion β is defined as

$$\beta = \frac{1}{T_f} \tag{3.58}$$

where T_f is the absolute film temperature and represents the variation of the density of a fluid with temperature at constant pressure.

The fluid temperature in the thermal boundary layer varies from T_s at the surface to about T_∞ at the outer layer of the boundary. The fluid properties also vary with temperature, and thus with position across the boundary layer. In order to account for the variation of the properties, the fluid properties are usually evaluated at what is known as the film temperature T_f,

$$T_f = \frac{T_s + T_\infty}{2} \tag{3.59}$$

which is the arithmetic mean between the surface and free-stream temperatures. Figure 3.3, Figure 3.4 and Figure 3.5 show the air temperature dependent thermal conductivity, *Prandtl number* and kinematic viscosity respectively.

If the heated surface of a 2D horizontal plate of length L is facing upward, Fujii and Imura [17] recommend the relation with a limited Ra range:

$$Nu = 0.16Ra^{\frac{1}{3}} \qquad \text{for} \quad 7 \times 10^6 < Ra < 2 \times 10^8 \tag{3.60}$$

$$Nu = 0.13Ra^{\frac{1}{3}} \qquad \text{for} \quad 5 \times 10^8 < Ra \tag{3.61}$$

For natural convection from a horizontal cylindrical surface, *Churchill-Chu* [18] proposed that the *Nusselt number* can be estimated using equation

$$Nu = \left\{ 0.6 + \frac{0.387Ra^{\frac{1}{6}}}{\left[1 + \left(\frac{0.559}{Pr}\right)^{\frac{9}{16}}\right]^{\frac{8}{27}}} \right\}^2 \tag{3.62}$$

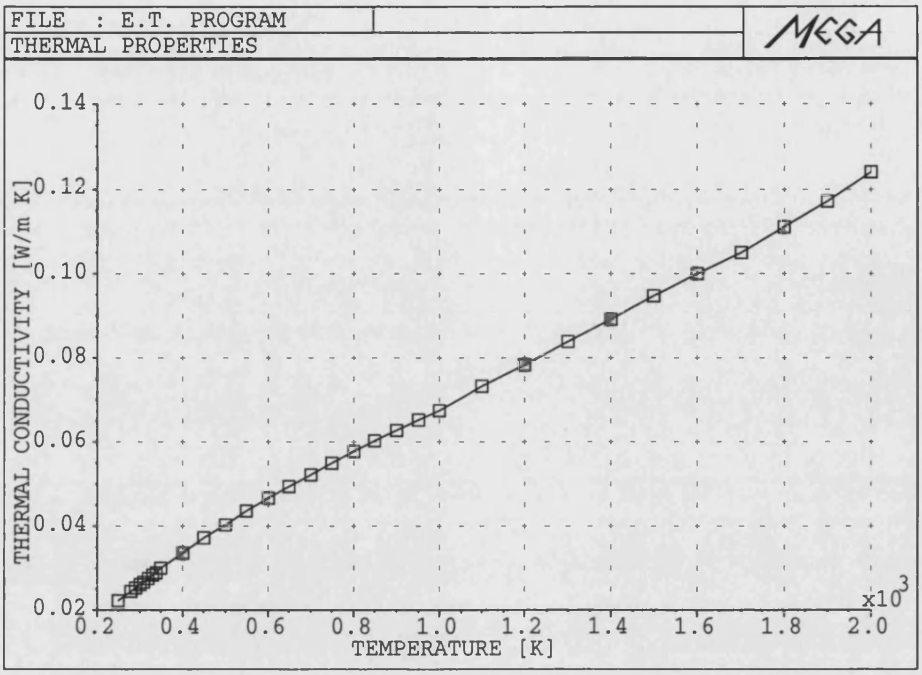

Figure 3.3: Air thermal conductivity.

And for flat vertical surface [19], the *Nusselt number* is

$$Nu = \left\{ 0.825 + \frac{0.387 Ra^{\frac{1}{6}}}{\left[1 + \left(\frac{0.492}{Pr} \right)^{\frac{9}{16}} \right]^{\frac{8}{27}}} \right\}^2 \tag{3.63}$$

Churchill-Chu correlations presented a more complicated expression for *Nusselt number* compared to other correlations given by Eckert [20], Gryzagoridis [21] and Morgan [22] but they are applicable to wider ranges of the *Rayleigh number*. A lengthy discussion on empirical correlations for *Nusselt number* of various other surfaces with different inclinations can be found in [23], [24].

Using the *Churchill-Chu* proposed *Nusselt numbers* for cylindrical and vertical plate surfaces, the non-linear convection coefficient $\hbar_c$ values could now be calculated over a range of temperatures.

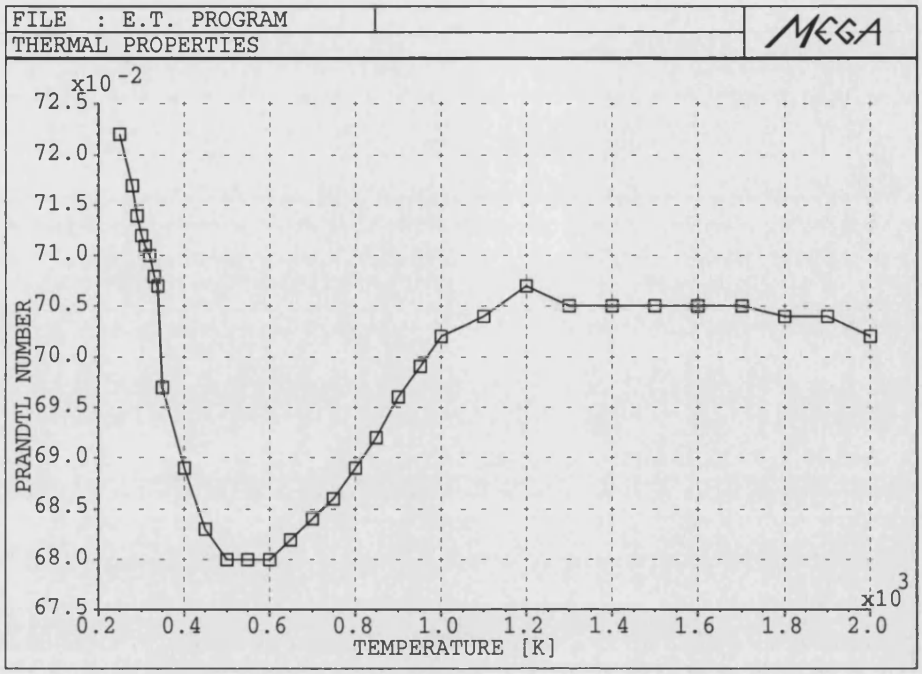

Figure 3.4: *Prandtl number* for air.

3.9.2 Forced Convection

In a forced convection environment, the flow regime is characterised by two flow types, external and internal. Osborne Reynolds discovered in 1880 that the flow fields are mainly influenced by the ratio of the inertia forces to viscous forces. This ratio is known as the *Reynolds number* in the present day.

Reynolds number for external flow is expressed as

$$Re = \frac{\text{inertia forces}}{\text{viscous forces}} = \frac{u_\infty \delta}{\nu} \tag{3.64}$$

where u_∞ is the free stream velocity (m/s), δ is the characteristic geometry (m) and ν is the kinematic viscosity of the fluid (m^2/s). The inertia forces are proportional to the density and the velocity of the fluid.

The flow is turbulent when the *Reynolds number* is large. At this stage the viscous

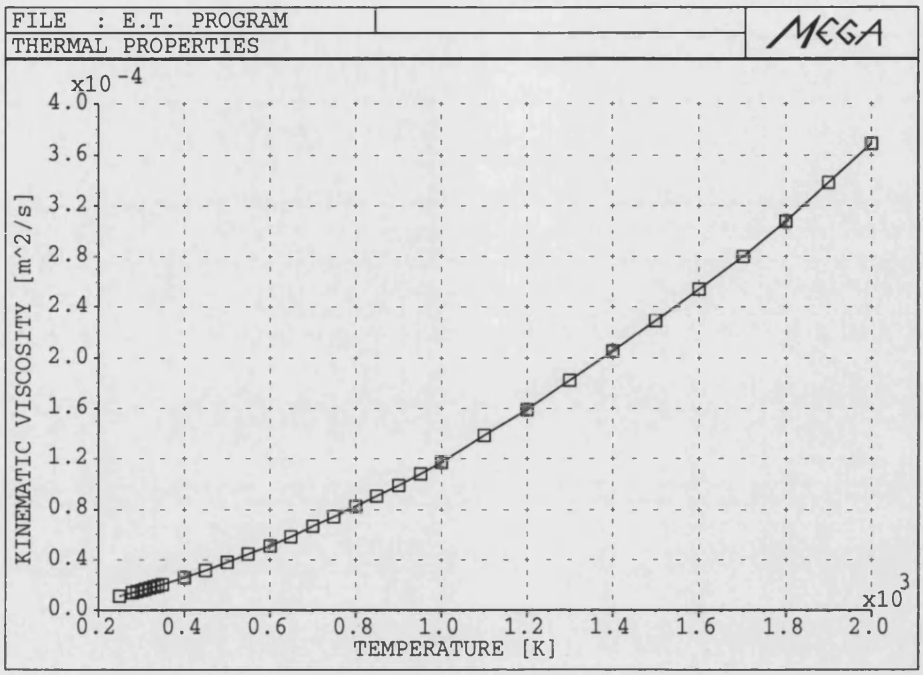

Figure 3.5: Air kinematic viscosity.

forces fail to prevent the random and rapid fluctuations of fluid since the inertia forces of the fluid are large in relative to the viscous forces. However, if the *Reynolds number* is small the fluid viscous forces will be large enough to overcome the inertia forces and keep the flow laminar {highly ordered motion}.

Fluid flows across various geometrical shapes, in general, involve flow boundary layer separation processes which are difficult to solve analytically. As such, flows are mostly studied experimentally. In this section only forced convection with external flow characteristics will be described.

The most common convective geometry in external flow is a circular cylinder immersed in a fluid cross-flow. Cross-flow over a cylinder as shown in Figure 3.6 for example exhibits a complex flow pattern. At the stagnation point O, the fluid flow stream is brought to a temporary halt, the flow transverse velocity $u_\infty = 0$ with an accompanying rise in pressure. As the flow progresses from this point at the front

end of the cylinder with increasing x distance, the pressure decreases. The fluid flow transverse velocity u_∞ is now dependent on the distance x from the stagnation point O. From $u_\infty = 0$ at the stagnation point, the fluid accelerates rapidly because of the low pressure gradient, $\frac{\partial P}{\partial x} < 0$ and reaches a maximum velocity when $\frac{\partial P}{\partial x} = 0$. Towards the rear, the adverse pressure gradient condition $\frac{\partial P}{\partial x} > 0$ causes a reduction in the transverse velocity of the fluid. The pressure-velocity behaviours are governed by the Bernoulli principle. The fluid flow continue to decelerate until it reaches the separation point $\left.\frac{\partial u}{\partial y}\right|_{y=0} = 0$ where the velocity gradient at the surface eventually becomes zero. The boundary layer detaches from the surface since the fluid near the surface lacks the momentum to overcome the pressure gradient in order to continue the downstream movement. As the flow proceeds past the separation point, reverse-flow phenomena occurs and eventually the wake region at the rear becomes turbulent and random in motion. Full details of cross-flow forced convection are discussed in [24].

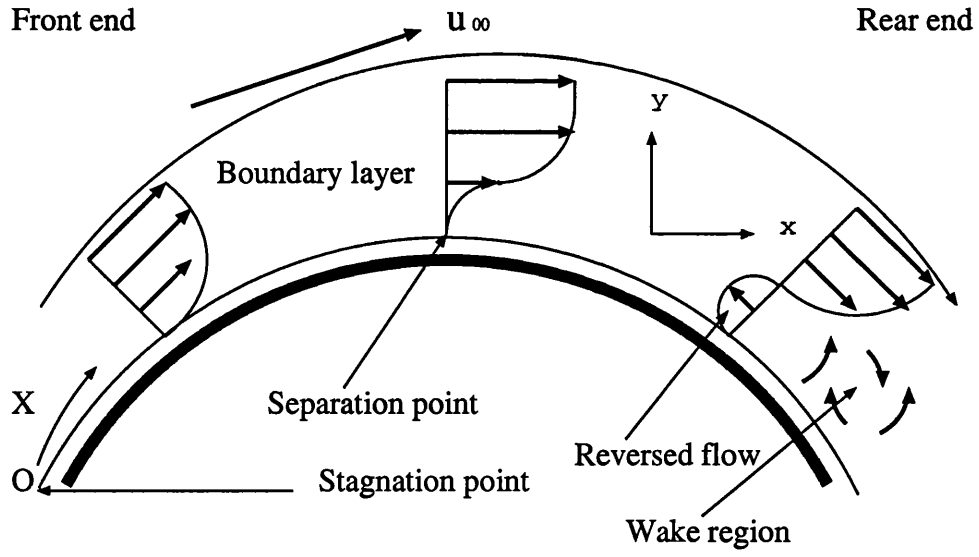

Figure 3.6: Circular cylinder in cross-flow.

The foregoing processes are sufficiently complex that an analytical description is virtually impossible. Hence, similar to solving natural convection problems, empirical

correlations developed by numerous investigators for the heat transfer coefficient are used for this external flow type of forced convection.

The average *Nusselt number* for flow field can be expressed compactly in terms of *Reynolds number* and *Prandtl number* as

$$Nu = \tilde{C}\, Re^m Pr^n \tag{3.65}$$

where $\tilde{C}$, m and n are constraints to be determined from the experimental data according to the heat transfer processes and geometry.

For external cross-flow over a horizontal cylinder, Churchill and Benstein suggested the correlated equation of

$$Nu = 0.3 + \frac{0.62 Re^{\frac{1}{2}} Pr^{\frac{1}{3}}}{\left[1 + \left(\frac{0.4}{Pr}\right)^{\frac{2}{3}}\right]^{\frac{1}{4}}} \left[1 + \left(\frac{Re}{282,000}\right)^{\frac{5}{8}}\right]^{\frac{4}{5}} \quad \text{for} \quad 10^2 < Re < 10^7;\ \alpha_w > 0.2 \tag{3.66}$$

This empirical equation is quite comprehensive in that it correlates all available data well for *Peclet number*, $\alpha_w > 0.2$.

Peclet number is the product of the *Reynolds number* and *Prandtl number* which occurs in the laminar flow correlations,

$$\alpha_w = \frac{d\, u_\infty\, \rho\, C_p}{\kappa_f} = Re\, Pr \tag{3.67}$$

where d is the diameter of the cylinder, u_∞ is the mean velocity of the fluid, ρ is the fluid density, C_p is the fluid specific heat capacity and κ_f is the fluid thermal conductivity.

3.10 Temperature Dependent Radiation

A body at a temperature above absolute zero emits radiation in all directions over a wide range of wavelengths. The amount of radiation energy emitted from the surface at a given wavelength depends on the material of the body and the conditions of its surface as well as the surface temperature.

A black body is defined as a perfect emitter and absorber of radiation. At a specified temperature and wavelength, no surface can emit more energy than a blackbody. A blackbody emits radiation in all directions.

In the absence of radiation heat exchanges between surfaces, a simplified method for representing the radiation heat transfer can be modelled along the similar approach of the convection heat transfer where the non-linearity is based on a temperature-dependent coefficient. Based on this method, the heat flux across the boundary is modelled as

$$\hat{\mathbf{n}} \cdot \kappa \nabla T = -\sigma_r \epsilon_r ({T_s}^4 - {T_\infty}^4) \tag{3.68}$$

which is equivalent to

$$\hat{\mathbf{n}} \cdot \kappa \nabla T = -\hbar_r(T)(T_s - T_\infty) \tag{3.69}$$

The temperature dependent radiation coefficient is therefore

$$\hbar_r(T) = \sigma_r \epsilon_r (T_s + T_\infty)({T_s}^2 + {T_\infty}^2) \tag{3.70}$$

where the Stefan-Boltzmann constant, $\sigma_r = 5.67 \times 10^{-8}$ W/(m^2 K^4) and ϵ_r is the surface radiation emissivity.

3.11 A Review of the Lumped Parameter Circuit Technique for Modelling Thermal Regions

In lumped parameter thermal modelling, the regions of interest are represented by a network of thermal resistances and thermal capacitances. This is equivalent to an electrical circuit in which heat flow is analogous to electrical current and temperature to electrical voltage. Each circuit represents a lumped region where the temperature and heat flow are regarded as uniform.

The thermal model relies on a complete knowledge of the dimensions of the region, material properties and heat generated at different nodes. The solution of the simultaneous equations arising from equating the flow of the heat into and out of each node subjected to the losses gives rise to the temperature distribution within the region.

3.11.1 Plane System

For a simple 1D steady-state heat flow through the plane wall of Figure 3.7 where the temperature gradient and heat flow is not time dependent and the cross-sectional area A_s is uniform, the Fourier's law can be simplified to

$$\frac{q}{A_s}\int_0^{\Delta x=L} dx = -\int_{T_1}^{T_2} \kappa \, dT \tag{3.71}$$

If κ is independent of T, integrating equation (3.71) yields the following expression for the rate of heat conduction through the plane wall

$$q = \frac{\kappa A_s}{L}(T_1 - T_2) = \frac{\Delta T}{L/\kappa A_s} \tag{3.72}$$

The quantity $L/\kappa A_s$ is equivalent to the thermal resistance R_k that the wall offers to the flow of heat by conduction:

$$R_k = \frac{L}{\kappa A_s} \tag{3.73}$$

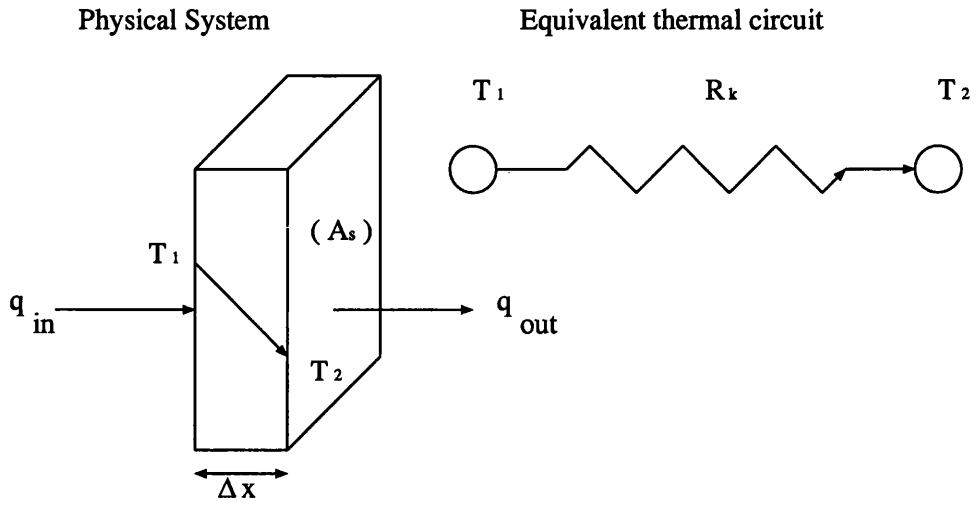

Figure 3.7: Heat transfer in a plane wall.

3.11.2 Radial System

In a solid cylindrical element, the heat flows by means of conduction. It is transferred radially, axially and circumferentially. Circumferential heat flow is normally neglected without any serious error in the outcome of the results. The heat flow in the radial and axial directions are assumed to be independent of each other to enable the use of 1D equations to model the conduction.

The 1D heat conduction which describes the radial temperature distribution is given by

$$\kappa \frac{1}{r} \frac{\partial}{\partial r} \left(r \frac{\partial T}{\partial r} \right) + \dot{q} = 0 \tag{3.74}$$

where κ is the thermal conductivity in the radial direction (W/m K) and $\dot{q}$ is the heat generated per unit volume (W/m^3) in the solid cylinder.

The expression for heat storage Q_s (J) in a cylindrical element such as Figure 3.8 can be defined as

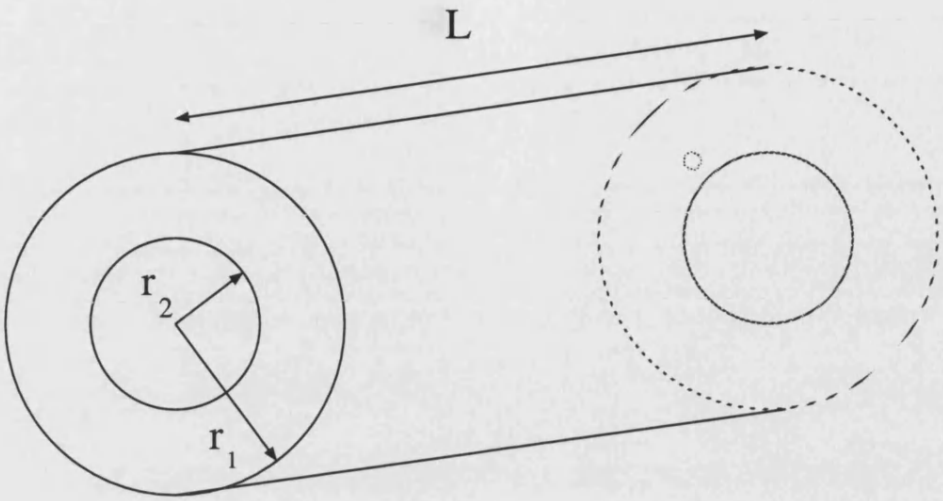

Figure 3.8: Cylindrical volume.

$$Q_s = \rho V_s C_p T_m \tag{3.75}$$

in which ρ is the cylinder material density (kg/m^3), V_s the component volume (m^3), C_p the cylinder specific heat capacity (J/kg K) and T_m the mean temperature of the cylinder (°C).

Or

$$Q_s = \rho\pi({r_1}^2 - {r_2}^2)\, L\, C_p\, T_m \tag{3.76}$$

Now consider a small elemental volume V_e with a uniform temperature T as shown in Figure 3.9.

The heat stored, Q_e is then given by

$$Q_e = \rho V_e C_p T \tag{3.77}$$

where $V_e = r dr\, d\theta\, dl$.

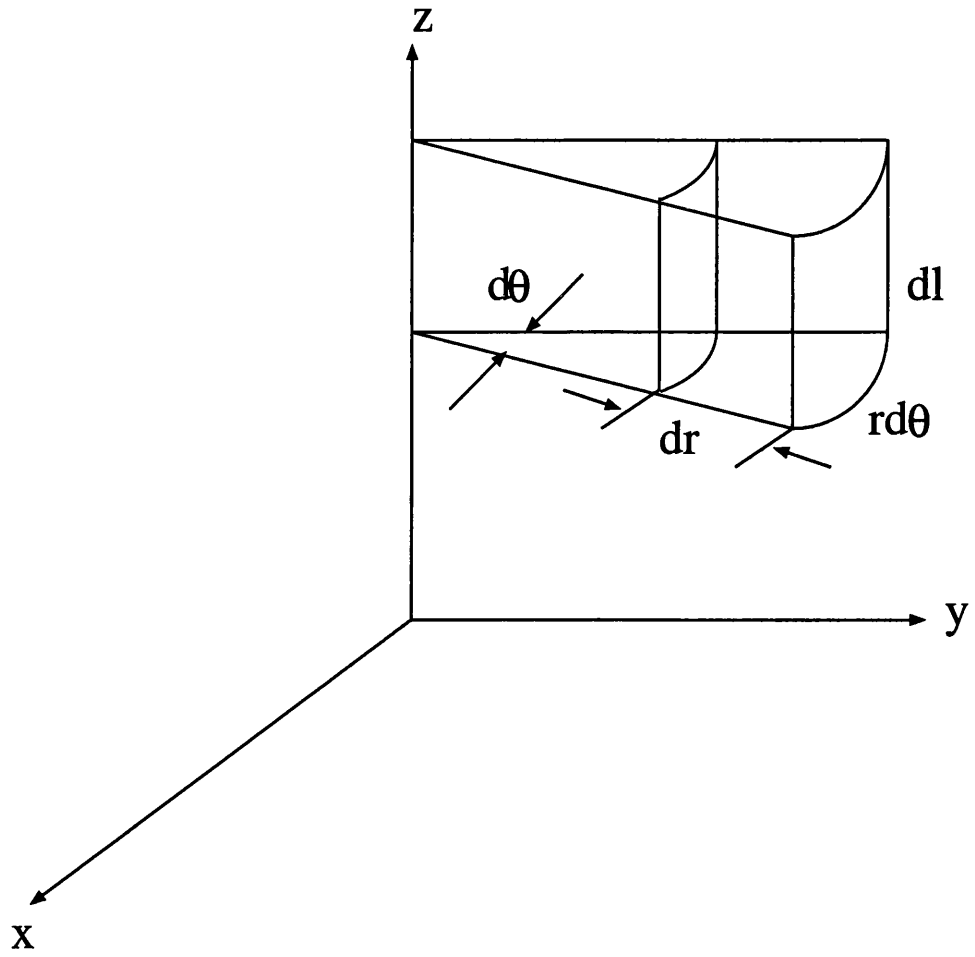

Figure 3.9: Small elemental volume in cylindrical coordinates.

Equating equations (3.76) and (3.77)

$$\rho\pi({r_1}^2 - {r_2}^2)LC_pT_m = \rho\, r\mathrm{d}r\,\mathrm{d}\theta\,\mathrm{d}\ell\, C_pT \tag{3.78}$$

The radial mean temperature is therefore, defined as

$$T_m = \frac{2}{{r_1}^2 - {r_2}^2}\int_{r_2}^{r_1} T_r\, r\mathrm{d}r \tag{3.79}$$

The axial mean temperature is given similarly by

$$T_m = \frac{1}{L}\int_0^L T_l \, d\ell \tag{3.80}$$

where T_r = radial temperature and T_l = axial temperature.

The general solution to equation (3.74),

$$T_r = -\frac{\dot{q}r^2}{4\kappa} + aln(r) + b \tag{3.81}$$

in which a, b are arbitrary constants.

Substituting $T_r = T_1$ at $r = r_1$ and $T_r = T_2$ at $r = r_2$ in the boundary conditions results in

$$a = \frac{1}{ln(r_1/r_2)}\left[T_1 - T_2 + \frac{\dot{q}({r_1}^2 - {r_2}^2)}{4\kappa}\right] \tag{3.82}$$

Similarly b can be determined from equation (3.81) after the constant a is found. Substituting equation (3.81) into equation (3.79) for T_m gives

$$T_m = \frac{2}{{r_1}^2 - {r_2}^2}\int_{r_2}^{r_1}\left[\frac{-\dot{q}r^2}{4\kappa} + aln(r) + b\right] r dr \tag{3.83}$$

Finally, by substituting equation (3.82) into equation (3.83) and then integrating the resultant equation gives the solution of the mean temperature in the radial direction as

$$\begin{aligned} T_m = T_1\left[\frac{{r_1}^2}{{r_1}^2 - {r_2}^2} - \frac{1}{2ln(r_1/r_2)}\right] + T_2\left[\frac{1}{2ln(r_1/r_2)} - \frac{{r_2}^2}{{r_1}^2 - {r_2}^2}\right] \\ + \frac{\dot{q}}{8\kappa}\left[({r_1}^2 + {r_2}^2) - \frac{({r_1}^2 - {r_2}^2)}{ln(r_1/r_2)}\right] \end{aligned} \tag{3.84}$$

For non-internal heat generation cases the network can be modelled by the resistor network shown in Figure 3.10.

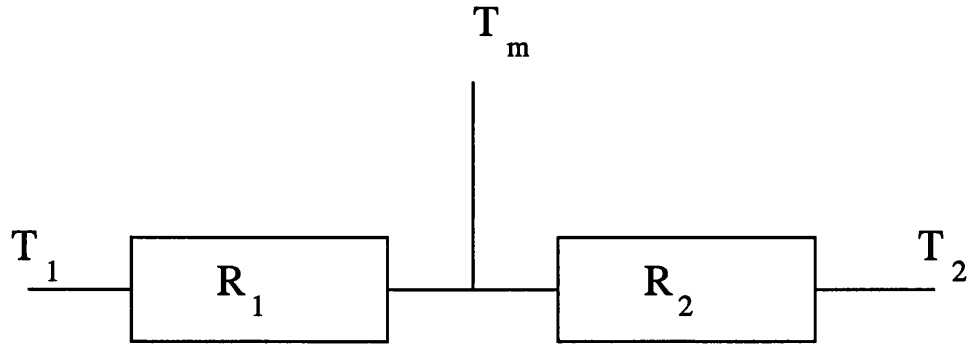

Figure 3.10: Two resistors network.

Using superposition, the mean temperature T_m can be expressed as

$$T_m = T_1\left[\frac{R_2}{R_1 + R_2}\right] + T_2\left[\frac{R_1}{R_1 + R_2}\right] \tag{3.85}$$

Comparing the coefficients of T_1 and T_2 in equations (3.84) and (3.85) with $\dot{q} = 0$, the thermal resistances R_1 and R_2 are defined as

$$R_1 = \frac{1}{4\pi\kappa L}\left[\frac{2{r_1}^2 ln(r_1/r_2)}{{r_1}^2 - {r_2}^2} - 1\right] \tag{3.86}$$

$$R_2 = \frac{1}{4\pi\kappa L}\left[1 - \frac{2{r_2}^2 ln(r_1/r_2)}{{r_1}^2 - {r_2}^2}\right] \tag{3.87}$$

For cases where heat generation $\dot{q}$ is not zero, Perez and Kassakian [25] proposed a T-equivalent network with an additional resistance R_m at the central node of Figure 3.10. The new equivalent circuit is shown in Figure 3.11.

Let $T_1 = T_2 = 0$:

$$T_m = q\left[R_m + \frac{R_1 R_2}{R_1 + R_2}\right] \tag{3.88}$$

where q is the total heat transfer in the component.

Since $T_1 = T_2 = 0$, the mean temperature T_m of equation (3.84) is reduced to

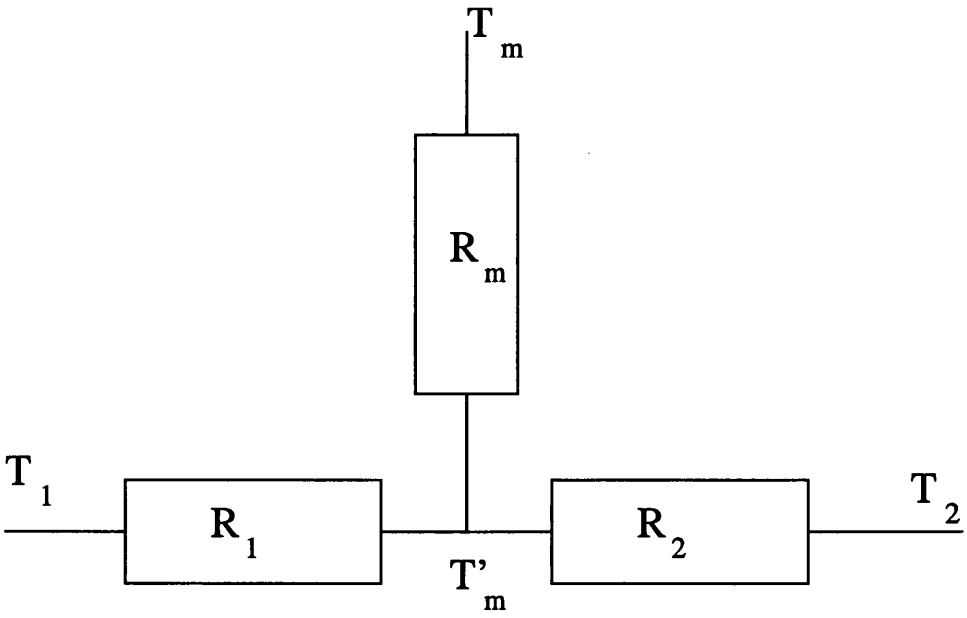

Figure 3.11: T-equivalent network.

$$T_m = \frac{\dot{q}({r_1}^2 + {r_2}^2)}{8\kappa} - \frac{\dot{q}({r_1}^2 - {r_2}^2)}{8\kappa[ln(r_1/r_2)]} \tag{3.89}$$

Comparing equations (3.88) and (3.89) gives

$$R_m = \frac{-1}{8\pi\kappa L({r_1}^2 - {r_2}^2)}\left[{r_1}^2 + {r_2}^2 - \frac{4{r_1}^2{r_2}^2 ln(r_1/r_2)}{{r_1}^2 - {r_2}^2}\right] \tag{3.90}$$

1D conductive heat transfer in axial direction is described by

$$\kappa\frac{\partial^2 T}{\partial l^2} + \dot{q} = 0 \tag{3.91}$$

with the general solution

$$T_l = -\frac{\dot{q}l^2}{2\kappa} + c(l) + d \tag{3.92}$$

The arbitrary constants c and d are found by letting the boundary conditions $T_l = T_3$ at $l = 0$ and $T_l = T_4$ at $l = L$. Therefore,

$$c = \frac{1}{L}\left[T_4 - T_3 + \frac{\dot{q}L^2}{2\kappa}\right] \tag{3.93}$$

$$d = T_3 \tag{3.94}$$

Solving equation (3.80) with the general solution gives

$$T_m = \frac{T_3 + T_4}{2} + \frac{\dot{q}L^2}{12\kappa} \tag{3.95}$$

The temperature in the axial direction is assumed to be symmetrical distributed. Therefore, equation (3.95) is simplified by making $T_3 = T_4$. Now the axial resistance R_3 can be determined by substituting the internal heat generated at the axial boundaries,

$$\dot{q} = \frac{q}{\pi({r_1}^2 - {r_2}^2)L} \tag{3.96}$$

Therefore, equation (3.95) is modified to

$$T_m = T_4 + \frac{qL}{12\pi\kappa({r_1}^2 - {r_2}^2)} \tag{3.97}$$

The last term on the *r.h.s* of equation (3.97) is the temperature T_3. Thus, R_3 is defined as

$$R_3 = \frac{L}{12\pi\kappa({r_1}^2 - {r_2}^2)} \tag{3.98}$$

3.12 Validation of Heat Transfer using Finite Element Method and Lumped Parameter Circuit Technique

The finite element and lumped parameter methods discussed earlier will be used to solve two problems involving non-linear temperature dependent boundary conditions. At this early stage, all the problems are modelled purely as thermal problems without any current flow.

The first problem to be modelled using finite elements is that of a vertical placed mild steel plate. The heat influx is tied to the left hand side of the plate as a known prescribed heat flow rate of 200 W. The surface on the right is exposed to an ambient air temperature of 20 °C.

The convection and radiation coefficients are temperature dependent. Both coefficients are computed at each iteration using the empirical correlation formula for vertical plate and linearised radiation equation with the emissivity rate (ϵ_r) of 0.07. This emissivity rate reflects the value of a mild steel with polished surface. The heat lost by radiation is somewhat limited by this factor. Table(3.1) shows the material properties of the mild steel used in the experiment.

Table 3.1: Material properties of mild steel.

Material properties	Mild Steel
Thermal conductivity, κ (W/m K)	54
Specific heat, C_p (J/kg K)	465
Density, ρ (kg/m^3)	7833
Electrical conductivity, σ (S/m)	4.5×10^6

With the lumped parameter model, a series of resistances and capacitances are constructed to represent the steel plate. Non-linear resistances are applied where appropriate to model the plate surface contact with air.

In the finite element model, *backward difference* time-stepping scheme is used. The *backward difference* time scheme is known to offer better stability characteristics. The

time-integration scheme used for the lumped parameter model employs a variable time-step size thus, ensuring a low error.

Figure 3.12 and Figure 3.13 show the coarse mesh and fine mesh 2D FE models of steel plate used in this validation exercise. Different time-steps $\Delta t = 100.0$ s and $\Delta t = 1000.0$ s, are employed to test the stability of the *backward difference* time scheme. Results from both the lumped parameter model and 2D finite element models with different mesh density compare well, as shown in Figure 3.14 and Figure 3.15.

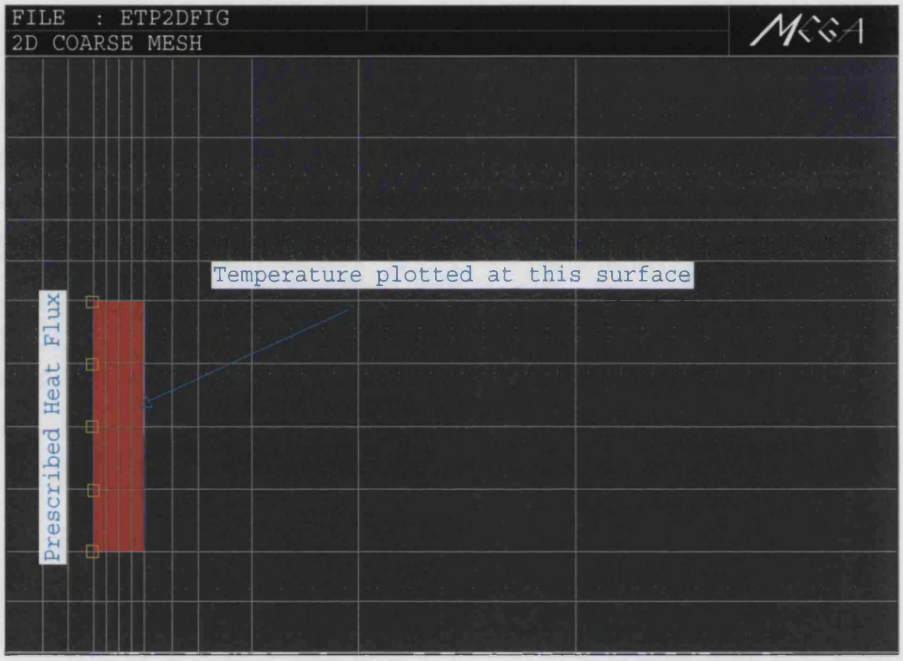

Figure 3.12: Coarse mesh 2D FE model of steel plate.

The 2D finite element method is then extended to 3D. A vertical plate test model using the 3D mesh as illustrated in Figure 3.16 was defined in order to verify the 3D method against the existing 2D code. The conductor is extended 1 m in the z-direction. This allows a 3D slice to be modelled, which should give the same results as the equivalent 2D model. Comparing the results in Figure 3.17 produced from solving the 2D and 3D models show a high level of agreement.

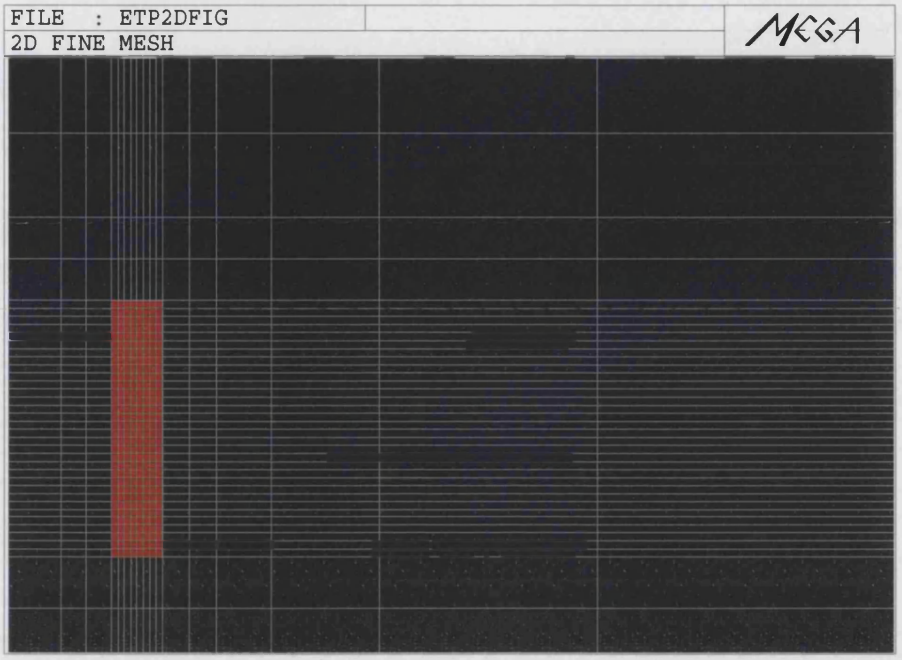

Figure 3.13: Fine mesh 2D FE model of steel plate.

In the following exercise, a finite element model of a hollow cylinder is built. Its material properties are similar to that of the steel plate but a heat influx of 800 W instead of 200 W is prescribed at the inner radius of the cylinder. Figure 3.18 shows the comparison of temperature results obtained from the lumped parameter model and the 2D FE model. As for 3D, the base plane is again extruded 1 m towards the z-axis as illustrated in Figure 3.19 and solved. The results are shown in Figure 3.20.

Figure 3.21 and Figure 3.22 show the temperature rise in the steel plate and cylinder with radiation emissivity factor ϵ_r changed from 0.07 to 0.9 to reflect a black painted body in the physical reality. The results show more heat escaped by radiation which generally lowers the overall temperature in the two solid conductors.

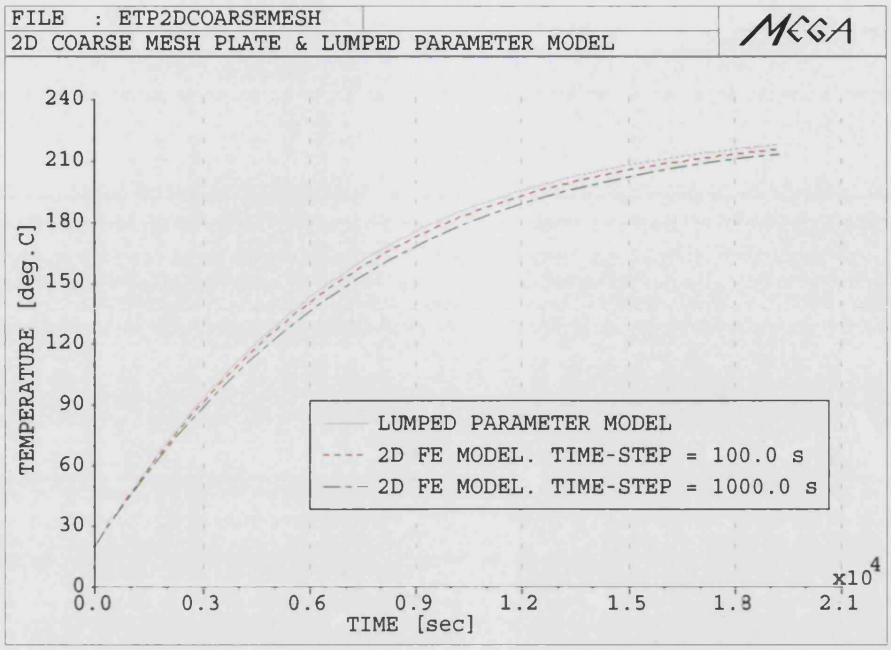

Figure 3.14: Temperature in lumped parameter and coarse mesh FE models of steel plate.

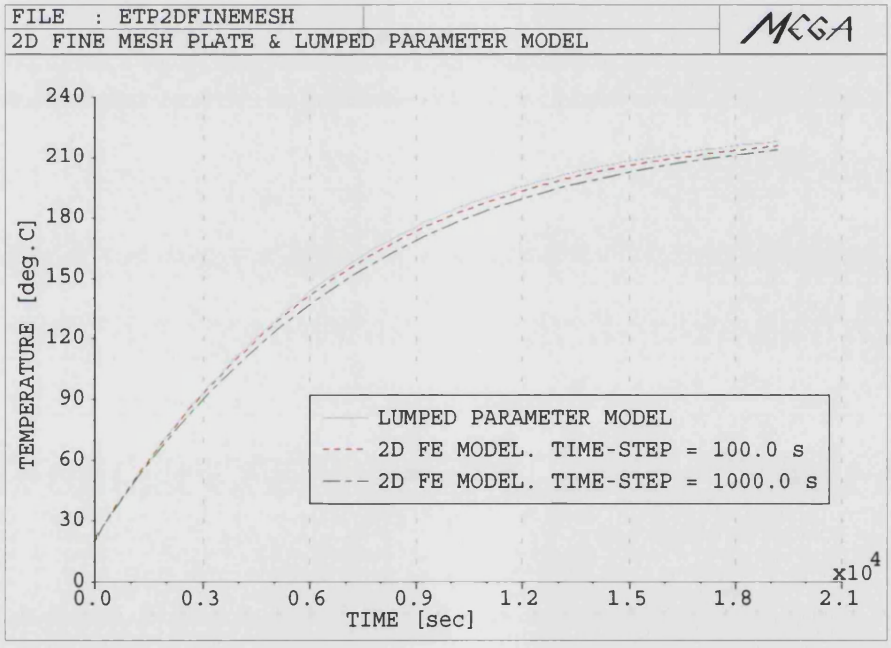

Figure 3.15: Temperature in lumped parameter and fine mesh FE models of steel plate.

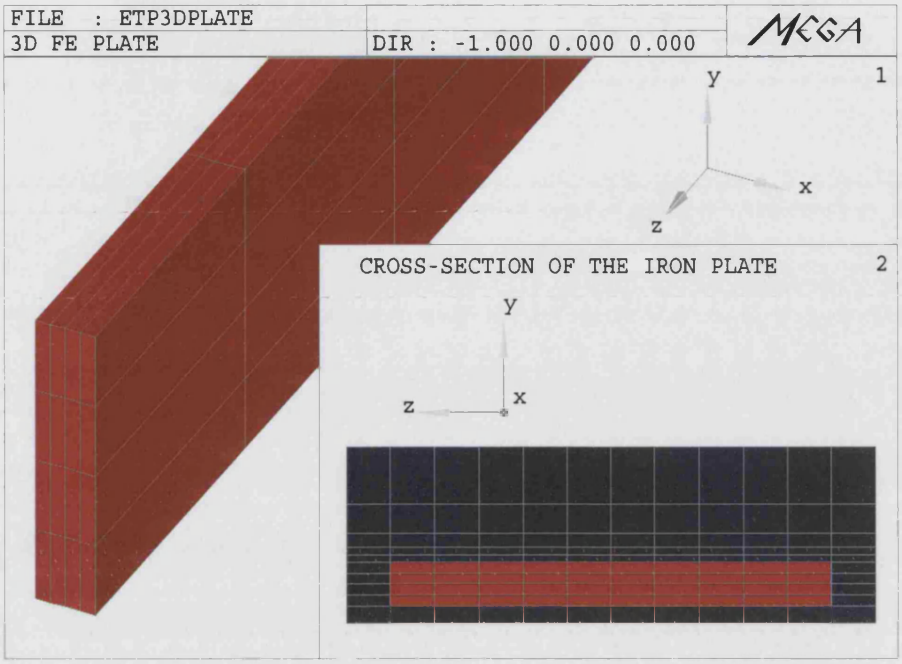

Figure 3.16: 3D FE model of steel plate.

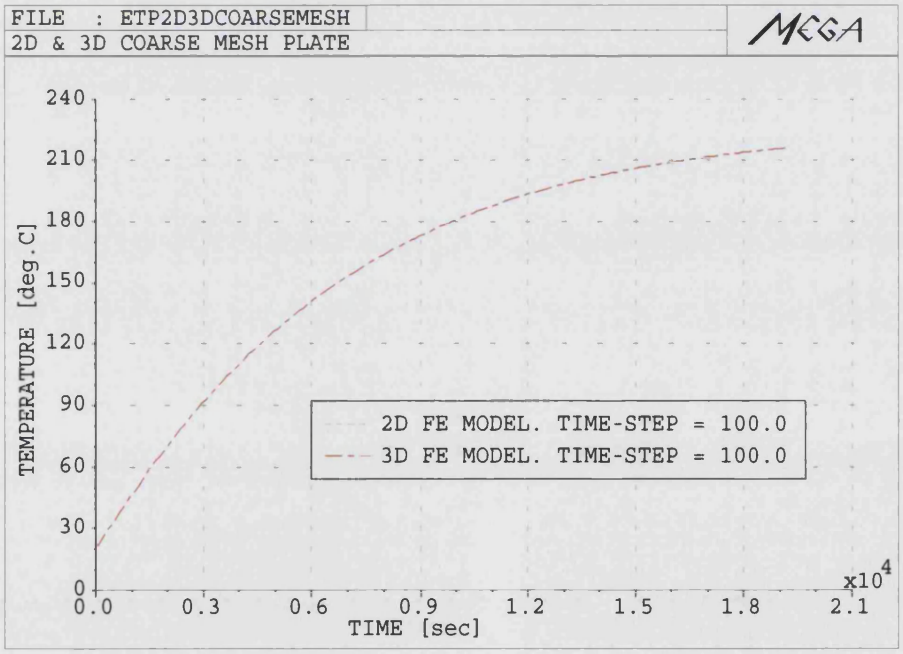

Figure 3.17: Temperature in 2D and 3D coarse mesh FE models of steel plate.

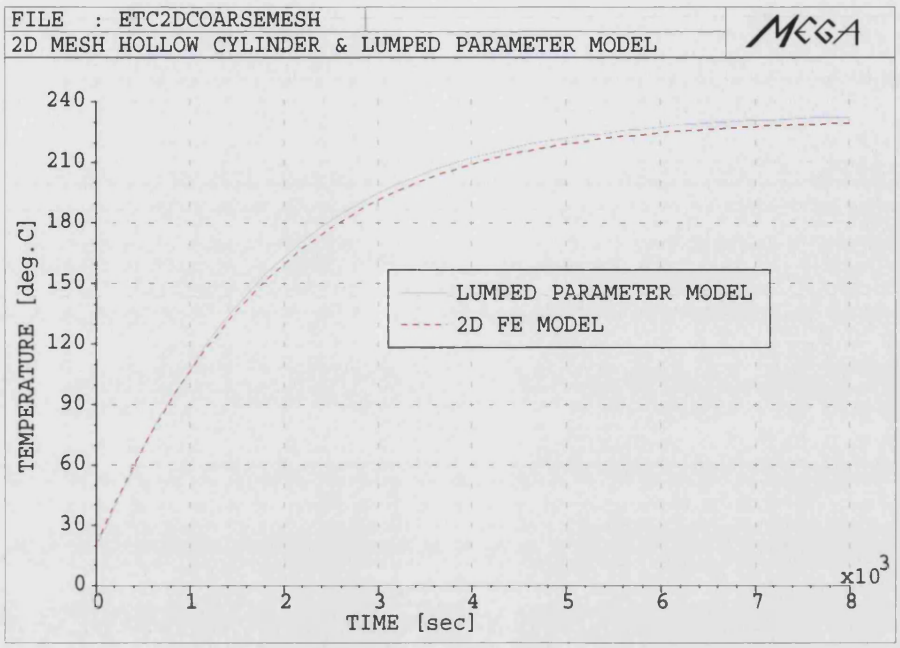

Figure 3.18: Temperature in lumped parameter and 2D FE models of hollow cylinder.

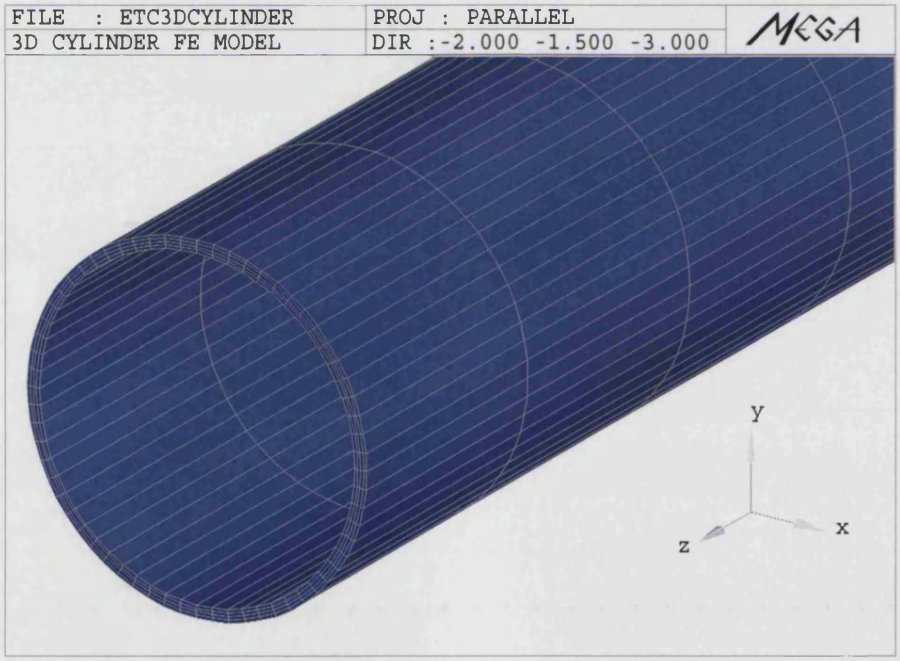

Figure 3.19: 3D FE model of hollow cylinder.

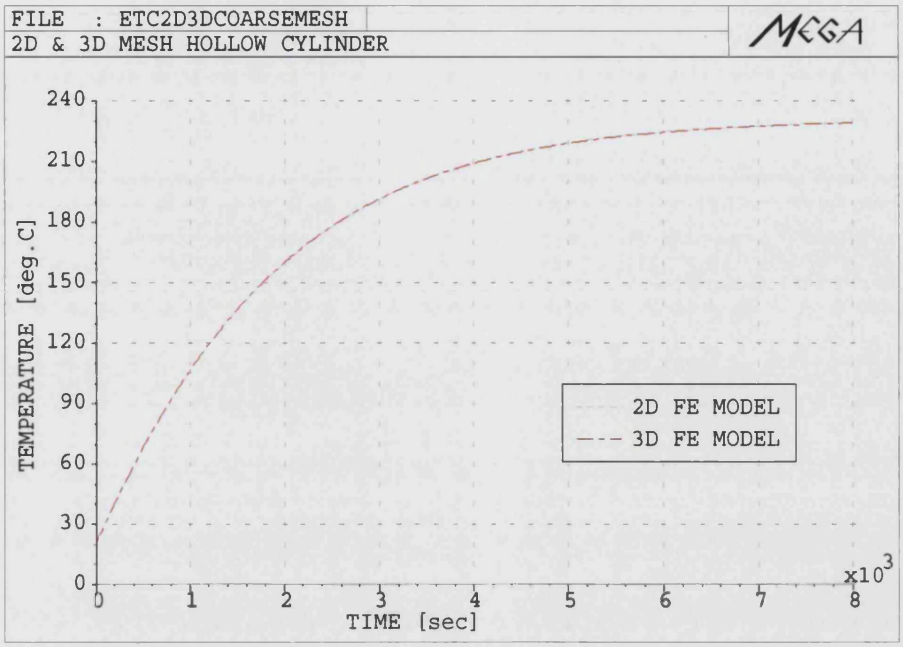

Figure 3.20: Temperature in 2D and 3D FE models of hollow cylinder.

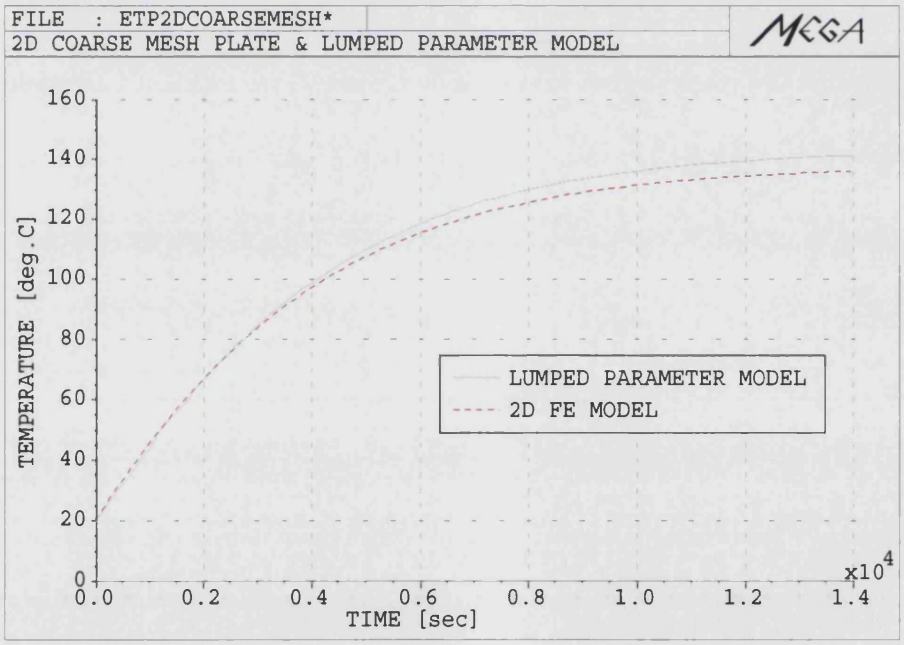

Figure 3.21: Temperature in vertical steel plate with $\epsilon_r = 0.9$.

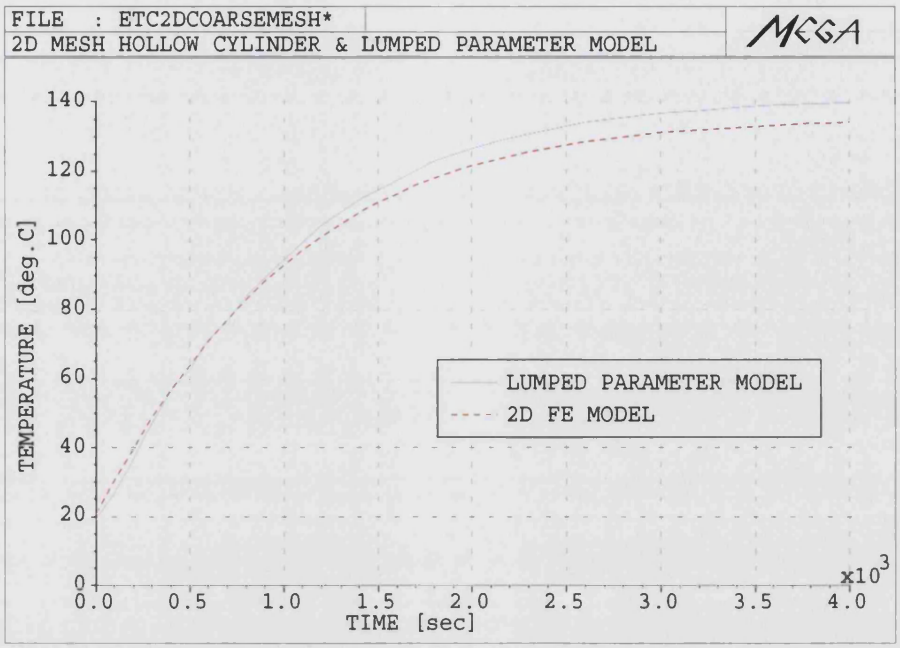

Figure 3.22: Temperature in hollow cylinder with $\epsilon_r = 0.9$.

Finally, the mild steel cylinder with polished surface is immersed into a region with transverse air flow of velocities 1.0 m/s and 2.0 m/s respectively. The results are shown in Figure 3.23. With the flow of air surrounding the cylinder, the heat dissipation rate of the cylinder has increased significantly. Figure 3.24 and Figure 3.25 show the comparison in temperature between the lumped parameter model and 2D finite element model at the two specified air velocities.

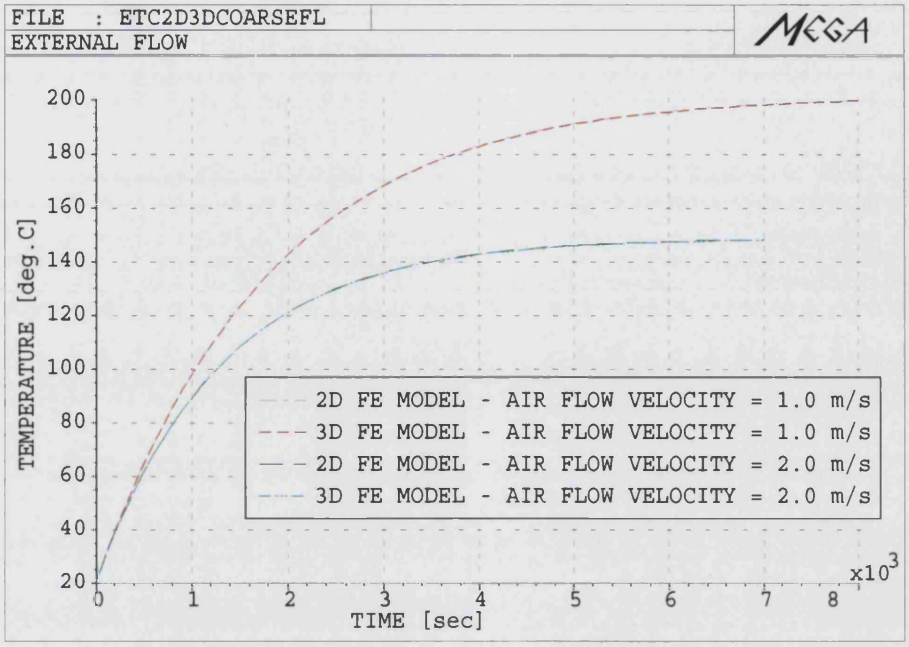

Figure 3.23: Temperature in 2D and 3D FE models of hollow cylinder with air flow.

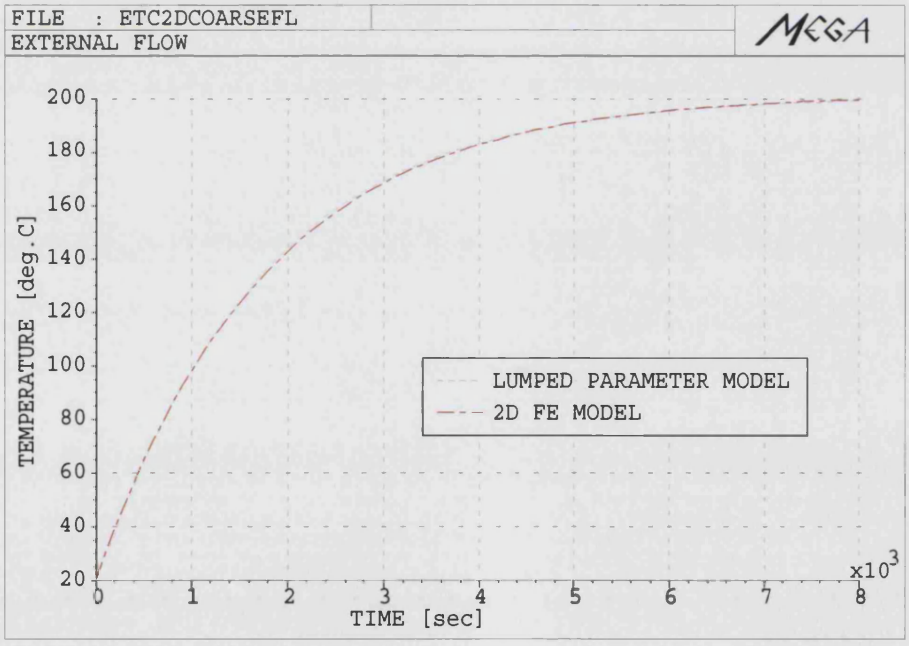

Figure 3.24: Temperature in hollow cylinder with air flow velocity at 1.0 m/s.

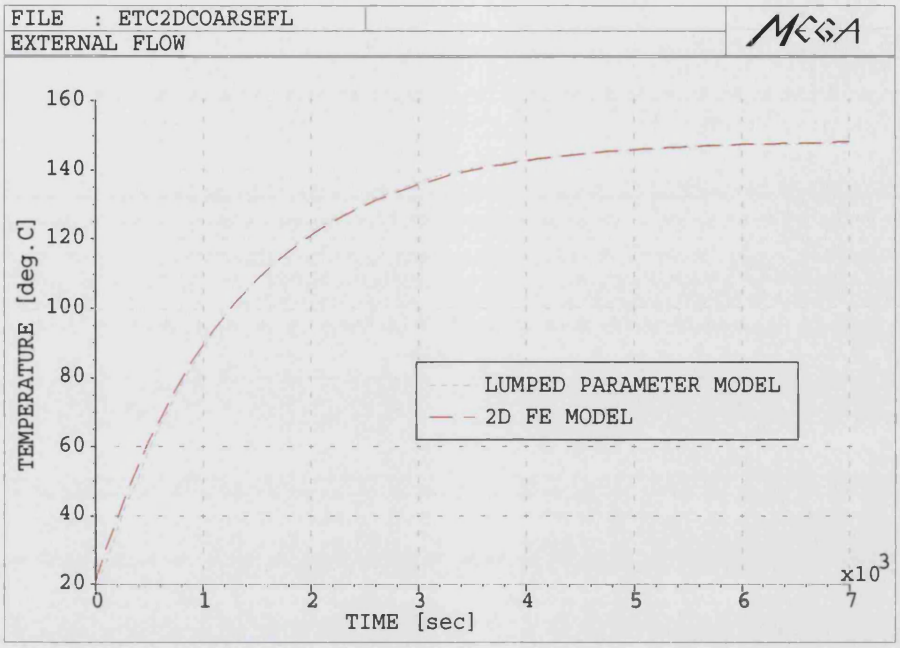

Figure 3.25: Temperature in hollow cylinder with air flow velocity at 2.0 m/s.

3.13 Summary

Numerical methods for modelling transient heat transfer in a thermal region have been presented in this chapter. The surface heat flow boundary conditions are prescribed to model the heat flow outward from the thermal system. The surface of the conductor is subjected to either forced or natural convection boundary conditions. These convection coefficients are obtained from the *Churchill-Chu* correlation data compilation for vertical plate and horizontal cylindrical surfaces. The surface radiation is also included for black coated surfaces.

A comparison is made between two numerical methods, the finite element and lumped parameter techniques. Both techniques compared well and could be used to complement each other. Whichever method, the accuracy of the model is still very much dependent on the external surface-ambient heat paths, the surrounding environment and the model layout.

Chapter 4

Finite Element Modelling of Thermo-Coupled Electromagnetic Problems

4.1 Introduction

The analysis of coupled thermo-magnetic problems in current-carrying conductors required the solution of a coupled thermo-magnetic problem and both magnetic and thermal diffusion should in principle be accounted for. This implies the solution of two parabolic partial differential equations coupled through the temperature dependence of electric conductivity σ, specific heat C_p, thermal conductivity κ and through the driving term of the thermal equation, due to the power losses in the conductor.

The mathematical model consists of a differential equation system comprising the magnetic vector potential for non-linear eddy current problems and scalar temperature variable for the Fourier's thermal conduction. The finite element method is applied in conjunction with the Galerkin method. The set of equations is consequently non-linear and required a time-marching solution scheme.

The discussion of this chapter focuses on the modelling of heat transfer with induced time-transient eddy current losses as the heat source in the conductor. Stationary and moving eddy current regions are considered. The stationary eddy current finite ele-

ment formulation involves the use of vector variable $\boldsymbol{A}$ to model eddy current regions and accompanied by the additional scalar V in cases of conducting regions having non-linear conductivities. In moving eddy current problems, the relative motion between the conductor and the magnetic field source also has the effect of inducing eddy currents. If the $\boldsymbol{B}$ field is time-varying and there is relative motion between the magnetic field source and the conductor, then both effects will combine to produce eddy currents.

Steady-state AC eddy current losses will also be modelled for material with large thermal time constant and linear **B-H** characteristics. In this case it is prudent to solve the electromagnetic equation once to compute the joule heat loss. Once the joule heating solution is obtained, the time-transient thermal system will be solved with temperature coupled convection heat transfer prescribed on the material surface.

Besides induced eddy currents, another important heat source in electromagnetic devices is the coil DC I^2R power dissipation. The existence of this heat source is the direct result of the flow of current in a resistive element. DC I^2R losses due to copper coils have proven to be the major source of heat generation in windings of electrical machinery.

The convection and radiation boundary conditions imposed will be similar to those discussed in Chapter 3. The *Churchill-Chu* correlation equations for convection will be reused for non-moving media. Two additional convection coefficients for rotating cylinder and disk will be added to model the heat transfer of the moving parts.

Finally, this chapter describes the thermal modelling of a disk induction machine. Temperature distribution inside an electrical machine is of interest for many reasons. Some machine parts, for instance the insulation and bearings can deteriorate rapidly at excessive winding temperatures. This affects the overall machine performance and efficiency as both ratings are predominantly governed by temperature rise. Therefore, to ensure a longer lifespan for the machine the temperature rise must be reduced to a safe level.

4.2 $A-V$ Field Theory for Inductive Heating

The thermal field is coupled to the magnetic field through the eddy currents and resistive joule heating. In conducting regions the $\boldsymbol{A}-V$ equation is used. This well-established finite element formulation is described in Chapter 2 and is briefly reviewed here for convenience.

According to Faraday's law the electric field in conducting regions is described as

$$\boldsymbol{E} = -\frac{\partial \boldsymbol{A}}{\partial t} - \nabla V \tag{4.1}$$

The electric scalar potential V is required in modelling moving conducting regions and modelling jumps in conductivity or introducing sources into massive circuit. If the conductivity in the eddy current region is constant then $V = 0$ and the field can be represented by the magnetic vector potential $\boldsymbol{A}$ alone, $\boldsymbol{B} = \nabla \times \boldsymbol{A}$.

Using the magnetic vector potential $\boldsymbol{A}$ to represent the magnetic flux density and substituting $\boldsymbol{J} = \sigma \boldsymbol{E}$ to solve the Maxwell equation $\nabla \times \boldsymbol{H} = \boldsymbol{J}$, yields the following $\boldsymbol{A} - V$ expression

$$\nabla \times \frac{1}{\mu} \nabla \times \boldsymbol{A} - \{\nabla \frac{1}{\mu} \nabla \cdot \boldsymbol{A}\} = \boldsymbol{J} \tag{4.2}$$

With $\boldsymbol{J} = \sigma \boldsymbol{E}$ then

$$\nabla \times \frac{1}{\mu} \nabla \times \boldsymbol{A} - \{\nabla \frac{1}{\mu} \nabla \cdot \boldsymbol{A}\} = -\sigma \frac{\partial \boldsymbol{A}}{\partial t} - \sigma \nabla V \tag{4.3}$$

and the continuity equation $\nabla \cdot \boldsymbol{J} = 0$ described as

$$\nabla \cdot \left(\sigma \frac{\partial \boldsymbol{A}}{\partial t} + \sigma \nabla V \right) = 0 \tag{4.4}$$

The penalty term in the curly bracket of equation (4.2) is sometimes added to gauge these equations. Typically $\frac{1}{\mu}$ is chosen as the penalty weight. To make the solution

unique $\boldsymbol{A} \cdot \hat{\mathbf{n}} = 0$ can be enforced on the boundary of the magnetic vector potential $\boldsymbol{A}$ regions.

If the device modelled is invariant in the z-direction then a 2D model with a single component of $\boldsymbol{A} = A_z\hat{\boldsymbol{z}}$ can be used. The induced *e.m.f* and magnetic flux density are

$$E_z = -\frac{\partial A_z}{\partial t} \quad ; \quad \boldsymbol{B} = \nabla \times A_z\hat{\boldsymbol{z}} \tag{4.5}$$

which reduces the equation (4.2) to a 'diffusion form'

$$-\nabla \cdot \frac{1}{\mu}\nabla A_z + \sigma\frac{\partial A_z}{\partial t} = J \tag{4.6}$$

The current is described by two terms, one due to induced eddy currents and a second prescribed source current term.

In electrical devices, the heat source $\dot{q}$ is the ohmic losses defined as

$$\dot{q} = \frac{\boldsymbol{J}^2}{\sigma} \tag{4.7}$$

$$\dot{q} = \sigma\left(\frac{\partial \boldsymbol{A}}{\partial t} + \nabla V\right)^2 \tag{4.8}$$

For the special case of isolated eddy current regions of constant conductivity or a 2D region, the scalar V may be set to zero throughout the conducting region without violating Maxwell's equations and thus eliminates the need to solve for ∇V in equation (4.8).

4.3 Coupled Electromagnetic Heating

In general the electrical and thermal properties are temperature dependent. If these changes are ignored the electromagnetic system is decoupled from the thermal system. The thermal software previously developed for *MEGA* was uncoupled. The electromagnetic heating effects or joule heating are calculated but the effects of the heating on the properties are ignored. These electromagnetic heating effects need to be included in the thermal system to model the coupled thermo-electromagnetic heating effects. The simplest procedure is to alternate between the electromagnetic solution and thermal solution.

The thermal model used by *MEGA* to calculate joule heating includes the temperature coefficient of resistivity and thus, coupling the material electrical conductivity to temperature. The temperature dependence of resistance can be approximated by the equation

$$R_T = R_o(1 + \alpha T + \grave{\beta} T^2) \tag{4.9}$$

where R_T is the resistance at absolute temperature T, R_o is the resistance at 293.71 K, and α and $\grave{\beta}$ are constants characteristic of the material of interest. In practice $\grave{\beta}$ can be ignored and the temperature coefficient of resistance depends on α only.

From equation (4.9) the material electrical conductivity σ at a given temperature can be expressed as

$$\sigma_T = \frac{\sigma_o}{1 + \alpha T} \tag{4.10}$$

The algorithm to solve this coupled problem is summarised as below:

1. Initialise the electromagnetic unknowns $\boldsymbol{A} = \boldsymbol{A}_o$ for time $t = 0$. Set $n = 0$ and the time-step Δt.

2. Assemble the electromagnetic system of equations for this position, x_n, $[K_n]$.

3. Calculate the electromagnetic solution, using the *backward difference scheme*

$$\alpha_n = ([C_n] + \Delta t[K_n])^{-1}\{f_n - [K_n][A_n]\}$$

$$A_{n+1} = A_n + \alpha_n \Delta t$$

4. Calculate the electromagnetic heating described previously using this result.

5. Calculate the temperature dependent value of σ and reassemble the matrix $[K_n]$.

6. Set $n = n + 1$ and repeat the algorithm from step 3.

Similarly the non-linear convection and radiation boundary conditions are solved using the *backward difference scheme.*

The thermal and electrical time constants have huge disparity. Solving the coupled electromagnetic-thermal system require a huge matrix. The solution is obtained by marching in time. However, in the electrical system the time-step will have to be small enough, which results in more computing. To solve this difficulty, the electromagnetic part of the problem is solved as an AC problem. The computed power dissipation then serves as the source term for the thermal system. In a sense the electrical and thermal systems are weakly coupled together.

4.4 Galerkin Weighted Residual Approximation

The unknown nodal potentials in the coupled region are approximated in the piecewise manner together with the shape function by

$$A = \sum N_i A_i \tag{4.11}$$

$$\psi = \sum N_i \psi_i \tag{4.12}$$

$$V = \sum N_i V_i \tag{4.13}$$

$$T = \sum N_i T_i \tag{4.14}$$

The Galerkin procedure give rise to the weak form of the governing equations. After the transformation using Green-Gauss theorem:

- Non-conducting regions

$$\int_{\Omega_\psi} \mu \nabla N \cdot \nabla \psi \, \mathrm{d}\Omega = \oint_{\Gamma_\psi} N \mu \frac{\partial \psi}{\partial n} \, \mathrm{d}\Gamma \tag{4.15}$$

- Conducting regions

$$\int_{\Omega_{\boldsymbol{A}}} \left[\frac{1}{\mu} (\nabla \times \boldsymbol{N}) \cdot (\nabla \times \boldsymbol{A}) + \sigma \boldsymbol{N} \cdot \left(\frac{\partial \boldsymbol{A}}{\partial t} + \nabla V \right) \right] \mathrm{d}\Omega = \oint_{\Gamma_{\boldsymbol{A}}} \boldsymbol{N} \cdot \frac{1}{\mu} (\nabla \times \boldsymbol{A} \times \hat{\mathbf{n}}) \, \mathrm{d}\Gamma \tag{4.16}$$

- Thermal regions

$$\int_{\Omega_T} \nabla N \cdot \kappa \nabla T \mathrm{d}\Omega + \int_{\Omega_T} N \rho C \frac{\partial T}{\partial t} \, \mathrm{d}\Omega - \int_{\Omega_T} N \frac{\boldsymbol{J}^2}{\sigma} \, \mathrm{d}\Omega = \oint_{\Gamma_T} N \kappa \nabla T \cdot \hat{\mathbf{n}} \, \mathrm{d}\Gamma \tag{4.17}$$

The surface integral terms naturally cancel when combining adjacent elements within the region.

4.5 Coupled Transient Electromagnetic-Thermal Field

For strong coupled modelling with temperature dependent electrical conductivity, a fully transient electromagnetic-thermal solution is required. To illustrate the effects of temperature dependent properties, a specific application is discussed here as an example in which the results of the two analyses are compared. The example evaluated is a very crude model of an hypothetical extended version of electromagnetic launcher. The 3D model of the launcher is shown in Figure 4.1. The launcher has two rails of 140 mm long. The armature is 40 mm long and 40 mm wide.

The rail and augmented rail are made of copper with the conductivity of 5.45×10^7 S/m. The moving armature is aluminium with electrical conductivity of 3.0×10^7 S/m. The thermal conductivities are 399 W/(m K) for copper and 204 W/(m K) for aluminium respectively.

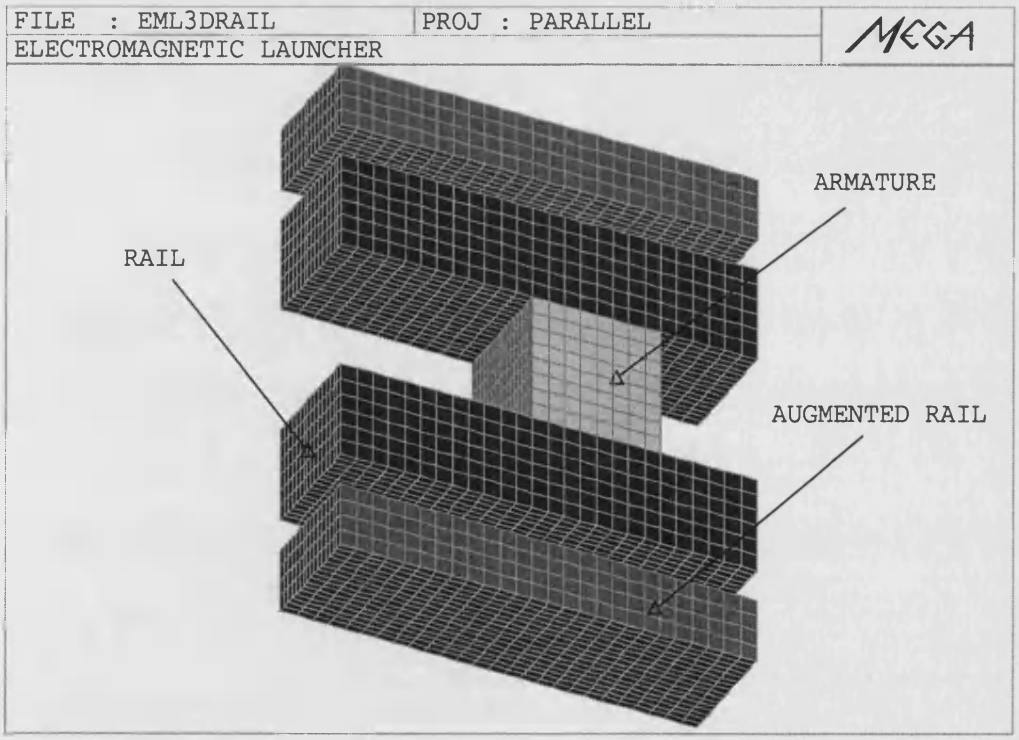

Figure 4.1: 3D electromagnetic launcher.

The rail 3D model is prescribed with specific boundary conditions to set up the required external current forced circuit. The forced current is fed into the rails on the left side of the model by setting the plane of symmetry ($x = 0$) to tangential flux. This boundary condition allows the current to flow at the normal angle to the boundary.

The Galerkin procedure for the eddy current equation yields the usual

$$\int_{\Omega_{\boldsymbol{A}}} \left[\frac{1}{\mu}\nabla \times \boldsymbol{N} \cdot \nabla \times \boldsymbol{A} + \boldsymbol{N} \cdot \sigma\left(\frac{\partial \boldsymbol{A}}{\partial t} + \nabla V\right)\right] \mathrm{d}\Omega = \oint_{\Gamma_{\boldsymbol{A}}} \boldsymbol{N} \cdot \frac{1}{\mu}\nabla \times \boldsymbol{A} \times \mathrm{d}\Gamma \quad (4.18)$$

The surface source term is used to weakly ensured that the current flow prescribed is normal to the boundary at the edge of the plane. For more information on external sources and massive conductor modelling, see papers [26], [27].

The tangential flux, $\boldsymbol{H} \times \hat{\mathbf{n}}$ boundary condition is prescribed by setting $\boldsymbol{A} = 0$ along the edges of the x and y planes of symmetry. The normal flux, $\boldsymbol{B} \cdot \hat{\mathbf{n}}$ is set by imposing $\oint_{\Gamma} N \frac{1}{\mu}\frac{\partial \boldsymbol{A}}{\partial n}\, d\Gamma = 0$ on the base plane ($z = 0$) of the model.

Two current pulses are fed into the proper and augmented rails. The current in the proper rail surged to the peak value of 0.1 MA in 0.3 ms. Perfect electrical contact is assumed along the rail-armature interface. Friction is also neglected in both models. At first due to skin effect, the current appears to flow on the periphery of the inner corner of the armature. This outer surface also produced the peak current density.

Figure 4.2 shows the eddy current density of the rail launcher with constant and temperature dependent electrical conductivities respectively. The induced current densities in the constant conductivity model show peak value occurring at the armature surface and those of the dependent conductivity case propagate into the armature, resulting in a more quickly broadening current sheath. This is caused by the fact that the lower electrical conductivity, due to temperature rise in the material, decreases

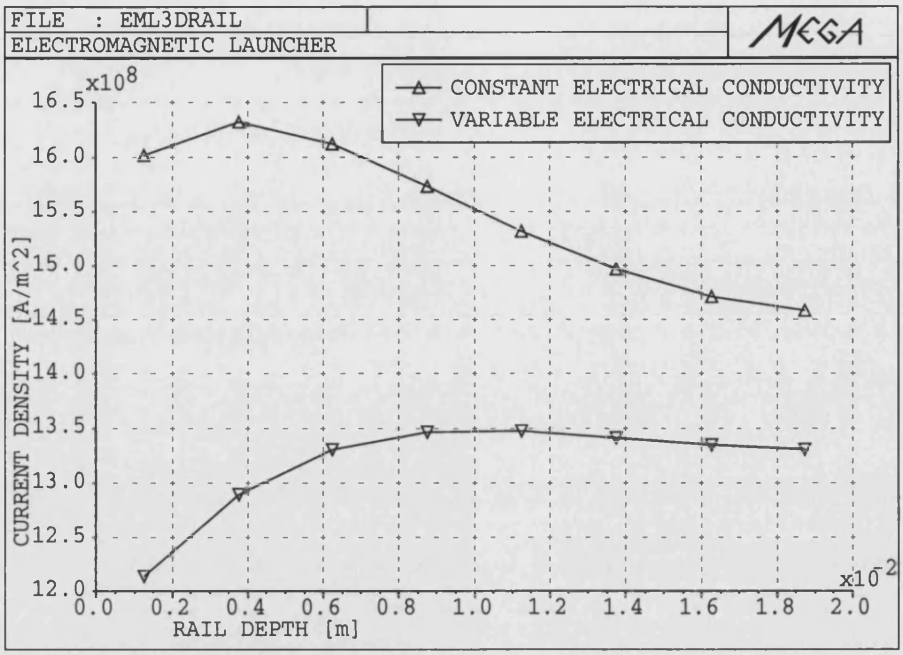

Figure 4.2: Current density at the armature.

the magnitude of the eddy currents. As a result of the reduced magnitude of the surface eddy currents, the eddy currents are able to penetrate deeper into the material, maintaining the required current density.

Obviously, the peak temperatures generated in the temperature dependent conductivity model are lower than those produced in the model with constant conductivity. This effect is shown by the different temperature distributions in the rail launcher of Figure 4.3 and Figure 4.4.

A new rail launcher without the augmented rail is modelled with the dimension based on [28] for comparison. Only the rail launcher with a stationary armature is considered. The material electrical conductivities are all temperature dependent. The prediction, shown in Figure 4.5, is in good agreement with the result obtained in [28]. The temperature rise in the rail launcher is shown in Figure 4.6.

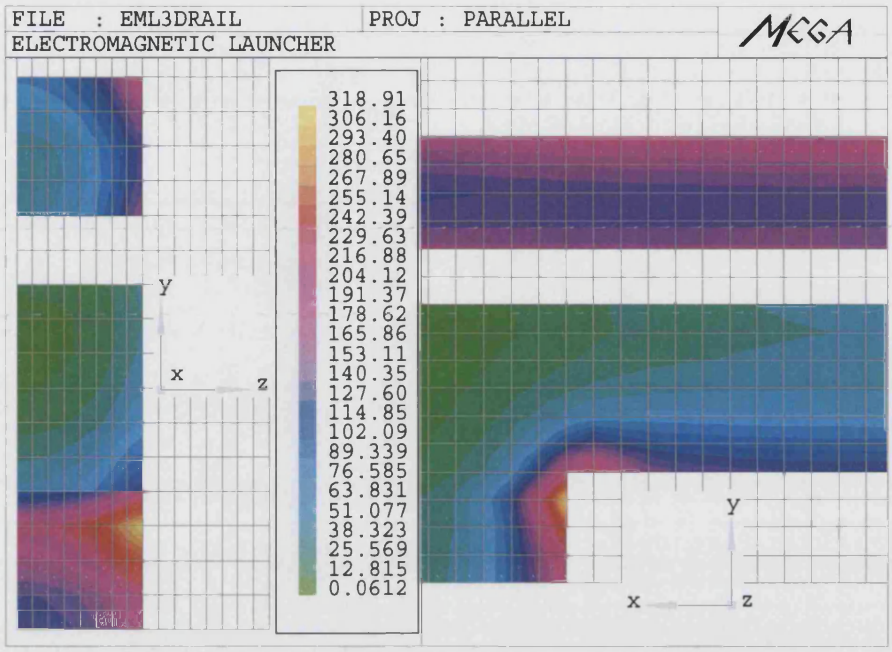

Figure 4.3: Temperature distribution in rail launcher with constant electrical conductivity.

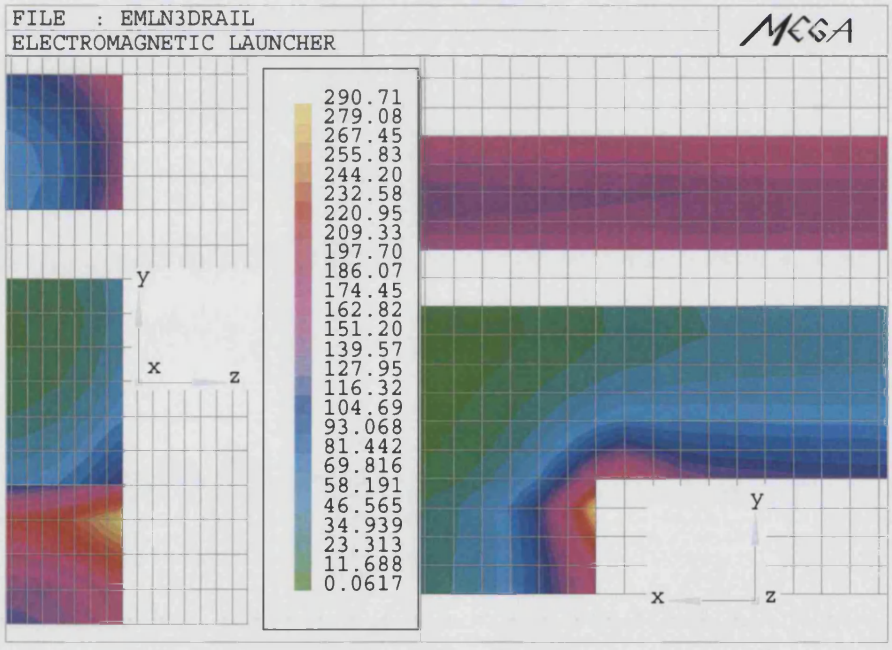

Figure 4.4: Temperature distribution in rail launcher with temperature dependent electrical conductivity.

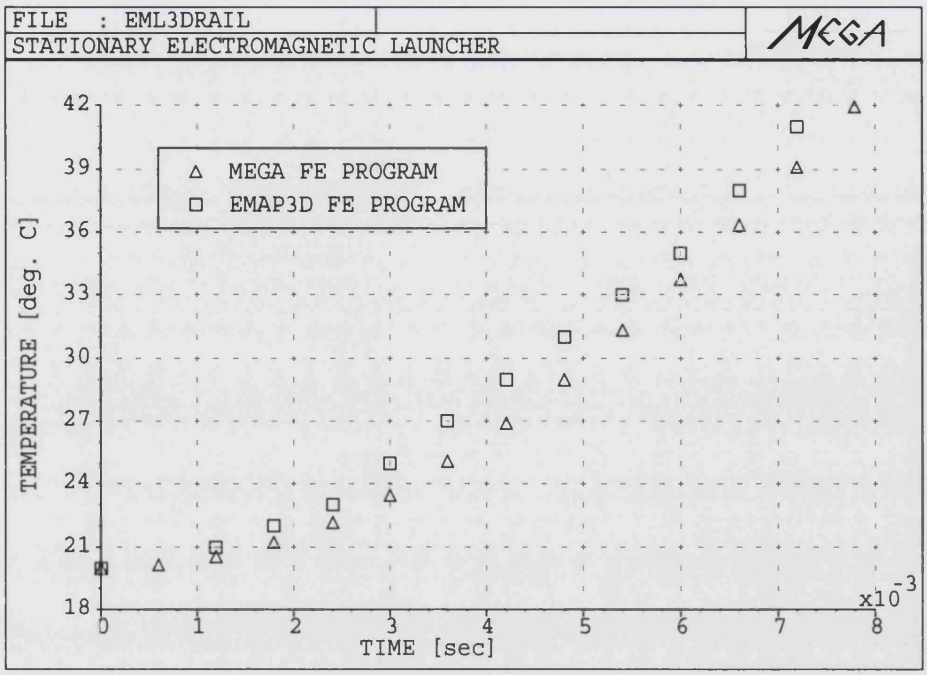

Figure 4.5: Comparison of simulated temperature in rail launcher.

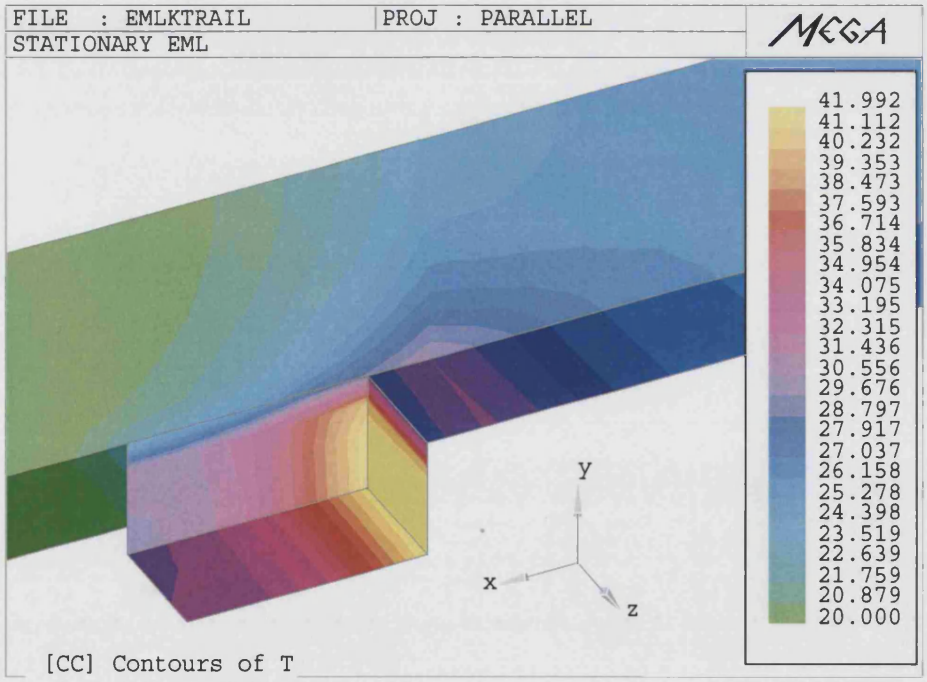

Figure 4.6: Temperature rise in the rail launcher.

4.6 Modelling Moving Conducting and Thermal Regions

4.6.1 An Eulerian Description for Eddy Current Regions

The relative motion between an eddy current region and the magnetic field source generates a motional component to the induced *e.m.f* in addition to the *transformer* effect, the existence of which is due to the time variation of the magnetic field. If the velocity of the eddy current conductor is constant and its cross-section invariant to the direction of motion then it is possible to apply the *Minkowski* technique to solve the problem.

In the conductor frame of reference, the $\boldsymbol{E}$ field is the result of the generated *e.m.f* due to the combined effects of time variation and motion. The $\boldsymbol{E}$ field in the source frame of reference is related only to the transformer effect.

Therefore, *e.m.f* can be regarded as having two components:

- The normal transformer effect which is due to the changing magnetic flux in the frame of reference, stationary $\boldsymbol{E} = -\dfrac{\partial \boldsymbol{A}}{\partial t}$
- *e.m.f* which is caused by the magnetic field motional effect, non-stationary $\boldsymbol{E} = \boldsymbol{u} \times \boldsymbol{B}$

The *e.m.f* which drives the current in the conductor frame of reference is then

$$\boldsymbol{E} = -\frac{\partial \boldsymbol{A}}{\partial t} + \boldsymbol{u} \times \boldsymbol{B} \tag{4.19}$$

which provides the *e.m.f* to drives the current

$$\boldsymbol{J} = \sigma(\boldsymbol{E} + \boldsymbol{u} \times \boldsymbol{B}) \tag{4.20}$$

The additional term $\boldsymbol{u} \times \boldsymbol{B}$ used for describing the moving region in stationary source of reference is the well-known *Minkowski transformation.*

Accordingly, the Ohm's law including the velocity term to be solved is expressed in terms of magnetic vector potential $\boldsymbol{A}$ and electric scalar potential V as

$$\nabla \times \frac{1}{\mu} \nabla \times \boldsymbol{A} = -\sigma \left[\frac{\partial \boldsymbol{A}}{\partial t} + \nabla V - \boldsymbol{u} \times (\nabla \times \boldsymbol{A}) \right] \tag{4.21}$$

The electric scalar potential V is required in modelling moving conducting regions but it can be set equal to $\boldsymbol{A} \cdot \boldsymbol{u}$, thus eliminating the need to solve for V directly. The voltage term ∇V is useful for modelling jumps in conductivity or introducing sources into massive circuit. If the conductivity in the eddy current region is constant then $V = 0$ and the field can be represented by the magnetic vector potential $\boldsymbol{A}$ alone.

Equating $V = \boldsymbol{A} \cdot \boldsymbol{u}$ and using the vector identity $\nabla(\boldsymbol{A} \cdot \boldsymbol{u}) = (\boldsymbol{u} \cdot \nabla)\boldsymbol{A} + (\boldsymbol{A} \cdot \nabla)\boldsymbol{u} + \boldsymbol{u} \times \nabla \times \boldsymbol{A} + \boldsymbol{A} \times \nabla \times \boldsymbol{u}$, equation (4.21) is reduced to

$$\nabla \times \frac{1}{\mu} \nabla \times \boldsymbol{A} = -\sigma \left[\frac{\partial \boldsymbol{A}}{\partial t} + (\boldsymbol{u} \cdot \nabla)\boldsymbol{A} + (\boldsymbol{A} \cdot \nabla)\boldsymbol{u} + (\nabla \times \boldsymbol{u}) \times \boldsymbol{A} \right] \tag{4.22}$$

The last two terms on the *r.h.s* of equation (4.22) disappear if the formulation is restricted to constant linear velocities. However, for rotational velocity these terms are non-zero. Using the definition $\boldsymbol{u} = \boldsymbol{r} \times \boldsymbol{\omega}$, where $\boldsymbol{r}$ is the position vector relative to the axis of rotation and $\boldsymbol{\omega}$ is the angular velocity, the two terms can be expressed as

$$(\boldsymbol{A} \cdot \nabla)\boldsymbol{u} = -\boldsymbol{A} \times \boldsymbol{\omega} \tag{4.23}$$

$$(\nabla \times \boldsymbol{u}) \times \boldsymbol{A} = 2\boldsymbol{A} \times \boldsymbol{\omega} \tag{4.24}$$

Substituting equations (4.23) and (4.24) into equation (4.22), the following alternative form of equation is obtained:

$$\nabla \times \frac{1}{\mu} \nabla \times \boldsymbol{A} = -\sigma \left[\frac{\partial \boldsymbol{A}}{\partial t} + (\boldsymbol{u} \cdot \nabla)\boldsymbol{A} + \boldsymbol{A} \times \boldsymbol{\omega} \right] \tag{4.25}$$

For translational velocity the angular velocity term can be discarded.

4.6.2 Governing Equation for Moving Thermal Regions

For a moving thermal region, the thermal diffusion equation is added with two velocity terms {},

$$\nabla \cdot \kappa \nabla T + \dot{q} = \rho C \left[\frac{\partial T}{\partial t} + \{ \boldsymbol{u} \cdot \nabla T + T \nabla \cdot \boldsymbol{u} \} \right] \tag{4.26}$$

where $\boldsymbol{u}$ is the velocity of the moving region. $\dot{q}$ is the internal volumetric heat generated by the induced eddy currents and is expressed as $\frac{J^2}{\sigma}$.

Constraining $\nabla \cdot \boldsymbol{u} = 0$ which represents the continuity equation reduces (4.26) to

$$\nabla \cdot \kappa \nabla T + \dot{q} = \rho C \left[\frac{\partial T}{\partial t} + \boldsymbol{u} \cdot \nabla T \right] \tag{4.27}$$

The additional velocity term describes the effect of movement on the heat diffusion for the translation or rotational invariant geometries.

4.7 Time-Harmonic Eddy Current Problems

The time-transient method for solving coupled magnetic thermal problem with long thermal time constants is very expensive. These time-stepping methods are expensive as it requires the solving of the final set of equations at each time-step. The time span simulated is very large due to the thermal time constants. This will lead to simulation lasting a vast time.

Much less expensive solution like the time-harmonic is practical for solving the eddy currents equation once provided the problem media is linear and the excitation consists of a single time frequency. The magnetic vector potential $\boldsymbol{A}$ in terms of time-harmonic is described by

$$\begin{aligned} \boldsymbol{A} &= (\boldsymbol{A}_R + j\boldsymbol{A}_I)\, e^{j\omega t} \\ &= (\acute{\boldsymbol{A}})\, e^{j\omega t} \end{aligned} \tag{4.28}$$

Thus, the time-harmonic eddy currents equation to solve for is

$$\nabla \times \frac{1}{\mu} \nabla \times \acute{\boldsymbol{A}} = \boldsymbol{J}_S - j\omega\sigma\acute{\boldsymbol{A}} \tag{4.29}$$

The volumetric joule heat is computed as

$$\dot{q} = \frac{1}{\sigma}[J_x * (conjJ_x) + J_y * (conjJ_y) + J_z * (conjJ_z)] \tag{4.30}$$

where $conjJ_x$, $conjJ_y$ and $conjJ_z$ are the conjugates of J_x, J_y and J_z respectively.

The heat equation is solved with 2D or 3D finite elements using time-stepping. The algorithm to solve this weakly coupled problem is summarised as below:

1. Initialise the electromagnetic unknowns $\acute{\boldsymbol{A}} = \acute{\boldsymbol{A}}_o$ with the given frequency.
2. Calculate the steady-state AC electromagnetic solution,

$$j\omega\acute{\boldsymbol{A}}[\boldsymbol{C}_a] + [\boldsymbol{K}_a]\acute{\boldsymbol{A}} = \boldsymbol{f}_a$$

3. Initialise the thermal unknowns $T = T_0$ for time $t = 0$. Set $n = 0$ and the time-step Δt.
4. Assemble the thermal system of equations for this position, $\boldsymbol{x}_n$, $[\boldsymbol{K}_n]$.

5. Calculate the thermal heating using the steady-state AC electromagnetic result obtained previously.

6. Calculate the thermal solution, using the *backward difference scheme*

$$\boldsymbol{\alpha}_n = ([\boldsymbol{C}_n] + \Delta t[\boldsymbol{K}_n])^{-1}\{\boldsymbol{f}_n - [\boldsymbol{K}_n][\boldsymbol{T}_n]\}$$

$$\boldsymbol{T}_{n+1} = \boldsymbol{T}_n + \boldsymbol{\alpha}_n \Delta t$$

7. Calculate the temperature dependent value of convection coefficient $\hbar_c$ and radiation coefficient $\hbar_r$, and reassemble the matrix $[\boldsymbol{K}_n]$.

8. Set $n = n + 1$ and repeat the algorithm from step 6.

During the iterative process, the electromagnetic problem can be resolved again if there are significant changes in the media electrical conductivity due to the increase in temperature.

4.8 Galerkin Upwinding

When the Galerkin technique is applied to the velocity terms of the electromagnetic and thermal equations, large numbers of negative entries are generated on the diagonal of the final matrix. This causes oscillations and poor results when the *Peclet number* α_w,

$$\alpha_w = \frac{\sigma \mu \boldsymbol{u} h}{2} > 1.0 \tag{4.31}$$

for moving eddy current regions and in moving thermal regions

$$\alpha_w = \frac{\rho C \boldsymbol{u} h}{2\kappa} > 1.0 \tag{4.32}$$

In equations (4.31), (4.32) h is the length of an element in the direction of velocity. This problem can be solved by discretising the model into finer meshes, effectively lowering h to keep down the *Peclet number.* But this will generate more nodal equations to be solved. The best alternative will be to use the upwinding method.

Upwinding scheme has been proposed in [29] for convective transport phenomena. T.J.R. Hughes [30] suggested a simpler upwind finite elements formulation which is used here. In the latter scheme only a 1-point evaluation of the advection term is considered, in which all other terms of the Galerkin formulation remain unaltered. With the technique the computational cost is greatly reduced compared with the scheme proposed in [29].

Basically, the scheme proposed that conditions under which there is no oscillations

$$\begin{aligned} \alpha_w &= 0 \quad \textit{all} \quad \xi \\ \alpha_w &> 0, \quad \xi > 1 - \frac{1}{\alpha_w} \\ \alpha_w &< 0, \quad \xi < -1 + \frac{1}{\alpha_w} \end{aligned} \tag{4.33}$$

In general, if $-1 < \alpha_w < 1$, $\xi = 0$ leads to no oscillations. As $\alpha_w \to \pm\infty$ requires that $\xi \to \pm 1$.

Upwind elements are advantageous in eliminating spurious oscillations in moving conducting regions and fluid temperature. The method consists of replacing the normal shape function N_i by N_w where N_w is a function defined by

$$\xi = \coth(\alpha_w) - \frac{1}{\alpha_w} \qquad \text{for} \quad 0 \leq \alpha_w \leq 1.0 \tag{4.34}$$

4th-order accuracy in α_w can be achieved if the evaluation point is taken to be

$$\xi = \frac{\alpha_w}{3}, \qquad -3 \leq \alpha_w \leq 3 \tag{4.35}$$

The new weighting function $N_w \neq N_i$ using the Galerkin upwinding scheme leads to the solving of following integrals that contain the description of velocity

1. Moving eddy current regions

$$\int N_w \, \sigma(\boldsymbol{u} \times \nabla \times \boldsymbol{A}) \, \mathrm{d}\Omega \tag{4.36}$$

2. Moving thermal regions

$$\int N_w \, \rho C(\boldsymbol{u} \cdot \nabla T) \, \mathrm{d}\Omega \tag{4.37}$$

These are generally evaluated using the Gaussian quadrature sampling the usual quadrature points. The upwinding scheme uses different points, which depend on the value of *Peclet number*:

$$\sum_{i=1}^{n} N_w(\alpha_w) \cdot \sigma[\boldsymbol{u}(o) \times \nabla \times \boldsymbol{A}] \, |\mathfrak{J}(o)| \, W \tag{4.38}$$

$$\sum_{i=1}^{n} N_w(\alpha_w) \cdot \rho C[\boldsymbol{u}(o) \cdot \nabla T] \, |\mathfrak{J}(o)| \, W \tag{4.39}$$

$\boldsymbol{u}$(o) is the velocity evaluated at the origin of the isoparametric coordinates of the element and —$\mathfrak{J}$(o)— is the Jacobian of the isoparametric transform. The weighting factor W equals to 4 for a 2D element and 8 for a 3D element. The upwinding shape function N_w is evaluated at the point α_w within the element.

4.9 Heating Effects by Coil DC Resistance

The *MEGA* code modelled 3D coils using a mesh that is distinct from the finite element discretisation. These basic building meshes are known as fragments and are combined in groups to form coils.

If a wound coil with n-turns is modelled, the current density is simply the current in a turn, times the number of turns per $m^2, \hat{\mathbf{t}}$. $\hat{\mathbf{t}}$ here is a vector quantity with direction associated with it.

$$\boldsymbol{J}_S = I_{coil}\,\hat{\mathbf{t}} \tag{4.40}$$

In the regions which contain the known source currents, the $\nabla \times \boldsymbol{H}$ is non-zero. However, since the current is known, the magnetic field is divided into two parts. The field due to the source current is solved using the Biot-Savart law,

$$\boldsymbol{H}_S = \frac{1}{4\pi}\int \boldsymbol{J}_S \times \nabla\left(\frac{1}{\boldsymbol{r}}\right) \mathrm{d}\Omega_S \tag{4.41}$$

The actual magnetic field is the sum of the source field $\boldsymbol{H}_S$ and the gradient of a reduced scalar potential ϕ,

$$\boldsymbol{H} = -\nabla\phi + \boldsymbol{H}_S \tag{4.42}$$

The region in which this calculation is performed is called the reduced scalar region. The coil must be totally embedded in a region which is modelled using the reduced scalar ϕ. Providing that the coils are totally immersed in a reduced scalar region, the reduced scalar potential region can be of any shape and the mesh can be independent of the coils. In this scheme, the reduced scalar potential region is restricted to approximate the shape of each coil and assign each coils to its own reduced scalar potential region.

In general, coils which are made up of bundles of filament wires have no eddy currents flowing in it and the DC resistance R_{dc} of the coil is given by the expression

$$R_{dc} = \frac{\rho_c \ell_c}{\mathrm{A}_c} \tag{4.43}$$

in which ρ_c is the resistivity, ℓ_c is the length and A_c is the cross-section area of the conductor respectively.

To model the heat transfer due to the copper I^2R losses, the reduced scalar region is used as an approximation to the real coil and the total power density can be calculated from

$$\dot{q} = \frac{I^2 R_{dc}}{\int\limits_S \mathrm{d}\Omega_S} \tag{4.44}$$

where $\int\limits_S \mathrm{d}\Omega_S$ is the volume integral of the reduced scalar region.

The assumption that current flow within the coils is uniform across their section, which means it suffer no eddy currents effect. This is not the case for thick wire which have considerable skin depth,

$$\delta = \frac{1}{\sqrt{\pi \mu \sigma f}} \tag{4.45}$$

The skin depth varies with $\frac{1}{\mu \sigma f}$. A thin skin depth means that the current is constrained to a smaller area and consequently the current density and the heating increases.

4.10 Validation

Several simple experiments were conducted in the laboratory to validate the computational results of the weakly coupled electromagnetic-thermal code. Tests were performed on two sets of aluminium and copper plates with different dimensions. The short plates have dimensions of $70mm \times 16mm \times 50mm$ while the longer ones are $180mm \times 16mm \times 50mm$. The material thermal properties are shown in Table(4.1).

Table 4.1: Material thermal properties.

Material properties	Aluminium	Copper
Thermal conductivity, κ (W/m K)	204	399
Specific heat, C_p (J/kg K)	896	383
Density, ρ (kg/m^3)	2707	8933

The electrical conductivities used in the experiment were measured on two specially cut aluminium and copper bars with $5mm \times 5mm$ cross-section. The measurement was performed using a set of increasing DC currents driven through the two bars. The voltage was measured across a fixed length of the two bars at known sample points. The resistance values are obtained by taking the gradients of the two plotted graphs in Figure 4.7. From these resistances, the conductivities for aluminium and copper are calculated to be 2.9×10^7 S/m and 5.4×10^7 S/m respectively.

4.10.1 Induction Heating by Eddy Currents and Thermal Conduction in Two Metallic Plates

In the first set of experiments, the steady-state code is verified against the transient code [31] using a constant material conductivity. Two 2D FE models of a thick aluminium plate surrounded by a coil were meshed with the first model having 2829 nodes, 2720 elements and 2987 matrix equations, and the second model with 11097 nodes, 10880 elements and 11663 equations respectively. The coil is made up of 800 turn of 0.8 mm diameter copper wire. Both models were solved using the transient and steady-state methods for computing the eddy current heat loss.

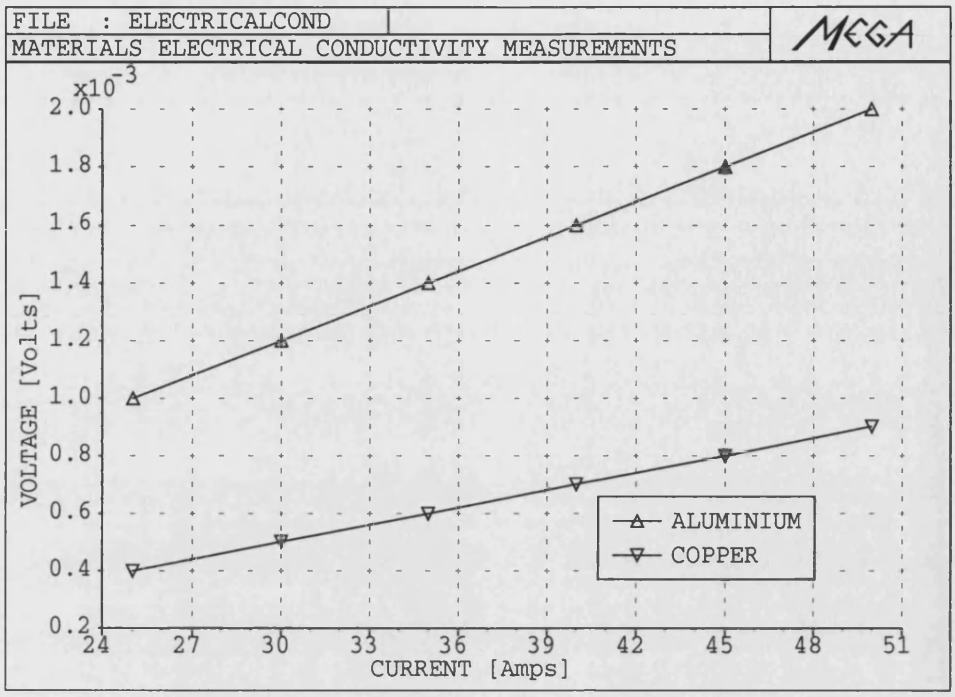

Figure 4.7: Measuring electrical conductivities for aluminium and copper.

The transient code was solved for two cycles with each cycle having the periodicity of 0.02 s while in steady-state method the models were solved for 50 Hz. The computed solutions by the two codes are shown in Table(4.2). Figure 4.8 shows the joule heating in the transient models and Figure 4.9 compares the temperature rise of the two methods.

The first 2D model is then extended to 3D as shown in Figure 4.10. An aluminium as well as a copper plate are used now. Both metal plates are completely insulated to prevent convection and radiation from their surfaces. Using the time-harmonic method, the excitation current applied is 2.5 A at 50 Hz. The induced eddy current density in the aluminium plate is shown in Figure 4.11. Only 1/4 of the models were meshed with boundary conditions appropriately applied where necessary. The predicted and measured results for conduction heat transfer are shown in Figure 4.12.

Table 4.2: Showing the peak and r.m.s joule heat loss.

	$\dot{q}_{peak}$	$\dot{q}_{rms}$
Transient		
Time-step = 5×10^{-4}		
TS 1	717225.8	
TS 2	717188.4	
Steady-state		
Frequency = 50.0 Hz		
SS 1		366907.0
SS 2		366716.0

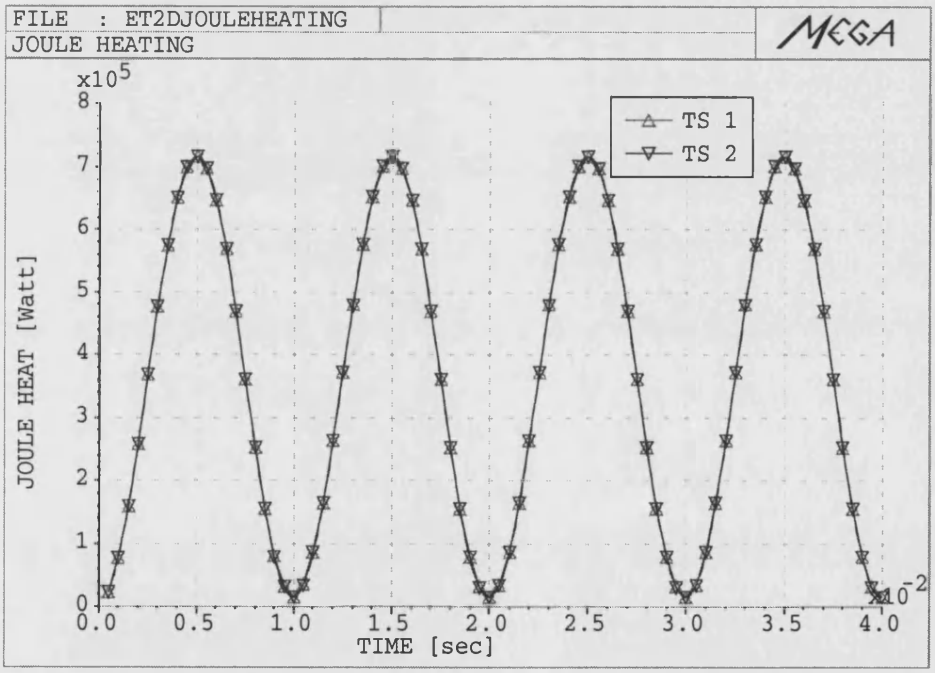

Figure 4.8: Joule heating in the transient models.

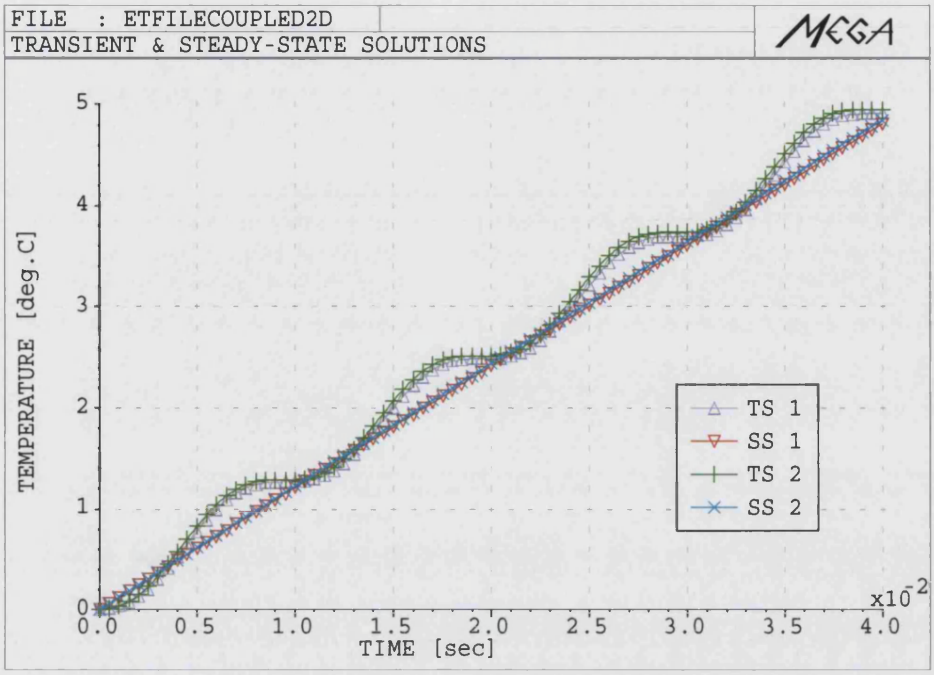

Figure 4.9: Temperature rise in the transient and steady-state models.

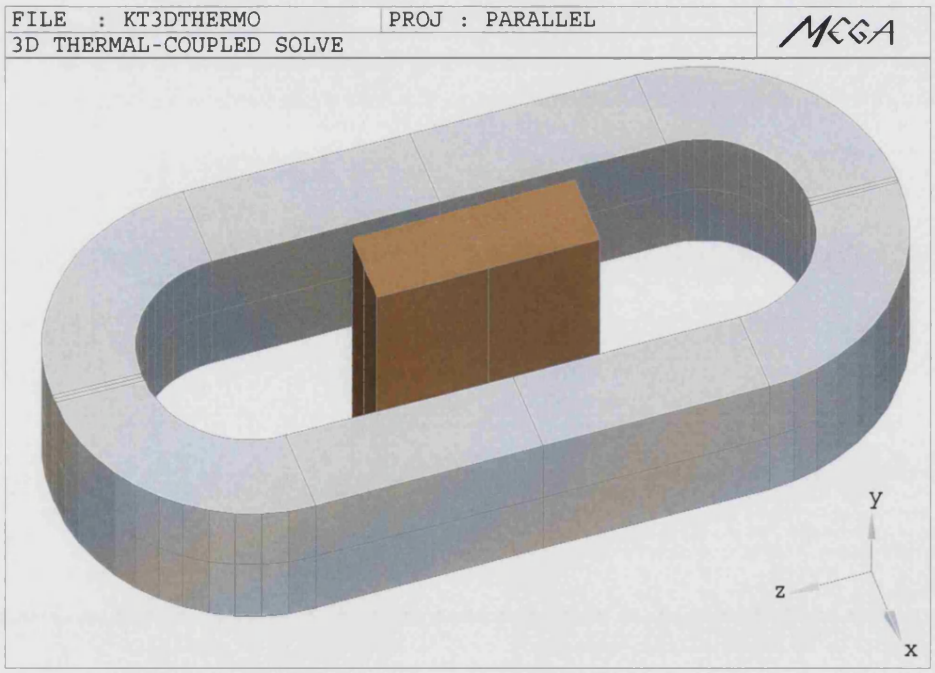

Figure 4.10: Metal plate with 800 turn coil.

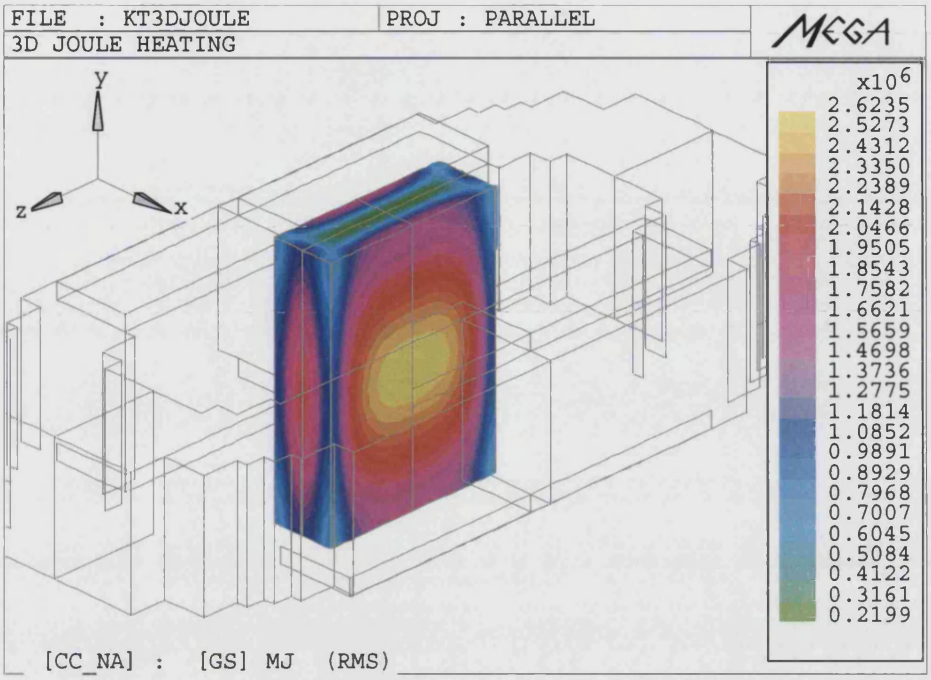

Figure 4.11: Eddy Current density in aluminium plate.

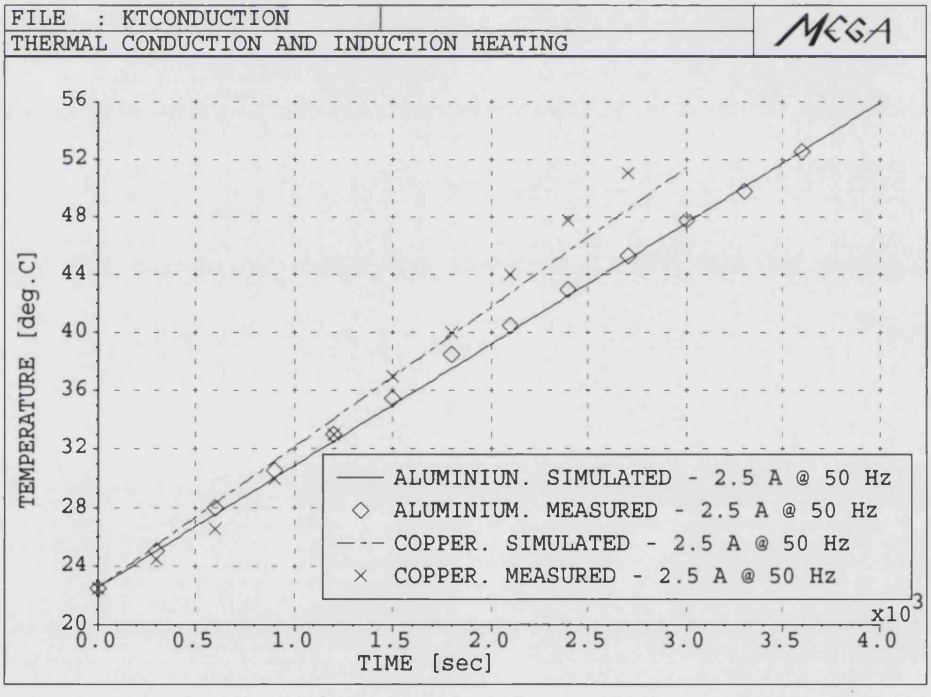

Figure 4.12: Temperature rise in the insulated aluminium and copper plates.

4.10.2 Thermal Conduction with Non-linear Convection and Radiation Boundary Conditions

In the following experiment, the long aluminium and copper plates of $180mm \times 16mm \times 50mm$ are placed separately into an area surrounded by a massive coil, as illustrated in the 3D model of Figure 4.13. The massive coil consists of 1600 turn of 1 mm diameter copper wire. A total of 62271 nodes and 57600 elements were used to create the 3D mesh, representing a finite element matrix of 65974 equations.

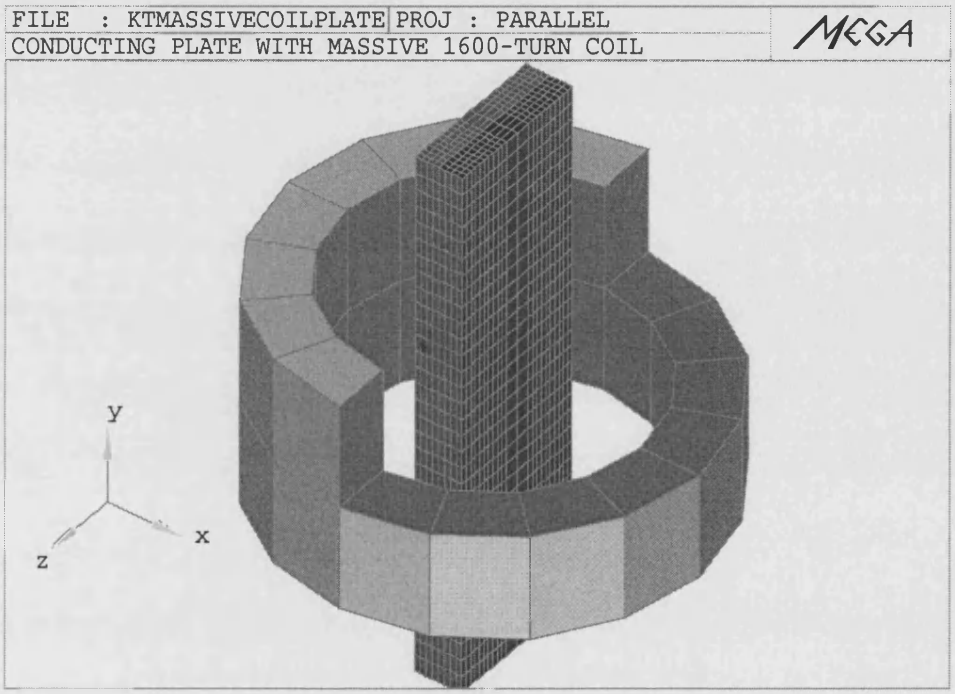

Figure 4.13: Metal plate with 1600 turn coil.

The aluminium and copper plates concerned are insulated at the two sides, top and bottom leaving only two vertically exposed surface areas of $180mm \times 50mm$ each. The empirical correlation for non-linear convection coefficient for vertical facing surface is provided by *Churchill-Chu*. The radiation emissivities ϵ_r of aluminium and copper are both set to 0.09 and 0.3 respectively. A near value for slightly oxidised commercial available aluminium and copper. The coefficients are given respectively as;

- convection coefficient for vertical plate,

$$\hbar_c = \frac{\kappa(T)}{\ell}\left\{0.825 + \frac{0.387[Ra(T)]^{\frac{1}{6}}}{\left[1+\left(\frac{0.492}{Pr(T)}\right)^{\frac{9}{16}}\right]^{\frac{8}{27}}}\right\}^2 \tag{4.46}$$

- convection coefficient for horizontal cylinder,

$$\hbar_c = \frac{\kappa(T)}{\ell}\left\{0.6 + \frac{0.387[Ra(T)]^{\frac{1}{6}}}{\left[1+\left(\frac{0.559}{Pr(T)}\right)^{\frac{9}{16}}\right]^{\frac{8}{27}}}\right\}^2 \tag{4.47}$$

- radiation coefficient,

$$\hbar_r = \sigma_r \epsilon_r (T_s + T_\infty)({T_s}^2 + {T_\infty}^2) \tag{4.48}$$

in which the thermal conductivity $\kappa(T)$, *Rayleigh number* $Ra(T)$ and *Prandtl number* $Pr(T)$ are functions of the surface temperature.

Likewise the electrical conductivity can be temperature dependent and its resistivity $\rho(T)$ approximated linearly as

$$\rho(T) = \rho_o(T)[1 + \alpha(\Delta T)] \tag{4.49}$$

The frequency used is 50 Hz with coil excitation current at 2.0 A (rms) and 2.8 A (rms) respectively. At this frequency the skin depth of the conductors according to equation (4.45) is $\approx$ 14 mm for aluminium and $\approx$ 10 mm for copper. The simulated and measured results of the temperature rise at the exposed surface for the aluminium and copper plates are shown in Figure 4.14 and Figure 4.15 respectively.

The discrepancy is larger for plates with excitation current of 2.8 A in comparison to those with excitation current of 2.0 A. This is due to the fact that both models are using constant electrical conductivities and at higher temperature level the heat dependency of the electrical conductivities cannot be ignored. This is further proven in the next set of experiments. The long metal plates are replaced with the shorter

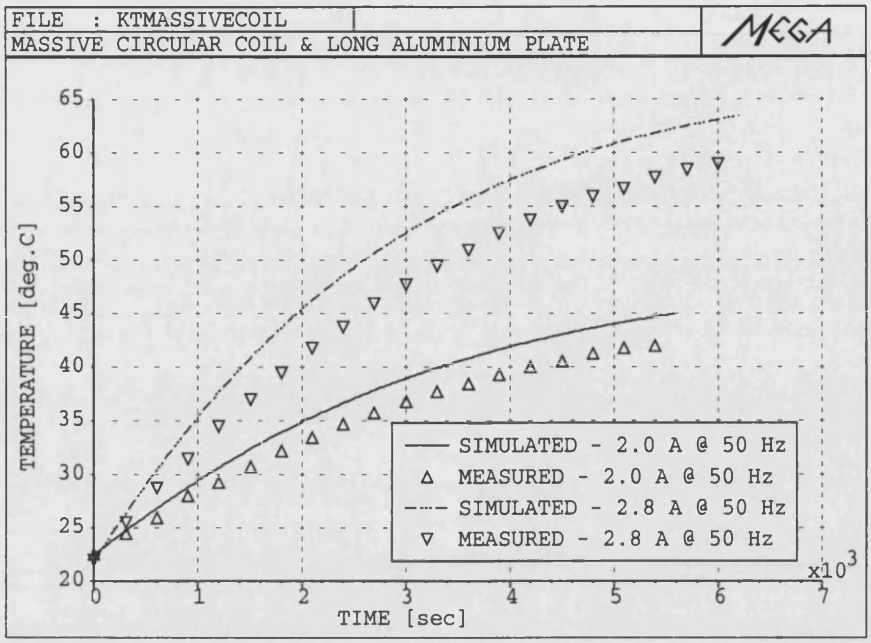

Figure 4.14: Simulated and measured temperatures of the long aluminium plate with constant electrical conductivity.

version ones of dimension $70mm \times 16mm \times 50mm$. The measured and computational results are shown in Figure 4.16 and Figure 4.17 for the short aluminium and copper plates respectively. As the temperature started to climb the divergence of the simulated and measured curves become increasingly significant. The aluminium and copper plate FE models with 2.8 A at 50 Hz excitation current are rerun again with temperature dependent electrical conductivity. The results are shown in Figure 4.18.

The long aluminium plate is now horizontally placed about 20 mm above the coil. The *Nusselt numbers* provided by Fujii and Imura in the previous chapter for horizontally positioned plate are only valid for a limited range of *Rayleigh number* and therefore not suitable. A revised equation which allows the calculation of convection coefficient $\hbar_c$ for covering a wider range of temperature is obtained from [32];

$$\hbar_c = \frac{\kappa(T)}{\ell}\left\{\left(\frac{1.4}{ln[1.0+1.4/Nu_u]}\right)^{10} + \left(Nu_t\right)^{10}\right\}^{0.1} \tag{4.50}$$

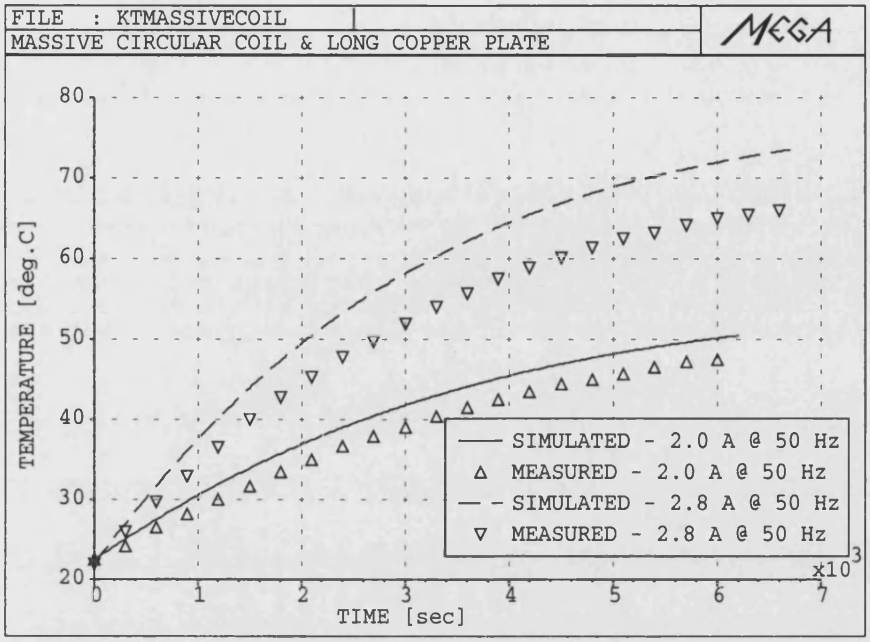

Figure 4.15: Simulated and measured temperatures of the long copper plate with constant electrical conductivity.

with,

$$Nu_u = \frac{0.56[Ra(T)]^{\frac{1}{4}}}{[1.0 + [0.492/Pr(T)]^{\frac{9}{16}}]^{\frac{4}{9}}}$$

$$Nu_t = 0.14\left(\frac{1.0 + 0.0107Pr(T)}{1.0 + 0.01Pr(T)}\right)[Ra(T)]^{\frac{1}{3}}$$

The surface facing the coil is heavily insulated to prevent heat transfer rising from the coil and the other surface is exposed to the ambient air. The temperature rise of the heated plate is shown in Figure 4.19. The measurement and simulated results agree well.

In the final experiment for heat transfer in non-moving media, a solid aluminium cylinder is placed horizontally into the 1600 turn coil as shown in Figure 4.20. The measured and simulated results are shown in Figure 4.21.

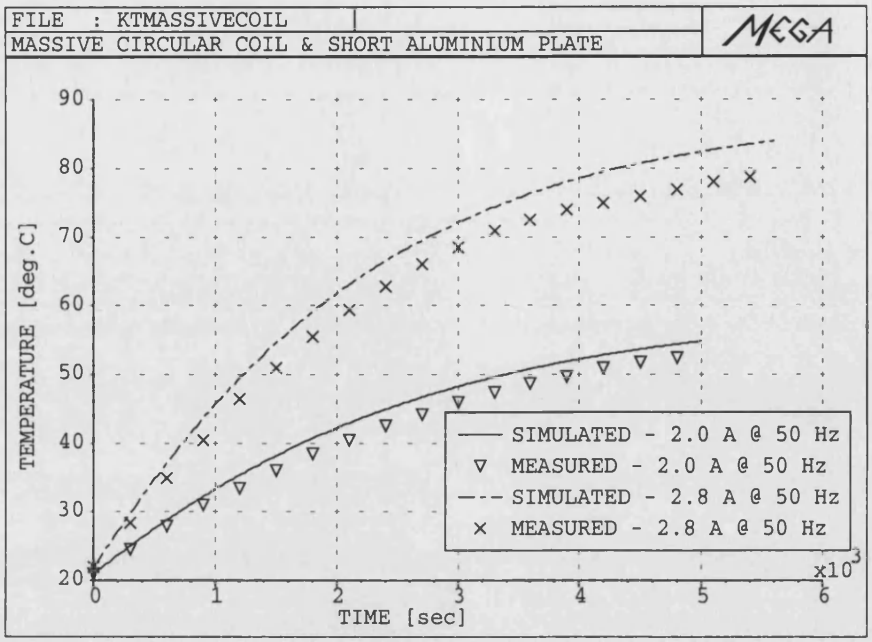

Figure 4.16: Simulated and measured temperatures of the short aluminium plate with constant electrical conductivity.

The unavailability of the convection coefficients make these experiments heavily dependent on the given empirical correlations for modelling heat flow from the surface. The experimental data for the empirical correlation scatter by as much as ± 15 percent or more. Thus, the simulated results are expected to have an error within the range $1\% - 20\%$ or higher compared to the measured ones.

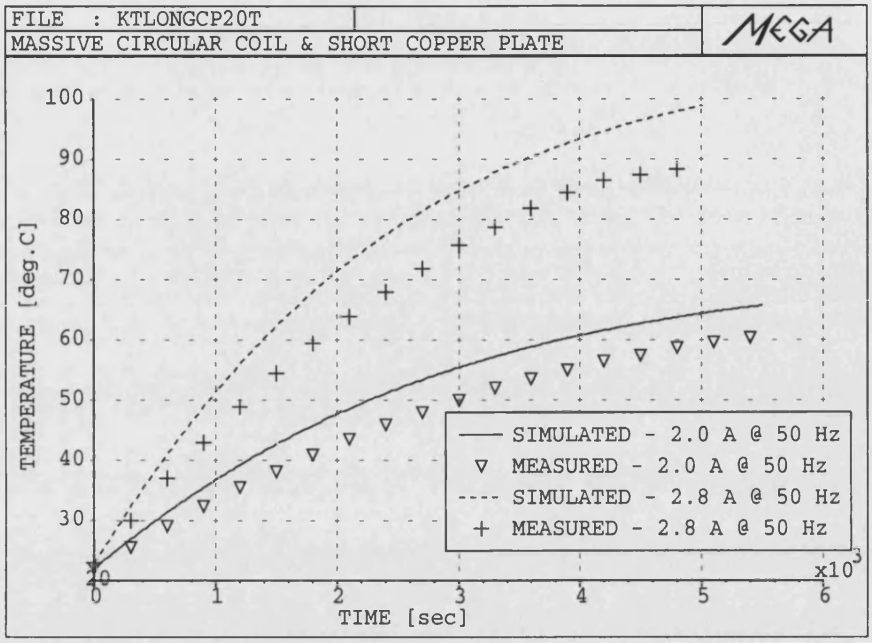

Figure 4.17: Simulated and measured temperatures of the short copper plate with constant electrical conductivity.

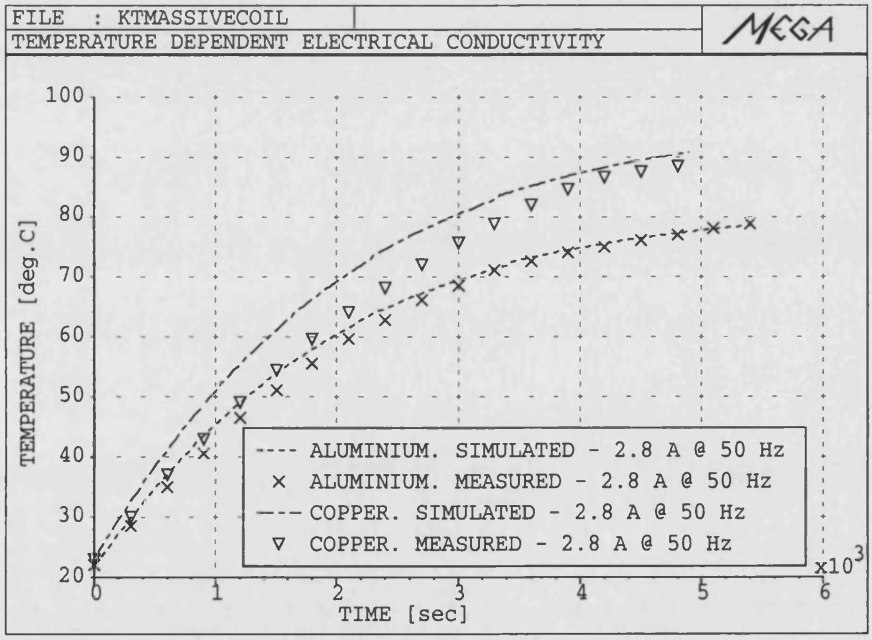

Figure 4.18: Simulated and measured temperatures of the short aluminium and copper plates with variable electrical conductivity.

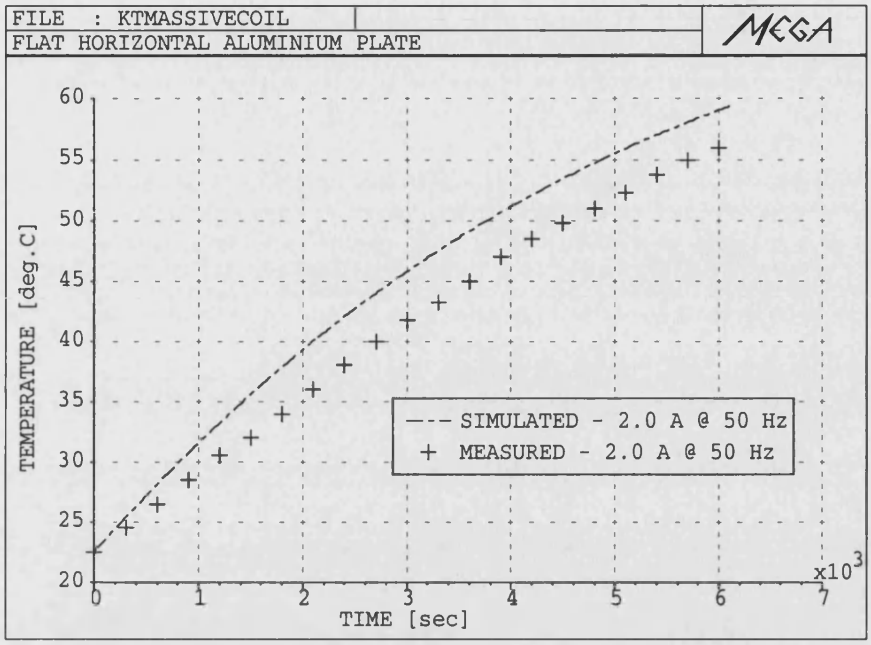

Figure 4.19: Simulated and measured temperatures of the horizontally placed long aluminium plate.

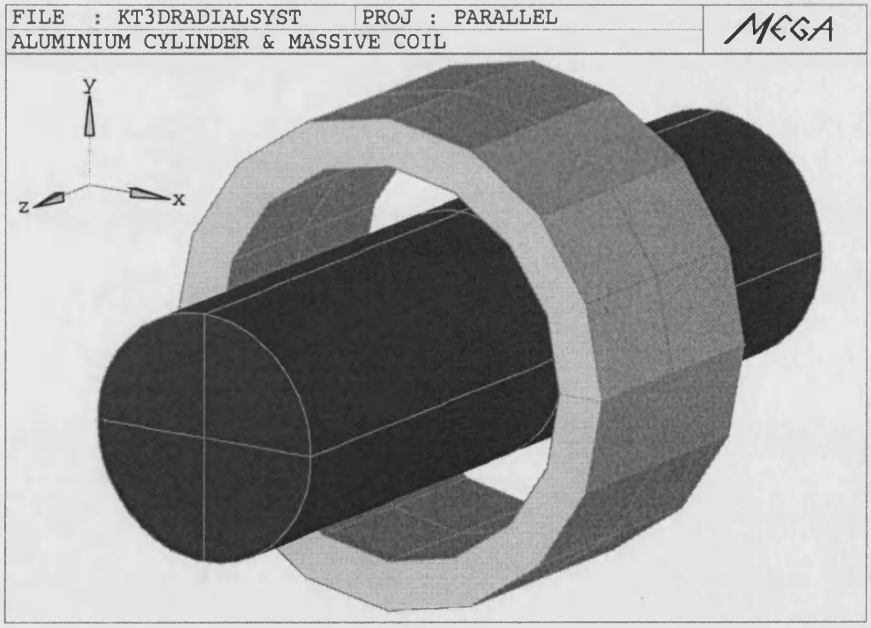

Figure 4.20: Aluminium cylinder with 1600 turn coil.

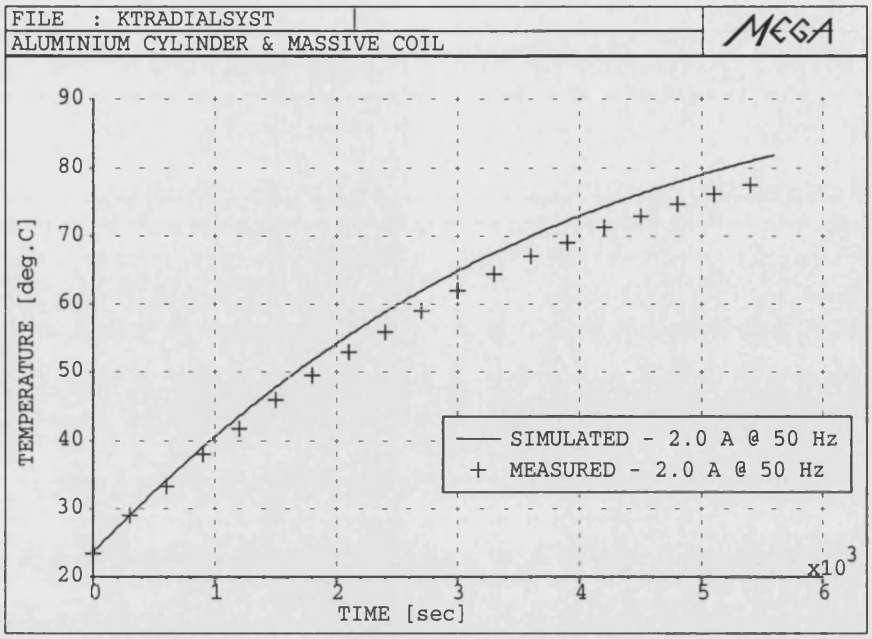

Figure 4.21: Temperature rise in the aluminium cylinder.

4.10.3 3D Modelling of Moving Conducting Regions and Heat Transfer in Electrical Machine

In the final part of the validation exercise, the *MEGA* code is used to evaluate the thermal performance of a disk induction machine. The 3D FE model of this machine is shown in Figure 4.22. The induction machine consists of a 12 slots stator and a rotating conducting disk made up of aluminium. The iron core of the stator is made of thin laminations of electrical sheets in order to reduce the eddy current losses. The stator has a total of 6 coils wound on the slots. Each coil has a 580 turn of 0.55 mm diameter of copper wire. It's a 3-phase machine with each phase having two coils connected in parallel. Table(4.3) shows the dimensions of the machine.

In general, moving conductors are expensive to model using finite elements because a fully time-transient solution is required and the moving object must be tracked through the mesh as time progresses. In modelling the moving conductor region (aluminium disk) with high electrical conductivity, the *Minkowski transformation* as

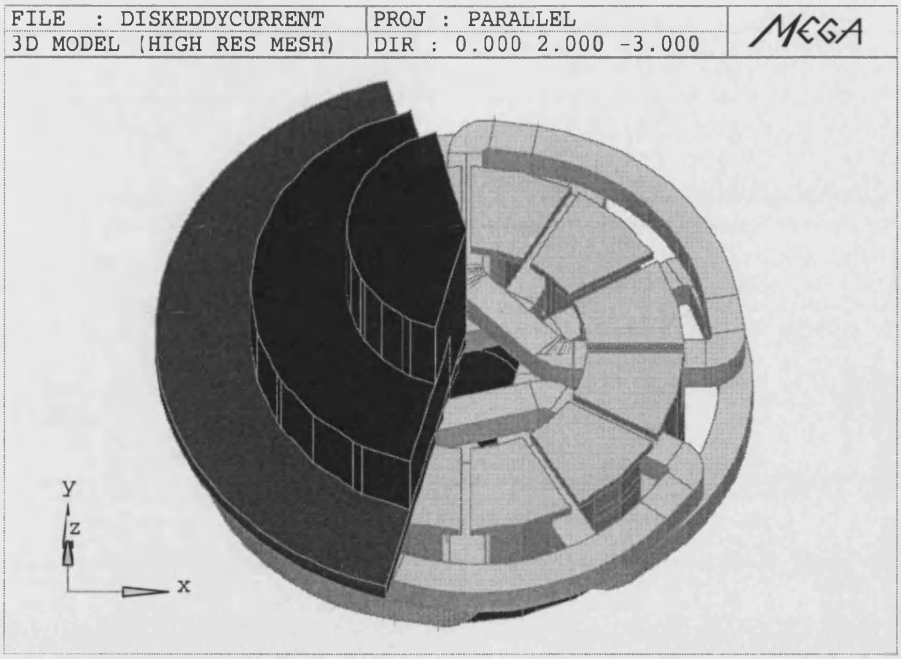

Figure 4.22: Disk induction machine.

explained earlier is used to formulate the eddy currents induced. The thermal equation is added with a velocity term (as shown in equation (4.27)) to model the influence of the specified velocity on the heat distribution in the rotating disk.

Heat transfer in the induction machine is a combination of conduction within the solid and laminated components of the machine and convection from the surfaces which are in contact with air. The dominant processes in heat transfer within a motor and to the environment are conduction and convection. Radiation is important only on the outer surfaces. Conduction is the first stage in the process of heat flow from the generation site to the outer surfaces after which convection takes over.

For surface cooled machines, the heat transfer coefficients for free convection and radiation from the outer surface of the machine are the main parameters to which the accuracy of the predictions is most sensitive. This is one of the difficulties encountered when designing a thermal model. Another problem is the separation of losses in the motor.

Table 4.3: Geometrical data of the disk induction machine.

	Machine Parameters	Dimensions in SI unit
1	Stator height	39.0 mm
2	Stator inner diameter	71.0 mm
3	Stator outer diameter	128.0 mm
4	Tooth height	27.0 mm
5	Slot width	14.0 mm
6	Slot opening width	3.0 mm
7	Air gap	1.0 mm
8	Aluminium disk diameter	184.0 mm
9	Shaft diameter	32.0 mm

The convection coefficients $\hbar_\omega$ used for the moving components [24], specifically for rotating cylinder and disk are listed as below:

- rotating cylinder,

$$\hbar_\omega = \frac{\kappa(T)}{D}\Big[0.11[0.5Re(T)^2 + Gr(T)Pr(T)]^{0.35}\Big] \tag{4.51}$$

- rotating disk in laminar flow,

$$\hbar_\omega = \frac{\kappa(T)}{D}\Big[0.36\Big(\frac{\omega_o r^2}{\nu(T)}\Big)^{0.5}\Big] \tag{4.52}$$

valid for $\dfrac{\omega_o r^2}{\nu(T)} < 2 \times 10^5$

- rotating disk in turbulent flow,

$$\hbar_\omega = \frac{\kappa(T)}{D}\Big[0.015\Big(\frac{\omega_o r^2}{\nu(T)}\Big)^{0.8}\Big] \tag{4.53}$$

where D is the diameter of the cylinder/disk, r is the radius of the cylinder/disk, ω_o is the angular velocity and $\nu(T)$ is the temperature dependent kinematic viscosity.

The induction machine is run with the aluminium disk rotating at 300 rpm at a load supplied by a DC brushless machine. The excitation current fed into the armature winding is 2.0 A and the resistance of each coil is 12.468 ohms. The main losses in the disk induction machine are the induced eddy currents in the rotating aluminium disk, the copper I^2R losses in the winding and the iron losses. The iron losses could be calculated very approximately using the normal empirical formula:

$$\begin{aligned} P_h &= k_h \hat{B}^m f \quad \text{for hysteresis losses} \\ P_e &= k_e \hat{B}^2 f^2 \quad \text{for eddy current losses} \end{aligned} \tag{4.54}$$

where k_h and k_e are the empirical constants, $\hat{B}$ is the peak magnetic field with $m = 1.76$ and f is the applied excitation frequency.

It is an intricate task to model the convective heat flow from the end winding of this disk machine. The lack of any convection correlation formulae corresponding to the winding geometrical shape means that the coefficient will have to be obtained by measurement. The measured heat transfer coefficient is shown in Figure 4.23. The heat capacity of the winding is calculated from the relative proportions and thermal capacities of the material, thus the heat capacity is approximated to that of the bulk copper heat capacity times the packing factor which is 0.67 in this case. The thermal conductivity is measured as 5.2 W/m K for a conductor bundle of 580 turn. The induction machine's material thermal properties are shown in Table(4.4). The stator, which is of cylindrical shape has two major heat losses at its exposed surface, that of the convection and radiation. The heat transfer in this region is modelled using the *Churchill-Chu* empirical coefficient for convection and the usual radiation coefficient.

The air gap is a very thin layer of air which is approximately 1 mm. The movement of air between the normally heated stator and rotor surfaces generally made the prediction of the convection coefficient across the air gap difficult. In modelling the heat transfer across the air gap, several assumptions will have to be made regarding

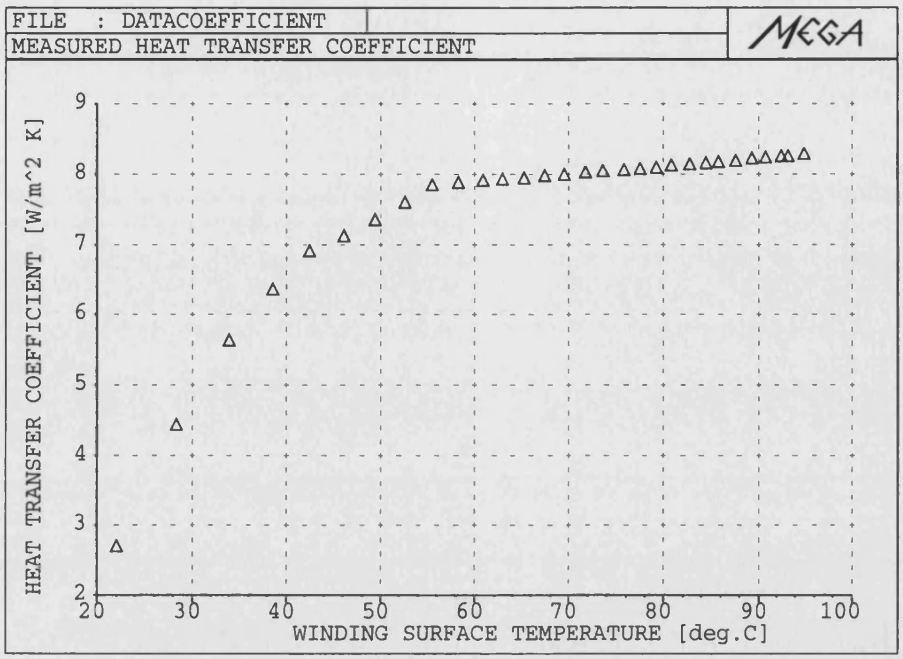

Figure 4.23: Measured heat transfer coefficient for the winding.

the two disk surfaces: 1). in small induction machines, any heat emitted from the stator surface would be transferred directly across the air gap to the rotor or vice versa, therefore the axial heat flow from the air gap could be neglected; 2). the stator surface is smooth; 3). the radiation effect is ignored. With these assumptions, the heat transfer across the air gap is simply modelled as

$$-\kappa_f \frac{\partial T}{\partial n} = \hbar_\omega (T_t - T_d) \tag{4.55}$$

in which κ_f is the fluid thermal conductivity, $\hbar_\omega$ is the convection coefficient for the rotating disk and T_t, T_d are temperatures of the stator and rotor surfaces facing the air gap respectively. In the actual machine, there will be greater heat loss across the air gap than is described by the rotating smooth disk surface equation, because of additional fluid disturbances caused by the slotting effect.

Four K-type thermocouples with the accuracy of $\pm$ 0.1 % of reading 0.7 °C are

Table 4.4: Material data for FE thermal model.

Machine components	Material	Thermal Conductivity (W/m K)	Specific Heat Capacity (J/kg K)	Density (kg/m^3)
Stator lamination	Mild Steel	54	465	7833
Winding (pf 0.67)	Copper	5.2	383	8933
Slot liner	Kapton	0.12	1100	1420
Shaft	Stainless Steel	15	480	8055
Disk	Aluminium	204	896	2707

positioned at the stator teeth, both end windings (one end is exposed to ambient air temperature and the other is located within the stator bore) and the surface of the rotating aluminium disk.

Figure 4.24 and Figure 4.25 show the calculated and measured transient temperatures in the end winding. The calculated curve indicated a significantly shorter thermal time constant than that which was measured for the end winding exposed at the ambient air. The explanation for this discrepancy could well be the lack of accuracy in modelling the thermal capacity of the winding and slot liner. Ill-defined convection heat path and non-linearity of the material properties further added to the error of the predicted result.

The calculated temperature of the end winding located within the centre region of the stator stack is lower compared to the measured result. This stator bore region, with its back end facing a close by rotating disk, is totally enclosed at the front end by a stainless steel cap. The major shortcomings are the unknown heat flow paths in this section of the model which appears to corrupt the accuracy of the transient

solution of the temperature rise of the winding. The lower predicted result is due to the difficulties in modelling the heat transfer between the heated stator teeth, aluminium disk and the end winding.

Figure 4.26 and Figure 4.27 show the transient temperatures for the stator teeth and aluminium disk. It can be seen that the predicted and measured results are in good agreement, with the greatest error being less than 10 °C. Figure 4.28 and Figure 4.29 illustrate the temperature distributions in the stator and winding of the induction machine.

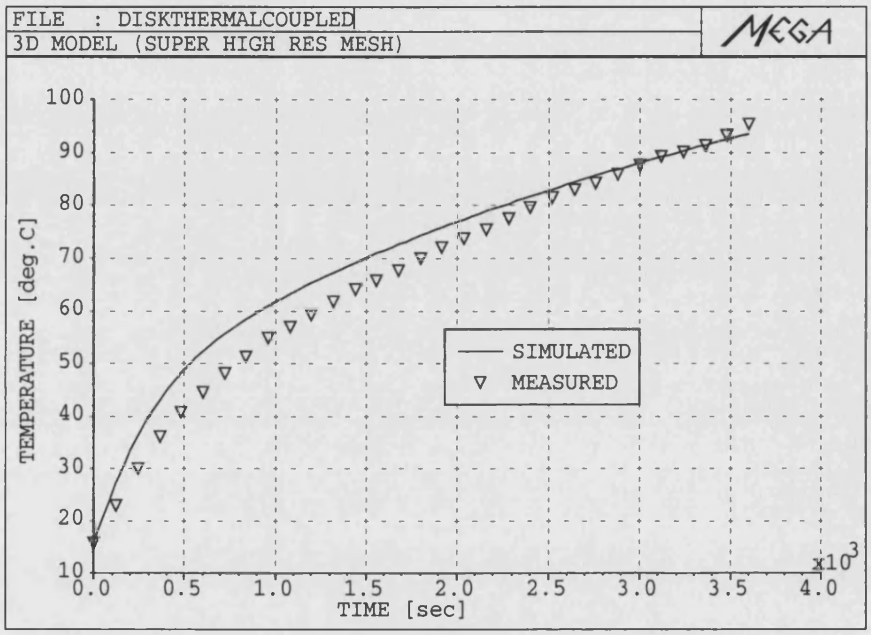

Figure 4.24: Simulated and measured temperatures of the end winding facing the ambient air.

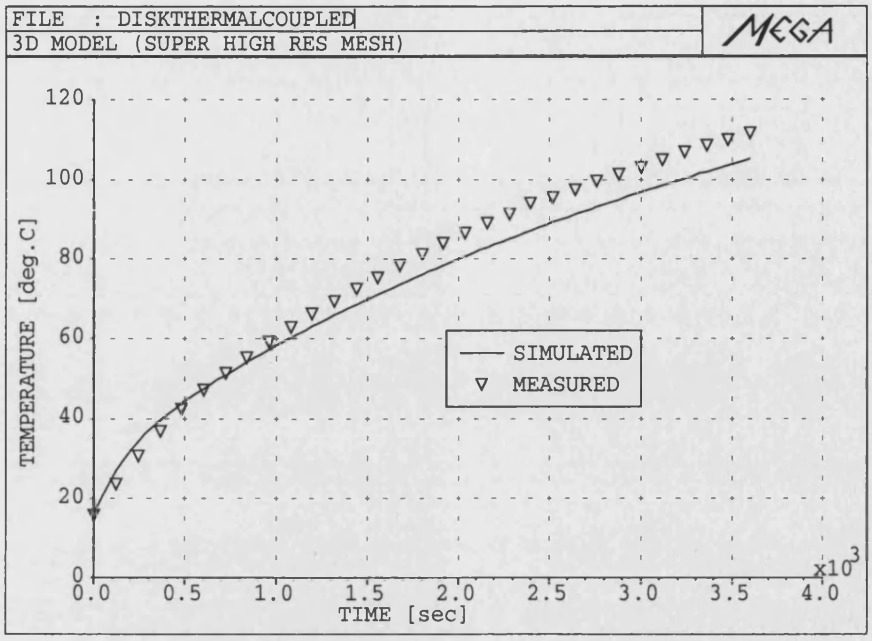

Figure 4.25: Simulated and measured temperatures of the end winding at the inner region of the stator.

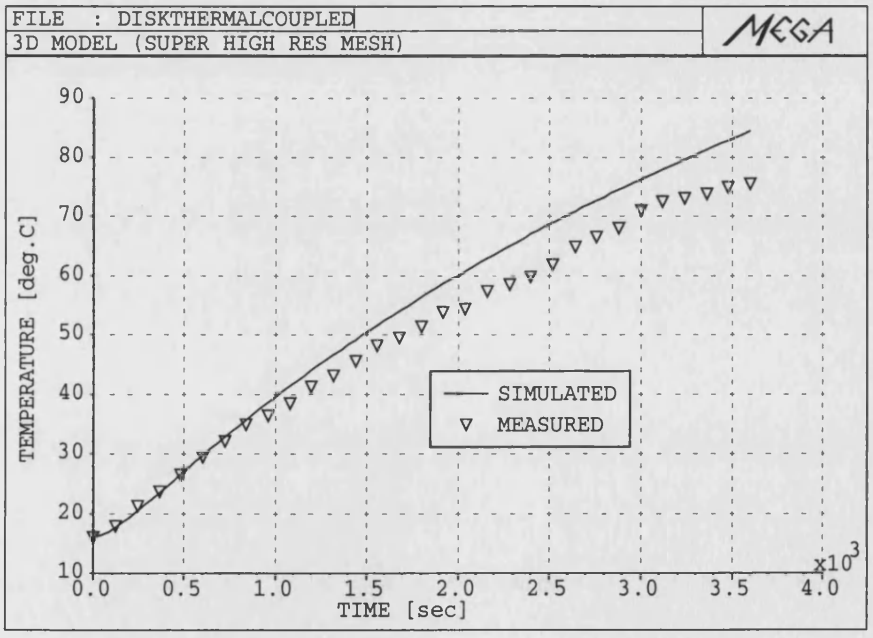

Figure 4.26: Simulated and measured temperatures of the stator teeth.

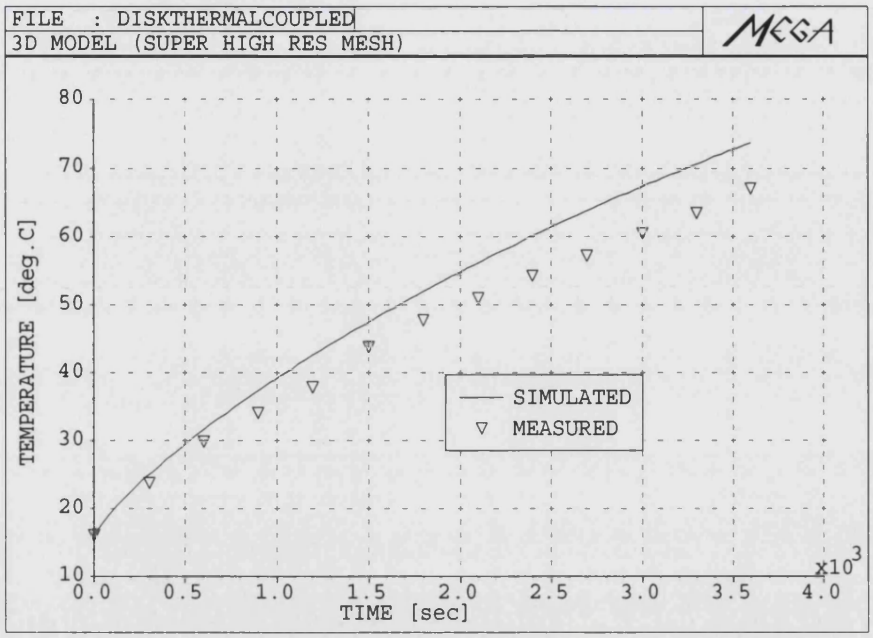

Figure 4.27: Simulated and measured temperatures of the disk.

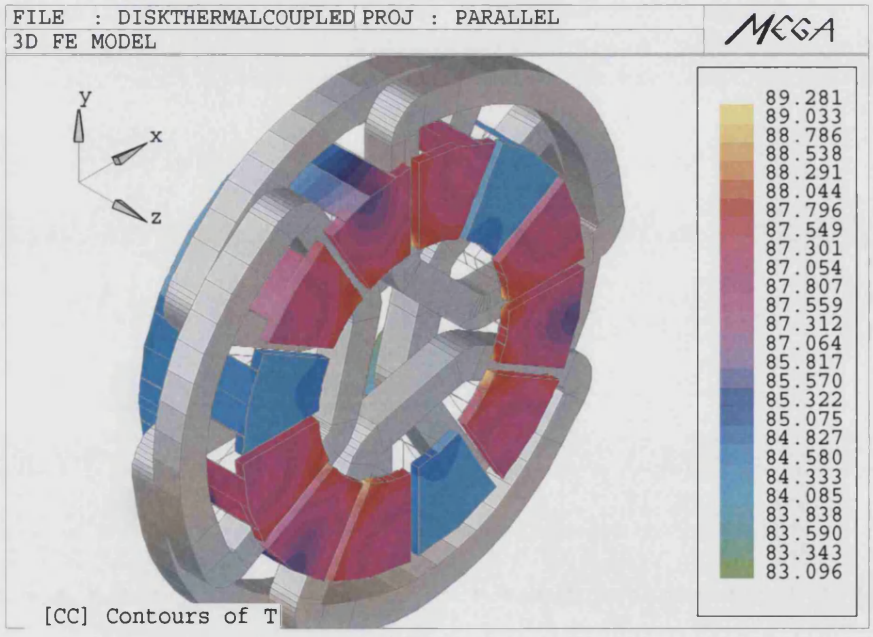

Figure 4.28: Temperature distribution in the stator stack.

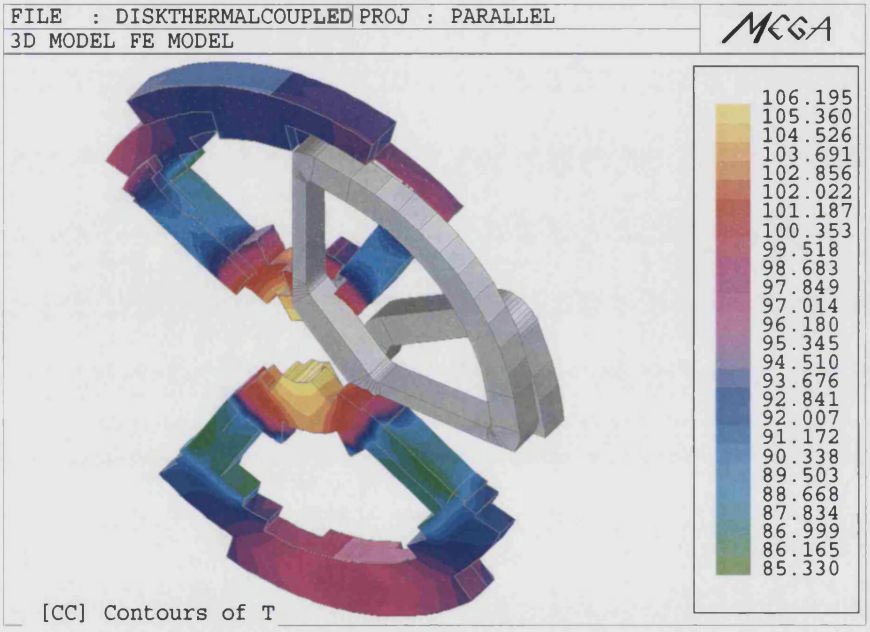

Figure 4.29: Temperature distribution in the winding.

4.11 Summary

A description of inductive heating together with DC I^2R losses are presented here. In the heating process the temperature changes are much slower than the variation of the electromagnetic field thus, the steady-state time-harmonic electromagnetic system is solved for each temperature. The variation of electrical conductivity is relatively small for temperature below the boiling point. Weak coupling in this sense allows the problem to be decoupled with the magnetic part solved first to compute the total heat loss and then used as the source term to solve the thermal heat transfer. Several benchmark coupled heat transfer problems are solved and validated by measurements.

Eulerian transport equation for moving media is also described here. Galerkin upwinding scheme could be implemented if necessary to avoid spurious oscillations when the velocity is prescribed at the moving conductor or thermal regions. The upwinding solution by Hughes is simpler and inexpensive as it only modifies the velocity term and leaves the rest of the equation unchanged.

A disk induction machine thermal performance is validated with measurement and computational results. For all the obvious reasons, a good thermal design to predict the machine thermal performance accurately is highly essential. Thermal design techniques tend to lag behind other contemporary aspects of machine design such as electromagnetic and mechanical strategies. This is easily understood as considerable uncertainties and difficulties exist in determining the various thermal constants accurately within the machine. As for analytical models, difficulties in defining heat generation and heat flow paths often lead to the oversimplification of the problem which only compromises the solution and causes excessive error at the end. Even with the finite element method considerable efforts are required with prior knowledge of machine dimensions, materials properties, power losses and heat paths.

Chapter 5

Finite Element Modelling of Cogging Torque in Permanent Magnet Machines

5.1 Introduction

Permanent magnet machines are increasingly being used in high performance applications where torque smoothness is essential. The major concern in these applications is the cogging torque produced. It is well-established that cogging torque which exists in slotted motors is perhaps one of the most detrimental elements in permanent magnet (PM) motor design.

As a result, a great deal of research has been devoted to identifying the sources, characteristics and minimisation of cogging torque. For example, applying stator excitation currents to cancel cogging torque is discussed in [33], [34]. Using predicted magnetic field distributions in [35], [36] show the influence of geometrical dimensions such as slot opening and magnet width on cogging torque production. In addition, various techniques are developed in [37], [38], [39] to predict cogging torque based on the motor magnetic field.

The most effective ways to reduce cogging torque is by proper motor design. Methods such as skewing, optimising the pole arc width, fractional slot pitch have been

vigorously used for this purpose. Permanent magnet AC machines generally show the greatest potential for cogging torque reduction using these well-known techniques. This chapter describes several modelling efforts for machine design using finite elements to examine some of these techniques.

5.2 Finite Element Schemes for PM Machines with Skew Design

The finite element software package *MEGA* is employed in this effort for the modelling of the motor designs. The stator and rotor of machine usually have different geometrical properties therefore, the meshes of the stator and rotor will definitely be incompatible. The level of difficulty in meshing is further increased if the motor required skewing in order to minimise cogging torque.

Skewing of stator teeth is commonly used to reduce cogging torque, this means that the stator winding is slightly more difficult to insert. It is also possible to skew the rotor magnets, this option will usually lead to more expensive magnets. Either of these options increases the difficulty in modelling the machines using finite elements, as the stator and rotor meshes are incompatible. The Lagrange interface technique is particularly useful in this case. It allows the stator and rotor of a rotating machine to be meshed up separately, then joined together and solved in different dynamic positions.

Apart from the magnet or stator skewing most of the action of the permanent magnet machine can be modelled reasonably accurate and economical using the conventional 2D finite element scheme.

5.2.1 Modelling Permanent Magnet Regions

Since current excitation is unnecessary in analysing cogging torque, the whole machine can be modelled as non-conducting regions which are less expensive to solve. The

finite element formulations on non-conducting and conducting regions have already been discussed in Chapter 2.

For modelling the magnetic regions, the permanent magnets are treated as magnetic distribution M. Thus, the magnetic flux density is defined as

$$\boldsymbol{B} = \mu_o(\mu_r \boldsymbol{H} + \boldsymbol{M}) \tag{5.1}$$

In terms of the remnant flux density $\boldsymbol{B}_r$,

$$\boldsymbol{B} = \mu_o \mu_r \boldsymbol{H} + \boldsymbol{B}_r \tag{5.2}$$

where $\boldsymbol{B}_r = \mu_o \boldsymbol{M}$.

Adopting this equation for the magnetic scalar gives

$$\nabla \cdot \mu \nabla \psi = \nabla \cdot \boldsymbol{B}_r \tag{5.3}$$

5.2.2 Coupling Meshes in 3D

In the analysis of electrical machines such as permanent magnet motor, it is often required to model the machine with its rotor at several different positions relative to the stator. This is necessary in order that characteristics of interest such as torque, flux linkages which vary with position can be evaluated.

Several different approaches are described as follows:

- A few different models can be meshed and used in turn. However, this is not feasible as it is rather expensive to produce many meshes.
- Remeshing locally is another alternative. The same mesh topology is retained and then remesh, joining the nearest nodes on the interface. This can cause distorted elements and loss of accuracy.

- Using boundary element technique to couple the finite element meshes together or the integral technique, the hassle of meshing the moving interface can be avoided. Unfortunately, integral techniques are not accurate for small air gap machines.

- Fourier techniques can be used to model the air gap and then coupled to both the stator and rotor [40].

In this research the technique proposed in [41], [42] is used for modelling the movement of electrical machines.

When cogging torque is of interest, it is necessary to model the rotor in many different positions. It is very convenient to mesh the stator and rotor separately, with a common interface in the air gap of the machine. The independent meshes can be coupled at their common interface using *Lagrange Multipliers.*

Stationary and moving parts can be meshed up independently and then brought together as shown in Figure 5.1. The distribution and density of the nodes on the interface need not be the same.

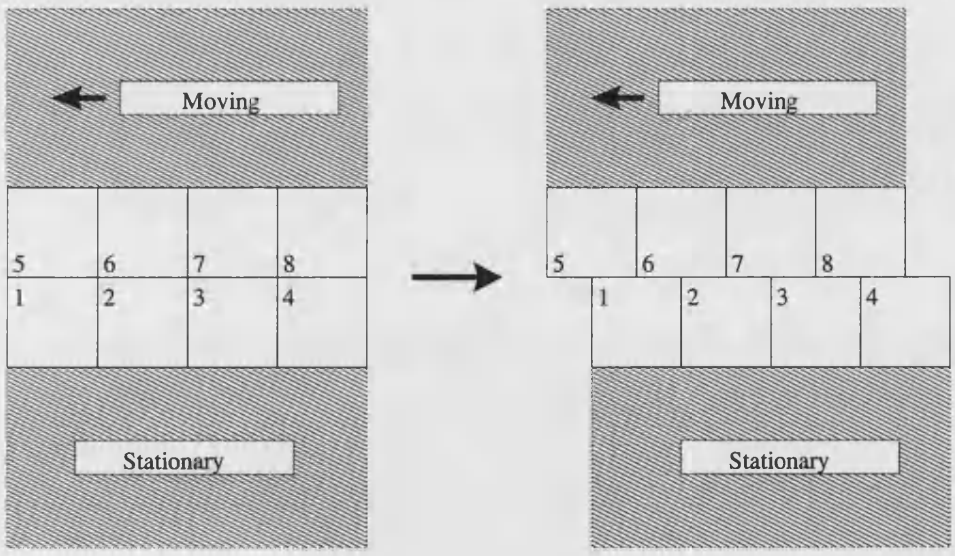

Figure 5.1: Lagrange interface.

A brief description of the underlying theory now follows:

Consider making a functional $\Pi(\phi)$ stationary subject to the constraints,

$$C(\phi) = 0 \qquad \text{in} \quad \Omega$$

This constraint is used to form a new functional

$$\overline{\Pi} = \Pi + \int_{\Omega} \gamma C(\phi)\, \mathrm{d}\Omega \tag{5.4}$$

where γ is a set of *Lagrange Multipliers.*

The variation of the new functional is now

$$\delta\overline{\Pi} = \delta\Pi + \int_{\Omega} \delta\gamma C(\phi)\, \mathrm{d}\Omega + \int_{\Omega} \gamma \delta C(\phi)\, \mathrm{d}\Omega \tag{5.5}$$

$\delta\overline{\Pi}$ is zero providing $C(\phi) = 0$ and $\delta\Pi = 0$.

$\nabla \cdot \mu\nabla\psi = 0$ can be solved by finding the stationary point of a functional Π:

$$\Pi = \frac{1}{2} \int_{\Omega} \nabla\psi \cdot \mu\nabla\psi\, \mathrm{d}\Omega \tag{5.6}$$

A functional for the whole problem can be written as

$$\Pi = \Pi_R + \Pi_S \tag{5.7}$$

Π_R and Π_S are functionals for region R and S which are shown in Figure 5.2. They are of the form (5.6).

Introducing an additional constraint to couple the variables on the interface Γ_L

$$\psi_r - \psi_s = 0 \qquad \text{on} \quad \Gamma_L \tag{5.8}$$

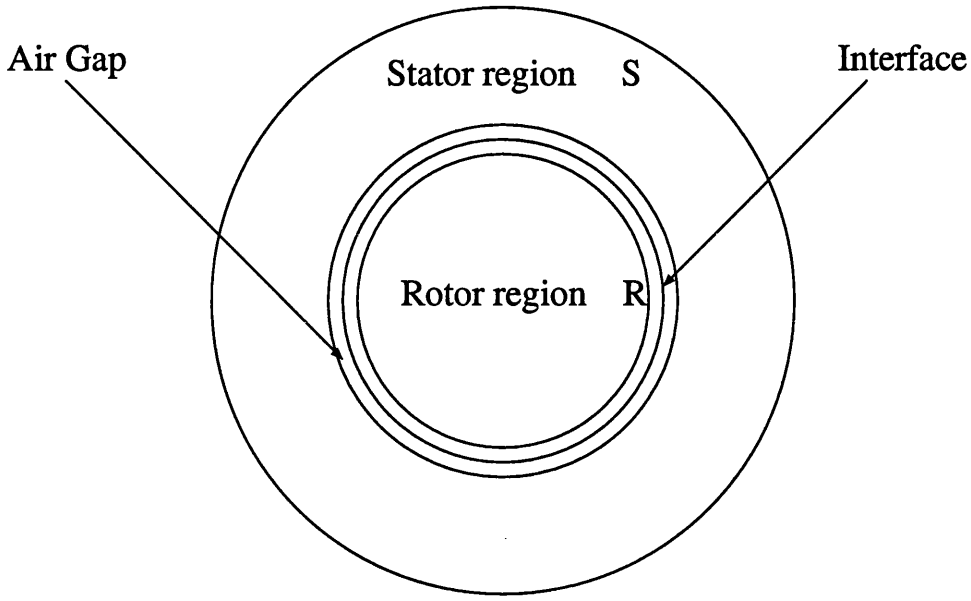

Figure 5.2: Stationary and moving regions.

where ψ_r and ψ_s are variables on Γ_L.

Form a new functional $\overline{\Pi}$ which incorporates the additional constraint

$$\overline{\Pi} = \Pi + \int_{\Gamma_L} \gamma(\psi_r - \psi_s)\, \mathrm{d}\Gamma \tag{5.9}$$

γ can be approximated in a similar way to the scalar potential by

$$\gamma = \sum_{i=1}^{m} \gamma_i N_i \tag{5.10}$$

The variation of this new functional is

$$\delta\overline{\Pi} = \delta\Pi + \int_{\Gamma_L} \delta\gamma(\psi_r - \psi_s)\, \mathrm{d}\Gamma + \int_{\Gamma_L} \delta\psi_r \left(\gamma + \mu\frac{\delta\psi_r}{\delta n}\right) \mathrm{d}\Gamma - \int_{\Gamma_L} \delta\psi_s \left(\gamma - \mu\frac{\delta\psi_s}{\delta n}\right) \mathrm{d}\Gamma \tag{5.11}$$

$\overline{\Pi}$ is stationary if both Π is stationary and the constraint $(\psi_r - \psi_s)$ is satisfied. The $\frac{\delta\psi}{\delta n}$ term in the above equation is the prescribed $\boldsymbol{B} \cdot \hat{\mathbf{n}}$ on the boundary. In 2D, a similar argument may be used for magnetic vector potential $\boldsymbol{A}$.

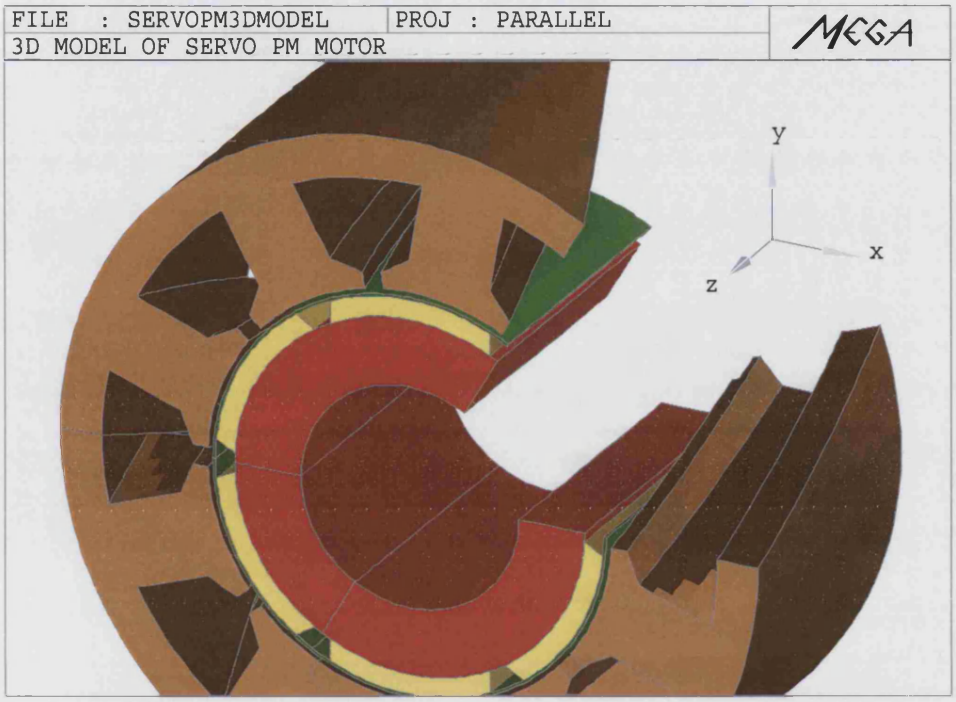

Figure 5.3: Coupled 3D model of skewed stator to rotor.

With the need of skewing either the stator and rotor for cogging torque analysis, the ability to construct the stator and rotor separately and then coupled together at a common interface facilitates the meshing of the more complex skewed region without having it *"crushing"* into the other mesh. Furthermore computational cost is greatly reduced without having to model the motor in 2D slices [43], [44], each rotated with a small angle for simulating the skewed effect as in conventional method. Figure 5.3 shows a coupled model of a permanent magnet motor with skewed stator and its interface is illustrated in Figure 5.4.

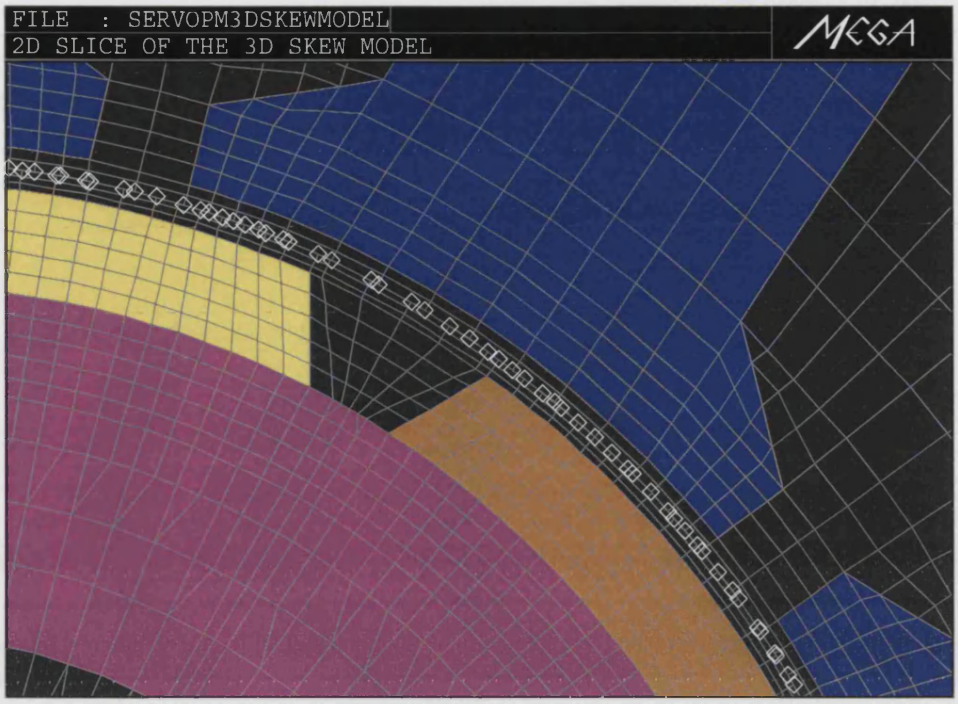

Figure 5.4: Cross-sectional cut of the 3D mesh showing the interface.

5.3 Cogging Torque: A Brief Introduction

Cogging torque results from the interaction between the stator slots and the permanent magnet magnetic fields. Its manifests itself by the tendency of the rotor to realign in a number of stable positions even when the motor is unexcited. Cogging torque can compromise positional accuracy and induce speed ripples, which may cause oscillations and instabilities. This will inevitably lead to the development of vibration, speed ripples and a pulsating torque which reduces the net effective torque. Therefore, while it is possible to eliminate the effects of cogging by use of sophisticated control strategies [45], it is desirable to eliminate, or at least minimised by skewing, fractional slot pitch design or optimising the pole arc of magnets.

The origin of cogging torque can be easily explained with the help of Figure 5.5. In the Figure, a stator tooth is rotated about three different positions with $\delta\theta$ representing

the displacement between the centre of a tooth and the centre of a magnet surface. The cogging torque experienced by the stator tooth is shown to be periodic with the period of $\delta\theta = 2\pi$ or one angular pole pitch $\theta_p = \frac{2\pi}{N_m}$, where N_m is the number of magnet poles.

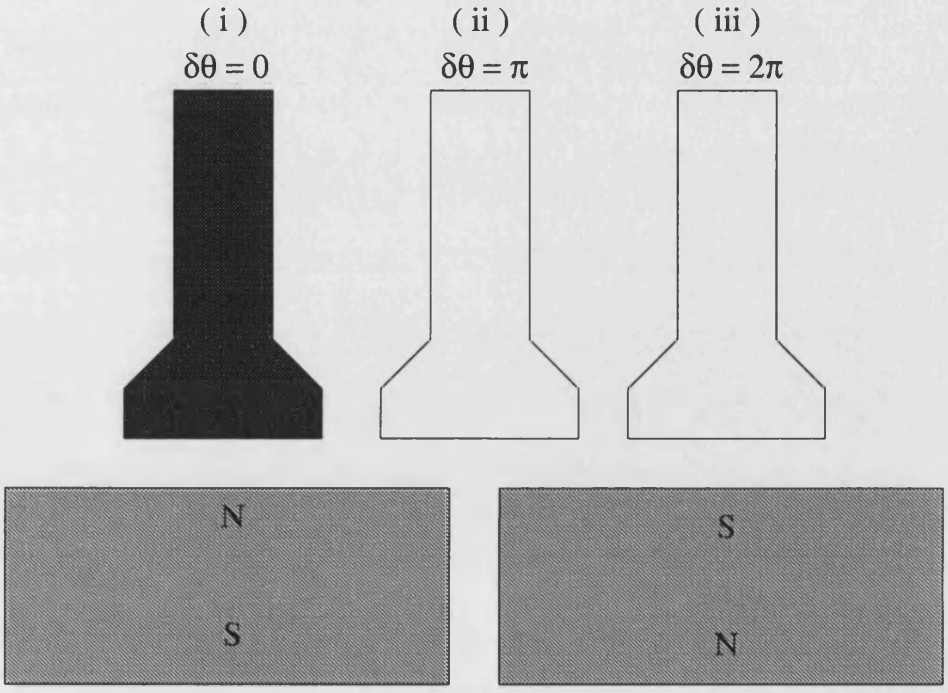

Figure 5.5: Stator and rotor diagrams.

At displacements (i) and (iii) in Figure 5.5, the stator tooth is aligned with the magnetic poles on the rotor. Therefore, the cogging torque is zero. At displacement (ii) the cogging torque is also zero since the stator tooth is balanced at the unaligned position.

If the tooth is rotated in clockwise direction the cogging torque is negative between displacements (i) and (ii) since the tooth will try to return to the stable position of displacement (i). On the contrary, between displacements (ii) and (iii) the cogging torque is positive since the tooth will try to reach the stable position of displacement (iii).

Based on this description, the cogging torque due to a single tooth is the odd function of $\delta\theta$ and can be written as the Fourier series

$$T(\delta\theta) = \sum_{n=1}^{\infty} T_n \sin(n\delta\theta) \tag{5.12}$$

For electrical machines with N_s stator slots, the cogging torque contributed by the j-th tooth in terms of mechanical position θ will then be

$$\begin{aligned} T_j(\theta) &= \sum_{n=0}^{\infty} T_n \sin[nN_m(\theta - j\theta_s)] \\ j &= 0, 1, 2, ..., N_s - 1 \end{aligned} \tag{5.13}$$

where θ_s is the angular slot pitch.

5.4 Cogging Torque Minimisation Techniques

It is not possible to eliminate cogging torque completely because of the complex interactions within electrical machines and limitations to economical production accuracies. Successful suppression of cogging torque ultimately relies on a balanced systems approach to all aspects of the permanent magnet machine and controller design which often requires a carefully selected combination of minimisation techniques.

These techniques fall into two major categories. The first class consists of methods for adjusting the permanent magnet machine design so that it approaches its ideal characteristics of achieving a smooth torque production. In this category, the techniques involved tend to address the fundamental electromagnetic sources of the pulsating torque and adjust the design in such a way as to drive it to ideal. The second class of techniques are based on active control schemes which modify the excitation to correct any non-ideal characteristics of the machine and/or its power inverter. Only the machine design aspects of permanent magnet AC motor in cogging torque reduction will be discussed here.

Despite the availability of a wide range of machine design methods for reducing cogging torque, there are many occasions when they are neither appropriate nor sufficient to achieve the required minimisation of this parasitic torque.

The following subsections give a brief review of a variety of different techniques used to address the problem of cogging torque.

5.4.1 Motor Magnetic Designs

Fractional slot motor designs are preferred over integral slot designs when it comes to reducing cogging torque. Symmetry in the integral slot design can lead to multiple magnetic pole edges entering and leaving the stator teeth simultaneously, producing high cogging torque. The reason for this is obvious since in motors having an even number of teeth, the edges of the north and south pole magnets all have the same relative position with respect to the stator teeth, which is not the case for motors having an odd slot.

For an even number of symmetrical magnetic poles, the stator should have odd number of slots so that only one magnet edge leaves a stator tip at any instant. A fractional slot configuration also minimises the need for skewing.

The number of slots and poles in motor play a significant role too in the development of cogging torque since this unwanted torque is produced by the rotor magnets interacting with the stator slot. The choice of the number of poles depends upon many factors. A few of these factors are listed below:

1. Inertia requirements
2. Magnet material
3. Rotational speed
4. Exterior type - rotor appears on the outside of the stator

5. Interior type - the usual motor with rotating rotor in the core and stationary stator outside

6. Axial gap type - steel disk rotor with magnets placed on one side

The number of poles should be inversely proportional to the maximum speed rotation. This is to avoid iron losses in the stator. If smooth torque is required at low speed a large number of poles would be needed but for very high speeds two to four poles motors are preferred.

The required thickness of the stator and rotor yokes can be significantly reduced by increasing the number of poles. Thus, for a given magnetic and electric loading, the overall diameter can be reduced by increasing the number of poles. Furthermore the stator ampere-conductors per pole decreases in inverse proportion, therefore as the number of poles increases the inductance and reactance of the motor decreases. Less poles motor will have the greatest susceptibility to magnetic imbalance which can lead to induced currents in the bearings and shaft flux.

With large number of slot/pole the cogging torque is inherently reduced. This is due to the fact that the relative permeance variation of the magnet is reduced as it successively covers and uncovers the slots at a time.

Alternatively cogging torque can also be reduced by decreasing the stator slot openings [46]. This can be done by using magnetic slots wedges or adjusting the slot opening [47]. However, these two techniques can sometimes reduce the average output torque and increase the magnetic flux leakage.

5.4.2 Permanent Magnet Magnetisation

The magnetic flux distribution at the air gap for permanent magnet AC motor should be a sinewave so that only minimum cogging torque is produced. The most common

types of permanent magnets are those arc-shaped with parallel and radial magnetisation. In practice, parallel magnetisation is most easily obtained. An isotropic magnet arc when magnetised using a magnetising coil will produce near parallel magnetisation.

Realisation of radial magnetisation using isotropic magnet material is virtually impossible for high energy magnets. Anisotropic magnet [48] material with preferred radial magnetisation can produce better radially oriented magnets. These magnets configurations are used to approximate the ideal sinewave flux distribution.

A more sinusoidal flux distribution can be obtained by using a thin magnetic retaining can on the rotor to increase the magnet leakage at the pole edges [49]. The retaining can also serves to retain the magnets and decrease the effective air gap counteracting some of the torque losses caused by magnet flux leakage.

Tapering the magnet poles, using breadloaf shape magnets and magnet poles with varying magnetisation directions are some of the other techniques used to reduce cogging torque.

5.4.3 Permanent Magnet Pole Arc

It is also possible to minimise cogging torque by selecting an appropriate magnet pole arc. The width of the arc plays such a significant importance since it is well-known that cogging torque existed is due to the interaction of the ends of magnet poles and the stator teeth.

The overall cogging torque is the summation of all the forces at each of the magnet tips. In [35] it is shown that an approximate expression for the optimal magnet pole arc τ_m when the stator slot opening is half the size of the slot pitch is given by

$$\tau_m = \left[\frac{n + 0.14}{N_{sm}}\right]\tau_p \tag{5.14}$$

where τ_p is one pole pitch, N_{sm} is the number of slots per magnet pole and n is any positive integer satisfying the constraint $\frac{\tau_m}{\tau_p} = \frac{n+0.14}{N_{sm}} < 1.0$.

Therefore, minimum cogging torque is achievable with the optimum magnet having pole arc width of an integer multiple of slot pitches with an additional 14 % of a slot pitch. Of course, the choice of pole arc also depends on other performance factors, such as the back-*e.m.f* waveforms and the average torque output.

5.4.4 Motor Axial Length and Air Gap

Differences in stator and rotor axial length will have effects on the amount of cogging torque produced. If the ratio of the axial length and the diameter of the motor is low, the percentage of reduction in cogging torque after skewing will be considerably lower as the end effects are at a higher proportion.

At the air gap, the shorter its length the lower the cogging torque. A very short air gap allows very little fringing about a slot opening and hence, reduces the flux ripple seen by the pole. Often shorter air gap gives the lowest cogging torque but in some cases longer gap is better, especially when it facilitates harmonic cancellation in the cogging waveform.

5.4.5 Skewing

One of the most common techniques to minimise cogging torque is to skew either the stator lamination stack or permanent magnets. Skewing reduces the permeance variation seen by the rotor magnets and hence, the cogging torque.

An analysis of this skewing effect is given by Hanselman [50]. In his paper, a Fourier analysis of the cogging torque is conducted on a motor of stack length L. The cogging torque in this machine is assumed to have the waveform of a general Fourier series

$$f = \frac{1}{L}\sum_{n=0}^{\infty} A_{nx}\cos(n\theta) + B_{ny}\sin(n\theta) \tag{5.15}$$

In skewed cases, the Fourier series of (5.15) must be modified to take into account the varying phase shift as a function of the axial distance - z. If the stator is skewed by α_s, equation (5.15) is then phase shifted at any point z along the motor axial length by the amount of skew and is described as

$$f = \frac{1}{L}\sum_{n=0}^{\infty} A_{nx}\cos\left[n\left(\theta - \frac{z}{L}\alpha_s\right)\right] + B_{ny}\sin\left[n\left(\theta - \frac{z}{L}\alpha_s\right)\right] \tag{5.16}$$

The total cogging torque on the single tooth is calculated by integrating the equation (5.16) along the axial length which yields

$$\begin{aligned} F(\theta) &= \int_{-L/2}^{L/2}\frac{1}{L}\left(\sum_{n=0}^{\infty} A_{nx}\cos\left[n\left(\theta - \frac{z}{L}\alpha_s\right)\right] + B_{ny}\sin\left[n\left(\theta - \frac{z}{L}\alpha_s\right)\right]\right)\mathrm{d}z \\ &= -\sum_{n=0}^{\infty}\frac{1}{n\alpha_s}\left[A_{nx}\sin\left(n\theta - \frac{n\alpha_s z}{L}\right) - B_{ny}\cos\left(n\theta - \frac{n\alpha_s z}{L}\right)\right]_{-L/2}^{L/2} \end{aligned} \tag{5.17}$$

Using the trigonometric identities in Appendix C

$$\begin{aligned} F(\theta) &= \sum_{n=0}^{\infty}\frac{2}{n\alpha_s}\left[A_{nx}\sin\left(\frac{n\alpha_s}{2}\right)\cos(n\theta) + B_{ny}\sin\left(\frac{n\alpha_s}{2}\right)\sin(n\theta)\right] \\ &= \sum_{n=0}^{\infty}\left\{sinc\left(\frac{n\alpha_s}{2}\right)\right\}\left[A_{nx}\cos(n\theta) + B_{ny}\sin(n\theta)\right] \end{aligned} \tag{5.18}$$

This simple expression shown the skewing amplitude modulates the original Fourier series by a *sinc(x)*=$\sin(x)/x$ function. Using these assumptions, equation (5.13) is rewritten to include the skew term {} as

$$T_j(\theta) = \sum_{n=0}^{\infty} T_n\left\{sinc\left(\frac{nN_m\alpha_s\theta}{2}\right)\right\}\sin[nN_m(\theta - j\theta_s)] \tag{5.19}$$

The net cogging torque is then calculated by summing up the cogging torque produced by each individual stator teeth of the electrical machine

$$
\begin{aligned}
T(\theta) &= \sum_{j=0}^{N_s-1} T_j(\theta) \\
&= \sum_{j=0}^{N_s-1} \sum_{n=0}^{\infty} T_n \left\{ sinc\left(\frac{nN_m\alpha_s\theta_s}{2} \right) \right\} \sin(nN_m\theta)\cos(nN_mj\theta_s) \qquad (5.20)
\end{aligned}
$$

Skewing has the effect of improving the stator winding distribution and substantially reduces the higher-order *back-e.m.f* harmonics. Hence, producing a more sinusoidal *back-e.m.f* waveforms. This helps to reduce the torque ripple in permanent magnet AC machines.

Skewing is an attractive technique since it is simple and yet effective but it does have its drawbacks. By opting for this technique, a more complex motor construction and loss of certain amount in the average torque are unavoidable. It also increases leakage inductance and stray losses.

The reduction in average torque is generally a few percent for motors with a moderate number of slots per pole per phase. However, for motors with small number of slots, skewing by a full slot pitch can result in substantial loss in average torque. If a full slot pitch skew is applied on a single phase machines with one slot per pole then the average torque output will be zero. But a partial skew could be beneficial.

5.4.6 Summary of Machine Design Techniques

Various techniques have been discussed for cogging torque minimisation in permanent magnet AC motors. Traditionally, the use of one slot pitch skewing of either the stator or permanent magnets will generally yield good results. For motors with low number of slots, partial slot pitch skewing will be adequate.

The selection of an appropriate slot/pole combination and optimising the pole arc width of the magnets mounted on the rotor are some of the parameters that can be design to reduce cogging torque.

Constructing dummy slots and teeth, using high number of phases, fractional slot pitch windings and chamfered magnet are some of the other alternative techniques that can be considered. Dummy slots have the similar effect to that of doubling the number of the stator slots. This caused the frequency of the cogging torque to be doubled with reduced magnitude and halved the amount of skew angle required to eliminate cogging.

5.5 Description of Test Machines

The test machines analysed here are two 3-phase permanent magnet AC motors with surface mounted Neodymium-iron-boron (NdFeB) magnets on the internal rotor. The main parameters of the two motors are given in Tables (5.1) and (5.2) respectively.

For excitation a new generation of rare earth magnet, Neodymium-iron-boron (NdFeB) is used. NdFeB has high energy density. However, it has a limited operating temperature range and suffers from corrosion [51].

Table 5.1: Test Machine I - 12 slots and 8 poles motor.

	Motor Parameters.	Dimensions in SI unit.
1	Outer diameter of stator	88.00 mm
2	Stator slot depth	17.50 mm
3	Outer diameter of rotor	37.00 mm
4	Shaft diameter	20.00 mm
5	Width of stator teeth	5.80 mm
6	Magnet width	13.96 mm
7	Magnet height	3.50 mm
8	Width of slot opening	2.50 mm
9	Air gap	0.75 mm
10	Axial length of stator	63.0 mm
11	Axial length of rotor	60.0 mm
12	No. of poles	8.0
13	No. of slots	12.0

Table 5.2: Test Machine II - 18 slots and 6 poles motor.

	Motor Parameters.	Dimensions in SI unit.
1	Outer diameter of stator	88.00 mm
2	Stator slot depth	12.00 mm
3	Outer diameter of rotor	44.50 mm
4	Shaft diameter	20.00 mm
5	Width of stator teeth	4.70 mm
6	Magnet width	20.95 mm
7	Magnet height	3.00 mm
8	Width of slot opening	2.50 mm
9	Air gap	0.75 mm
10	Axial length of stator	162.50 mm
11	Axial length of rotor	146.00 mm
12	No. of poles	6.0
13	No. of slots	18.0

The NdFeB magnet used in the 12 slots and 8 poles motor has a remanence of $\boldsymbol{B_r}$ = 1.15 T with the coercivity of 870 kA-t/m. For the 18 slots and 6 poles motor, the NdFeB magnet has $\boldsymbol{B_r}$ = 1.19 T and coercivity of 930 kA-t/m. The non-linear **B-H** curves for both machines are shown in Figure 5.6 and Figure 5.7 respectively.

5.6 Validations and Discussion

Electromagnetic torque can be determined either analytically [37] or numerically [52] in a number of means such as the Maxwell Stress method and the energy method. For analytical analysis, particularly for predicting cogging torque, a reliable physical model is essential while highly accurate field solutions are the prerequisite for the numerical method.

The *MEGA* program can compute the electromagnetic forces by calculating the Maxwell Stress. It requires accurate field solutions since the calculations are dependent upon local field quantities.

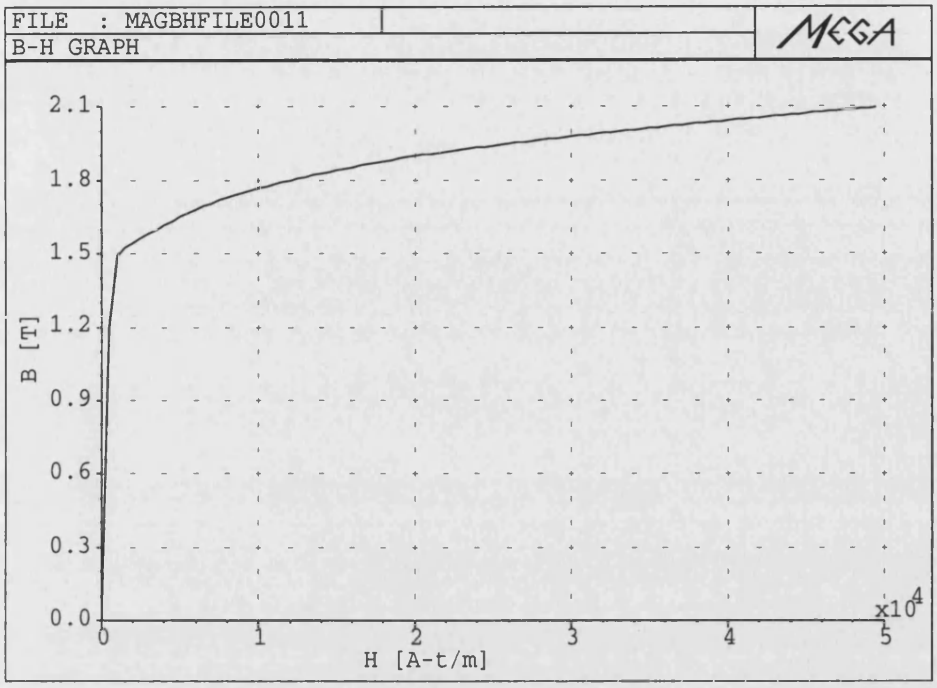

Figure 5.6: **B-H** curve for the 12 slots and 8 poles motor.

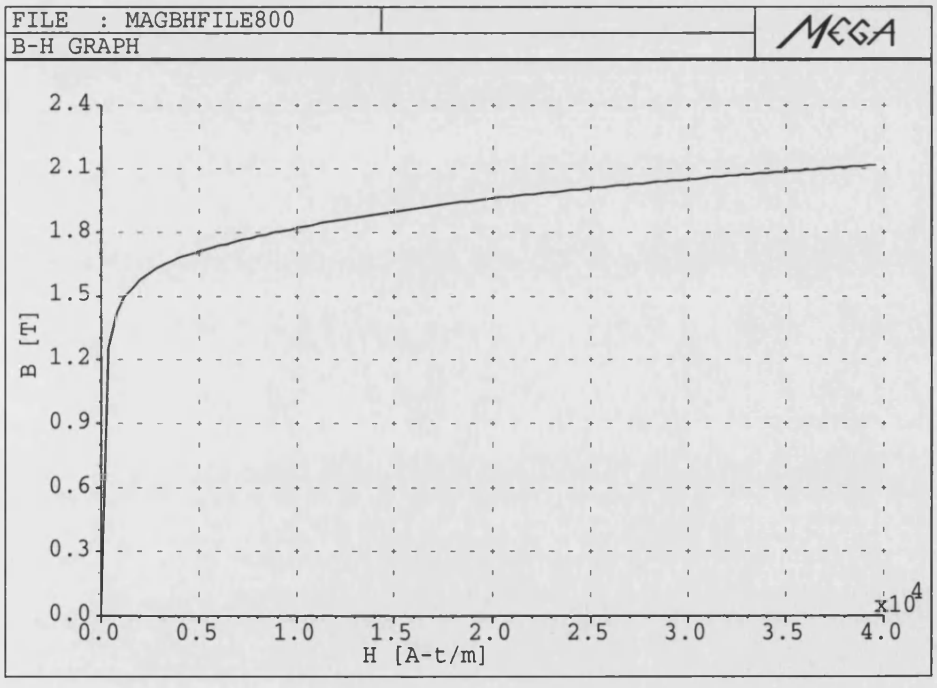

Figure 5.7: **B-H** curve for the 18 slots and 6 poles motor.

The calculation of the cogging torque by Maxwell Stress integration required a very fine spatial discretisation because of the short wavelength of the cogging torque waveform which is usually less than a stator slot pitch.

This work presents a fully three dimensional field computation. The configuration of the two motors modelled in 3D are shown in Figure 5.8 and Figure 5.9 respectively. By taking advantage of the symmetrical property of the motors, only a section of each motor was modelled. This can be done by assigning the appropriate boundary conditions on the motors. The periodic boundary conditions were imposed on the two symmetrical radial planes of the models and the tangential field on the outer boundary. With this scheme less computational time is required to solve the problems.

Special attention is paid to the air gap where good results of the cogging torque calculation can be obtained. Cogging torque is computed by Maxwell Stress integration over the circular path in the central layer of the air gap elements. In additions to employing a fine mesh discretisation, it is always better to integrate through the central layer of the air gap elements in order to get the most accurate results when using Maxwell Stress. A transverse cut of the 18/6 PM motor's 3D model to illustrate the magnetic flux path is given in Figure 5.10.

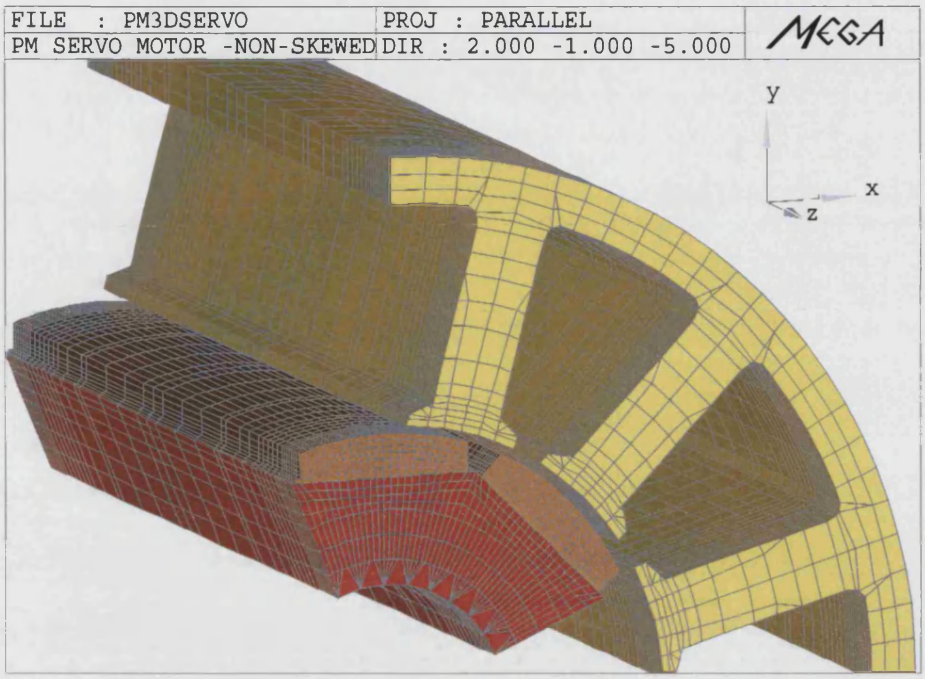

Figure 5.8: 3D FE model of 12 slots and 8 poles motor.

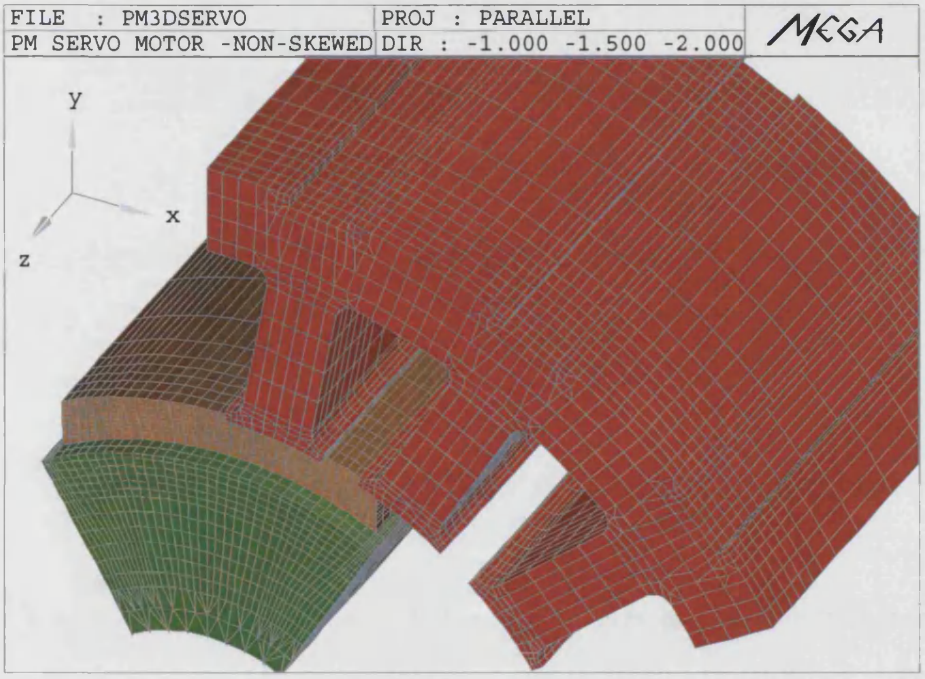

Figure 5.9: 3D FE model of 18 slots and 6 poles motor.

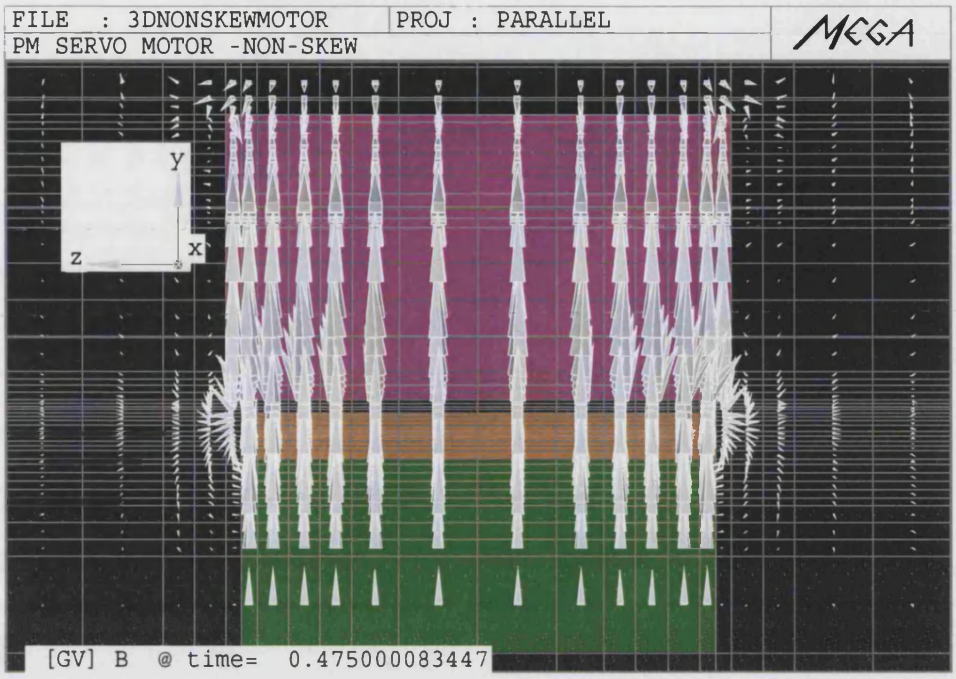

Figure 5.10: Magnetic flux path in the 18 slots and 6 poles motor.

5.6.1 Computational and Measured Results

The two 3D FE models were solved as non-linear transient problems with the magnetic saturation effect taken into account. In the case of cogging torque, the eddy currents are neglected, each magnetic sample corresponds to a magnetostatic solution stepping through time. Figure 5.11 and Figure 5.12 show the predicted cogging torque waveforms for the non-skewed motors.

In the 18/6 PM motor, every three stator teeth successively covered and uncovered a permanent magnet for every one slot pitch of 20.0° rotation. The six magnet pole-edges would be aligned with the stator slots simultaneously which means for every 20.0° rotation a single sinusoidal cogging torque waveform is produced. This is proven in Figure 5.12.

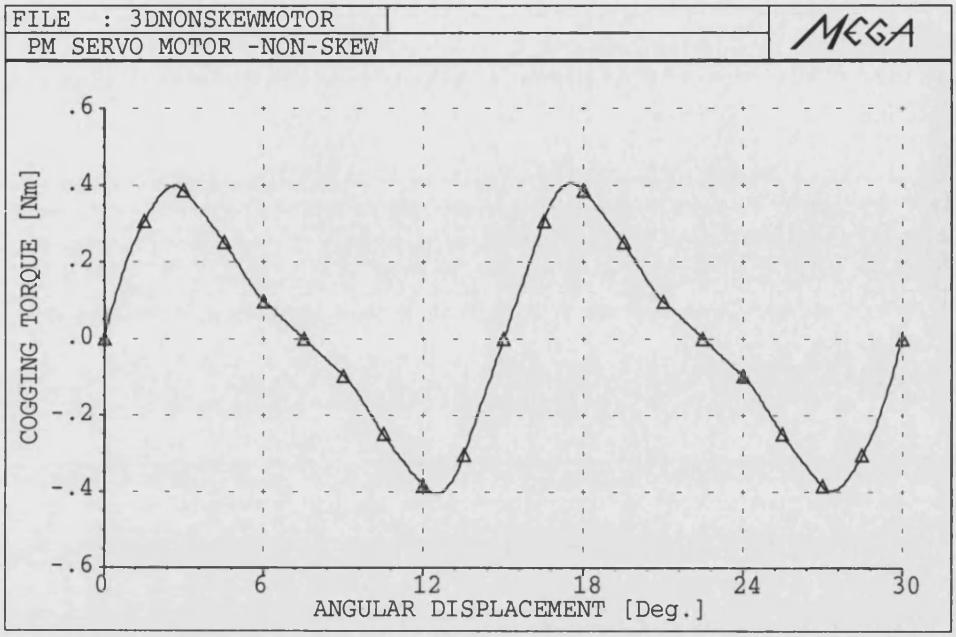

Figure 5.11: Predicted cogging torque for non-skewed 12/8 PM motor.

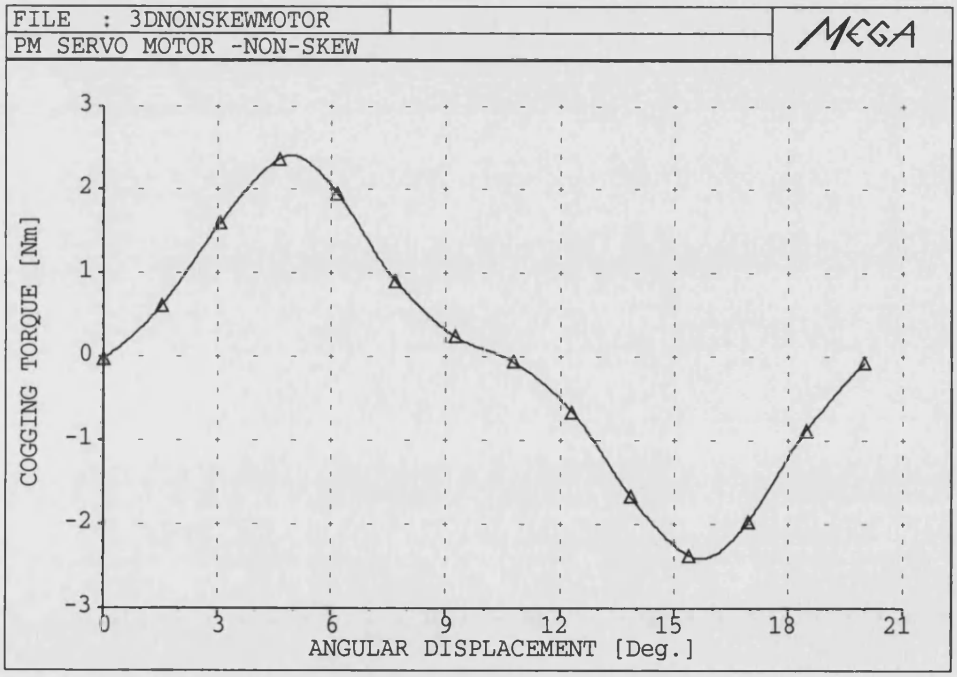

Figure 5.12: Predicted cogging torque for non-skewed 18/6 PM motor.

However, in the 12/8 PM motor the slot/pole combination is 12 slots and 8 poles, therefore, for every successive one slot pitch rotation, two repetitive cogging torque waveforms are produced. Even though the size of the 18/6 PM motor is almost similar to the 12/8 PM motor, the cogging torque in the latter is generally lower and spread out with double frequency in a period compare to the former where the detent effects are added up resulting in a higher cogging torque.

The Effects of Skewing

The stator of the 12/8 PM motor is now skewed half a slot pitch or 15.0° and the stator of the 18/6 PM motor is skewed a full slot pitch or 20.0°. Figure 5.13 shows an example of a 3D FE model of skewed stator.

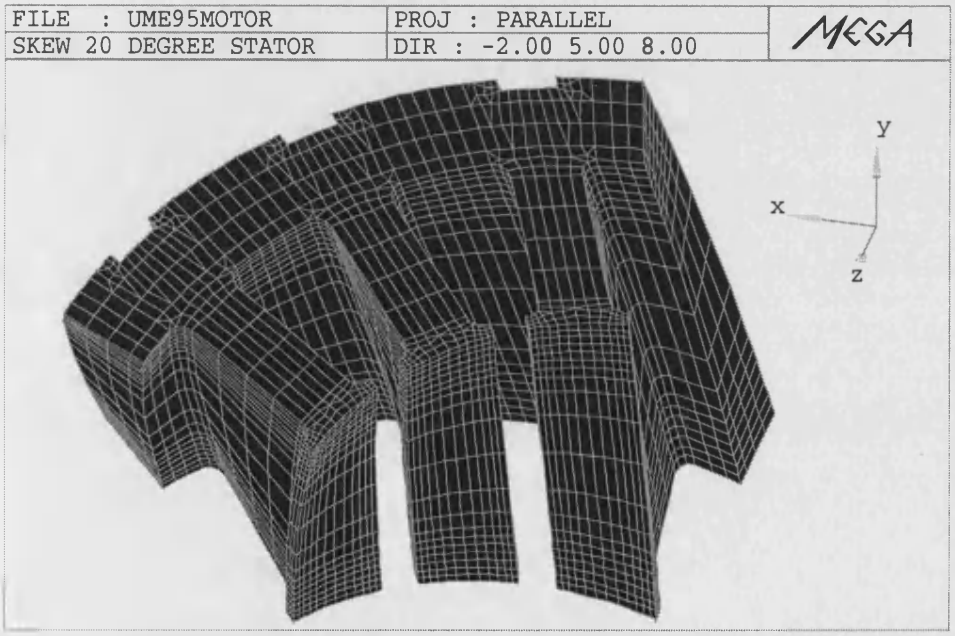

Figure 5.13: Skewed stator.

Figure 5.14 and Figure 5.15 show the simulated and measured cogging torques. Good agreement between the two is obtained. Figure 5.16 and Figure 5.17 show the magnetic flux density of the 18/6 PM motor at time = 0.34 s when the rotor has rotated 19.8° from its initial position.

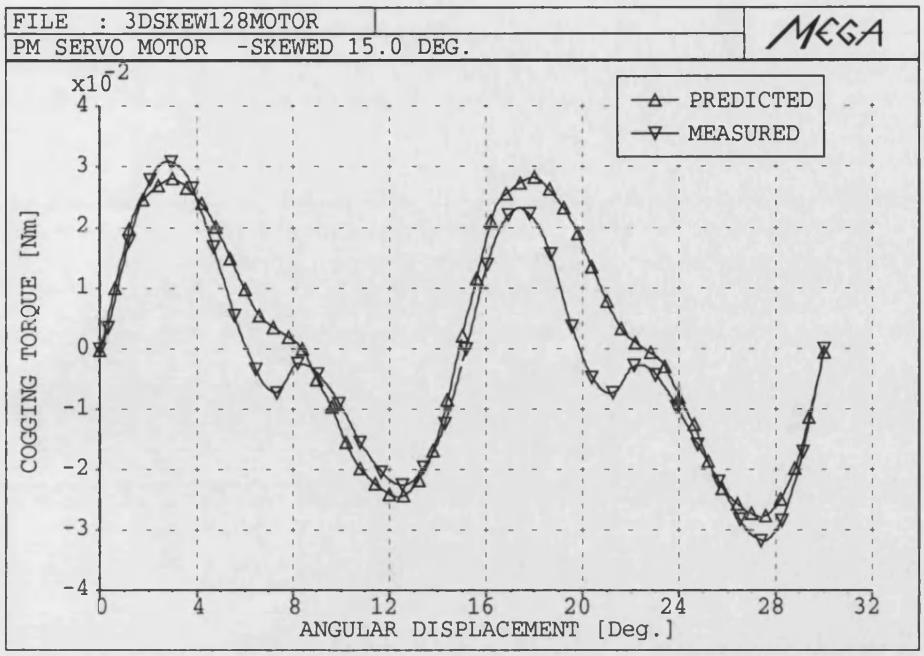

Figure 5.14: Predicted and measured cogging torques for 12/8 PM motor with skewed stator.

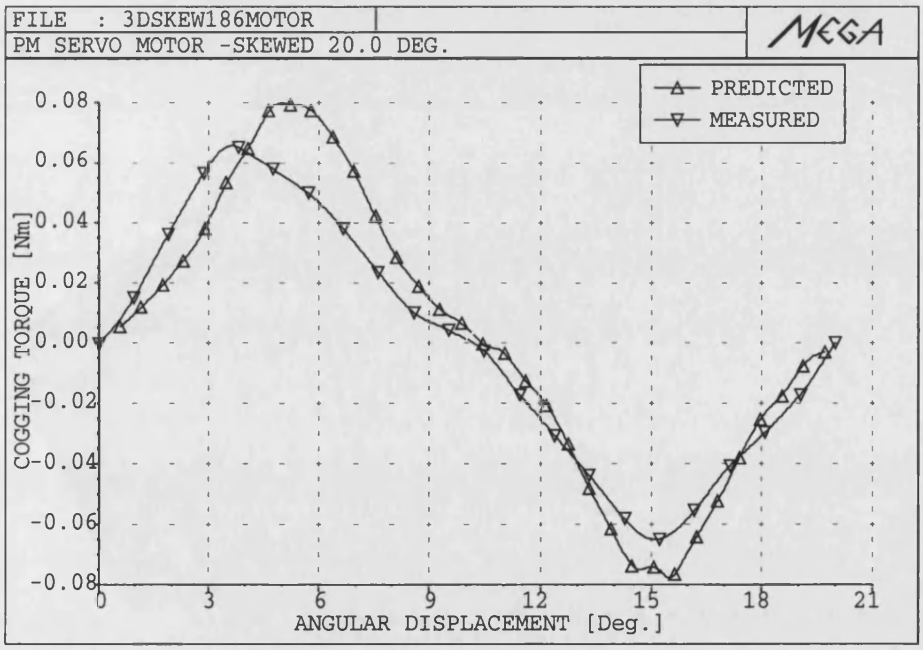

Figure 5.15: Predicted and measured cogging torques for 18/6 PM motor with skewed stator.

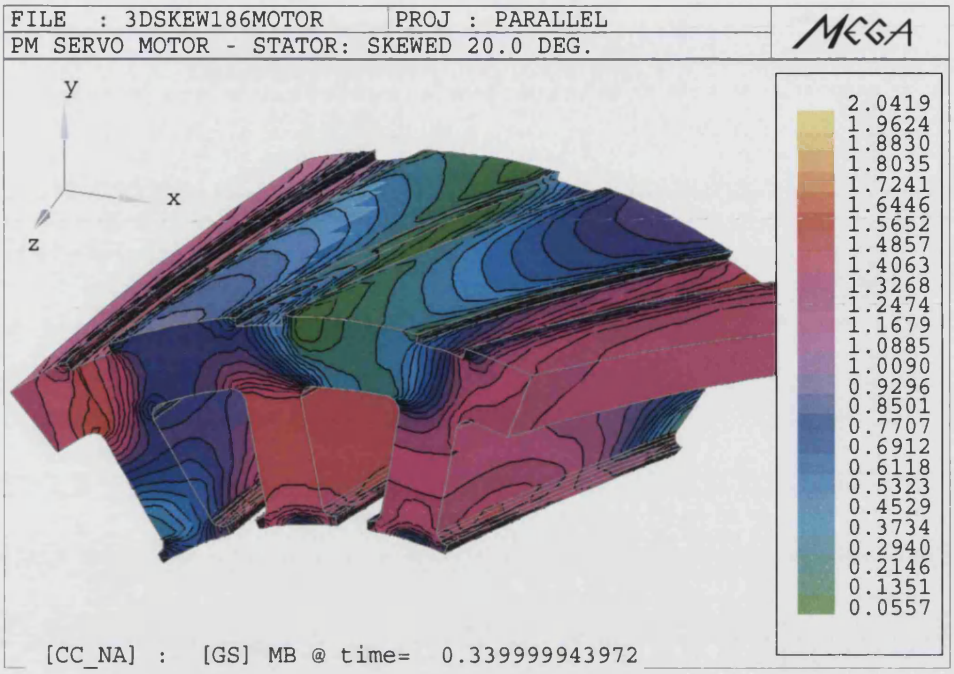

Figure 5.16: Magnetic flux density of the 18/6 PM motor's skewed stator.

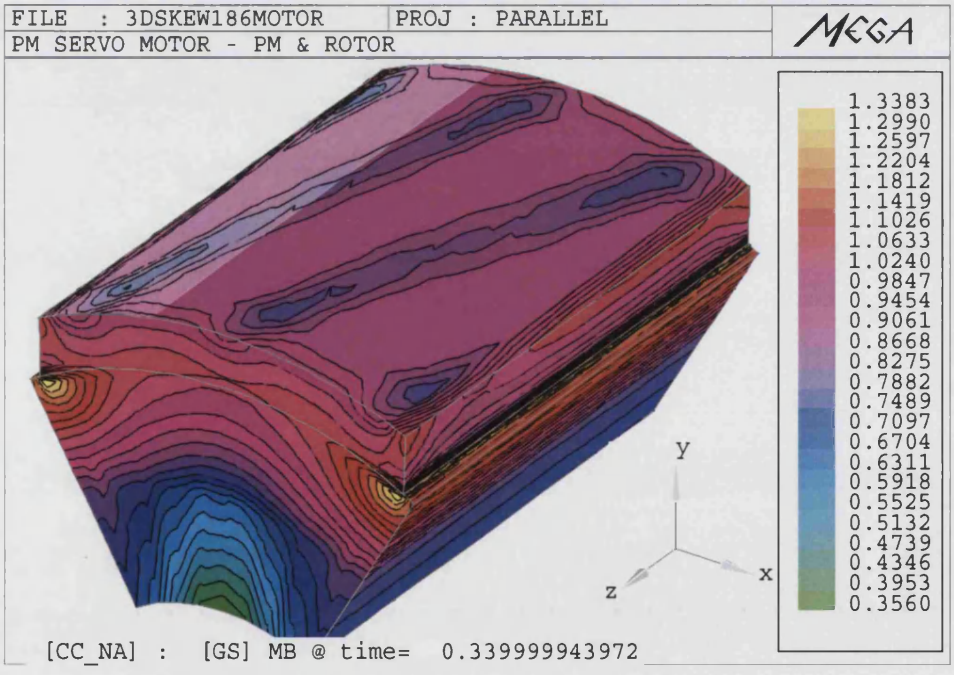

Figure 5.17: Magnetic flux density of the 18/6 PM motor's magnet and rotor.

Cogging Torque Sensitivity Analysis of the 12/8 PM Motor

Three case studies are conducted to analyse the sensitivity of the cogging torque produced in the 12/8 PM motor. The stator stack remained unskewed throughout the analysis.

In the first case, permanent magnets with radial offset of 5 mm, which results in a general "bowl" shape with tapered edges at the surface, are compared with the original breadloaf magnets. Figure 5.18 shows the effect on cogging torque when the tapered edge magnets were used. Tapered magnets produced a more sinusoidal flux density along the poles which reduces the cogging torque.

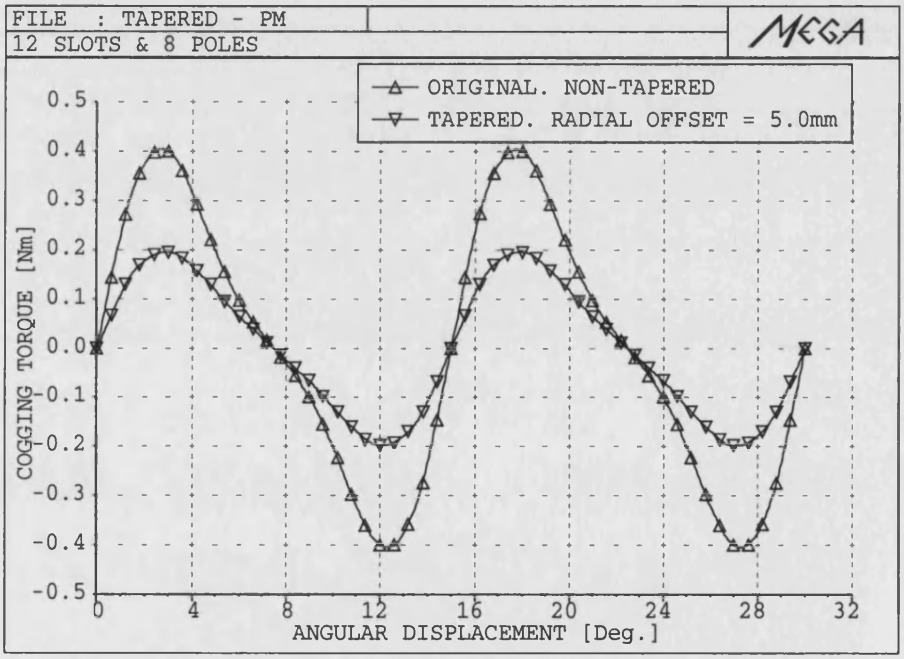

Figure 5.18: Predicted cogging torque for tapered and non-tapered magnets.

The axial length of the rotor also affects the cogging torque produced in PM machines for which it is impossible for either the analytical method or 2D FE method to give a prediction. In the second case, three 3D models of the 12/8 PM motor with different rotor lengths are simulated to show the influence of end effects on cogging torque:

1. the rotor axial length is shorter than the stator stack length

2. the rotor and the stator stack having the same axial length

3. the rotor axial length is longer than the stator stack length

The stator stack length is maintained at 63 mm for all three cases. Figure 5.19 shows the cogging torque waveforms due to the three different rotor lengths. This shows that a longer rotor length will result in a higher cogging torque being produced.

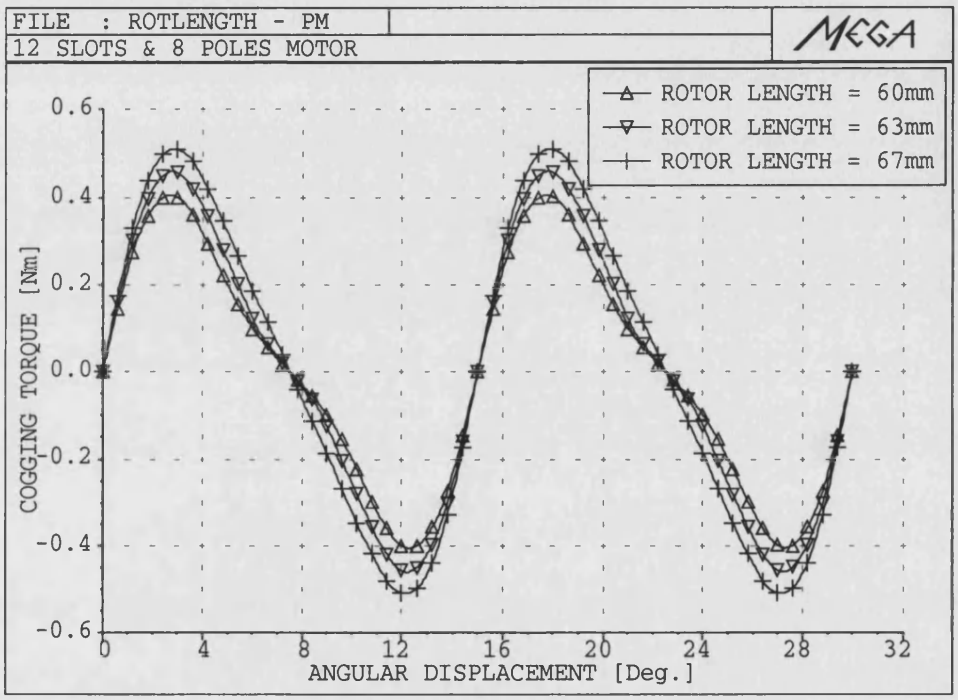

Figure 5.19: Predicted cogging torque for different rotor lengths.

In the third case, two set of permanent magnets with different pole arc width are mounted separately on the machine's rotor. These magnets, which dimensions are provided by the manufacturer are simulated in two 3D finite element models. The sensitivity of the cogging torque when changes occurred in this design parameter is clearly demonstrated in Figure 5.20.

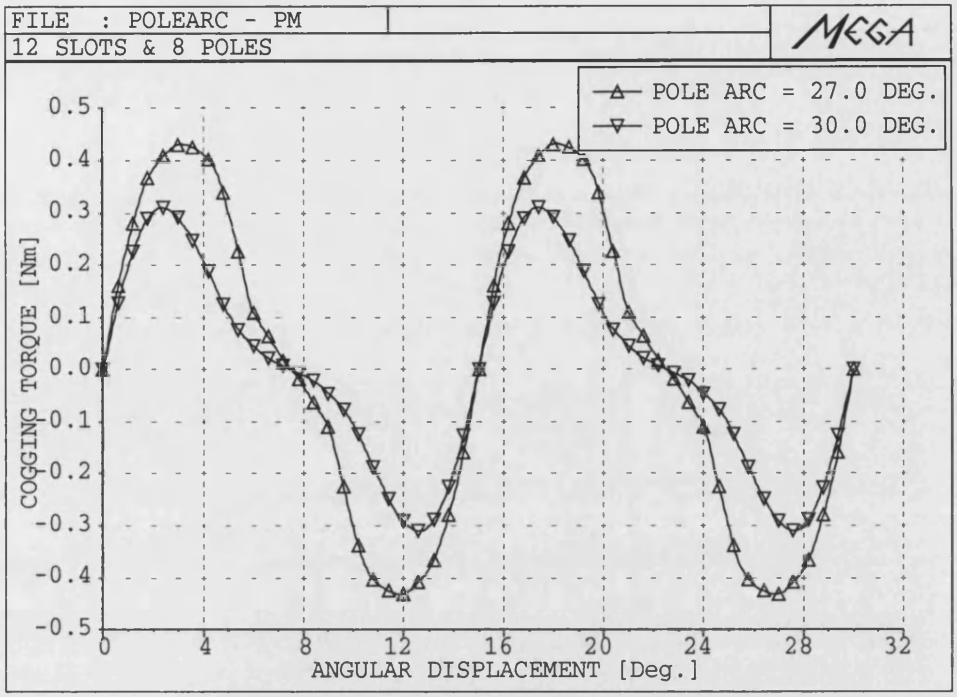

Figure 5.20: Predicted cogging torque for stator with different pole arcs.

However, these pole arc widths are not necessarily the optimum value. They could be at the same time undermining the production of the average output torque. Optimal pole arc shaping could also mean geometrical irregularities at the edge of the permanent magnet which would then pose manufacturing difficulties. A balance compromise will have to be established. Generally, a pole arc width of 2/3 or slightly more of a pole pitch serves as a good guide.

Fractional Slot Design

In the final analysis, the number of stator slots in the 12/8 PM motor is increased to 21 slots. The motor configuration is now changed from its previous integral slot design to that of a fractional slot and the stator remains unskewed. A complete model of the 21 slots and 8 poles machine is shown in Figure 5.21.

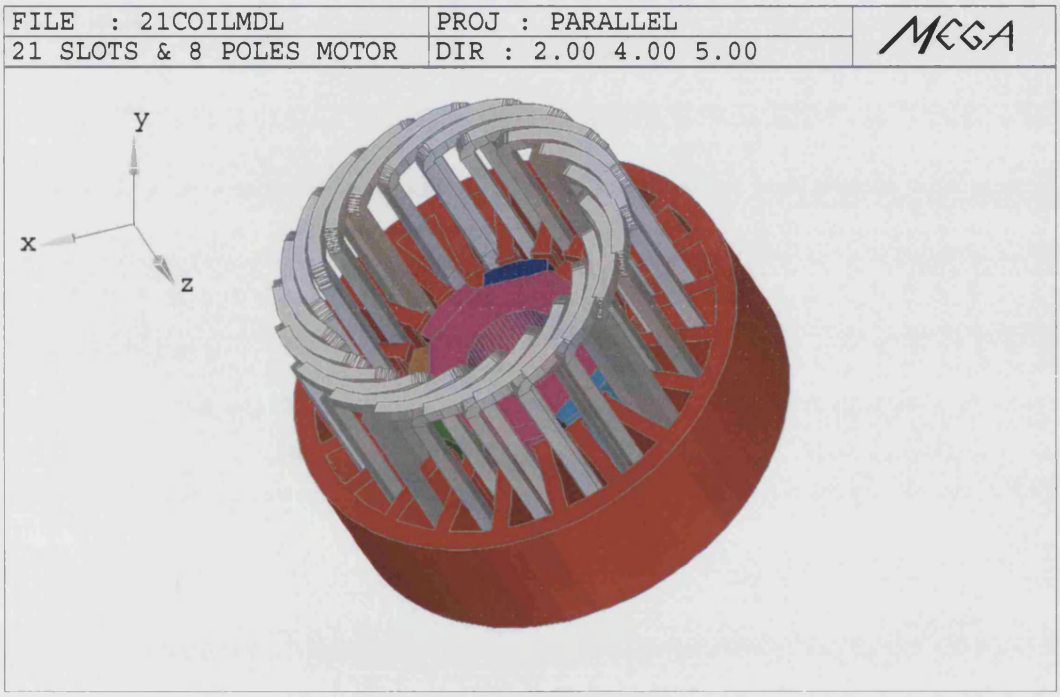

Figure 5.21: 21 slots and 8 poles motor with complete 3-phase winding.

The cogging torque shown in Figure 5.22 is even lower compared to the skewed integral slot design. Fractional slot design remains the feasible option when skewing is not desired.

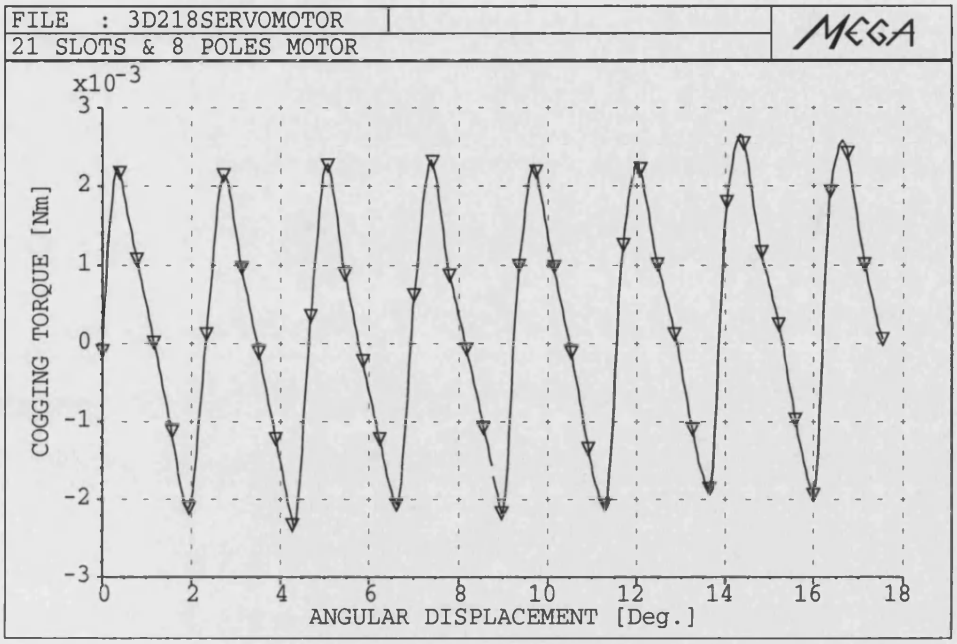

Figure 5.22: Predicted cogging torque for non-skewed fractional slot design.

5.7 Summary

This chapter described some of the motor design techniques for cogging torque reduction in permanent magnet AC machines. It is generally preferable to eliminate cogging torque by improving the motor design rather than depending on control-based techniques to cancel the undesired harmonic torque components.

These machines are well-suited to the established AC techniques such as slot skewing, magnet skewing and fractional slot pitch design for minimisation of cogging torque. An appropriate choice of magnet pole arc width may also help in reducing this unwanted torque.

There is inherently a trade-off in permanent magnet AC machine design between obtaining maximum average torque and minimum cogging torque. Cogging torque can be minimised but at the same time some reduction in the average torque should be expected. Another important issue when applying techniques for reducing cogging torque is the sensitivity to manufacturing tolerances. Some techniques which require high efficiency in the assembly floor and high monetary cost may proved to be impractical for low-cost high volume production.

The achievement of smooth torque production in permanent magnet AC machines requires painstaking attention to every aspect of machine and controller design. No universally effective solution has yet appeared for all applications despite the expanding number of various techniques found to date for the minimisation of cogging torque. This is the testimony of the underlying difficulty in solving the problem.

Chapter 6

Optimisation of Electromagnetic Devices using Parameterised Templates

6.1 Introduction

Designing electromagnetic devices with finite elements could be a laborious work and time consuming. The idea here is to generate a software which could construct a template where all future alterations of the design during the optimisation period could be done easily based on this early map of the design.

Many users of finite element packages have very little time to spend on this activity. On the other hand, many electrical device designers like to explore various candidate devices particularly at an early stage in their deliberations. Very often in the case of devices like electrical machines and transformers, all of these candidate designs will be very similar to each other in appearance, differing only in small details such as tooth width, tooth number, rotor diameter and so on.

A few software packages address this problem via automatic meshing, perhaps also coupled with automatic refinement based on some error criterion. Often this results in very large meshes, usually due to the poor quality of elements which must be used in most automatic mesh generators, nearly always triangles for 2D and tetrahedrons for 3D.

This chapter describes a new parameterisation technique which allows alteration of an initial generic template mesh to be carried out while retaining the freedom to choose the type of elements and mesh density. The first step consists of setting up a 2D or 3D finite element model of the problem, with all the dimensions which are required to vary defined as input parameters. Once the template mesh is set up, new devices similar to the template can be modelled easily by altering the parameter input file. This simple design sheet contains a list of parameters which describe the basic dimensions of the device and names of the non-linear material curves. Thus, the method allows semi or completely automatic meshing of a device to be used.

An advantage of this method is that once a template mesh has been set up, new devices similar to that of the template can be modelled easily by altering the contents of a simple form or file. These alterations can be easily carried out by a casual user or by an optimisation program. However, the major disadvantage of the method is that since all meshes will be topologically similar, radical changes to a device are not possible, for example it would be unlikely to be able to start an optimisation run with an induction machine and end up with a brushless DC machine.

A device as complex as an induction machine is then modelled using no more than a design sheet containing a list of parameters which describe the basic dimensions of the machine and the names of the non-linear material curves. A disadvantage of this method is that it would be of little use in optimising the design of a device where the final shape was completely unknown in advance. This situation is unusual however, for instance most electrical machines of a given type look very similar to each other.

In this chapter, several case studies are conducted to evaluate the feasibilities of the method described. The first example is that of cogging torque analyses in a brushless permanent magnet servo machine. Cogging torque is of interest as it is commercially very important. It is also an example of a case in which automatic mesh generators do not perform particularly well, as the required force is relatively small and must be calculated accurately. The second example consists of the voltage generated by a

wound rotor generator and finally, the technique is used to build a Fluxset magnetic field measuring device.

6.2 Parameterised Template Meshing Technique

The template mesh method is straightforward and could be implemented in most finite element software. The method is based on producing a monitor (or log) file while the initial mesh is created.

The main steps in mesh creation are as follows:

- A list of parameter names and values is created. Parameters may be simple values, or functions of other parameters. This would enable changing (say) the rotor diameter of a rotating machine while keeping the stator radial dimensions constant.

- The template mesh is created in the usual way employing the user's favourite techniques, the only extra requirement is that where required, any quantity which would normally be entered as a character string, integer, real or complex number is entered as the parameter name.

- A monitor file is used to record all the actions which took place in creating the mesh. The trick which allows the template mesh scheme to work is that spatial information in the file is accompanied by node or element number information in a separate auxiliary file. This spatial information may perhaps be a node or point position. For instance if all the elements within a certain polygonal boundary have been marked for refinement at the creation stage, the identifiers of the elements which are affected by this operation are stored in the auxiliary file. Since any spatial information is useless when dimensions of the mesh have been changed, the number information from the auxiliary file is used as input to the program on second and subsequent runs of the monitor file.

In order to change the template mesh, the steps are as follows:

- The parameter values are changed as necessary.
- The monitor file which creates the mesh is run again. The mesh is then built up in the same way as before but this time uses all of the new values from the parameter file. The program ignores any spatial information in the monitor file and uses the invariant number data in the auxiliary file.

This 'alter and run again' phase is very easily automated and can be controlled by a user or by an optimisation program.

In creating the template, the user enters the parameter name in describing the device dimensions instead of the usual numerical values. Once the parameters are altered and the program rerun, the monitor file will initiate the sequence of events in creating the new mesh. The optimisation stage can be carried out either manually, here the user observes the results of previous solutions and alters values in the parameter file, or is computer controlled, where the parameter file is altered by a program according to the requirements of an optimisation algorithm.

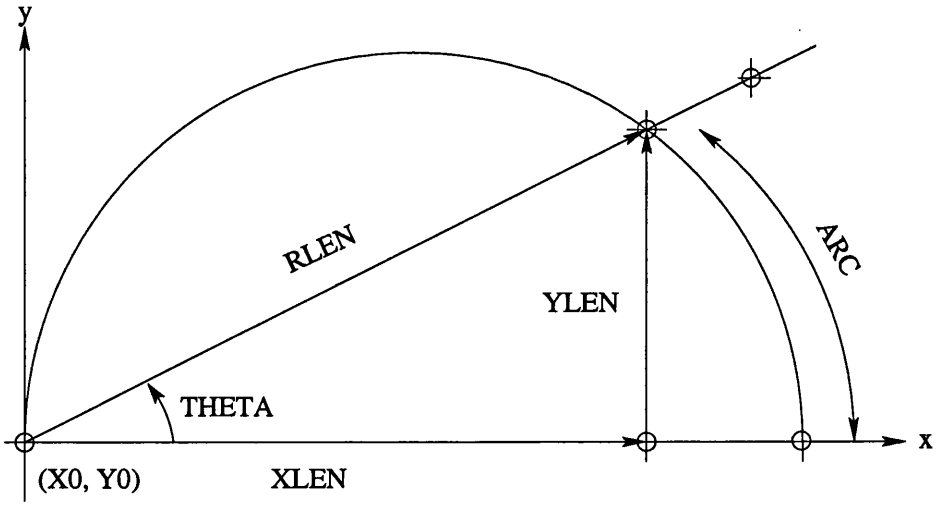

Figure 6.1: Controlling parameters for 2D geometry.

Figure 6.1 shows the modelling of a simple geometry of arc and triangle. The monitor file will contain the set of values for **THETA**, **RLEN**, **XLEN**, **YLEN** and **ARC**. The center node is at (X0, Y0). The user would be able to define all these simple values or using mathematical geometry formula in the monitor file:

$$\text{RLEN} = \text{SQRT}(\text{XLEN}*\text{XLEN} + \text{YLEN}*\text{YLEN})$$

$$\text{ARC} = \text{RLEN}*\text{THETA}*\left(\frac{\pi}{180}\right)$$

Or if XLEN and YLEN are the only unknown values, then

$$\text{YLEN} = \text{RLEN}*\text{SIN}(\text{THETA})$$

$$\text{XLEN} = \text{RLEN}*\text{COS}(\text{THETA})$$

If the unknown parameter is the angle, then THETA can be defined by the expression:

$$\text{THETA} = \text{ATAN}\left(\frac{\text{YLEN}}{\text{XLEN}}\right)$$

Similarly, a slightly more complex pole model shown in Figure 6.2 can also be parameterised. The user could alter the values of

- **DEGMAX** for the pole angle of the model.
- **OUTXRAD, INXRAD** to resize the radial dimension of the magnet.
- **XJRADN** to enable the radius of the air gap to be changed.
- **DEGMIN** to redefine the angle of the magnet pole arc. DEGMIN in this simple example could be made dependent on POLEARC and OUTXRAD by just defining it as DEGMIN = (POLEARC/OUTXRAD)*(180/π) in the file. PARAMETER list. POLEARC could be another calculated parameter.

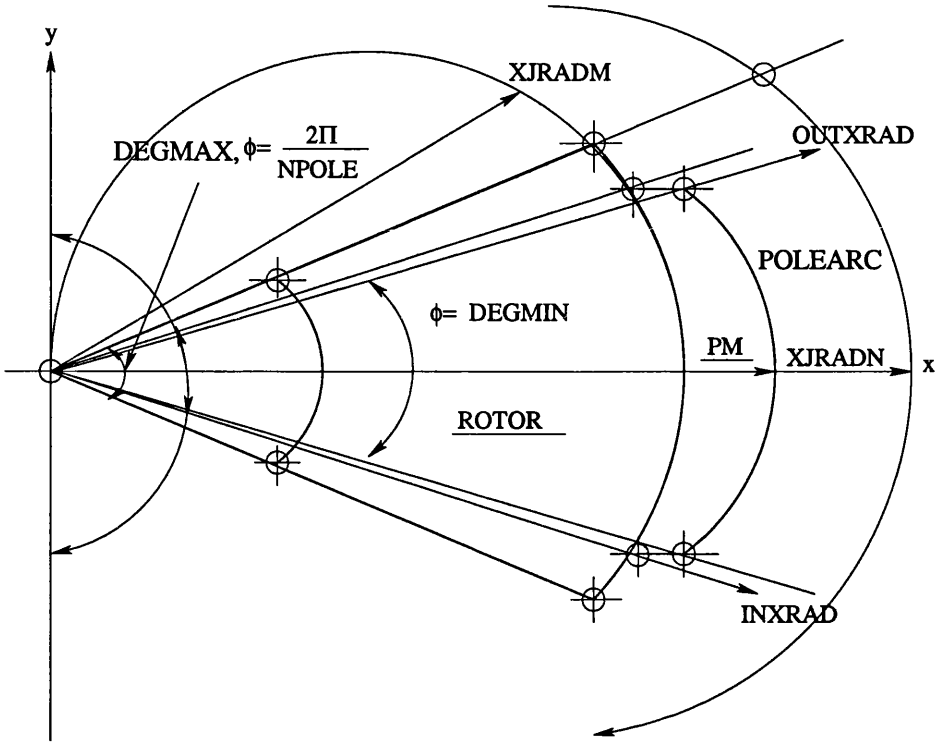

Figure 6.2: Controlling parameters for pole geometry.

General summary of the set of instructions for the Parameterised Templates modelling:

- file.PARAMETER contains the lists of designated variables and values assigned by the user. To create a new model, user will have to edit this file.
- file.MONIT which is the monitor file serves as an archive that records the "history" of the events when the user is creating the mesh and parameterising its variables. Not normally edited.
- file.GEOMONIT contains a series of computer codes. This file is ignored and normally not edited.

To create a new mesh, the user is required to follow closely the subsequent subcommands in *MEGA*:

1. The user begins by opening a new mesh file
   OF - OPEN NEW MESH FILE

2. To edit the parameter file, the user is to read in the file.PARAMETER via the commands

   EP - EDIT PARAMETERS
   RP - READ PARAMETERS

3. Once the editing is finished the new file.PARAMETER can be saved using the command

   WP - WRITE PARAMETERS

4. To regenerate a new model with the altered dimensions use
   AL - ALTER OLD MESH

A new model will be constructed based on the new file.PARAMETER input and dimensions altered easily by the user to home in onto the most optimum device.

6.3 Parameterised Templates for Modelling Permanent Magnet Servo Motor

Cogging torque in a brushless permanent magnet servo motor is used as an example. For a rotating electrical machines problem, it is very convenient to use two distinct meshes, one for the stationary stator, and the other for the moving rotor. The electromagnetic unknowns are coupled across a common interface in the air gap using *Lagrange Multipliers.*

During the meshing process all the radii, angles, tooth width, magnet width etc of the stator and rotor are parameterised so as to provide geometrical flexibility. In this example, 13 parameterised values are implemented for the stator while the rotor has 7 values. An example of the parameterised values in a parameter file is shown in

Tables (6.1) and (6.2). Figure 6.3 and Figure 6.4 show the parameterised values used in describing the geometry of a half stator slot and rotor pole respectively.

Table 6.1: Monitor file for stator mesh.

Parameter No.	Variables.	Values.
1	R-AG	25.5e-3
2	R-ST1	26.0e-3
3	R-ST2	28.0e-3
4	R-ST3	29.0e-3
5	R-SC1	39.7e-3
6	R-SC2	45.0e-3
7	NTEETH	9.0
8	THW	5.25e-3
9	HS	1.25e-3
10	ANGLE1	180/NTEETH
11	ANGLE2	(ANGLE1-ANGLE4)
12	ANGLE3	ASIN(THW/R-ST3)
13	ANGLE4	(HS/R-ST1)*(180/PI)

Obviously more parameters can be used for a more complex geometry. It may be observed from Tables (6.1) and (6.2) that some parameters depend on others, it is often convenient to define some parameters as simple geometric expressions involving some of the other parameters and constants such as π, written as PI in the list. The values of the parameters must be found before use by using an internal calculator in the finite element mesh generator, if this is not available some other program could be used as a preprocessor.

It is important that the calculator is able to deal with finding the values of the parameters if they are presented to it in any order, it is too difficult for a user to present the list in such a way that all the independent parameters are resolved first, followed by all the dependent parameters in the correct order. This is easily carried out by making sure that the calculator passes through the list several times from

Table 6.2: Monitor file for rotor mesh.

Parameter No.	Variables.	Values.
1	R-AG	25.5e-3
2	R-PM	25.0e-3
3	R-RT	22.5e-3
4	R-SH	14.0e-3
5	NPOLE	6.0
6	OUTMAGR	25.0
7	INMAGR	28.2

appropriate starting points.

Other methods for generating values from parameters have been described, among them, algebraic methods [53] and variational geometry methods.[54]. All of these probably have their merits, and any of them could easily be slotted into the template mesh technique described here.

In the FE program, the rotor and stator template mesh would typically consist only of one half pole or half slot pitch. The complete machine (or a periodic section of it) is then created by appropriate duplication of the template mesh. The number of teeth (or magnets etc) required is itself a parameter and therefore, can easily be altered. The user will have the flexibility of changing or redesigning the machine rapidly. Figure 6.5, Figure 6.6, Figure 6.7 show for clarity, how a very coarse mesh was finally transformed into the required finite element model. This gives an idea of the parameters which can be altered [55].

Various slot/pole combinations can be built easily. Figure 6.8, Figure 6.9 and Figure 6.10 are motors with 9/6, 18/6 and 18/8 slots, and poles respectively. In this case, the meshes were generated from a common template mesh by changing just two parameters. The creation process itself took less than one second for each mesh.

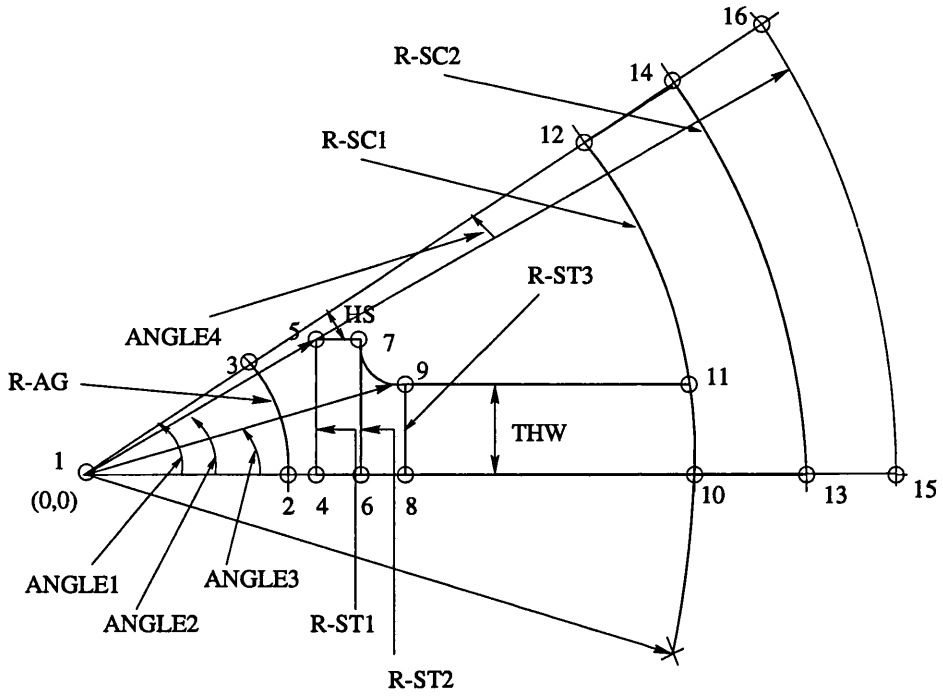

Figure 6.3: Simple geometry of a half stator slot.

There are many combinations of slot/pole numbers that can be used effectively. Figure 6.11 and Figure 6.12 show the 2D predicted results of various slot/pole combinations. The graphs of torque versus rotor position are very easily generated, the amount of rotation and the rotor increment are parameters which can be altered to suit the purpose. The cogging torque is particularly significant when the number of stator slots is an integer multiple of the rotor poles, avoiding this situation is beneficial.

It is also possible to minimise cogging torque by selecting an appropriate magnet pole arc. The width of the arc is significant since the cogging torque is due to the interaction of the edges of the magnet poles and the stator teeth. The overall cogging torque is the summation of all forces at each of the magnet edges. Figure 6.13 shows the 2D predicted cogging torque for the 18 slots/8 poles machine for various different pole arcs.

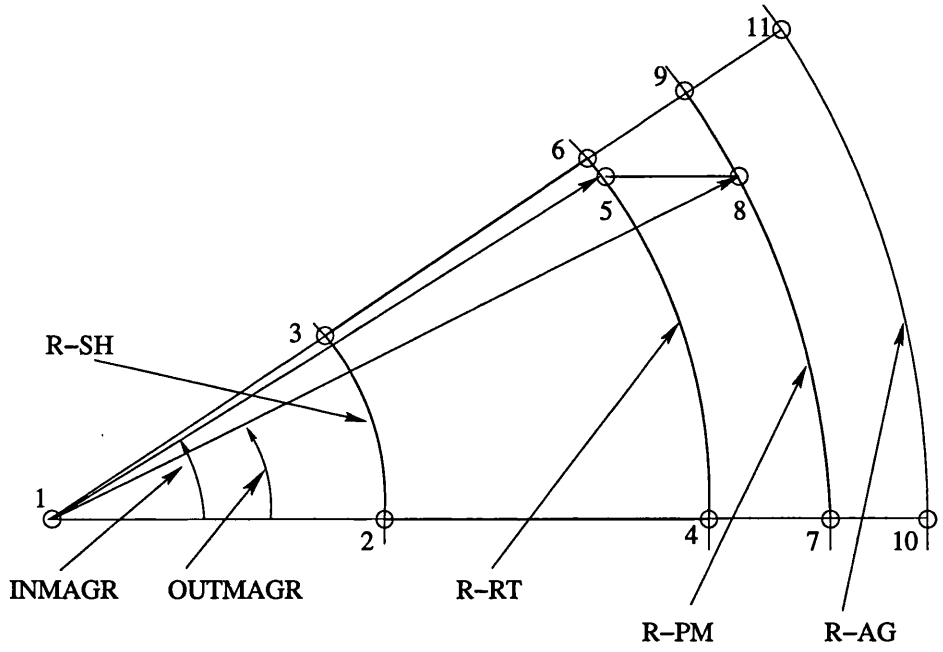

Figure 6.4: Simple geometry of a half rotor pole.

Finally, the 18 slots and 6 poles motor which has the worst cogging torque is expanded into a 3D model and solved. The results in Figure 6.14 show that good agreement is obtained in the 2D and 3D models. To reduce the cogging torque, the stator of the motor is skewed one slot pitch as shown in Figure 6.15. Only one parameter has to be altered in order to change the skew angle in the 3D model, this is possible because the method used in [41] allows the rotor and stator meshes to be incompatible.

Figure 6.16 shows the reduced cogging torque due to the stator skewing technique. The unwanted torque is about 40 times smaller. Skewing has the effect of reducing the permeance variation seen by the rotor magnets and hence, the cogging torque.

This simple and yet effective technique does have its drawbacks. By opting for this technique, losses in the average torque, increased leakage inductance and a more complex motor construction are unavoidable.

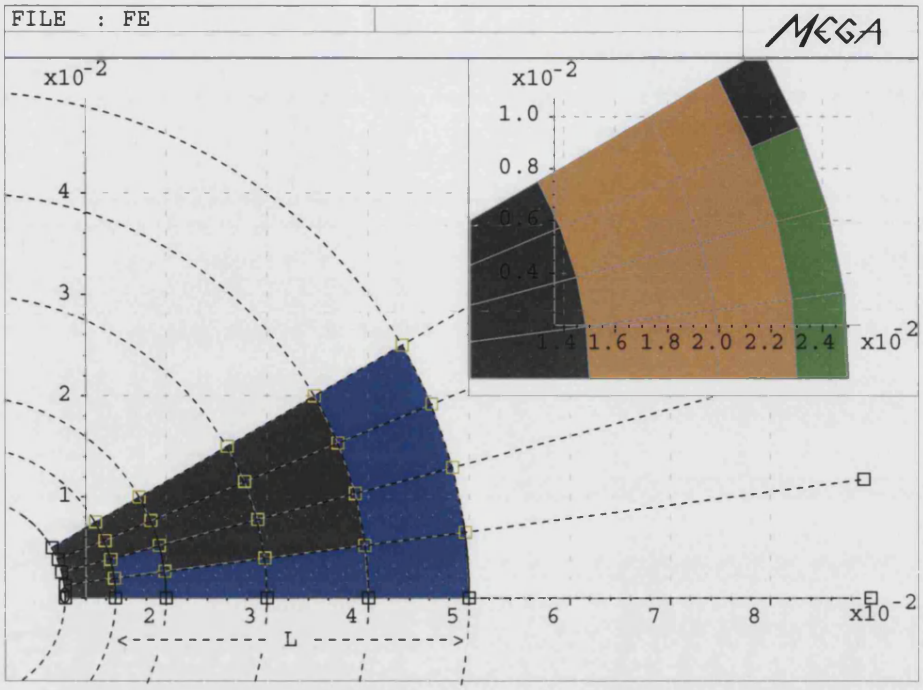

Figure 6.5: Beginning with a coarse mesh.

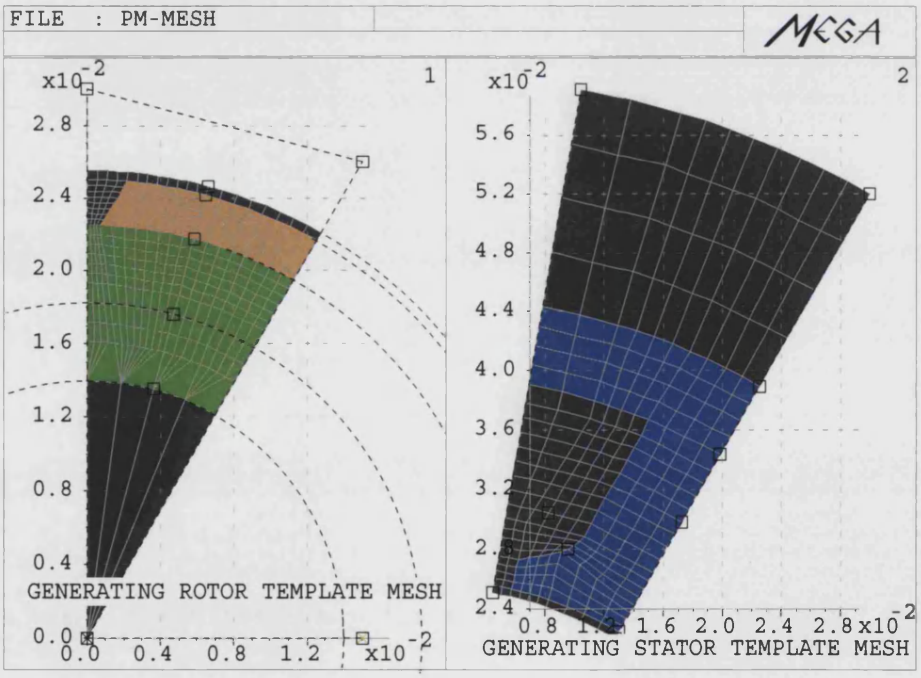

Figure 6.6: Generating templates.

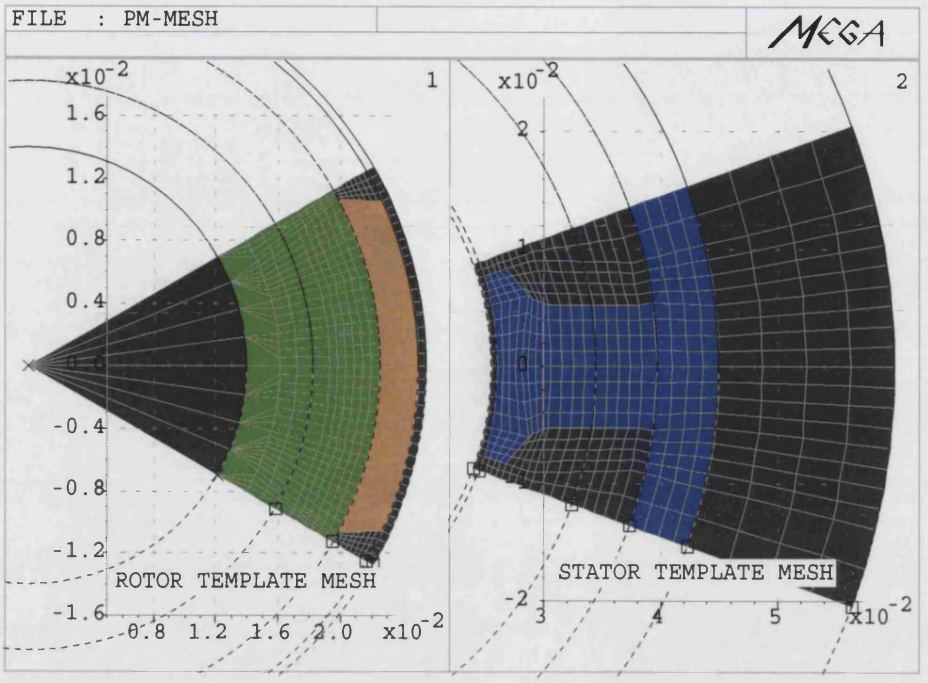

Figure 6.7: Parameterised templates.

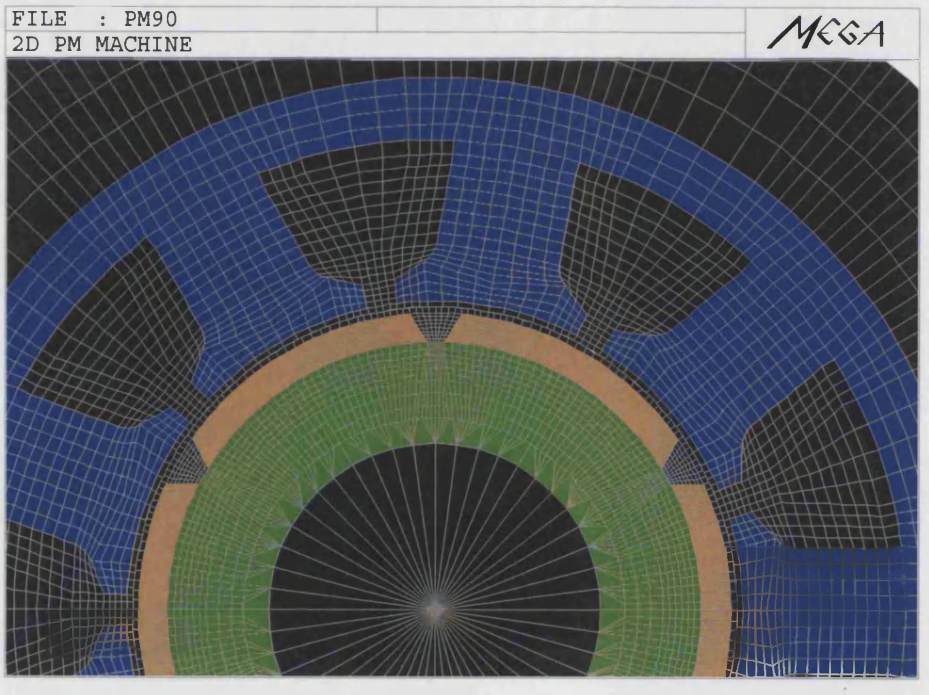

Figure 6.8: 2D FE model of 9 slots and 6 poles motor.

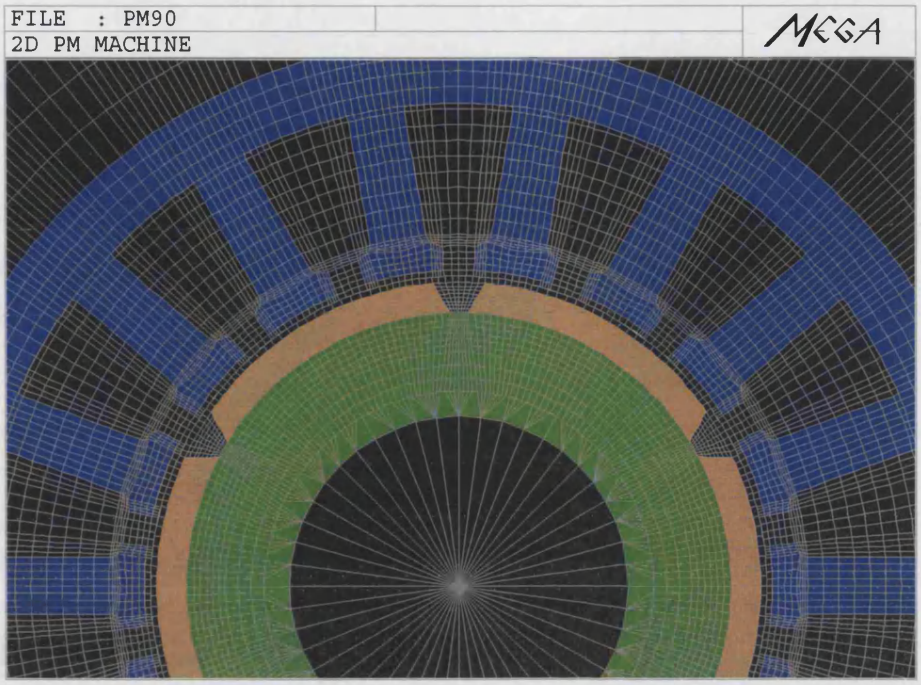

Figure 6.9: 2D FE model of 18 slots and 6 poles motor.

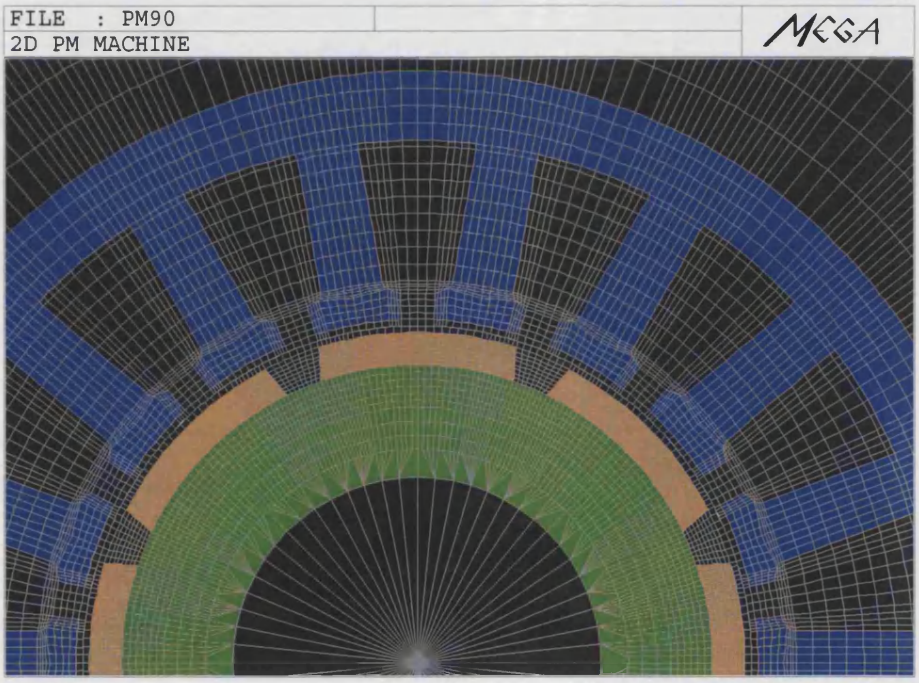

Figure 6.10: 2D FE model of 18 slots and 8 poles motor.

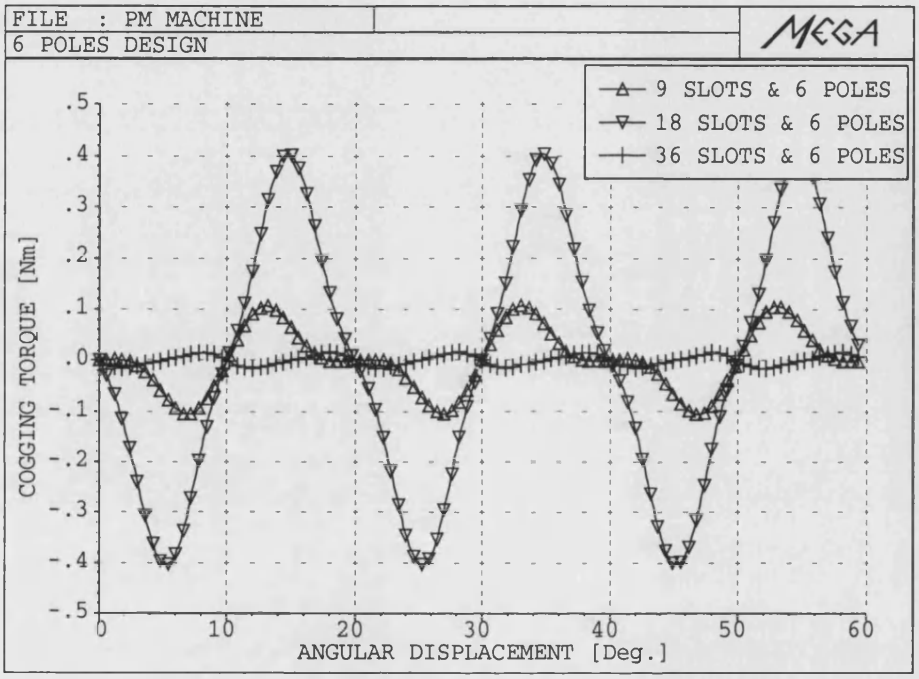

Figure 6.11: Predicted cogging torque for 6 poles motor with three different slot numbers.

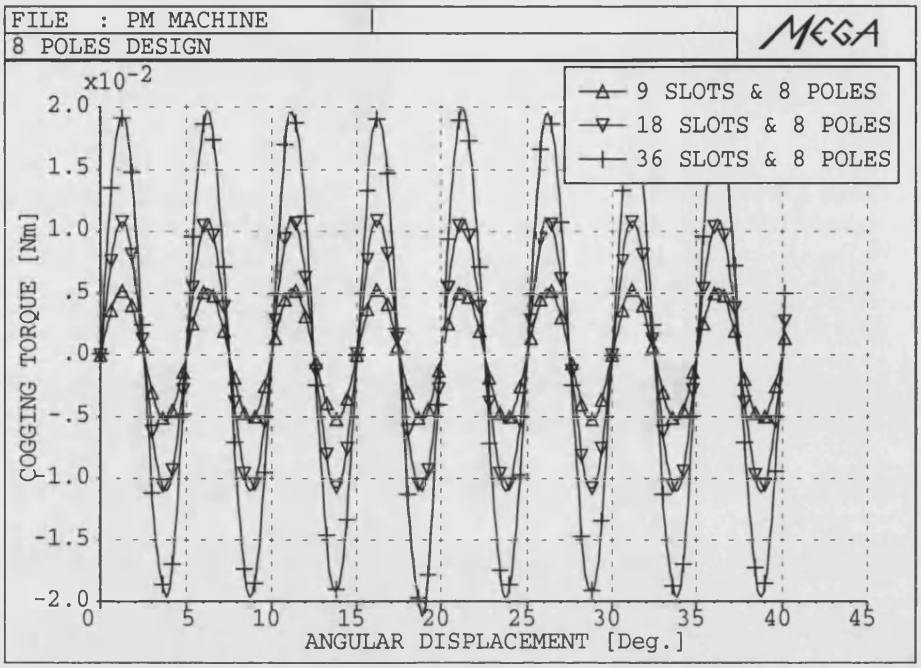

Figure 6.12: Predicted cogging torque for 8 poles motor with three different slot numbers.

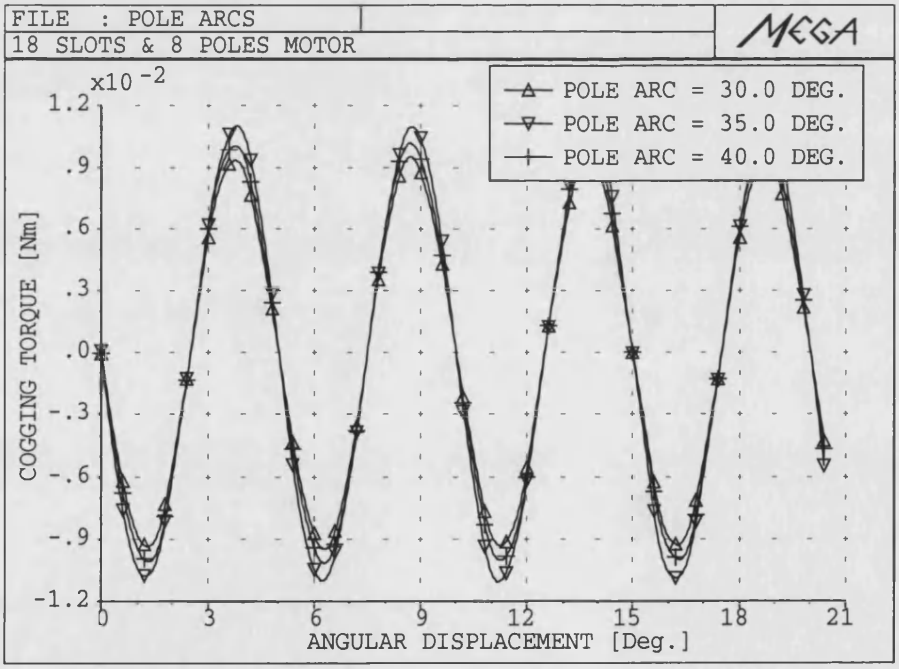

Figure 6.13: Predicted cogging torque for various pole arcs.

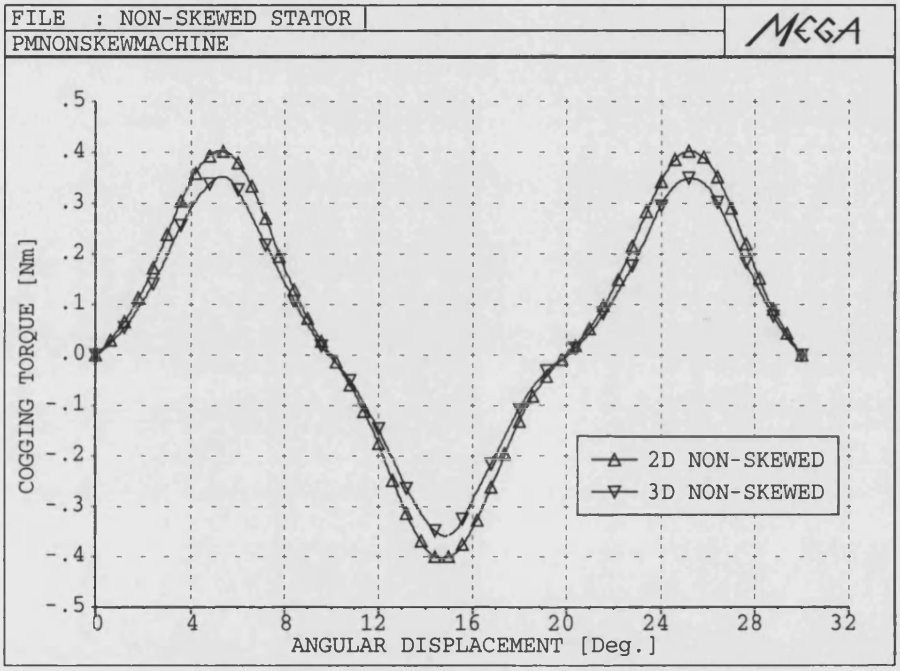

Figure 6.14: Predicted cogging torque for 2D and 3D FE models of non-skewed PM motor.

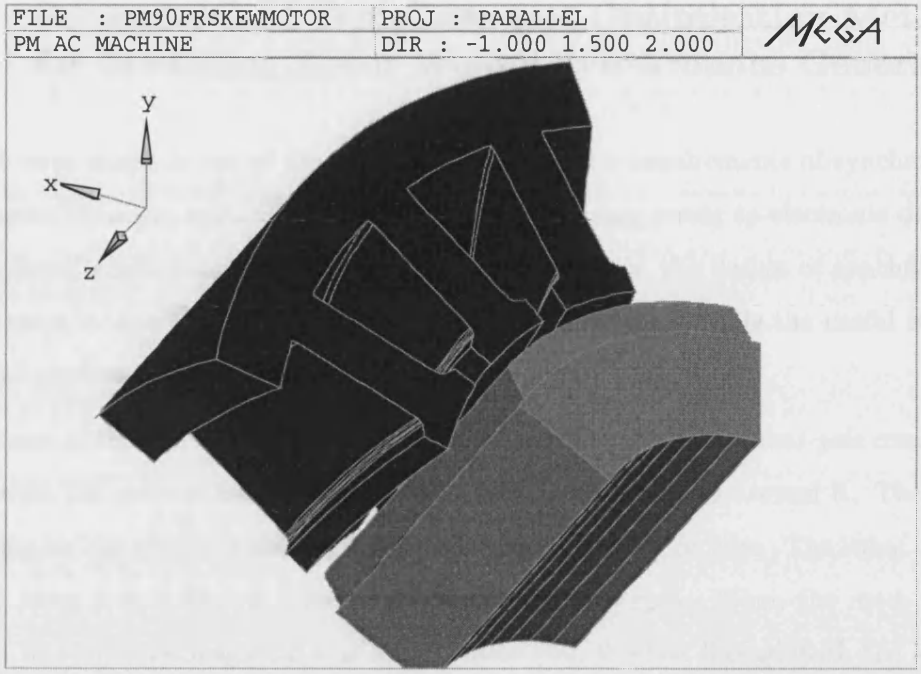

Figure 6.15: 3D FE model of PM motor with skewed stator.

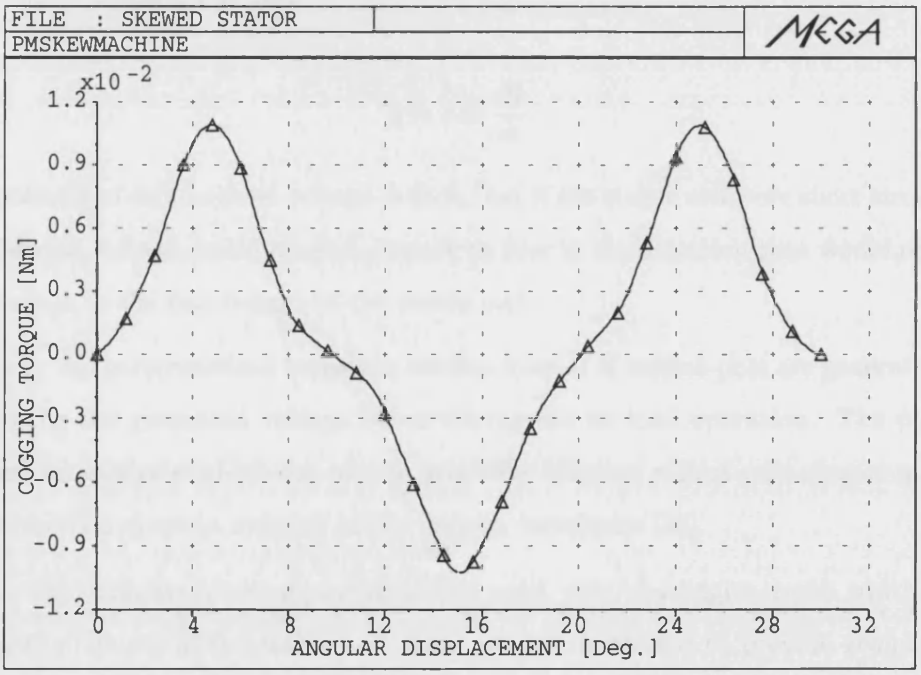

Figure 6.16: Predicted cogging torque for 3D FE model of skewed PM motor.

6.4 Parameterised Templates and Optimisation Method for Modelling Rotor Wound Synchronous Generator

Good wave shape is one of the important performance requirements of synchronous generator for many applications, especially for supplying power to electronic devices and control applications. An important consideration in the design of synchronous generators is that the harmonic effects should be minimised while the useful fundamental generated voltage is made as large as possible.

The rotor of the synchronous generator considered here is of the *salient-pole* construction with DC current being supply to the field winding wound around it. The field winding on the rotor consists of 6 coils, each with a 315 turn wire. The rotor which has 6 poles is spinning at a constant velocity of 8000 rpm. When the rotor poles are in line with the magnetic axis of the stator coil, the flux linkage with the stator N-turn coils is $N\Phi$, where Φ is the air gap flux per pole. According to Faraday's law the induced voltage, e is then

$$e = -N\frac{d\Phi}{dt} \tag{6.1}$$

The polarity of this induced voltage is such that if the stator coil were short circuited, the induced voltage would cause a current to flow in the direction that would oppose any change in the flux linkage of the stator coil.

By using the parameterised template, various shapes of salient-pole are generated for optimising the generated voltage waves during the no load operation. The parameterised templates enabled the user to generate different salient-pole shapes quickly for harmonic reduction analysis in the voltage waveforms [56].

During the template meshing process all the radii, pole/slot angles, tooth width, pole arc, pole pitch etc of the stator and rotor are parameterised to provide geometrical flexibility. A parameterised template with several parameter constraints is shown in

Figure 6.17. These parameterised values are as usual saved in a simple ASCII file. They can either be defined by using simple geometric expressions or input values entered by the user. Some of the parameters involved are defined as expressions in terms of other parameters and constants.

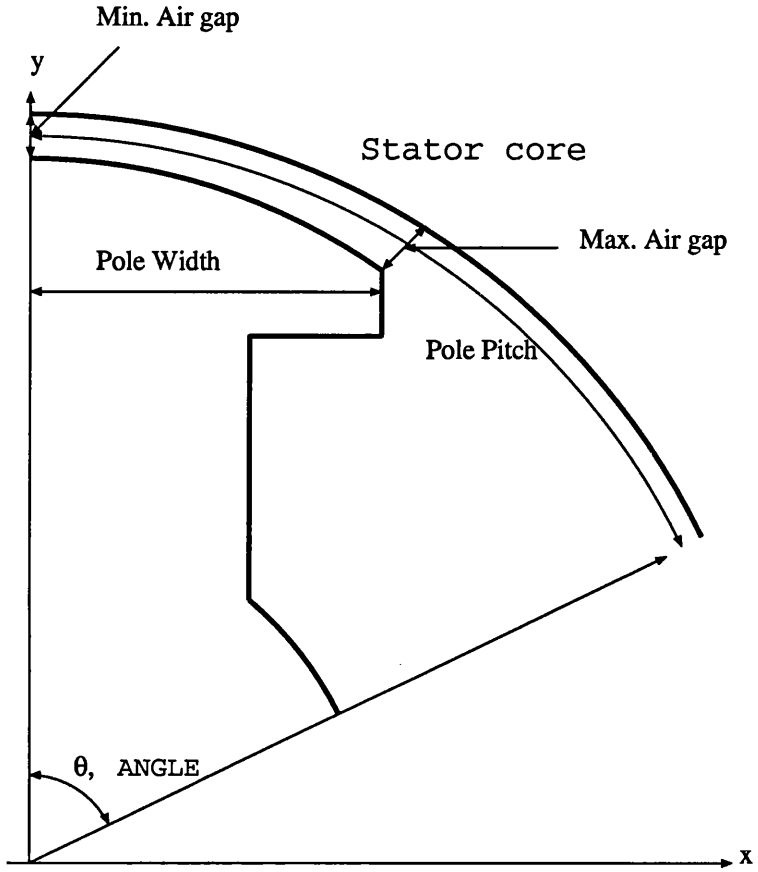

Figure 6.17: Pole configuration.

The rotor and stator templates would typically consist of half a pole/slot pitch or a periodic section of the entire machine. The complete machine is then created by appropriate duplication of the template mesh. The number of rotor poles or stator slots required is itself a parameter and therefore, can be altered easily. This enables the user to rapidly redesign the machine. Results produced by the manual method and one optimisation method, the Nelder Mead Simplex algorithm [57], are compared.

6.4.1 Design Optimisation Technique

In a nutshell: All optimisation algorithms operate on the same basis - given a function $f(x)$ that depends on one or more independent variables, $x = x_1, x_2, x_3, ..., x_n$, find the value for x such that $f(x)$ equals its minimum or maximum value. The function $f(x)$ is referred as the cost or objective function. Often the computational effort is dominated by the cost of evaluating $f(x)$. As such the process should be performed with as few evaluations of $f(x)$ as possible.

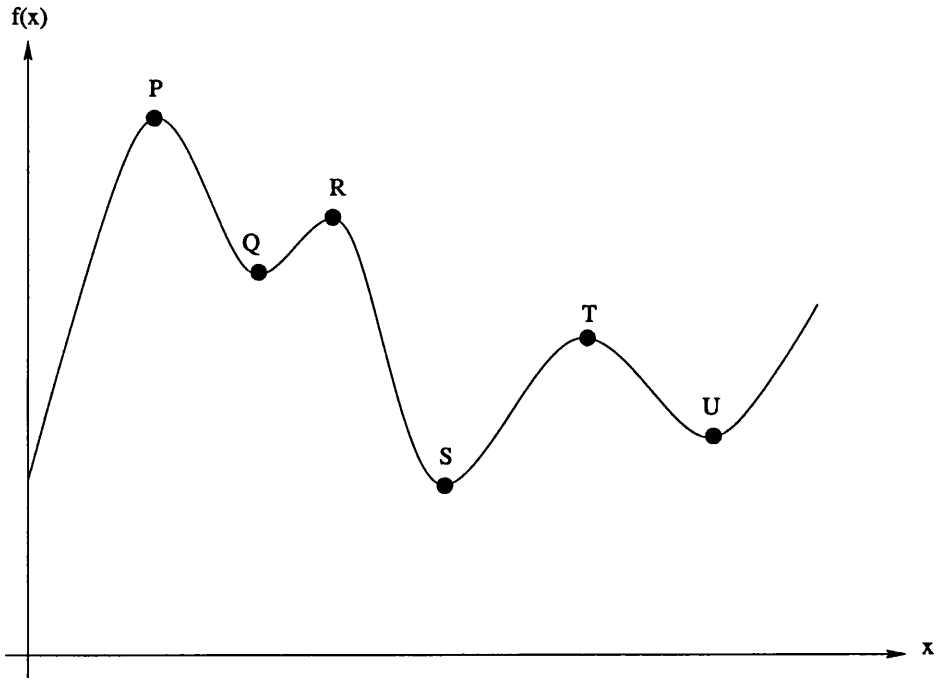

Figure 6.18: Global and local extrema.

A maximum or minimum point can be either *global* or *local*. According to Figure 6.18, points R and T are known as the local maxima and not global maxima. The global maximum is located at point P. The global minimum is at S while Q and U are the local minimum.

Naturally it is desirable to find the global extremum but this represents, in general, a very difficult problem. Normally, the usual possibility to circumvent this problem

is to find the local extrema starting from a widely random chosen initial values of the independent variables and select the most extreme of these. The confidence on the method accuracy can be further enhanced if the local optimiser routine always converge to the same point after being perturbed.

Global optimisation schemes generally employ an element of randomness to enable them to jump out of the local extremum. If the objective function $\boldsymbol{f}(x)$ is known to have a single maximum or minimum, which is rarely the case for problems with conflicting goals, a local optimisation will be adequate to solve the problem.

There is no perfect optimisation schemes, suitable for all problems. The choice of method is based on whether the case is one-dimensional or multidimensional, and methods that need only the evaluations of the function or methods that also require the evaluations of the function's derivative.

The Downhill Simplex Method of Nelder and Mead is used to optimise the wave shape of the induced voltage of a synchronous generator subjected to several constraints. This algorithm requires only the function evaluations and not derivatives. A *simplex* is the geometrical figure consisting of, in N-dimension, N+1 points with all their interconnecting line segments and polygonal facets. In another word, a *simplex* is simply a triangle in 2D or in the case of 3D, a tetrahedron.

The Downhill Simplex algorithm is initialised with N+1 points defining an initial simplex. The algorithm then takes a series of steps moving downhill through the N-dimension topography until it reaches a local minimum. These 'moving downhill steps', known as reflections, are just the algorithm way of moving the point of the simplex where the function is largest to a lower point through the opposite face of the simplex. These steps are constructed to conserve the volume of the simplex and hence, guarantee its non-degeneracy. An outline of this method can be found in chap.10 of [58].

6.4.2 Human Controlled Design

The object of a good design includes maximising the first harmonic voltage while also minimising the amplitudes of all the other harmonics. A human designer soon becomes swamped if the number of variables in a design problem is high. Here, the problem is simplified by using a classical design method [59] which uses experience and analytical techniques to describe the problem in terms of three variables.

In designing the synchronous generator, the pole shapes are constrained by the following three variables:

$$Var.X = \left[\frac{Pole\ Width}{Pole\ Pitch}\right] \qquad 0.50 \leq Var.X \leq 0.75$$

$$Var.Y = \left[\frac{Max.\ Air\ gap}{Min.\ Air\ gap}\right] \qquad 1.0 \leq Var.Y \leq 3.0$$

$$Var.Z = \left[\frac{Min.\ Air\ gap}{Pole\ Pitch}\right] \qquad 0.01 \leq Var.Z \leq 0.05$$

The pole surface is constrained to be of cylindrical shape, the dimensions of which are defined by the max. and min. air gaps shown in Figure 6.17. For machines with a small air gap, $Var.Z$ can be fixed. $Var.Z$ is maintained at 0.015 throughout the investigation, as recommended in [60]. These three variables are parameterised and stored in the geometry monitor file. Changes in one of the ratios results in a new generator pole with the required pole pitch, pole arc and air gap size. Different pole shapes are generated easily for harmonic analysis of the induced voltage at no load.

The triplen harmonics {3rd harmonic and multiples of it} can be ignored since they virtually cancel each other out at the terminals of the 3-phase Y-connected generator. Since even harmonics do not exist and triplen harmonics are naturally cancelled, we are left with the 'belt harmonics' of 5th and 7th, and 'slot harmonics' of 11th and

13th. A fractional coil pitch design has greatly reduced the 5th and 7th harmonics. The slot harmonics of 11th and 13th cannot be suppressed by a coil short pitching and distribution method. Using pole surface shaping, we hope to suppress the slot harmonics and achieve a further reduction in the belt harmonics without having to rearrange the coil structure.

Twenty five designs were generated, with $Var.X$ and $Var.Y$ varying as shown in Figures 6.19 - 6.23. The **B-H** characteristics of the iron parts were non-linear (provided in Appendix D).

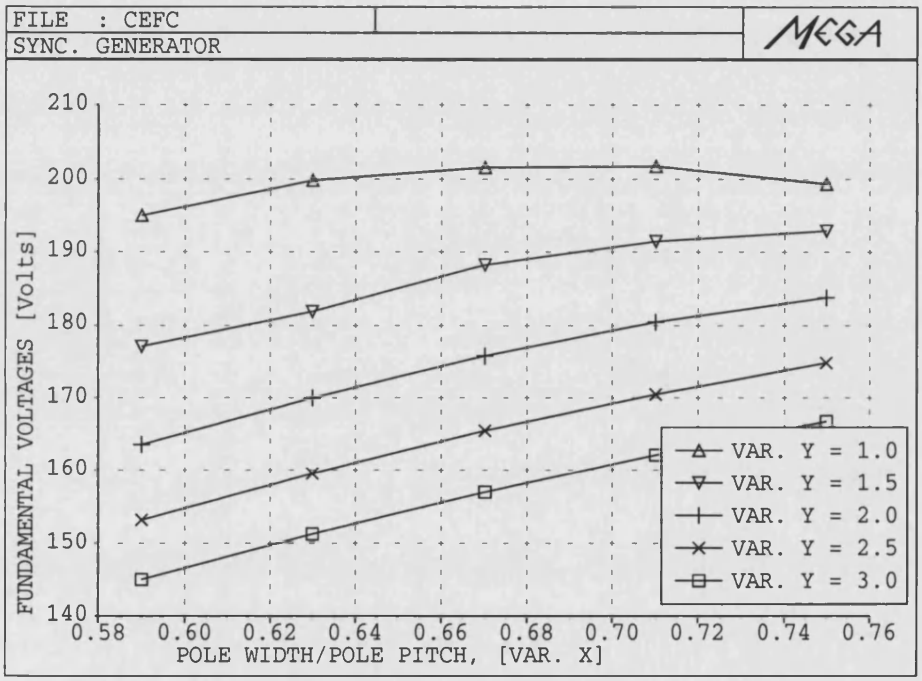

Figure 6.19: Generated fundamental voltages.

Figure 6.19 shows the generated fundamental voltages while Figure 6.20, Figure 6.21, Figure 6.22 and Figure 6.23 show the harmonic voltages. A large reduction of harmonic voltages is achieved especially in the 11th harmonic when $Var.X = 0.71$.

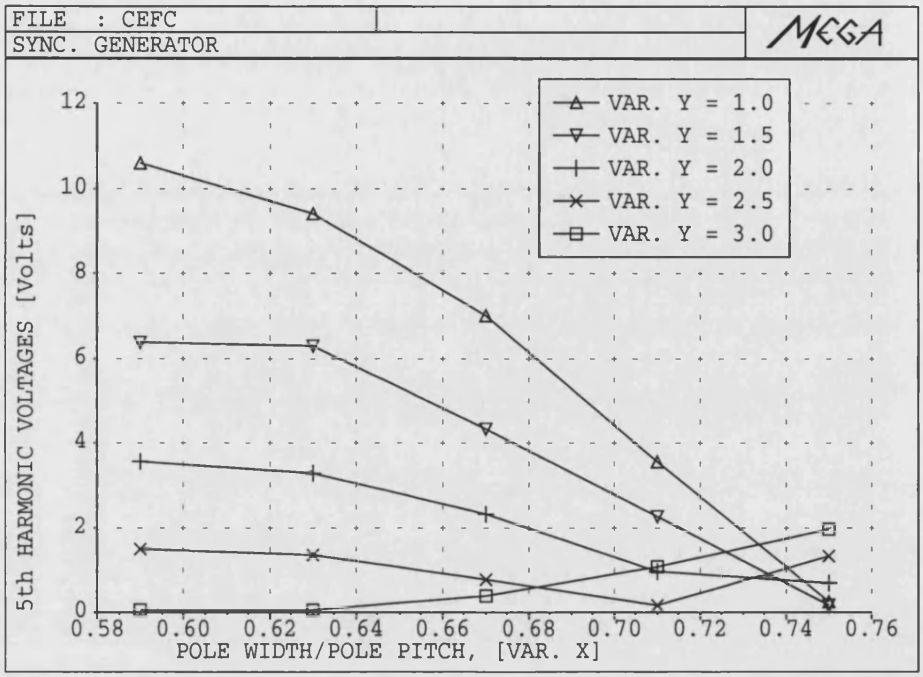

Figure 6.20: Generated 5th harmonic voltages.

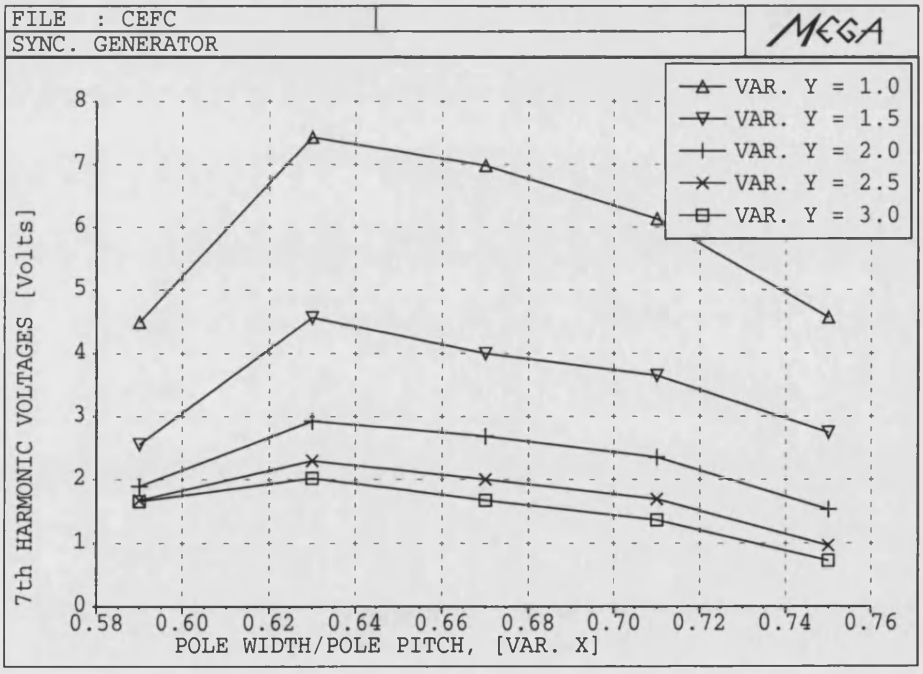

Figure 6.21: Generated 7th harmonic voltages.

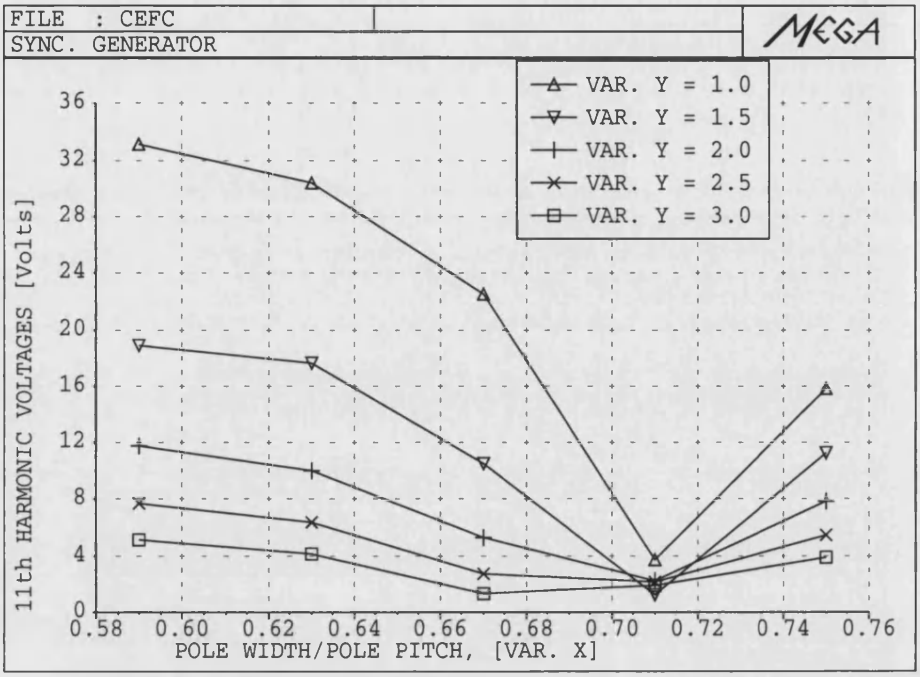

Figure 6.22: Generated 11th harmonic voltages.

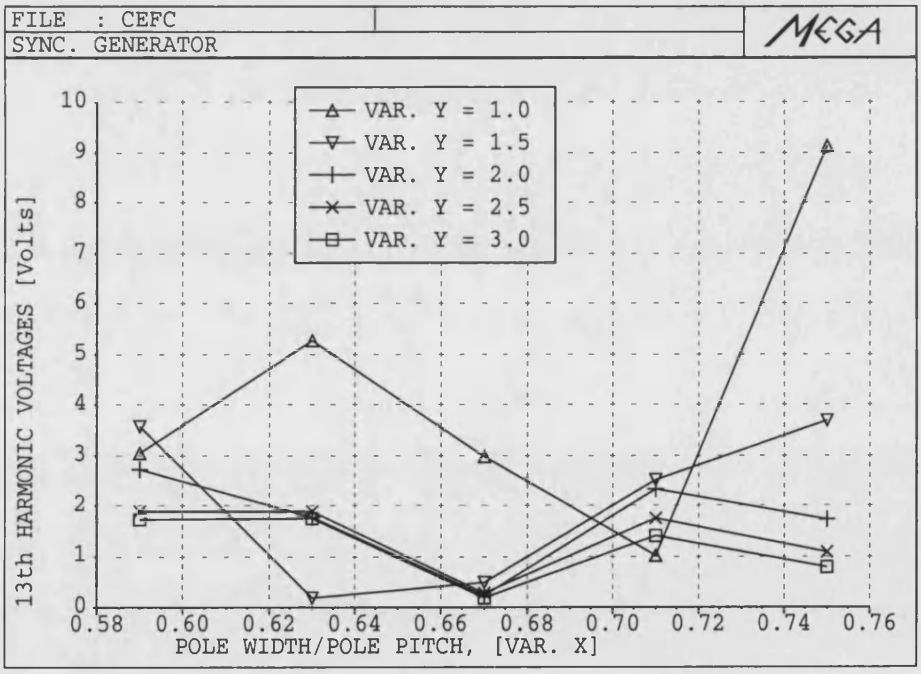

Figure 6.23: Generated 13th harmonic voltages.

However, the magnitude of the fundamental voltages generated are lower. A trade-off between harmonic reduction and fundamental magnitude of generated voltage has to be found.

Table 6.3: % Total Harmonic Distortion.

	Var.Y				
Var.X	1.0	1.5	2.0	2.5	3.0
0.59	18.1	11.5	7.8	5.4	3.9
0.63	16.6	10.6	6.5	4.5	3.3
0.67	12.3	6.4	3.6	2.1	1.4
0.71	4.0	2.7	2.3	1.9	1.8
0.75	9.5	6.3	4.5	3.3	2.7

Table(6.3) shows the percentage of the Total Harmonic Distortion (**THD**) of the generated voltages. **% THD** is defined as

$$\% \ \mathbf{THD} = \frac{1}{V_1}\left(\sqrt{\sum_{h\neq 1}^{\infty} {V_h}^2}\right) \times 100 \tag{6.2}$$

where V_1 is the fundamental RMS value of voltage and V_h is the harmonic RMS values of voltage.

Using the information in Table(6.3), a machine designer would probably choose values of $Var.X$ and $Var.Y$ around 0.71 and 3.0 respectively.

All the models so far are in 2D, for 3D modelling the 2D mesh is used as a base plane and extruded into the required length. Figure 6.24 shows the complete model with coils placed in the stator and rotor. The rotor's magnetic flux is shown in Figure 6.25. Figure 6.26 compares the generated voltages of the 2D and 3D finite element models for $Var.X = 0.71$ and $Var.Y = 3.0$. It may be observed that the finite length effects in the 3D model give rise to slightly different results from 2D, but that the effects are not large. The results suggest that a good design strategy would be to use 2D models to 'home in' close to an optimal design, and then use 3D to finish the study.

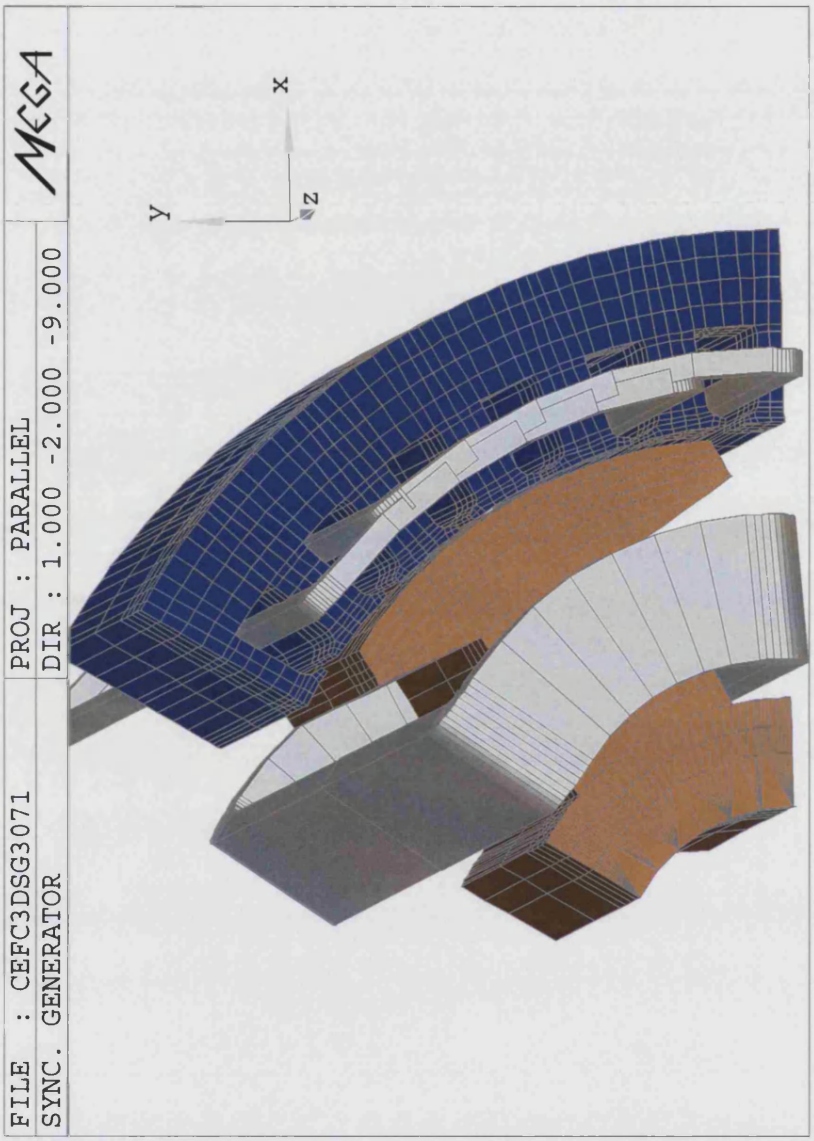

Figure 6.24: Wound rotor generator.

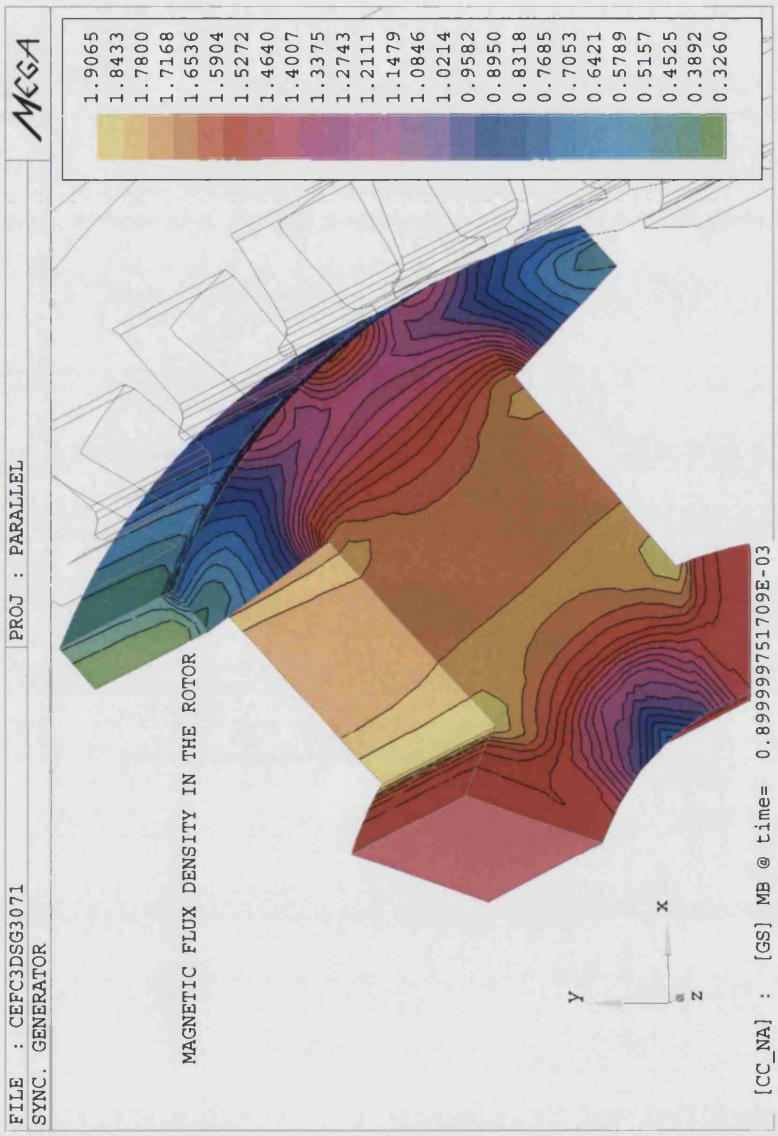

Figure 6.25: Magnetic flux density in the rotor.

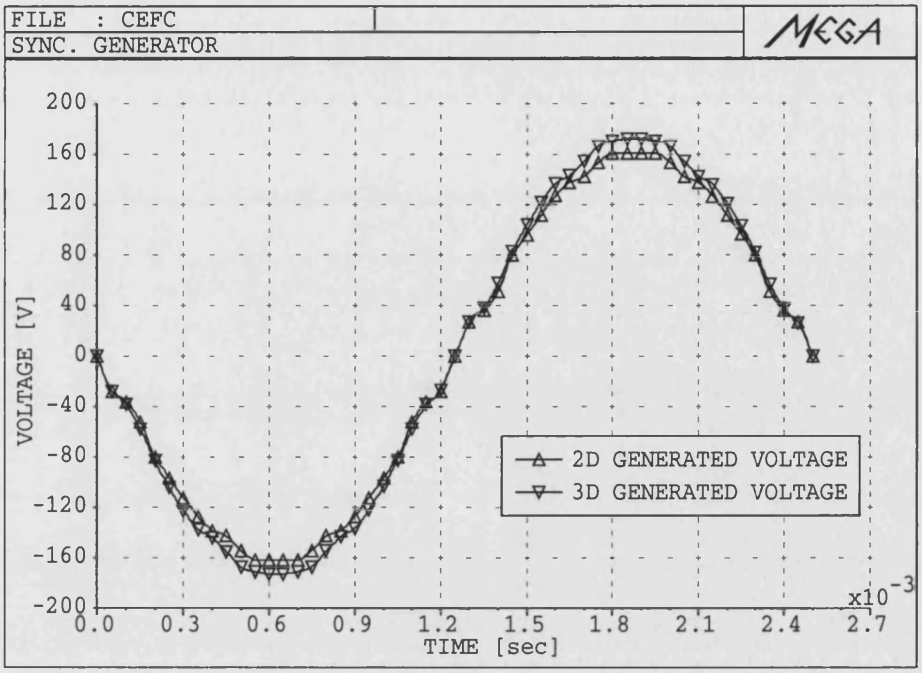

Figure 6.26: Calculated induced voltages.

6.4.3 Computer Controlled Design

The variables $Var.X$ and $Var.Y$ were also optimised by a fully automated optimisation technique using the Downhill Simplex algorithm [57]. The quantity to minimise is the **THD** in (6.2). Our finite element program is used to evaluate the objective function at the sampling point generated by the optimisation program. This involves, for each step of the optimisation, setting up a mesh according to the latest information, solving the problem, and post-processing the result using the interactive post-processing program. All of this is controlled by simple scripts and requires no intervention once started.

Table(6.4) shows the initial value of **THD** at the corner of the starting simplex and also the final value. Figure 6.27 shows how the value of the objective function decreases with the optimisation iterations. This shows that the automated system predicts an optimum in the same area as a machine designer would. The optimum is

of course lower in the former case, since the 'human' optimum found in the previous section is based on a fairly coarse sweep of the available parameters.

Table 6.4: Showing the starting and finishing sampling points.

	$Var.X$	$Var.Y$	THD
Starting corner 1	0.7	2.0	0.0367
Starting corner 2	0.72	1.8	0.0515
Starting corner 3	0.74	1.6	0.0701
Final	0.696	2.041	0.0322

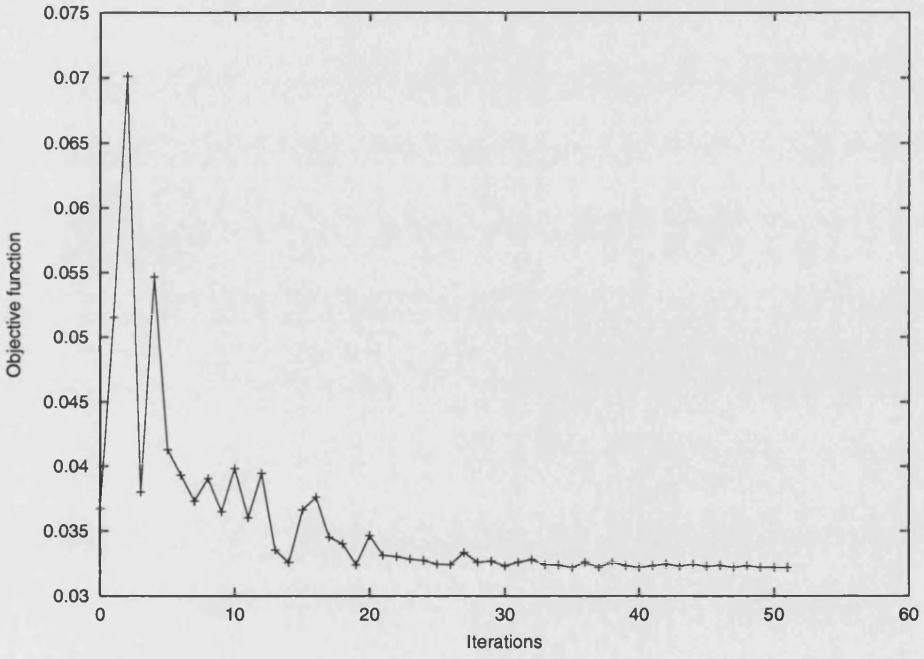

Figure 6.27: Decrease of the objective function.

Optimising only the **THD** as in (6.2) resulted in a fairly low value of first harmonic, around 160-170 Volts. The optimisation scheme was run again, allowing $Var.X$, $Var.Y$ and $Var.Z$ to vary. The objective was to minimise **THD** and also to maximise the fundamental component. This resulted in values of $Var.X$, $Var.Y$, $Var.Z$ and fundamental of voltage to be 0.51, 1.0, 0.01 and 208 respectively.

6.5 Fluxset Sensor

The Fluxset sensor is described in [61], it consists of a driving solenoid and pick up coil, concentric with a metallic glass core. Figure 6.28 shows the 3D FE model.

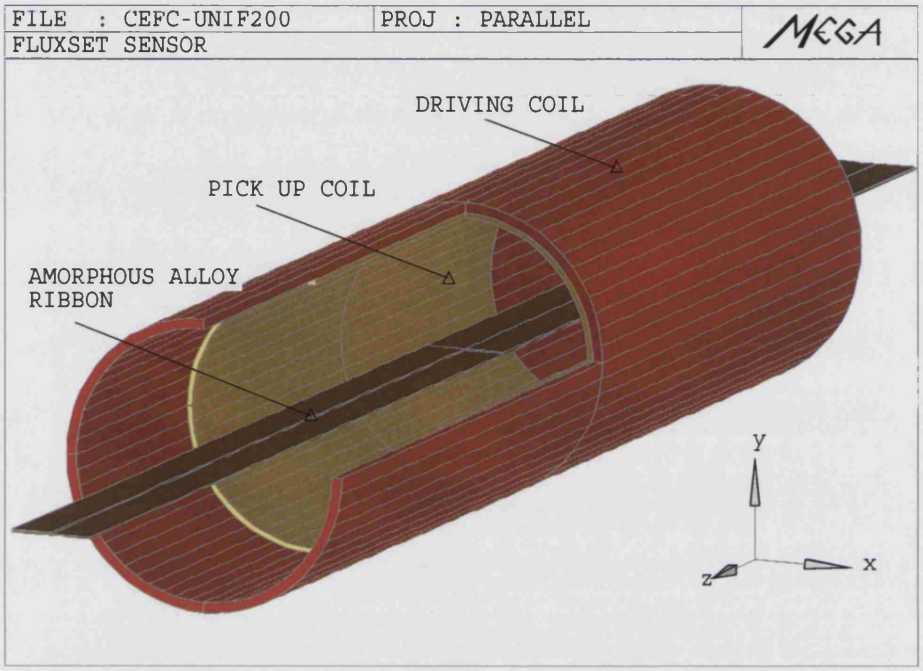

Figure 6.28: Fluxset sensor.

The non-conducting regions are modelled using the magnetic scalar potential ψ and solved as

$$\nabla \cdot \mu \nabla \psi = 0 \tag{6.3}$$

while the conducting regions are modelled using the magnetic vector potential $\boldsymbol{A}$ and solved as

$$\nabla \times \frac{1}{\mu} \nabla \times \boldsymbol{A} = -\sigma \frac{\partial \boldsymbol{A}}{\partial t} \tag{6.4}$$

For the thin ribbon, it is economical to use the thin sheet formulation since thin elements are required. Modelling the ribbon as a thin sheet will avoid an excessively fine and ill-conditioned mesh. Applying the usual Galerkin method to the Laplace equation gives,

$$\int_{\Omega} \nabla N \cdot \mu \nabla \psi = \oint_{\Gamma} \mu \frac{\partial \psi}{\partial n} \mathrm{d}\Gamma \tag{6.5}$$

In a thin region, the volume integral in equation (6.5) is replaced by

$$\int H \left[\frac{\partial N}{\partial \Gamma_x} \mu \frac{\partial \psi}{\partial \Gamma_x} + \frac{\partial N}{\partial \Gamma_y} \mu \frac{\partial \psi}{\partial \Gamma_y} \right] \mathrm{d}\Gamma_x \, \mathrm{d}\Gamma_y \tag{6.6}$$

In equation (6.6) Γ_x and Γ_y are two tangential directions on the thin region surface and H is the thickness of the thin region.

The core in [62] has an approximately piecewise linear **B-H** curve of $\mu_r = 85000$ for $|B| < 0.65$ T and $\mu_r = 1.0$ thereafter. The driving solenoid is fed with current with a triangular waveform, an external field produces more saturation in one direction along the ribbon than the other, hence a time shift in induced *e.m.f* which can be measured.

The device was modelled using the parameterised templates technique, while immersed in an axial external field of $200\,\mu$T. In optimising the design, only the ribbon length is varied. Results for the average flux in the pick up coil are shown in Figure 6.29. Since the pick up coil voltage depends on the time differential of this flux, it may be observed that more signal results from the longer core. Although a 3D mesh is required, the template method simplified this process greatly, as it only had to be generated once.

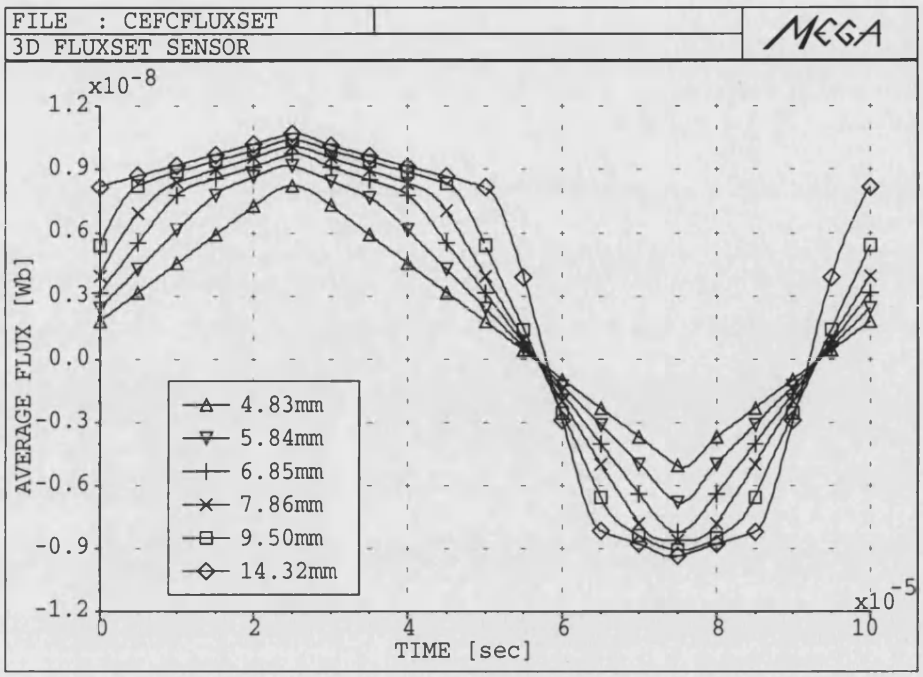

Figure 6.29: Average flux in the pick up coil.

6.6 Summary

A parameterisation technique is described. The geometrical dimensions can be altered rapidly for designing various types of electromagnetic device. The method should be useful in both manual and computer controlled optimisation.

As examples, the technique is used to address a major concern in permanent magnet machines; cogging torque, and harmonic reduction in synchronous generator's induced voltage. The ability of the parameterisation technique to rapidly alter machine dimensions enables designers to examine various options quickly by using old fashioned 'cut and try' methods. The technique can also be easily used along with a computer optimisation method so that designs can be automatically generated.

The method differs from most others in that the mesh can be generated using any technique, anything from a full automatic mesh generator to manual methods can be used. This allows the user a great deal of control over mesh quality, once a good mesh

is created it can be recycled for similar geometries.

A disadvantage of the method is that all the meshes derived from a given template will be topologically similar to it, this means that designs which differ greatly from each other cannot be generated.

The finite element method has been used for many years for optimisation. It is usually very easy to move a few nodes (particularly in 2D), but other changes can be very awkward. The method described here makes it easy to make global changes to a mesh, such as altering the number of teeth, pole pitch etc. It is therefore useful for electrical machine design, based on either computer controlled optimisation or on design studies based on running many cases.

Chapter 7

Some Practical Applications of Parameterised Templates in Modelling Linear Induction and PM Machines

7.1 Introduction

Electrical machines and other electromagnetic devices can be difficult to model using finite elements. They are usually constructed from magnetic materials which are non-linear and have complex geometry. In addition, rotational or translational movement is involved and machines are usually coupled to external circuitry and a dynamic load. The previous chapter have shown how a parameterised technique coupled with optimisation can be implemented for 2D and 3D finite elements modelling of electromagnetic devices.

The technique has been implemented into *MEGA* and in this chapter, the effectives of the parameterised technique and its designing capability will be examined closely. In particular, the method will be applied in the modelling of two types of linear electrical machine: linear permanent magnet machine and linear induction machine [63].

There are two basic approaches to modelling the electromagnetic behaviour of moving conductors. If the moving region does not vary in cross-section at the right angles to the direction of motion or "smooth", the *Minkowski transformation* can be used to introduce the effect of motion [64], [65]. On the contrary, if the moving region is "unsmooth" the *Lagrange Multipliers* method is used together with a time-transient scheme which track the moving conductors through space with a mesh which moves in the exact way as the real device moves in reality.

The linear PM machine has a slightly complicated stator and moving component (rotor). The stator and rotor have "notched surface" with coils on the stator and permanent magnets on the rotor. The incompatible regions were meshed up separately before joining at an interface using the *Lagrange Multipliers* method. The model was solved using a transient time-stepping method.

The linear induction machine on the other hand has a smooth moving conductor which enable the application of *Minkowski transformation* in the modelling of the machine movement. For this case in contrast to reality, the conducting aluminium track was modelled as the moving region while the armature of the linear machine was kept stationary.

Some aspect of the machines behaviours are studied here with two experimental linear tracks specially designed and built for evaluation. The *MEGA* software used to design the machine has been validated against experiments carried out on the two linear electrical machines.

7.2 Finite Element Modelling

7.2.1 Modelling Non-smooth Moving Conductor Regions

If the moving conductor cross-section normal to the direction of movement is not invariant, as in the case of linear permanent magnet machines or servo motors, no steady-state solution is possible. In cases like these, a time-transient solution is required and the moving components must be meshed at each time-step [66].

In this chapter, a linear PM machine was modelled using this technique. The linear PM machine was modelled using two separate meshes: stationary part and moving part. The air gap is 3 mm wide. To ensure the continuity of the normal flux $\boldsymbol{B} \cdot \hat{\mathbf{n}}$ and tangential $\boldsymbol{H} \times \hat{\mathbf{n}}$ across the interface at the air gap, the unknown potentials $\boldsymbol{A}(z)$ on the stationary mesh and $\grave{\boldsymbol{A}}(\grave{z})$ on the moving mesh need to be coupled.

The *Lagrange Multipliers* method was used to mesh up the moving carriage and the stationary track. z and $\grave{z}$ are positions measured in the two different frames of reference. If the relative displacement between the two meshes is δz the coupling is therefore

$$\boldsymbol{A}(z) = \grave{\boldsymbol{A}}(z - \delta z) \tag{7.1}$$

The Lagrangian method is used to weakly enforced $\boldsymbol{A}(z) = \grave{\boldsymbol{A}}(\grave{z})$ using a set of weighting functions, W_i which is associated with the *Lagrange Multipliers*

$$\int W_i(z)[\boldsymbol{A}(z) - \grave{\boldsymbol{A}}(z - \delta z)]\,\mathrm{d}z = 0 \tag{7.2}$$

7.2.2 Modelling Smooth Moving Conductor Regions

In the modelling of linear induction machine, the major advantage is the possibility of modelling the moving carriage using the *Minkowski* method since the model fulfilled the major criteria of being invariant in cross-section of the moving component or *smooth*.

The velocity is taken care of by modifying the $\boldsymbol{E}$ field by adding a $\boldsymbol{u} \times \boldsymbol{B}$ term, where $\boldsymbol{u}$ is the velocity term. Therefore, the governing equations are the usual

$$\nabla \times \frac{1}{\mu} \nabla \times \boldsymbol{A} = -\sigma \left(\frac{\partial \boldsymbol{A}}{\partial t} + \nabla V - \boldsymbol{u} \times \nabla \times \boldsymbol{A} \right) \tag{7.3}$$

$$\nabla \cdot \sigma \left(\frac{\partial \boldsymbol{A}}{\partial t} + \nabla V - \boldsymbol{u} \times \nabla \times \boldsymbol{A} \right) = 0 \tag{7.4}$$

The method is economical in the sense that under these conditions only steady-state solution is required. However, the resulting equations are asymmetric and often Galerkin's upwinding technique is required to obtain a solution.

7.2.3 Periodic Boundary Conditions

Modelling electrical machines and electromagnetic devices based on their symmetrical configurations could lead to significant computational savings. This section of the chapter deals with the periodicity, which is a function of the device shape and the state of the field within it.

Periodic boundary conditions have long been exploited in finite elements for modelling electromagnetics. In general, if periodic boundary conditions exist on some parts of a device, a relationship between some boundaries is implied and of the form

$$slave\,variable = \overline{P} * master\,variable \tag{7.5}$$

Only the master variable appear as degrees of freedom, the slave variables are totally dependent on the master variables. For scalar and vector variables at a periodic note, the slave variables are relate to master variable using a transformation matrix and a periodic parameter;

$$\psi_{slave} = \overline{P}\, \psi_{master} \tag{7.6}$$

$$\begin{bmatrix} A_x \\ A_y \\ A_z \end{bmatrix}_{slave} = \overline{P} \begin{bmatrix} \ell_{xx} & \ell_{xy} & \ell_{xz} \\ \ell_{yx} & \ell_{yy} & \ell_{yz} \\ \ell_{zx} & \ell_{zy} & \ell_{zz} \end{bmatrix} \begin{bmatrix} A_x \\ A_y \\ A_z \end{bmatrix}_{master} \tag{7.7}$$

The transformation matrix rotates the slave vector to realign it to the master component [67]. In a typical electrical machine model, the information required for the formation of the periodic constraints are the location of the axis of rotational or translation symmetry together with a defined master-slave boundary and the degrees of electrical and mechanical differences.

7.3 Treatment of External Circuits

MEGA has the facility which allows the finite element model to be connected to an external circuit through *'ports'* [68]. These ports are basically terminals which can be in turn connected to other *'circuit branches'* consisting of more fundamental circuit element like capacitors, inductors, resistors and diodes.

The finite element method typically gives a system of equations for the magnetic field model connected to two ports, 1 and 2 in the form

$$\begin{bmatrix} \boldsymbol{K} & \boldsymbol{Y} & 0 & 0 \\ \boldsymbol{Y}^T & \boldsymbol{X} & -1 & 1 \\ 0 & -1 & 0 & 0 \\ 0 & 1 & 0 & 0 \end{bmatrix} \begin{bmatrix} \mathbf{A} - \psi \\ I_a \\ \int V_1 \\ \int V_2 \end{bmatrix} = \begin{bmatrix} 0 \\ 0 \\ I_1 \\ I_2 \end{bmatrix} \tag{7.8}$$

where $\boldsymbol{K}$ is the normal finite element matrix, $\boldsymbol{Y}$ contains basic circuit elements like resistors, capacitors, $\boldsymbol{Y}^T$ is the *e.m.f* and column $\boldsymbol{X}$ expresses the source due to the unknown current I_a. The last two rows in the matrix equations represent the Kirchhoff's current law in open circuit with injected currents I_1 and I_2.

7.4 Design of Linear Permanent Magnet Machine

7.4.1 General Description

There is an increasing demand for controlled high speed linear motion over a long track. In this region, the linear brushless permanent magnet (PM) machine offers significant advantages in terms of efficiency, positional accuracy and speed control. However, linear PM machine can exhibit significant cogging forces due to the interaction of the permanent magnets with the iron in the armature.

This chapter describes the design work which has been carried out in constructing a low speed linear PM machine and high speed linear induction machine for camera system integration. The linear PM machine specification called for a design which would be able to produced a force of 22.5 N in order to move a combined camera and mount mass of 10 kg up to 4.5 m/s with an acceleration of 2.25 m/s^2. Further, the machine is required to translate smoothly along its track. Towards achieving this end of minimising the cogging effects, a slotless design was used. The design specification for the linear induction machine will be discussed later in the chapter.

The PM linear machine described here, demonstrates the ability of this type of machine to provide lateral movement using wheels as an integral part of the design. The linear PM machine is mounted on wheels and runs along an U-shaped 4 m aluminium track containing 126 copper coils. Each coil has a 50 turn of copper wire. The machine is 190 mm long and 63.0 mm wide. The permanent magnet is of type Neodymium-Iron-Boron (NdFeB). The non-moving iron core is made up of powdered iron (PERMITE). This made it less susceptible to the flow of induced eddy currents. A general view of the linear machine dimensions is shown in Figure 7.1.

All the 126 copper coils, placed on the surface of the powdered iron core, are used to energise the magnetic circuit. The mechanical clearance between the permanent magnets and the coils is 3 mm. The moving carriage consists of 4 permanent magnets mounted on a back iron. The powdered iron core and coils are placed along the

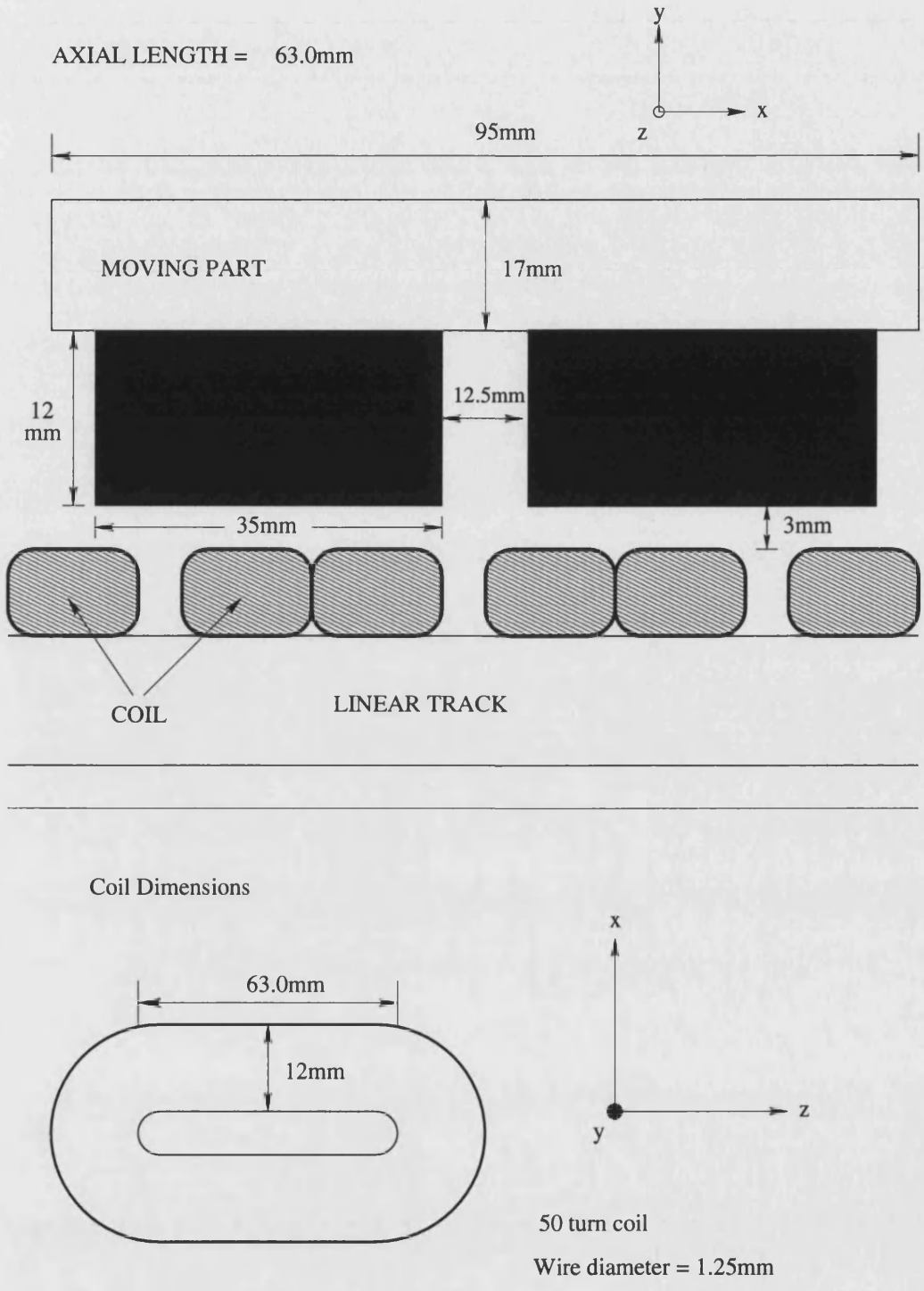

Figure 7.1: Schematic of linear PM machine and coil dimensions.

aluminium track. The moving carriage is designed to carry a camera system. Without magnetic teeth and slots, smooth translation is ensured with cogging practically at zero.

7.4.2 Validation for Linear Permanent Magnet Machine

A non-linear 2D time-transient model was used to design the machine and investigate its performance. To reduce computational time, advantage is taken of the geometrical symmetry by modelling only 1/2 of the machine with the appropriate periodic boundary conditions prescribed. The 2D model has 10394 nodes, 9936 elements and 57515 of non-zeros. The FE model of the entire machine is shown in Figure 7.2.

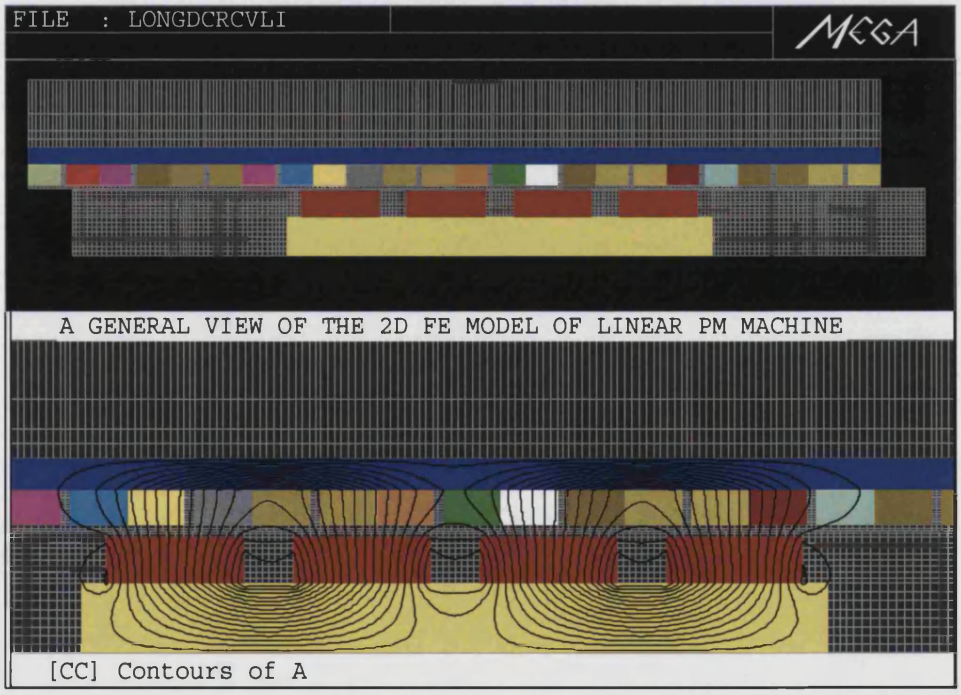

Figure 7.2: 2D FE mesh of linear PM machine.

The field coil is easily defined by selecting from an extensive library of coils provided by the software package. Coil inductances and resistances were modelled as external circuit and connected between the terminals of the 3-phase linear machine. Each

terminal phase was fed with a sinusoidal voltage source of 50 Hz. The cross-sectional area for one slot in this design is about 130 mm^2. By using a conductor of diameter 1.25 mm, a 50 turn coil will fit into this space envelope. The total per phase inductance is 1.367 mH and the phase resistance is measured to be 3.1 ohms.

A DC current of 4 A was fed into one of the three phases with -2 A in the other two to emulate a travelling wave at one instant in time. The carriage was displaced by 2 mm increments along the track and the force measurement taken at each interval. The calculated and measured thrust forces are shown in Figure 7.3.

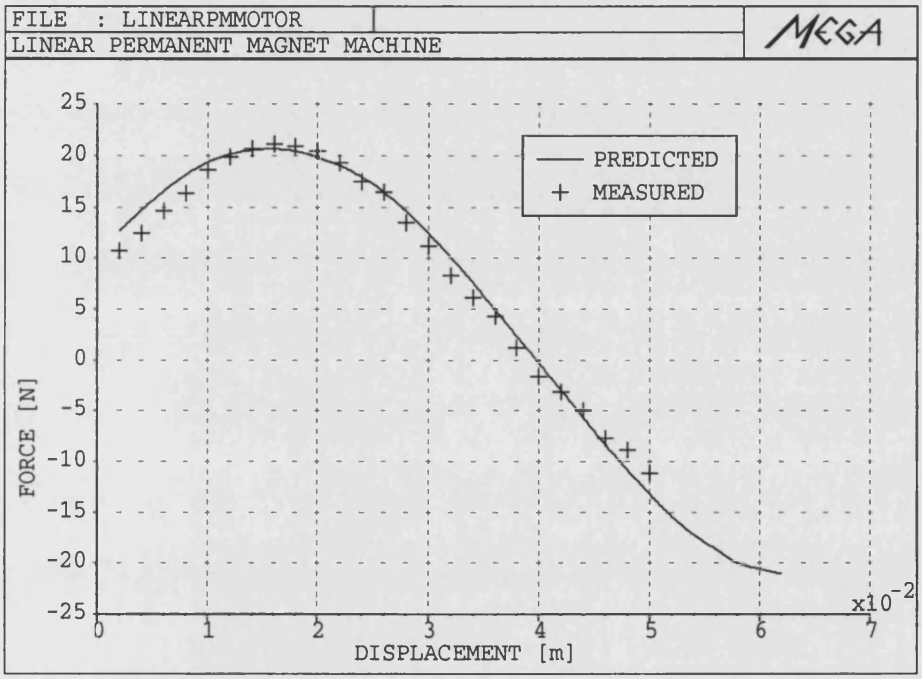

Figure 7.3: Thrust force.

For the production of a steady unidirectional force, the primary carriage must move at a precise synchronous speed V_s so that the fields of stator and rotor are moving at the same speed. In this case, $V_s = 2pf$ where p is the pole pitch of the machine and f is the supply frequency. The synchronous speed V_s in this case with pole pitch = 47.5 mm and frequency = 50 Hz is calculated to be 4.75 m/s. A sinusoidal voltage

of 32 V_{peak} was applied at each phase in the Y-connected system. The thrust force produced at synchronous speed with the correct load angle is shown in Figure 7.4.

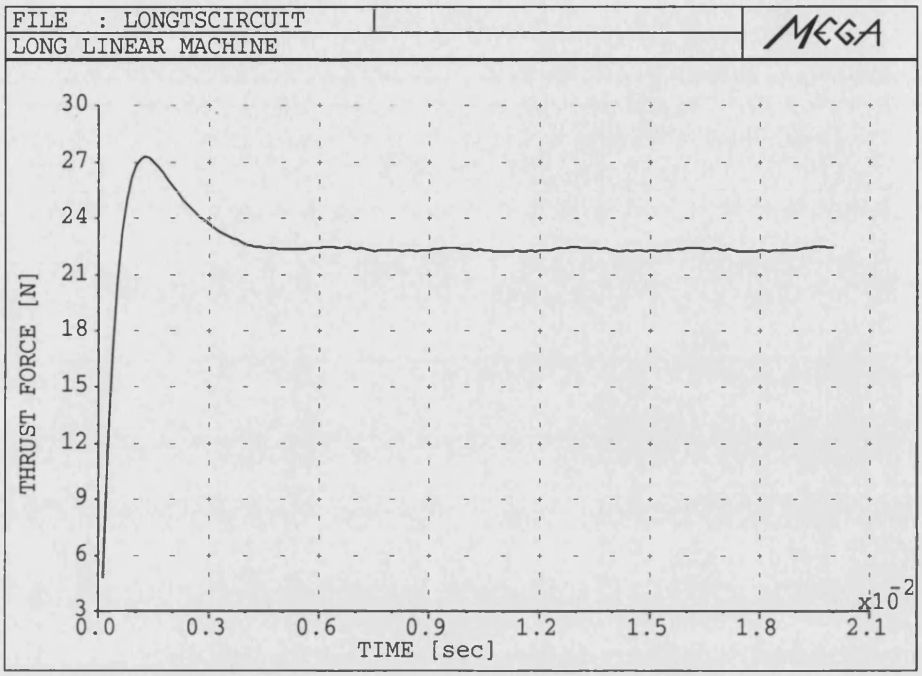

Figure 7.4: Thrust force at synchronous speed.

7.5 Design of Linear Induction Machine

7.5.1 General Description

The linear induction machine is required to drive a camera and all associated hardware around a 250 m track containing a curve at speeds up to 20 m/s. The induction machine consists of a moving primary of 8 poles stator and a secondary conducting aluminium sheet. One pole pitch is 114.3 mm long which made the machine's total length equal to 914.4 mm. The width of the machine is 80 mm. The stator has 48 slots and slide on a smooth 6 or 8 mm aluminium sheet. The aluminium sheet is backed by a solid mild steel and the air gap mechanical clearance is set at 5 mm. Photographs of the induction machine and the aluminium track are provided in Appendix E.

The coil is made up of 18 turn of 1 mm diameter copper wire. The winding layout is that of a double layer winding with half-filled end slots. This arrangement often results in a linear induction machine exhibiting good performance.

The linear induction machine is designed to carry a payload of up to 100 kg and the capability to accelerate up to 4 m/s^2 . In addition to the payload, the stator with coils weighted about 70 kg. The machine is attached to a buggy moving along a rail. The arrangement is shown in the simplified schematic of Figure 7.5.

The stator and reactionary plate of the linear induction machine have a finite width with the aluminium track wider than the stator. The consequences of this physical feature are called *transverse edge effects.* The general assumptions of which currents are only in the z- direction and field does not vary in the same direction.

The major influence of the transverse edge effects is to increase the resistivity of the conducting track. In the 2D modelling, the returning paths of these currents on the conducting plate are taken into account by using a factor which increases the value of the conductor resistivity. A simple approach based on the reference of Russell and Norsworthy is used to determine the resistivity factor for the conducting plate:

$$\begin{aligned} k_r &= \frac{1}{1-\left[\dfrac{\delta_{tp}\cdot\tanh(k_s)}{k_s(\delta_{tp}+\delta_{ot}\cdot\tanh(k_s)\cdot\tanh(k_p))}\right]} \\ k_s &= \frac{1}{2}\delta_{sw}\frac{\pi}{p} \\ k_p &= \frac{1}{2}(\delta_{pw}-\delta_{sw})\frac{\pi}{p} \end{aligned} \tag{7.9}$$

where p is the pole pitch, δ_{sw} is the moving primary (stator) width, δ_{pw} is the width of the secondary plate. δ_{tp} is thickness of the secondary plate under the moving primary and δ_{ot} is plate thickness outside the primary.

Using the above resistivity factor, the measured conductivity of the aluminium plate of 3.2×10^7 S/m is corrected to 1.7×10^7 S/m.

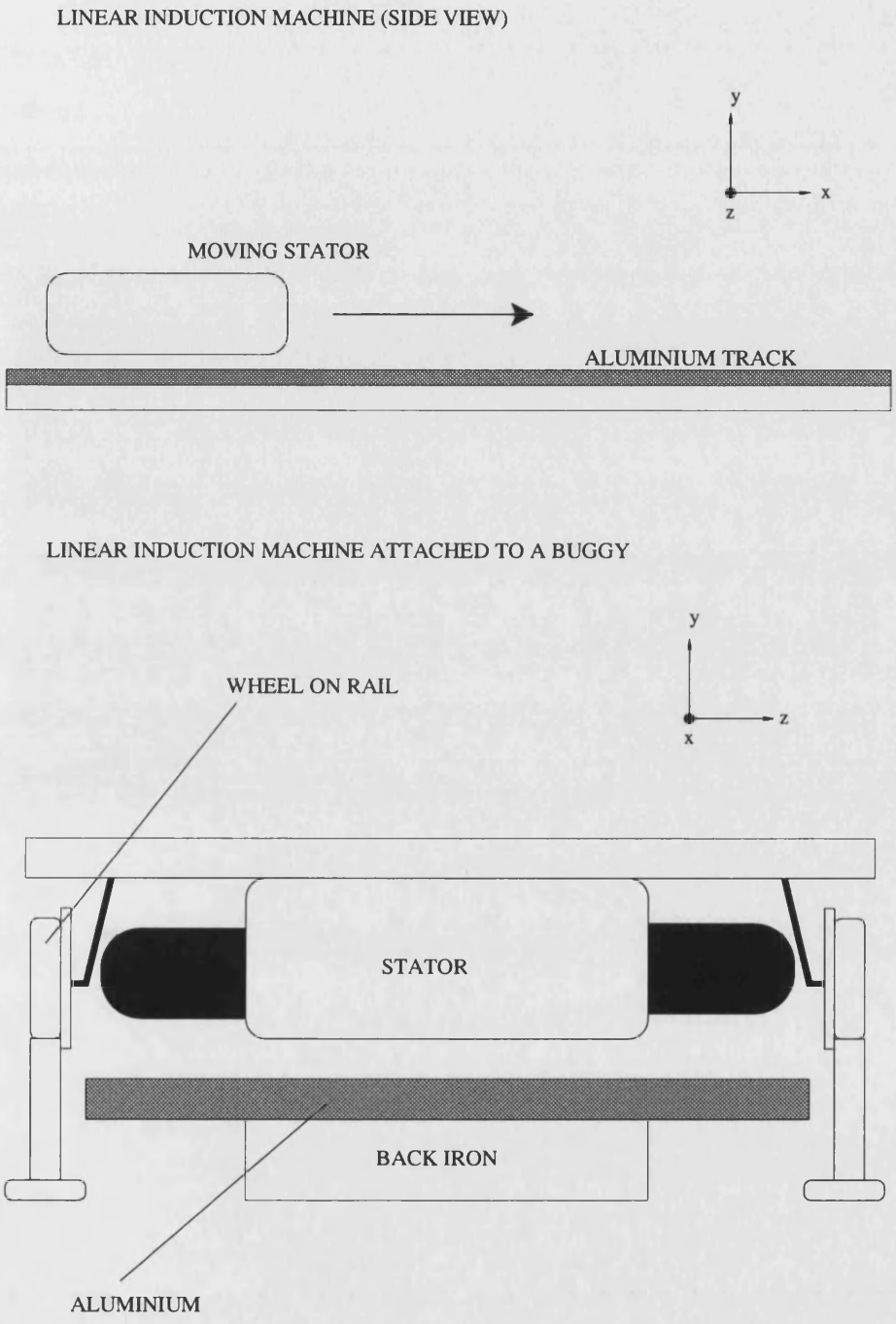

Figure 7.5: Schematic of linear induction machine.

7.5.2 Validation for Linear Induction Machine

The 2D finite element model of the linear induction machine is made of 147520 nodes and 145152 elements. Figure 7.6 illustrates the 2D FE model. The laminations of the moving primary are of TRANSIL315 steel and the **B-H** characteristic used in the FE analysis is shown in Figure 7.7.

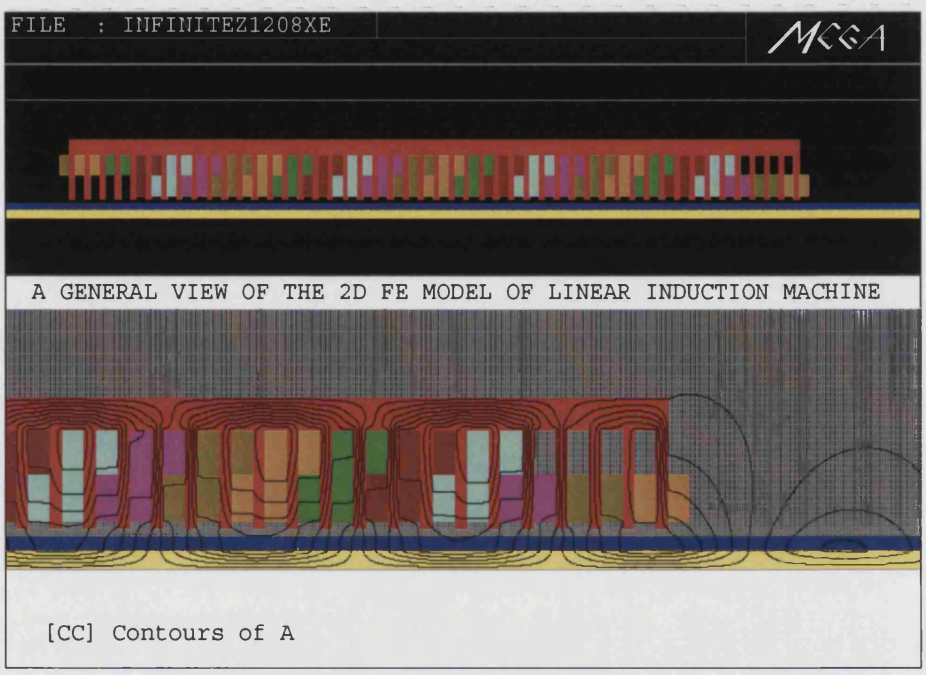

Figure 7.6: 2D FE mesh of linear induction machine.

In the absence of the conducting aluminium sheet, a double layer winding arrangement with half-filled end slots produces a desirable distribution of air gap field of a 8 poles machine, as shown in Figure 7.8.

The winding of the linear induction machine was fed from an AC source with 50 Hz frequency. The thrust force measurements were carried out when the phase currents were fixed and the machine at standstill. Figure 7.9 shows the computational results from *MEGA* validated by a set of thrust force measurements at different currents input.

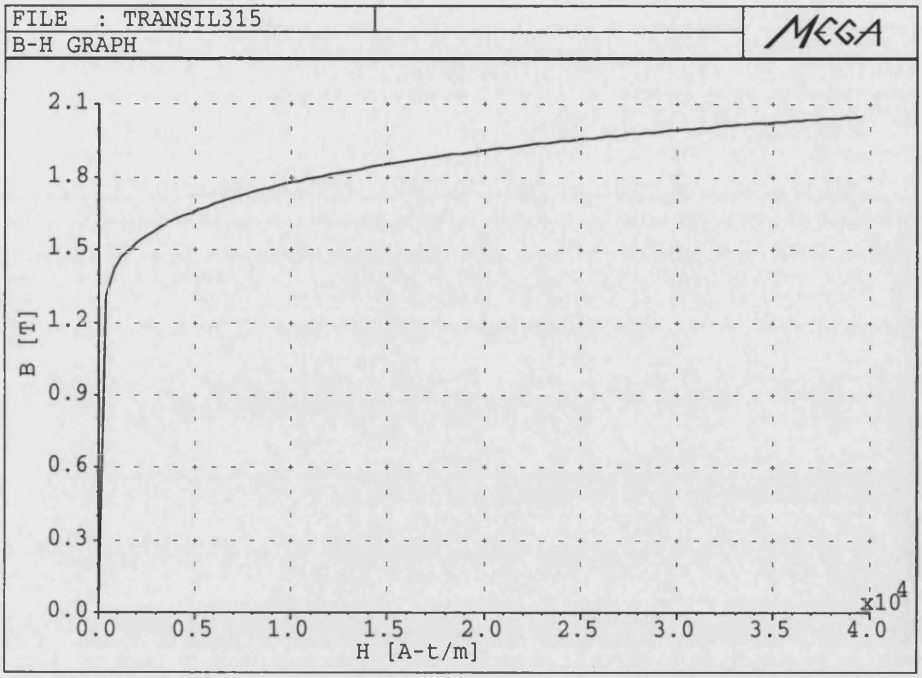

Figure 7.7: **B-H** curve for the iron laminations.

The maximum supply frequency is given as 120 Hz with the current input of 70 A. The machine drive is one which gives continuous variable voltage and frequency supply such that the machine is always operating at the chosen optimum position. Two force/speed curves are shown in Figure 7.10. The efficiency and force produced by an induction machine varies along the force/speed curve, with the optimal running area for efficiency and stability typically being just on the faster side of the maximum thrust force. However, for this machine which runs on a 8 mm thick aluminium (AL) sheet, the optimum position is identified at speed 21 m/s where the slip is about 0.22, less than optimum in terms of efficiency but was compensated by the fact that the normal attractive force is almost negligible in this region. This is important as the attractive force increases the apparent weight of the vehicle and so stresses the secondary mounting.

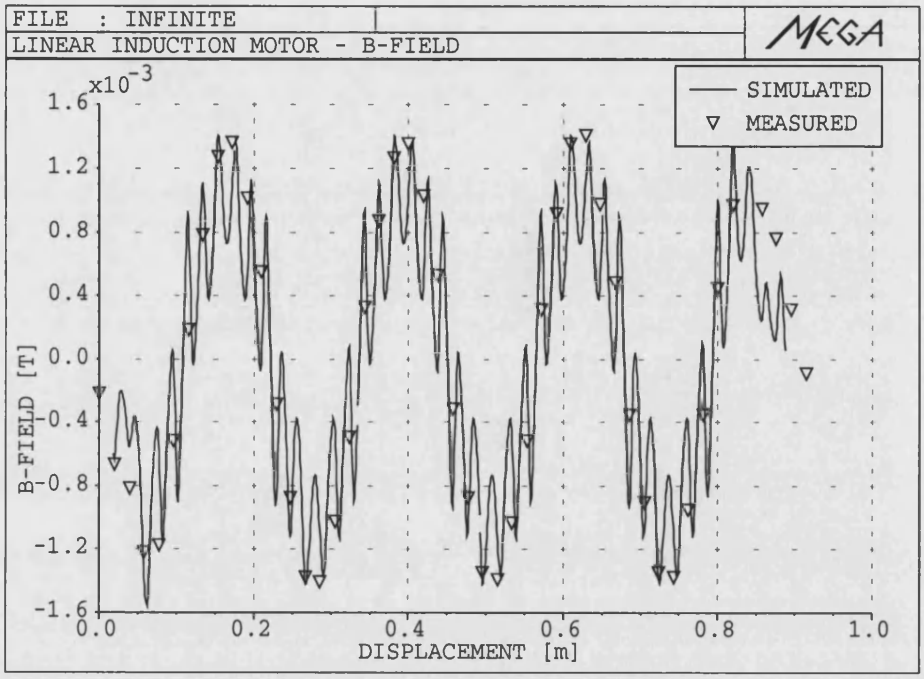

Figure 7.8: Simulated and measured normal B-fields.

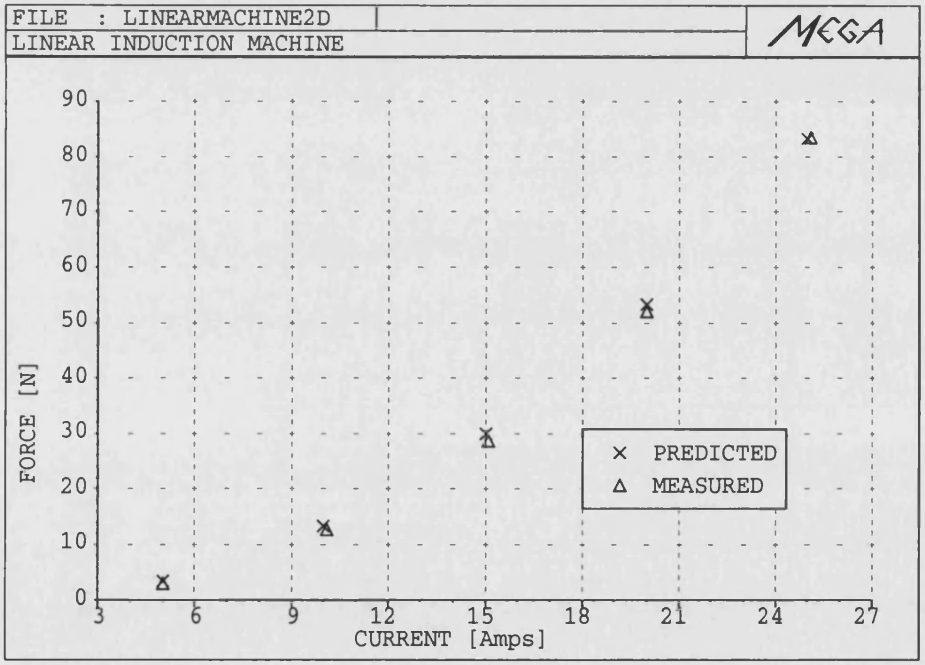

Figure 7.9: Thrust force at standstill.

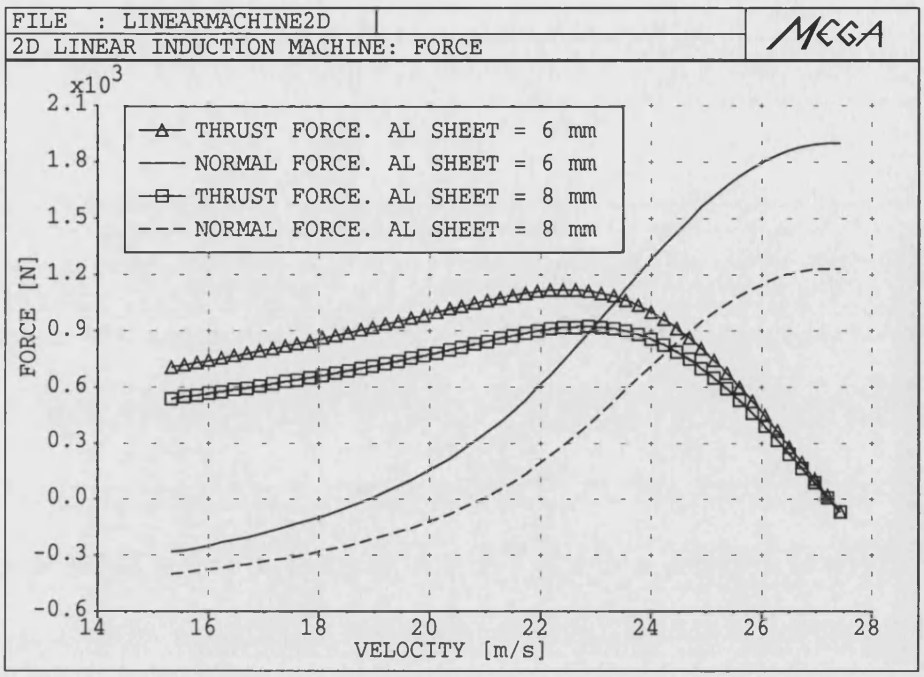

Figure 7.10: Thrust force and normal force at 120 Hz.

The force/speed curves in Figure 7.10 show two sets of thrust force and normal force results for the 6 mm and 8 mm thick aluminium sheets. The linear induction machine with the thicker conducting sheet will have a larger magnetic gap which is a combination of the mechanical clearance and the thickness of the sheet. A larger magnetic gap will lower the thrust force and normal force produced by the machine.

7.6 Summary

Some practical applications on modelling linear electrical machines using finite elements are described here. Two examples of the modelling efforts are demonstrated together with the application of the parameterised templates technique and two methods in modelling moving domain, that of *Minkowski transformation* and *Lagrange Multipliers*. Each method has it merits and disadvantages depending on the situation and requirements.

Chapter 8

Conclusions

The rapid growth in engineering usage of computer technology in an era where the technology can offer cutting edge solutions to so many problems will undoubtedly continue to significantly affect the acceptance of the finite element method. With continued economic pressure to increase engineering efficiency and productivity through advanced technology, this beginning of the new millennia will see an accelerated role of an increasing sophisticated finite element method in the industrial design. Already in many design offices the finite element method enjoys routine use.

This work gives a detailed insight into the solving of complex problems related to electromagnetic devices using the finite elements method. In the initial stage, some heat transfer problems are solved. Detailed thermal modelling of electrical devices is much more complex compared to electromagnetic modelling as it involved complex fluid flow and radiation. Furthermore, conducting regions thermal properties tend to be associated with a degree of uncertainty and critically dependent on the manufacturing techniques employed. Mostly in this research, the fluid dynamics are avoided by replacing them with the appropriate boundary conditions. Several benchmark tests are conducted to evaluate the accuracy of these convective and radiation boundary conditions. It appears that for material with long time constants, these conditions are fairly applicable. This greatly reduced the computational time and difficulty in solv-

ing for a full 3D heat transfer of fluid dynamics coupled electromagnetic conditions. The analysis of the coupled electromagnetic-thermal problem requires the solution of two parabolic differential equations coupled through the temperature dependent electrical conductivity. The thermal time constants are typically 10^4 times larger than the electrical time constant. This means that a fully coupled system would be very expensive to solve. Therefore, the electrical problem is modelled as a time-harmonic system weakly coupled to a time-transient non-linear thermal system. In moving eddy current and thermal regions, the application of Galerkin's upwinding might be necessary at higher speed in order to avoid the possible occurrences of oscillations in the solution.

The next stage of the research mainly dealt with the analysis of cogging torque in permanent magnet (PM) servo motor. Solving for cogging torque using analytical method is particularly difficult, time consuming and almost impossible if skewing is involved. The analysis of cogging torque in PM servo motor provide a good understanding on the root of the the problem and various ideas of minimising this intransgression problems are explore. One useful method of reducing cogging is by skewing the rotor or stator of the machines by a slot pitch. However, the major obstacle is the rotating rotor mesh and stationary stator is vastly incompatible and difficult to mesh up as a sole unit. The *Lagrange Multipliers* method has been adopted successfully in confronting this problem. The technique is based on the idea that the stationary and rotationary members of the model are separately discretised as disconnected meshes with the possibilities of each having different nodal densities and distribution patterns at a common interface. The meshes are then coupled together by the enforcement of an extra constraint condition to ensure the continuity of potentials across the Lagrangian interface. The measurements and predictions have been observed to compare very favourably. Besides skewing, the appropriate pole arc and magnetisation of the permanent magnet help in reducing cogging torque.

Finally, a parameterised templates method in meshing up electromagnetic devices is

described. The main aim is to provide a more flexible and economical environment for the user in designing/optimising various electrical machineries. The design process is further simplified with the adaptation of an optimisation algorithm. There are various optimisation schemes, in this case the Simplex method is used. The algorithm will iteratively call the simulation FE model in the attempt to find the best design. However, before commencing the optimisation process, it is necessary to set the aims of the devices and the design criteria which cannot be altered. Simply exploring every possible combination of parameters is highly impractical and inefficient in all but trivial cases. The parameterised templates method is verified with the modelling of several electromagnetic devices such as permanent magnet (PM) servo motor, synchronous generator, Fluxset sensor, linear permanent magnet (PM) machine and linear induction machine. Measurements were obtained from the two linear electrical machines which were part of the ongoing project with the industry. The measurements show a high level of agreement between the computational results and experimental ones.

Future work on the subject of thermal analysis is going to include computer fluid dynamics (CFD) implementation for modelling surface fluid convection. Another area of interest is the modelling of a more robust iron losses model.

Appendix A

Vector Analysis

A.1 Vector Identities

$$(\boldsymbol{A}+\boldsymbol{B})\cdot\boldsymbol{C}=\boldsymbol{A}\cdot\boldsymbol{C}+\boldsymbol{B}\cdot\boldsymbol{C} \tag{A.1}$$

$$(\boldsymbol{A}+\boldsymbol{B})\times\boldsymbol{C}=\boldsymbol{A}\times\boldsymbol{C}+\boldsymbol{B}\times\boldsymbol{C} \tag{A.2}$$

$$\boldsymbol{A}\cdot\boldsymbol{B}\times\boldsymbol{C}=\boldsymbol{B}\cdot\boldsymbol{C}\times\boldsymbol{A}=\boldsymbol{C}\cdot\boldsymbol{A}\times\boldsymbol{B} \tag{A.3}$$

$$\boldsymbol{A}\times(\boldsymbol{B}\times\boldsymbol{C})=(\boldsymbol{A}\cdot\boldsymbol{C})\boldsymbol{B}-(\boldsymbol{A}\cdot\boldsymbol{B})\boldsymbol{C} \tag{A.4}$$

A.2 Differentiation of Vectors

$$\nabla(U+V)=\nabla U+\nabla V \tag{A.5}$$

$$\nabla\cdot(\boldsymbol{A}+\boldsymbol{B})=\nabla\cdot\boldsymbol{A}+\nabla\cdot\boldsymbol{B} \tag{A.6}$$

$$\nabla\times(\boldsymbol{A}+\boldsymbol{B})=\nabla\times\boldsymbol{A}+\nabla\times\boldsymbol{B}$$

$$\nabla(UV) = U\nabla V + V\nabla U \tag{A.7}$$

$$\nabla \cdot (V\boldsymbol{A}) = \boldsymbol{A} \cdot \nabla V + V\nabla \cdot \boldsymbol{A} \tag{A.8}$$

$$\nabla \times (V\boldsymbol{A}) = \nabla V \times \boldsymbol{A} + V\nabla \times \boldsymbol{A} \tag{A.9}$$

$$\nabla \cdot (\boldsymbol{A} \times \boldsymbol{B}) = \boldsymbol{B} \cdot \nabla \times \boldsymbol{A} - \boldsymbol{A} \cdot \nabla \times \boldsymbol{B} \tag{A.10}$$

$$\nabla(\boldsymbol{A} \cdot \boldsymbol{B}) = (\boldsymbol{A} \cdot \nabla)\boldsymbol{B} + (\boldsymbol{B} \cdot \nabla)\boldsymbol{A} + \boldsymbol{A} \times (\nabla \times \boldsymbol{B}) + \boldsymbol{B} \times (\nabla \times \boldsymbol{A}) \tag{A.11}$$

$$\nabla \times (\boldsymbol{A} \times \boldsymbol{B}) = \boldsymbol{A}\nabla \cdot \boldsymbol{B} - \boldsymbol{B}\nabla \cdot \boldsymbol{A} + (\boldsymbol{B} \cdot \nabla)\boldsymbol{A} - (\boldsymbol{A} \cdot \nabla)\boldsymbol{B} \tag{A.12}$$

$$\nabla \cdot \nabla V = \nabla^2 V \tag{A.13}$$

$$\nabla \cdot \nabla \times \boldsymbol{A} = 0 \tag{A.14}$$

$$\nabla \times \nabla V = 0 \tag{A.15}$$

$$\nabla \times \nabla \times \boldsymbol{A} = \nabla(\nabla \cdot \boldsymbol{A}) - \nabla^2 \boldsymbol{A} \tag{A.16}$$

A.3 Integral of Vectors

$$\int \nabla V \, \mathrm{d}v = \oint V \, \mathrm{d}s \tag{A.17}$$

$$\int \nabla \times \boldsymbol{A} \, \mathrm{d}v = -\oint \boldsymbol{A} \times \mathrm{d}s \tag{A.18}$$

A.3.1 Gauss's Theorem

$$\int \nabla \cdot \boldsymbol{A} \, \mathrm{d}v = \oint \boldsymbol{A} \cdot \mathrm{d}s \tag{A.19}$$

A.3.2 Stokes's Theorem

$$\int \nabla \times \boldsymbol{A} \cdot \mathrm{d}s = \oint \boldsymbol{A} \cdot \mathrm{d}\ell \tag{A.20}$$

A.3.3 Green's Theorem

$$\int (\nabla U \cdot \nabla V + U \nabla^2 V) \, \mathrm{d}v = \oint U \nabla V \cdot \mathrm{d}s \tag{A.21}$$

$$\int \boldsymbol{A} \cdot (\nabla \times \nabla \times \mathrm{B}) \, \mathrm{d}v = \int (\nabla \times \boldsymbol{A}) \cdot (\nabla \times \boldsymbol{B}) \, \mathrm{d}v - \oint (\boldsymbol{A} \times \nabla \times \boldsymbol{B}) \cdot \hat{\mathrm{n}} \, \mathrm{d}s \tag{A.22}$$

Appendix B

Finite Element Discretisation and Numerical Integration

B.1 Element Matrices Computation

The governing equation to be solved for each 3D linear element shown in Figure B.1, with the shape functions to depict the spatial variation of the nodal temperature T is written as

$$\int_{\Omega} \kappa \left(\frac{\partial N_i}{\partial x} \sum_{j=1}^{8} \frac{\partial N_j}{\partial x}[T_j] + \frac{\partial N_i}{\partial y} \sum_{j=1}^{8} \frac{\partial N_j}{\partial y}[T_j] + \frac{\partial N_i}{\partial z} \sum_{j=1}^{8} \frac{\partial N_j}{\partial z}[T_j] \right) \mathrm{d}\Omega$$
$$- \oint_{\Gamma} \kappa N_i \sum_{j=1}^{4} N_j \frac{\partial T_j}{\partial n} \mathrm{d}\Gamma + \int_{\Omega} \rho C N_i \sum_{j=1}^{8} N_j \left[\frac{\partial T_j}{\partial t} \right] \mathrm{d}\Omega = \int_{\Omega} N_i \dot{q} \, \mathrm{d}\Omega \qquad \text{(B.1)}$$

Without loss of generality, the surface integral term in equation (B.1) can be ignored since the boundary integral cancels at the element interfaces. If the interface is on the outer layer then surface convection and radiation boundary conditions can be enforced.

The 3D isoparametric linear brick element contains eight nodes leading to a 8×8 symmetric matrix, where $[\boldsymbol{K}_{ij}] = [\boldsymbol{K}_{ji}]$ the diffusive matrix on the *l.h.s* are non-zeros,

$$\begin{bmatrix} \begin{vmatrix} K_{11} & K_{12} \\ K_{21} & K_{22} \end{vmatrix} & 0 & 0 & 0 \\ 0 & \begin{vmatrix} K_{33} & K_{34} \\ K_{43} & K_{44} \end{vmatrix} & 0 & 0 \\ 0 & 0 & \begin{vmatrix} K_{55} & K_{56} \\ K_{65} & K_{66} \end{vmatrix} & 0 \\ 0 & 0 & 0 & \begin{vmatrix} K_{77} & K_{78} \\ K_{87} & K_{88} \end{vmatrix} \end{bmatrix} \begin{bmatrix} T_1 \\ T_2 \\ T_3 \\ T_4 \\ T_5 \\ T_6 \\ T_7 \\ T_8 \end{bmatrix} \tag{B.2}$$

The governing equation for heat transfer is computed using the standard summation of the unknown T nodal values and corresponding shape functions in local coordinates (ξ, η, ζ),

$$T(\xi, \eta, \zeta, t) = \sum N_i(\xi, \eta, \zeta, t) T_i \tag{B.3}$$

The nodes in the local (ξ, η, ζ) coordinates are mapped onto the corresponding nodes in the (x, y, z) global coordinates by

$$x = \sum_{i=1}^{8} N_i(\xi, \eta, \zeta)\, x_i \quad y = \sum_{i=1}^{8} N_i(\xi, \eta, \zeta)\, y_i \quad z = \sum_{i=1}^{8} N_i(\xi, \eta, \zeta)\, z_i \tag{B.4}$$

The transformation between the local coordinates and global coordinates is unique. Each point in one system has a corresponding point in the other system as shown in Figure B.2. The transformation maps a point in the local coordinates (ξ, η, ζ) element onto a point in the global coordinates (x, y, z) element. The relations for the temperature derivatives in terms of local coordinates and the isoparametric description of the element geometry are provided by the expression

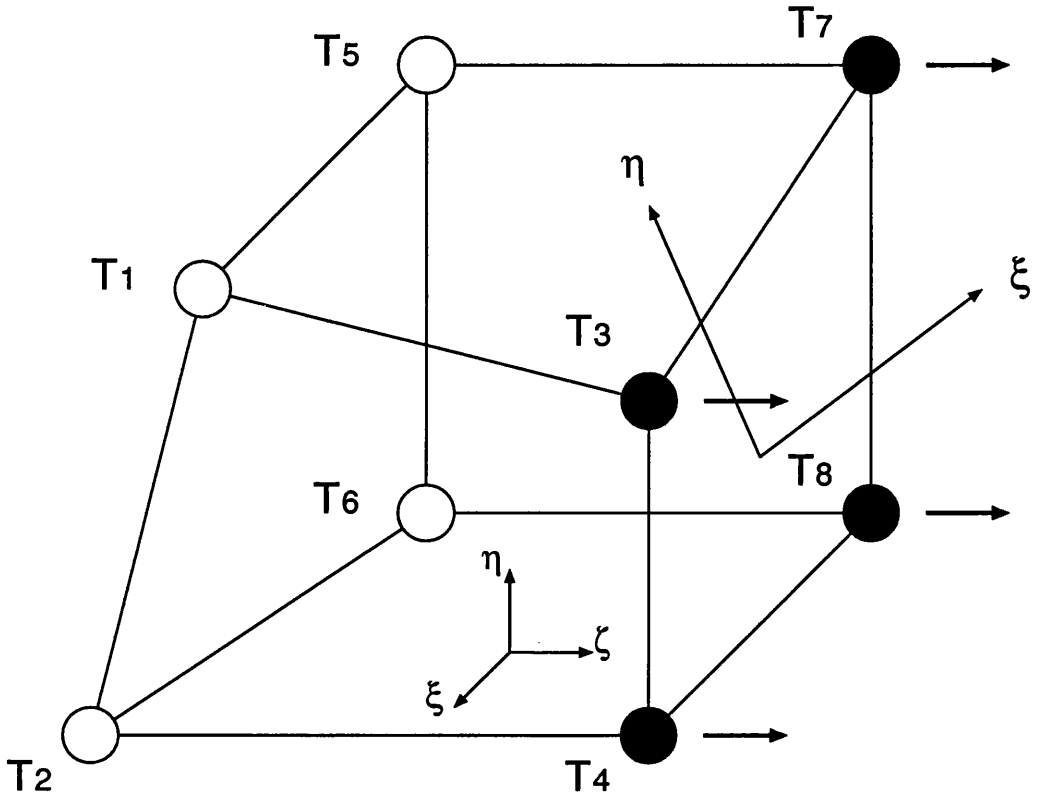

Figure B.1: 8 nodes quadrilateral element .

$$\begin{bmatrix} \frac{\partial N_i^e}{\partial \xi} \\ \frac{\partial N_i^e}{\partial \eta} \\ \frac{\partial N_i^e}{\partial \zeta} \end{bmatrix} = \begin{bmatrix} \frac{\partial x}{\partial \xi} & \frac{\partial y}{\partial \xi} & \frac{\partial z}{\partial \xi} \\ \frac{\partial x}{\partial \eta} & \frac{\partial y}{\partial \eta} & \frac{\partial z}{\partial \eta} \\ \frac{\partial x}{\partial \zeta} & \frac{\partial y}{\partial \zeta} & \frac{\partial z}{\partial \zeta} \end{bmatrix} \begin{bmatrix} \frac{\partial N_i^e}{\partial x} \\ \frac{\partial N_i^e}{\partial y} \\ \frac{\partial N_i^e}{\partial z} \end{bmatrix} \tag{B.5}$$

which also shows the relation between the derivatives of the shape functions N_i^e with respect to the global and local coordinates. The required derivatives $\frac{\partial N_i^e}{\partial x}$, $\frac{\partial N_i^e}{\partial y}$ and $\frac{\partial N_i^e}{\partial z}$ are obtained by inverting (B.5) provided that $[\mathfrak{J}]$, the *Jacobian matrix* of the transformation is non-singular,

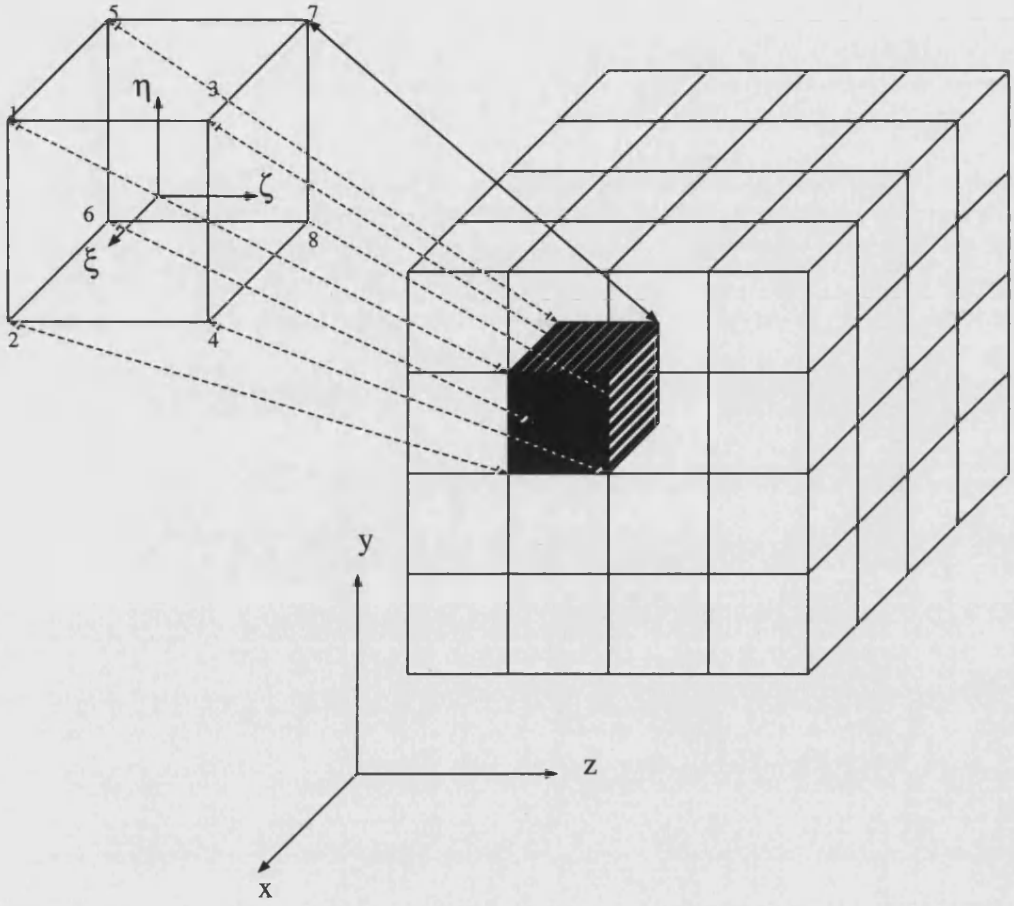

Figure B.2: Mapping between local and global elements .

$$\begin{bmatrix} \frac{\partial N_i^e}{\partial x} \\ \frac{\partial N_i^e}{\partial y} \\ \frac{\partial N_i^e}{\partial z} \end{bmatrix} = \begin{bmatrix} \\ \mathcal{J}^{-1} \\ \\ \end{bmatrix} \begin{bmatrix} \frac{\partial N_i^e}{\partial \xi} \\ \frac{\partial N_i^e}{\partial \eta} \\ \frac{\partial N_i^e}{\partial \zeta} \end{bmatrix}, \quad \mathcal{J} = \begin{bmatrix} \frac{\partial x}{\partial \xi} & \frac{\partial y}{\partial \xi} & \frac{\partial z}{\partial \xi} \\ \frac{\partial x}{\partial \eta} & \frac{\partial y}{\partial \eta} & \frac{\partial z}{\partial \eta} \\ \frac{\partial x}{\partial \zeta} & \frac{\partial y}{\partial \zeta} & \frac{\partial z}{\partial \zeta} \end{bmatrix} \tag{B.6}$$

The element volume $d\Omega$ is replaced by an equivalent in terms of the local (ξ, η, ζ) coordinates,

$$d\Omega = |\mathcal{J}|\, d\xi\, d\eta\, d\zeta \tag{B.7}$$

A necessary condition for $[\mathfrak{J}^{-1}]$ to exist is that the determinant of the *Jacobian matrix* $|\mathfrak{J}|$ be non-zero at every nodal point (ξ, η, ζ) in the region Ω :

$$|\mathfrak{J}| = \frac{\partial x}{\partial \xi}\left[\frac{\partial y}{\partial \eta}\frac{\partial z}{\partial \zeta} - \frac{\partial z}{\partial \eta}\frac{\partial y}{\partial \zeta}\right] - \frac{\partial y}{\partial \xi}\left[\frac{\partial x}{\partial \eta}\frac{\partial z}{\partial \zeta} - \frac{\partial z}{\partial \eta}\frac{\partial x}{\partial \zeta}\right] + \frac{\partial z}{\partial \xi}\left[\frac{\partial x}{\partial \eta}\frac{\partial y}{\partial \zeta} - \frac{\partial y}{\partial \eta}\frac{\partial x}{\partial \zeta}\right] \neq 0 \quad \text{(B.8)}$$

The integration limits for the integral transform on the local coordinates (ξ, η, ζ) are from -1 to +1. Therefore, the computational form of the diffusion matrix $[\boldsymbol{K}_{ij}]$ is written as

$$\begin{aligned}[\boldsymbol{K}_{ij}] \;=\; & \int_{-1}^{1}\int_{-1}^{1}\int_{-1}^{1} \sum_{n=1}^{3} \kappa\left[\left([\mathfrak{J}_{n1}]^{-1}\frac{\partial N_i}{\partial \xi} + [\mathfrak{J}_{n2}]^{-1}\frac{\partial N_i}{\partial \eta} + [\mathfrak{J}_{n3}]^{-1}\frac{\partial N_i}{\partial \zeta}\right)\cdot\right. \\ & \left.\left([\mathfrak{J}_{n1}]^{-1}\frac{\partial N_j}{\partial \xi} + [\mathfrak{J}_{n2}]^{-1}\frac{\partial N_j}{\partial \eta} + [\mathfrak{J}_{n3}]^{-1}\frac{\partial N_j}{\partial \zeta}\right)\right] |\mathfrak{J}|\, \mathrm{d}\xi\, \mathrm{d}\eta\, \mathrm{d}\zeta \qquad \text{(B.9)}\end{aligned}$$

B.2 Surface Element Computation

The prescribed nodal boundary conditions need only be computed for those element sides that coincide with the boundary of the region of interest. Contributions from the interior element boundary are cancelled by adjoining elements.

The total surface heat flux q_e at the boundary is given by

$$q_e = \oint_{\Gamma} N_i\, q_i\, \mathrm{d}\Gamma = \oint_{\Gamma} N_i\, (-q_n - q_c - q_r)\, \mathrm{d}\Gamma \qquad \text{(B.10)}$$

where q_n, q_c, q_r denote the prescribed heat flux, convection and radiation heat flows normal to the surface respectively.

The computation of the specified surface integral is carried out in the natural coordinate system (ξ, η) for the edge or face of the element. The element $\mathrm{d}\Gamma$, as shown in Figure B.1, generally lie on a surface where one of the coordinates is constant. The most convenient process of dealing with the problem is to consider $\mathrm{d}\Gamma$ as a vector

oriented in the direction normal to the surface. The surface area of the element $d\Gamma$ in terms of the global coordinates (x, y, z) is related to the elemental area in natural coordinates by

$$d\Gamma = |\mathcal{J}_s| \, d\xi \, d\eta \tag{B.11}$$

where $|\mathcal{J}_s|$ is the Jacobian determinant of the coordinate transformation.

If a known heat flux q_n is applied on the surface then

$$\boldsymbol{q_n} = \int_{-1}^{1} \int_{-1}^{1} \boldsymbol{N}(\xi, \eta) q_n(\xi, \eta) \, |\mathcal{J}_s| \, d\xi \, d\eta \tag{B.12}$$

In 2D cases, the linear shape functions $\boldsymbol{N}$ corresponds to the 1D shape functions of

$$\begin{aligned} N_1 &= \frac{1}{2}(1 - \xi) \\ N_2 &= \frac{1}{2}(1 + \xi) \end{aligned} \tag{B.13}$$

and the integral of equation $(B.12)$ is integrated over the edge. For 3D cases, the surface shape functions $\boldsymbol{N}$ correspond directly to the 2D shape functions

$$\begin{aligned} N_1 &= \frac{1}{4}(1 - \xi)(1 - \eta) \\ N_2 &= \frac{1}{4}(1 + \xi)(1 - \eta) \\ N_3 &= \frac{1}{4}(1 + \xi)(1 + \eta) \\ N_4 &= \frac{1}{4}(1 - \xi)(1 + \eta) \end{aligned} \tag{B.14}$$

Once the normal flux $q_n(\xi, \eta)$ at the surface of the element is known, equation $(B.12)$ is evaluated using the Gaussian numerical quadrature. The number of integration

points is typically the same as that used on the volume/area integral constituting the diffusive $[\boldsymbol{K}_{ij}]$ and capacitance $[\boldsymbol{C}]$ matrices.

If the contributions of the surface heat flow to the global conductance matrix $[\boldsymbol{K}]$ is due to convection and the known ambient temperature is given as $T_\infty(\xi,\eta)$ then the expression for boundary conditions is

$$\begin{aligned} \boldsymbol{q}_c = & - \left(\int_{-1}^{1}\int_{-1}^{1} \hbar_c \, \boldsymbol{N}(\xi,\eta)\, \boldsymbol{N}^T(\xi,\eta)\, |\mathfrak{J}_s| \, \mathrm{d}\xi \, \mathrm{d}\eta \right) \{\boldsymbol{T}\} \\ & + \int_{-1}^{1}\int_{-1}^{1} \hbar_c \, \boldsymbol{N}(\xi,\eta)\, T_\infty(\xi,\eta)\, |\mathfrak{J}_s| \mathrm{d}\xi \, \mathrm{d}\eta \end{aligned} \tag{B.15}$$

The first term on the *r.h.s* of equation (B.15) is added into the thermal conductance matrix $[\boldsymbol{K}]$ while the second term is put into the load vector matrix $\boldsymbol{f}$. If the convection coefficient $\hbar_c$ is the function of temperature then the problem is non-linear. A similar computation can be carried out for the radiation boundary condition.

B.3 Numerical Integration using Gauss Quadrature

Integrals defined over the 3D brick element are numerically evaluated using the Gaussian quadrature method. In general the integrals are approximated over 1D, 2D or 3D dimensional domains by using a simple summation of the integrand terms, evaluated at specified points in the domain and then multiply by suitable weightings. The Gauss quadrature algorithms are usually stated in terms of integral over the interval -1 to + 1 :

$$\begin{aligned} \boldsymbol{I} &= \int_{-1}^{1} F(\xi)\, \mathrm{d}\xi \\ &\approx W_1\, G(\xi_1) + W_2\, G(\xi_2) + W_3\, G(\xi_3) + ... + \sum_{i=n}^{M_i} G(\xi_n) W_n \end{aligned} \tag{B.16}$$

in which $W_1, W_2, ...W_n$ are the weighting factors, $\xi_1, \xi_2.....\xi_n$ are the corresponding local coordinates and M_i is the sampling point.

For the four nodes bilinear isoparametric quadrilateral element, it is customary to employ a 2×2 integration point Gauss quadrature. The number of sampling points is therefore $M_{i,j,k} = 2$ with $\xi_i = \pm 0.57735$. The weighting coefficients are $W_{i,j,k} = 1$. Figure B.3 illustrates the discrete sampling points of the 2×2 Gaussian quadrature technique.

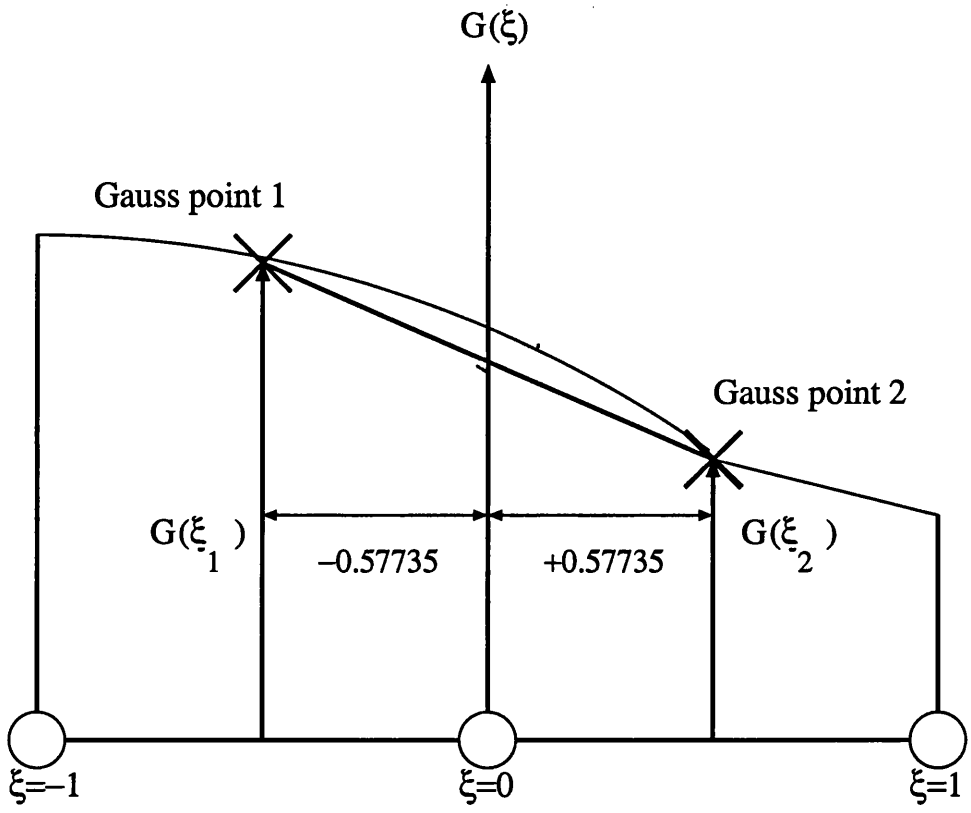

Figure B.3: Unidimensional 2 points Gaussian integration.

In a 2D context, the Gaussian quadrature is obtained by performing two numerical integrations in the ξ and η directions independently. The procedure begins by evaluating the inner loop of the double integral using the 1D Gaussian formula and obtain

$$I = \int_{-1}^{1}\int_{-1}^{1}\left[G(\xi,\eta)\,\mathrm{d}\xi\right]\mathrm{d}\eta \approx \int_{-1}^{1}\left[\sum_{i=1}^{M_i} G(\xi,\eta)\,W_i\right]\mathrm{d}\eta \tag{B.17}$$

and follow by a similar integration of the outer loop in the η direction, which resulted in

$$\int_{-1}^{1}\left[\sum_{i=1}^{M_i} G(\xi,\eta)W_i\right]\mathrm{d}\eta \approx \sum_{j=1}^{M_j} W_j\left[\sum_{i=1}^{M_i} G(\xi,\eta)\,W_i\right] \tag{B.18}$$

Similarly, the 3D extension to the evaluation of integrals over a right prism is trivial, resulting in

$$\begin{aligned} I &= \int_{-1}^{1}\int_{-1}^{1}\int_{-1}^{1} G(\xi,\eta,\zeta)\,\mathrm{d}\xi\,\mathrm{d}\eta\,\mathrm{d}\zeta \\ &\approx \sum_{i=1}^{M_i}\sum_{j=1}^{M_j}\sum_{k=1}^{M_k} G(\xi,\eta,\zeta)W_iW_jW_k \end{aligned} \tag{B.19}$$

B.4 The Global Matrix System

After completing the isoparametric transformation and numerical integration on each local element, all the individual local element matrices of the thermal domain are assembled into a global finite element matrix system which have the standard system of

$$\begin{bmatrix} \\ \boldsymbol{K} = \boldsymbol{K}_{ij} + \boldsymbol{K}_c + \boldsymbol{K}_r \\ \\ \end{bmatrix}\begin{bmatrix} T_1 \\ T_2 \\ \vdots \\ T_n \end{bmatrix} + \begin{bmatrix} \\ \boldsymbol{C} \\ \\ \end{bmatrix}\begin{bmatrix} \\ \dfrac{\partial T}{\partial t} \\ \\ \end{bmatrix} = \begin{bmatrix} & f_{\dot{q}} \\ r.h.s = & f_c \\ & f_r \end{bmatrix} \tag{B.20}$$

The conductance matrix $[\boldsymbol{K}]$ consists of the conduction contribution $[\boldsymbol{K}_{ij}]$ from the thermal region besides the convection $[\boldsymbol{K}_c]$ and radiation $[\boldsymbol{K}_r]$ heat transfer. The convection and radiation matrices are computed only for elements with specified convection and radiation coefficients. The contribution from the heat conduction alone is defined as

$$[\boldsymbol{K}_{ij}] = \sum_{i=1}^{M_i}\sum_{j=1}^{M_j}\sum_{k=1}^{M_k}\kappa\sum_{n=1}^{3}\left[\left([\mathfrak{J}_{n1}]^{-1}\frac{\partial N_i}{\partial \xi} + [\mathfrak{J}_{n2}]^{-1}\frac{\partial N_i}{\partial \eta} + [\mathfrak{J}_{n3}]^{-1}\frac{\partial N_i}{\partial \zeta}\right)\cdot \left([\mathfrak{J}_{n1}]^{-1}\frac{\partial N_j}{\partial \xi} + [\mathfrak{J}_{n2}]^{-1}\frac{\partial N_j}{\partial \eta} + [\mathfrak{J}_{n3}]^{-1}\frac{\partial N_j}{\partial \zeta}\right)\right]|\mathfrak{J}|\, W_i\, W_j\, W_k \quad \text{(B.21)}$$

The capacitance matrix,

$$[\boldsymbol{C}] = \sum_{i=1}^{M_i}\sum_{j=1}^{M_j}\sum_{k=1}^{M_k}\rho C\boldsymbol{N}(\xi,\eta,\zeta)\boldsymbol{N}^T(\xi,\eta,\zeta)\,|\mathfrak{J}|\, W_i\, W_j\, W_k \quad \text{(B.22)}$$

is the time-derivative of the nodal temperatures and can be ignored if steady-state and not transient solution is required.

The convective and radiation equations are separated into two parts, with the part containing the unknown temperature nodals assembled into the $[\boldsymbol{K}]$ matrix as :

$$[\boldsymbol{K}_c] = \sum_{i=1}^{M_i}\sum_{j=1}^{M_j}\hbar_c\boldsymbol{N}(\xi,\eta)\boldsymbol{N}^T(\xi,\eta)\,|\mathfrak{J}_s|\, W_i\, W_j \quad \text{(B.23)}$$

$$[\boldsymbol{K}_r] = \sum_{i=1}^{M_i}\sum_{j=1}^{M_j}\boldsymbol{N}(\xi,\eta)\boldsymbol{N}^T(\xi,\eta)\epsilon_r\sigma_r(T_s(\xi,\eta)+T_\infty(\xi,\eta))\cdot (T_s^2(\xi,\eta)+T_\infty^2(\xi,\eta))\,|\mathfrak{J}_s|\, W_i\, W_j \quad \text{(B.24)}$$

The part of the equations with the known ambient temperature are put into the load vector on the *r.h.s* together with the computed heat flux $\boldsymbol{f}_{\dot{q}}$ as $\boldsymbol{f}_c$ and $\boldsymbol{f}_r$ for the convection and radiation loads respectively :

$$[\boldsymbol{f}_{\dot{q}}] = \sum_{i=1}^{M_i} \sum_{j=1}^{M_j} \sum_{k=1}^{M_k} \boldsymbol{N}(\xi,\eta,\zeta)\, \dot{q}\, |\mathcal{J}|\, W_i\, W_j\, W_k \tag{B.25}$$

$$[\boldsymbol{f}_c] = \sum_{i=1}^{M_i} \sum_{j=1}^{M_j} \hbar_c \boldsymbol{N}(\xi,\eta) T_\infty(\xi,\eta)\, |\mathcal{J}_s|\, W_i\, W_j \tag{B.26}$$

$$\begin{aligned}[\boldsymbol{f}_r] = \sum_{i=1}^{M_i} \sum_{j=1}^{M_j} & \boldsymbol{N}(\xi,\eta) \epsilon_r \sigma_r (T_s(\xi,\eta) + T_\infty(\xi,\eta)) \cdot \\ & (T_s^2(\xi,\eta) + T_\infty^2(\xi,\eta)) T_\infty(\xi,\eta)\, |\mathcal{J}_s|\, W_i\, W_j \end{aligned} \tag{B.27}$$

Appendix C

Trigonometric Identities

$$\sin(A \pm B) = \sin A \cos B \pm \sin B \cos A \tag{C.1}$$

$$\cos(A \pm B) = \cos A \cos B \mp \sin A \sin B \tag{C.2}$$

$$\tan(A \pm B) = \frac{\tan A \pm \tan B}{1 \mp \tan A \tan B} \tag{C.3}$$

$$2 \sin A \cos B = \sin(A + B) + \sin(A - B) \tag{C.4}$$

$$2 \cos A \cos B = \cos(A + B) + \cos(A - B) \tag{C.5}$$

$$2 \sin A \sin B = \cos(A - B) - \cos(A + B) \tag{C.6}$$

$$\sin^2 A + \cos^2 A = 1 \tag{C.7}$$

$$1 + \cot^2 A = \csc^2 A \tag{C.8}$$

$$\tan^2 A + 1 = \sec^2 A \tag{C.9}$$

$$\cos 2A = 1 - 2\sin^2 A \tag{C.10}$$

$$\cos 2A = 2\cos^2 A - 1 \tag{C.11}$$

$$\cos 2A = \cos^2 A - \sin^2 A \tag{C.12}$$

$$\sin 2A = 2\sin A \cos A \tag{C.13}$$

$$\sin^2 A = \frac{1 - \cos 2A}{2} \tag{C.14}$$

$$\cos^2 A = \frac{1 + \cos 2A}{2} \tag{C.15}$$

Appendix D

Steel Lamination Properties

D.1 Electrical Characteristics

Cobalt Iron

Resistivity = 4.200E-07 ohm-m

Permeability (refer to Table(D.1))

D.2 Iron Loss Characteristics

Iron loss coefficients, W/lb

k_e = 1.0995E-06, k_h = 0.0136, m = 1.6523, n = -0.0454

D.3 Structural Characteristics

Thickness = 29 gauge (0.3429 mm)

Density = 8150.000 kg/m^3

Young's Modulus = 2.000E+05 kN/mm^2

Yield Strength = 300.000 N/mm^2

Tensile Strength = 500.000 N/mm^2

D.4 Thermal Characteristics

Thermal conductivity = 30.000 W/m K

Specific heat capacity = 420.000 J/kg K

D.5 Measured B-H points provided by Vickers Systems

Table D.1: Non-linear B-H curve.

Point No.	B (T).	H (A-t/m).
1	0.0000	0.0000
2	1.0000	100.0000
3	1.1000	110.0000
4	1.2000	120.0000
5	1.3000	135.0000
6	1.4000	150.0000
7	1.5000	170.0000
8	1.6000	200.0000
9	1.7000	240.0000
10	1.8000	310.0000
11	1.9000	440.0000
12	2.0000	700.0000
13	2.1000	1250.0000
14	2.1500	1800.0000
15	2.2000	3200.0000
16	2.2500	6500.0000
17	2.3000	25000.0000

Appendix E

Linear Induction Machine

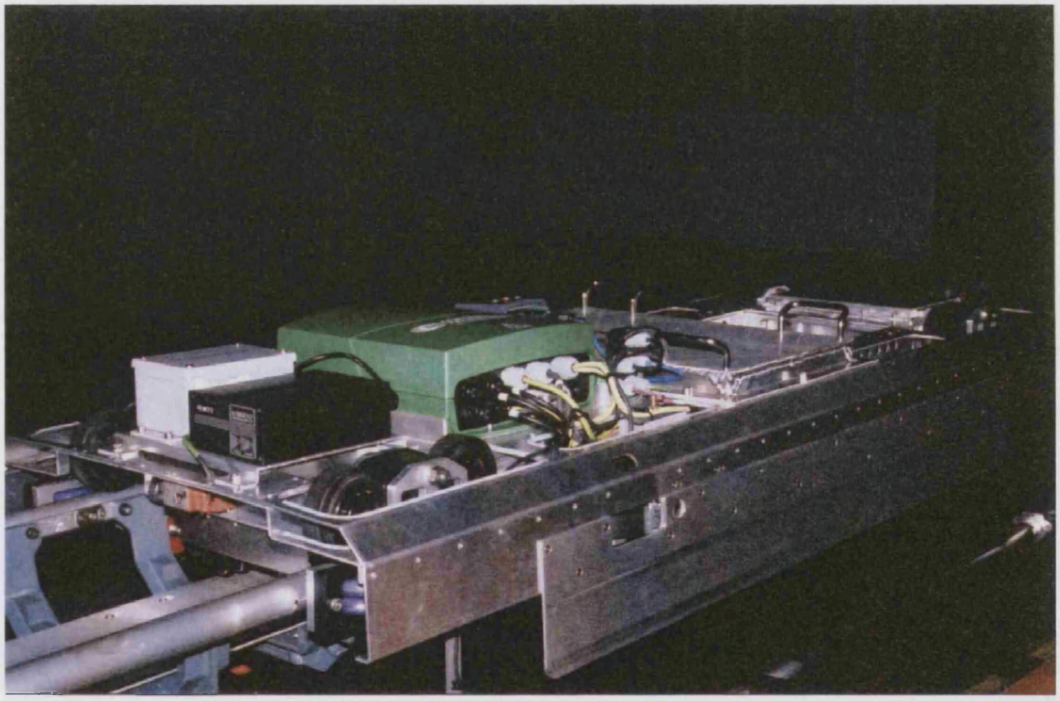

Figure E.1: Photograph of linear induction machine and drive. (Courtesy of Camera Tracking.)

Figure E.2: Photograph of straight aluminium track. (Courtesy of Camera Tracking.)

Figure E.3: Photograph of semi-circular aluminium track. (Courtesy of Camera Tracking.)

Appendix F

Related Publications

1. "Some Finite Element Models of the FLUXSET Sensor".
   Ref: Electromagnetic Nondestructive Evaluation (III), IOS Press, 1999.

2. "Parameterized Template Meshes for 2D and 3D Finite Element Modelling".
   Ref: IEEE Transactions on Magnetics, vol.36, no.2, July 2000.

3. "Optimization of Electromagnetic Devices using Parameterized Templates".
   Ref: IEEE Transactions on Magnetics, vol.37, no.5, September 2001.

4. "Finite Element Models of Eddy Current Brakes".
   Ref: IEE Computation in Electromagnetics (CEM 2002), no.02/063, April 2002.

5. "On Modelling Weakly Coupled Electromagnetic-Thermal Problems with Prescribed Non-linear Surface Heat Transfer".
   Ref: IEE Power Electronics, Machines and Drives (PEMD 2002), no.487, April 16-18 2002.

6. "Coupled Electromagnetic-Thermal Modelling of Electrical Machines".
   Ref: 10th Biennial IEEE Conference on Electromagnetic Field Computation (CEFC 2002), Perugia Italy, June 16-19 2002.

Some Finite Element Models of the FLUXSET Sensor

D.Rodger and P.K.Vong
University of Bath, Claverton Down, Bath, BA2 7AY, UK

Abstract. Some finite element models of a FLUXSET sensor are described. These are of varying degrees of complexity and can take into account magnet non-linearities and eddy currents in the amorphous ribbon material. Results from volume and thin sheet methods are compared.

1 Introduction

The FLUXSET sensor consists of a strip of amorphous alloy ribbon with a set of excitation coils and pick up coils wrapped around it. A typical arrangement is shown in Figure 1. In this contribution various finite element techniques for modelling the FLUXSET are compared.

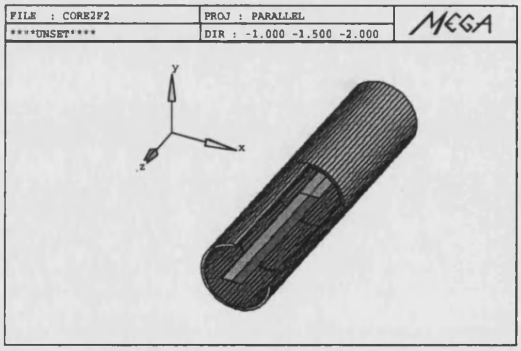

Figure 1: A FLUXSET sensor.

2 Finite Element Formulations

Nodal variable finite elements are described here, non-conductors are modelled in terms of magnetic scalar potentials and conductors are modelled using magnetic vector potentials.

2.1 Non-conductors

Non-conducting regions may be modelled economically in 3D using magnetic scalar potentials, either the total scalar ψ ,defined as $\mathbf{H}_T = -\nabla\psi$, or the reduced scalar ϕ, defined as $\mathbf{H}_T = -\nabla\phi + \mathbf{H}_S$. Here $\mathbf{H}_T$ is the total magnetic field intensity and $\mathbf{H}_S$ is the field defined as $\nabla\times\mathbf{H}_S = \mathbf{J}_S$, where $\mathbf{J}_S$ is the source current density. The basic total and reduced scalar method can be extended to allow multiply connected conditions [1], and to produce cuts for solving multiply connected problems. Both scalars give rise to a Laplacian type equation which has to be solved:

$$\nabla\cdot\mu\nabla\psi = 0 \tag{1}$$

2.2 Thin Non-conducting Regions

The ribbon is thin compared with the other dimensions (20μ m compared with a length of 9mm), it is therefore useful to consider using a thin sheet formulation for the ribbon. The formulation described here has been shown to compare favourably with measurements around thin iron sheets, of thickness comparable to an electrical machine lamination [2], here we show that it is applicable to amorphous material. If the conductivity of the ribbon may be assumed to be zero as was done in [3],[4], all of the regions may be modelled using magnetic scalar potentials, either total or reduced. Thin elements are required in the ribbon. This may give rise to numerical ill-conditioning or an excessively fine mesh. In order to avoid this, the thin high permeability ribbon can be modelled as a sheet, as follows: The Galerkin method applied to the Laplace equation yields,

$$\int_{V_e} \nabla N_i \cdot \mu\nabla\psi \,\mathrm{d}V = \int_{\Omega_e} \mu N_i \frac{\partial\psi}{\partial n} dS \tag{2}$$

In a thin region, the volume integral in (2) may be replaced by

$$\int_{\Omega_e} h\left[\frac{\partial N_i}{\partial s}\mu\frac{\partial\psi}{\partial s} + \frac{\partial N_i}{\partial t}\mu\frac{\partial\psi}{\partial t}\right] ds dt \tag{3}$$

In (3) s and t are two tangential directions on the sheet surface and h is the thickness of the sheet. This implies that the field is constant across the thickness of the sheet. The boundary conditions for ψ on the sheet surface are exactly the same as those which would be applied to a volume region under the same conditions.

2.3 Conducting Regions

Fields in conductors can be modelled using $\mathbf{A}$, the magnetic vector potential, and V, the electric scalar potential. In regions of constant conductivity, surrounded by

magnetic scalar potential, it is sometimes possible to avoid using V. In this case, using $\mathbf{B} = \nabla \times \mathbf{A}$ and $\mathbf{E} = -\frac{\partial \mathbf{A}}{\partial t}$, we obtain

$$\nabla \times \frac{1}{\mu} \nabla \times \mathbf{A} = -\sigma \frac{\partial \mathbf{A}}{\partial t} \tag{4}$$

2.4 Time Transient Conditions

Application of the Galerkin technique and 3D finite elements to (1) and (4) results in a system of equations which has the following standard form,

$$[\mathbf{K_a}]\boldsymbol{x_a} + [\mathbf{C_a}]\dot{\boldsymbol{x}}_a = \boldsymbol{f_a} \tag{5}$$

in which $\boldsymbol{x_a}$ is a vector of the unknown ψ and $\mathbf{A}$ variables.This is solved as follows: Calculate $\boldsymbol{\alpha}_n$ from

$$\boldsymbol{\alpha}_n = ([\mathbf{C_a}] + \Theta \Delta t [\mathbf{K_a}])^{-1} \{\boldsymbol{f}_{an} - [\mathbf{K_a}]\boldsymbol{x}_{an}\} \tag{6}$$

Then calculate the new $\boldsymbol{x_a}$

$$\boldsymbol{x}_{an+1} = \boldsymbol{x}_{an} + \boldsymbol{\alpha}_n \Delta t \tag{7}$$

When non-linear materials are involved, (5) becomes non-linear and is solved using standard iteration techniques, such as Newton Raphson [5] or simple iteration.

3 Results

A device with the same dimensions as that given in [3] and[4] was modelled using both a conventional volume 3D finite element scheme and also the thin sheet method. Main dimensions are given in Table 1.

Figs 2 and 3 show the normal and axial components of $\mathbf{B}$ along the centre line of the ribbon, plotted from the centre to one end. Both volume and sheet finite elements were used for the calculations. Here the conductivity of the ribbon was neglected. A constant unsaturated ribbon permeability was used. Exploiting symmetry, only one eighth of the device had to be modelled. The results show that both methods give similar results.

4 Response to External Fields

In this section it is assumed that the conductivity of the ribbon may be taken to be zero. The magnetic non-linearity is taken into account. The FLUXSET is intended to be used to measure magnetic fields and is intended to respond only to the axial component of external field. Here we confirm that this is likely to be the case.

Table 1: FLUXSET dimensions

drive coil i.d. m	2 mm
drive coil length	9 mm
drive coil turns	470
pick up coil i.d.	2 mm
pick up coil length	5 mm
pick up coil turns	100
ribbon length	9.5 mm
ribbon thickness	20μm
ribbon width	0.6 mm
ribbon conductivity	1×10^5 S/m
ribbon ribbon relative permeability magnitude $B = 0 - 0.65T$	85000
ribbon ribbon relative permeability magnitude $B > 0.65T$	1

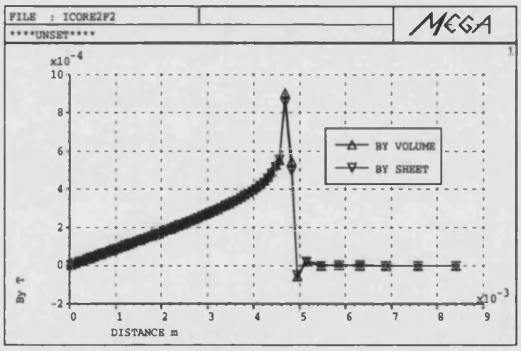

Figure 2: B_y just above the ribbon.

4.1 Axial External Fields

The FLUXSET was modelled immersed in various axial external fields. Fig 4 shows the average magnetic flux in the pickup coil for external fields of 0 and 200 μT respectively. Multiplication of this graph by the pickup coil turns and differentiation with respect to time gives the pickup coil voltage, which is the desired output of the device. Also shown on Fig 4 is the triangular drive coil current (peak 12mA). The resultant pickup coil voltage is shown on Fig 5.

4.2 Non-axial External Fields

In order to find out whether the device will measure only the axial component of field, or whether it would be affected by transverse components of field, the device

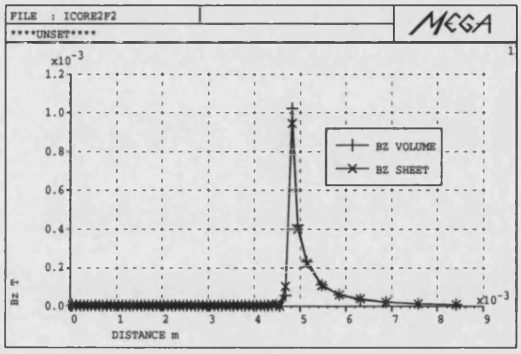

Figure 3: B_z just above the ribbon.

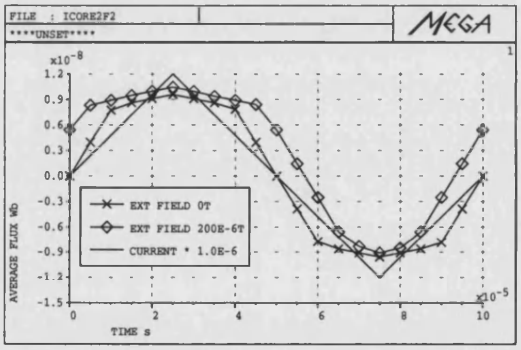

Figure 4: Average flux in the pick up coil.

was modelled while placed in an external magnetic field at various angles to the axis of the device. Fig 6 shows results for a 200 and 20 μT external field at an angle of 45° to the ribbon axis. Also shown are results for two uniform axial fields of magnitude 200 $\cos(\pi/4)$ and 20 $\cos(\pi/4)$. The results are identical, which would confirm that the device is unaffected by transverse fields. The numerical test carried out here is more stringent than required, considering what will happen in reality, since the permeability in the transverse direction of the real ribbon material is much poorer than in the axial direction. In the numerical test, the same permeability was used in both directions.

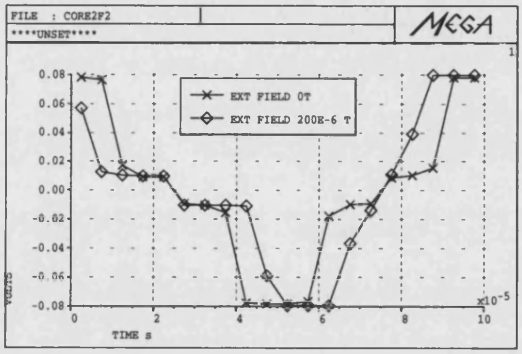

Figure 5: Volts in the pick up coil.

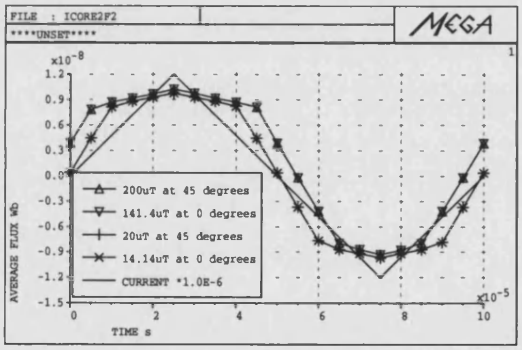

Figure 6: Average flux for various transverse fields.

5 Eddy Current Simulation

Consideration of the classical eddy current skin depth, $\delta = \sqrt{2/(\omega\sigma\mu)}$ implies that at 100kHz δ is around 17μm, comparable with the thickness of the ribbon. A time transient simulation was therefore carried out, allowing eddy currents to flow in the ribbon but allowing the permeability to remain constant, to save computer time. The drive coil current was as already described. Fig 7 shows that there is negligible eddy current effect at this frequency. The average magnetic flux in the pick up coil is shown for both conducting and non-conducting ribbons; these are substantially identical.

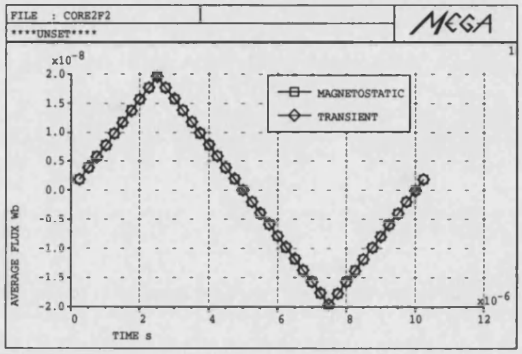

Figure 7: Time transient solution at 100kHz.

6 Conclusions

It has been shown that the thin sheet method can be useful for modelling amorphous ribbon material in that results are similar to those of volume elements and computer times are faster. Preliminary work appears to indicate that transverse fields do not adversely affect the described FLUXSET sensor. Since the device is 'long and thin', it behaves in a similar way to the classical long magnetic rod in a uniform field.

Acknowledgement Work supported by EU contract IC15-CT96-0703.

References

[1] P.J.Leonard and D.Rodger. "Modelling voltage forced coils using the reduced scalar potential method". *IEEE Trans. Magn.*, 28(2):1615–1617, March 1992.

[2] D.Rodger, P.J.Leonard, and H.C.Lai. "Surface elements for modelling 3D fields around thin iron sheets". *IEEE Trans. Magn.*, 29(2):1483–1486, 1993.

[3] D.Ioan, M.Rebican, G.Ciuprina, and P.Leonard. "3D FEM model of a fluxset sensor". *E'NDE 97 Proc, Reggio Calabria ITALY*, September 1997.

[4] K.Preis, I.Bardi, J.Pavo, A.Gasparics, I.Ticar, O.Biro, and K.Richter. "Numerical simulation and design of a fluxset sensor by finite element method". *IEEE Trans. Magn.*, 34(5):3475–3478, September 1998.

[5] D.Rodger, N.Allen, H.C.Lai, and P.J.Leonard. " Calculation of transient 3D eddy currents in non linear media - Verification using a rotational test rig". *IEEE Trans. Magn.*, 30(5):2988–2991, September 1994.

Parameterized Template Meshes for 2D and 3D Finite Element Modelling

D. Rodger, R.J. Hill-Cottingham and P.K. Vong
Applied Electromagnetics Research Centre, University of Bath, Claverton Down, BATH. BA2 7AY

***Abstract*—A new parameterization technique which allows rapid alteration of an initial template 2D or 3D finite element mesh is described. An advantage of this method is that once a template mesh has been set up, new devices similar to that of the template can be modelled easily by altering the contents of a simple form or file. These alterations can be easily carried out by a casual user or by an optimization program.**

I. Introduction

Many users of finite element packages have very little time to spend on this noble activity. On the other hand, many electrical device designers like to explore various candidate devices particularly at an early stage in their deliberations. Very often in the case of devices like electrical machines and transformers, all of these candidate designs will be very similar to each other in appearance, differing only in small details such as tooth width, tooth number, rotor diameter and so on.

A few software packages address this problem via automatic meshing, perhaps also coupled with automatic refinement based on some error criterion. Often this results in very large meshes, usually due to the poor quality of elements which must be used in most automatic mesh generators, nearly always triangles for 2D and tetrahedrons for 3D.

This paper describes a new parameterization technique which allows alteration of an initial generic template mesh to be carried out while retaining the freedom to choose the type of elements and mesh density. An advantage of this method is that once a template mesh has been set up, new devices similar to that of the template can be modelled easily by altering the contents of a simple form or file. A device as complex as an induction machine is then modelled using no more than a design sheet containing a list of parameters which describe the basic dimensions of the machine and the names of the non linear material curves. A disadvantage of this method is that it would be of little use in optimizing the design of a device where the final shape was completely unknown in advance. This situation is unusual however, for instance most electrical machines of a given type look very similar to each other.

Manuscript received Oct 25, 1999.

In this paper the method is described and a case study is cited as an example. The example, that of cogging torque in a brushless permanent magnet servo machine, is of interest as it is commercially very important. It is also an example of a case in which automatic mesh generators do not perform particularly well, as the required force is relatively small and must be calculated accurately.

II. The Template Mesh Technique

The template mesh method is straightforward and could be implemented in most finite element software. The method is based on producing a monitor (or log) file while the initial mesh is created.

The main steps in mesh creation are as follows:

- A list of parameter names and values is created. Parameters may be simple values, or functions of other parameters. This would enable changing (say) the rotor diameter of a rotating machine while keeping the stator radial dimensions constant.
- The template mesh is created in the usual way employing the user's favourite techniques, the only extra requirement is that where required, any quantity which would normally be entered as a character string, integer, real or complex number is entered as the parameter name.
- A monitor file is used to record all the actions which took place in creating the mesh. The trick which allows the template mesh scheme to work is that spatial information in the file is accompanied by node or element number information in a separate auxiliary file. This spatial information may perhaps be a node or point position. For instance if all the elements within a certain polygonal boundary have been marked for refinement at the creation stage, the identifiers of the elements which are affected by this operation are stored in the auxiliary file. Since any spatial information is useless when dimensions of the mesh have been changed, the number information from the auxiliary file is used as input to the program on second and subsequent runs of the monitor file.

In order to change the template mesh, the steps are as follows:

- The parameter values are changed as necessary.

- The monitor file which creates the mesh is run again. The mesh is then built up in the same way as before but this time uses all of the new values from the parameter file. The program ignores any spatial information in the monitor file and uses the invariant number data in the auxiliary file.

This 'alter and run again' phase is very easily automated and can be controlled by a user or by an optimization program.

III. Modelling with Parameterization Case Study

Cogging torque in a brushless permanent magnet servo motor is used as an example. For a rotating electrical machines problem, it is very convenient to use two distinct meshes, one for the stationary stator, and the other for the moving rotor. The electromagnetic unknowns are coupled across a common interface in the air gap using Lagrange multipliers [1].

During the meshing process all the radii, angles, tooth width, magnet width etc of the stator and rotor are parameterized so as to provide geometrical flexibility. In this example, 13 parameterized values are implemented for the stator while the rotor has 7 values. An example of the parameterized values in a parameter file is shown in Table I. Fig. 1 shows the 13 parameterized values used in describing the geometry of a half stator slot. Obviously more parameters can be used for a more complex geometry. It may be observed from Table I that some parameters depend on others, it is often convenient to define some parameters as simple geometric expressions involving some of the other parameters and constants such as π, written as PI in the list. The values of the parameters must be found before use by using an internal calculator in the finite element mesh generator, if this is not available some other program could be used as a preprocessor. It is important that the calculator is able to deal with finding the values of the parameters if they are presented to it in any order, it is too difficult for a user to present the list in such a way that all the independent parameters are resolved first, followed by all the dependent parameters in the correct order. This is easily carried out by making sure that the calculator passes through the list several times from appropriate starting points.

Other methods for generating values from parameters have been described, among them, algebraic methods [2] and variational geometry methods.[3]. All of these probably have their merits, and any of them could easily be slotted into the template mesh technique described here.

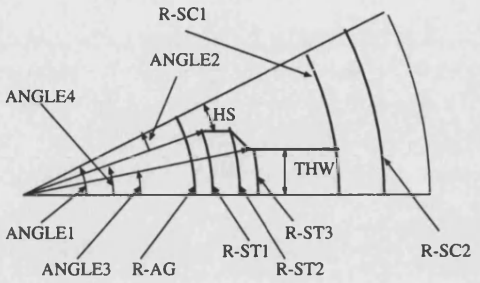

Fig. 1. Simple geometry of a half stator slot.

Table I
Monitor File for Stator Mesh

Parameter No.	Variables.	Values.
1	R-AG	25.5e-3
2	R-ST1	26.0e-3
3	R-ST2	28.0e-3
4	R-ST3	29.0e-3
5	R-SC1	39.7e-3
6	R-SC2	45.0e-3
7	NTEETH	9.0
8	THW	5.25e-3
9	HS	1.25e-3
10	ANGLE1	180/NTEETH
11	ANGLE2	(HS/R-ST1)*(180/PI)
12	ANGLE3	ASIN(THW/R-ST3)*(180/PI)
13	ANGLE4	(ANGLE1-ANGLE2)

In the FE program the rotor and stator template mesh would typically consist only of one half pole or half slot pitch. The complete machine (or a periodic section of it) is then created by appropriate duplication of the template mesh. The number of teeth (or magnets etc) required is itself a parameter and therefore can easily be altered. The user will have the flexibility of changing or redesigning the machine rapidly. Fig. 2 shows, for clarity, a very coarse mesh. This gives an idea of the parameters which can be altered.

Various slot/pole combinations can be built easily. Fig. 3 and Fig. 4 are motors with 9/6 and 18/8 slots and poles respectively. In this case, the meshes were generated from a common template mesh by changing just two parameters. The creation process itself took less than one second for each mesh.

There are many combinations of slot/pole numbers that can be used effectively. Fig. 5 and Fig. 6 show the 2D predicted results of various slot/pole combinations. The graphs of torque versus rotor position are very easily generated, the amount of rotation and the rotor increment

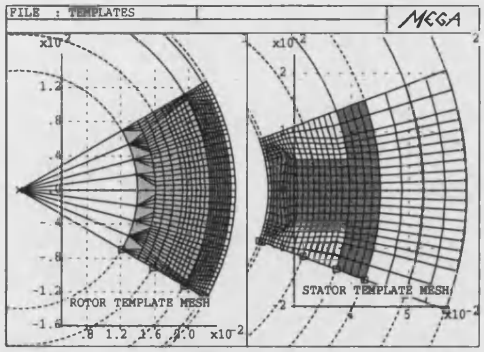

Fig. 2. Parameterized templates.

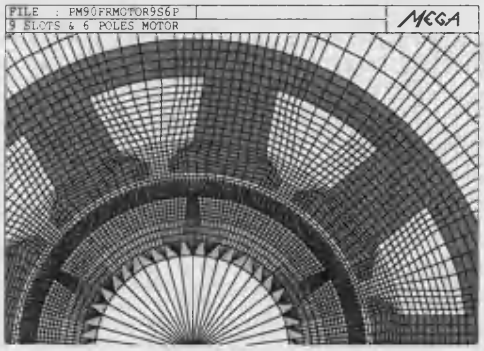

Fig. 3. 2D FE model of 9 slots and 6 poles motor.

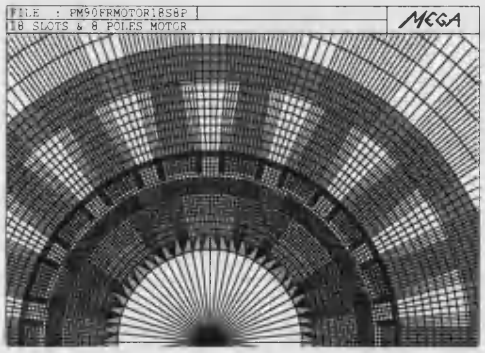

Fig. 4. 2D FE model of 18 slots and 8 poles motor.

are parameters which can be altered to suit the purpose. The cogging torque is particularly significant when the number of stator slots is an integer multiple of the rotor poles, avoiding this situation is beneficial.

It is also possible to minimize cogging torque by select-

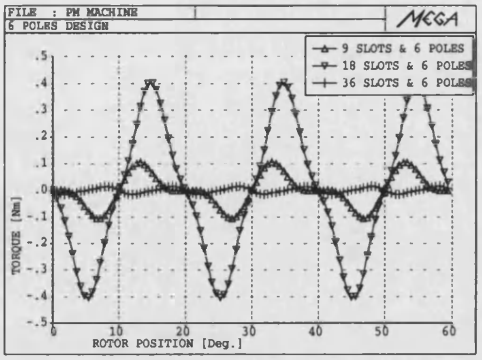

Fig. 5. Predicted cogging torque for 6 poles motor with three different slot numbers.

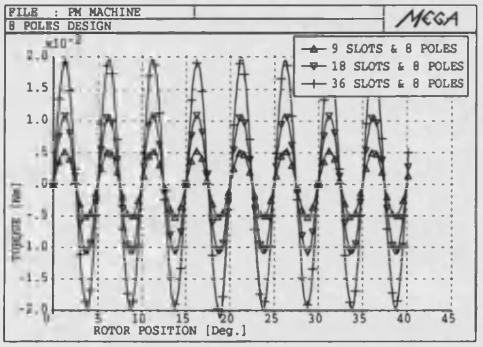

Fig. 6. Predicted cogging torque for 8 poles motor with three different slot numbers.

ing an appropriate magnet pole arc. The width of the arc is significant since the cogging torque is due to the interaction of the edges of the magnet poles and the stator teeth. The overall cogging torque is the summation of all forces at each of the magnet edges. Fig. 7 shows the 2D predicted cogging torque for the 18 slots/8 poles machine for various different pole arcs.

Finally the 18 slots and 6 poles motor which has the worst cogging torque is expanded into a 3D model and solved. The results in Fig 8 show that good agreement is obtained in the 2D and 3D models. To reduce the cogging torque the stator of the motor is skewed one slot pitch as shown in Fig. 9. Only one parameter has to be altered in order to change the skew angle in the 3D model, this is possible because the method used in [1] allows the rotor and stator meshes to be incompatible.

Fig. 10 show the reduced cogging torque due to the stator skewing technique. The unwanted torque is about 40 times smaller. Skewing has the effect of reducing the permeance variation seen by the rotor magnets and hence

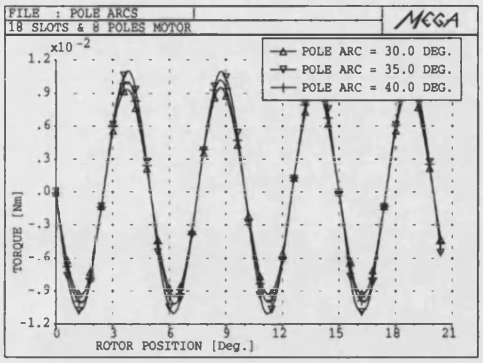

Fig. 7. Predicted cogging torque for various pole arcs.

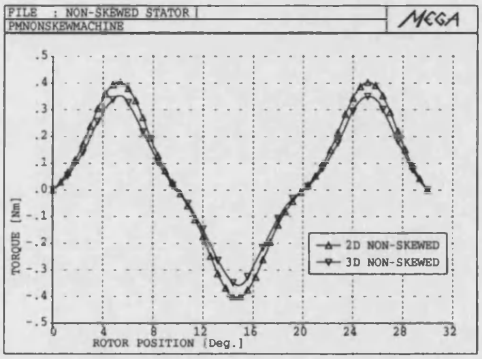

Fig. 8. Predicted cogging torque for 2D and 3D FE models of non-skewed PM motor.

the cogging torque.

This simple and yet effective technique does have its drawbacks. By opting for this technique, losses in the average torque, increased leakage inductance and a more complex motor construction are unavoidable.

IV. Conclusions

A parameterization technique is described. The geometrical dimensions can be altered rapidly for designing various types of electromagnetic device. The method should be useful in both manual and computer controlled optimization.

As an example the technique is used to address a major concern in permanent magnet machines; cogging torque. The ability of the parameterization technique to rapidly alter machine dimensions enables designers to examine various options quickly by using old fashioned 'cut and try' methods. The technique can also be easily used along with a computer optimisation method so that designs can be automatically generated.

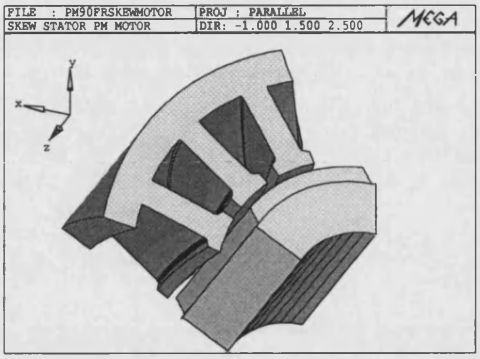

Fig. 9. 3D FE model of PM motor with skewed stator.

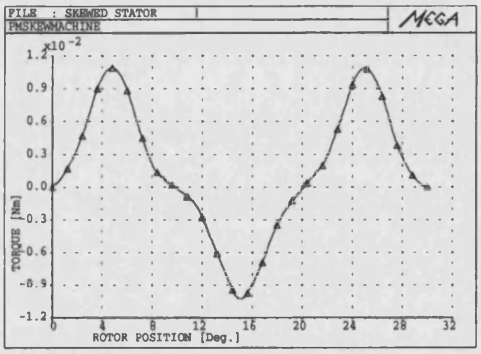

Fig. 10. Predicted cogging torque for 3D FE model of skewed PM motor.

The method differs from most others in that the mesh can be generated using any technique, anything from a full automatic mesh generator to manual methods can be used. This allows the user a great deal of control over mesh quality, once a good mesh is created it can be recycled for similar geometries.

A disadvantage of the method is that all the meshes derived from a given template will be topologically similar to it, this means that designs which differ greatly from each other cannot be generated.

References

[1] D.Rodger, H.C.Lai and P.J.Leonard. "Coupled elements for problems involving movement". *IEEE Trans. Magn.*, 26(2):548-550, March 1990.

[2] K.Kondo. "Algebraic method for manipulation of dimensional relationships in geometric models". *Computer Aided Design*, 24:141-147, March 1992.

[3] C.F.Parker, J.K.Sykulski and S.C.Taylor. "Parametric environment for em computer aided design". *IEEE Trans. Magn.*, 32(3):1433-1436, May 1996.

Optimization of Electromagnetic Devices using Parameterized Templates

P.K. Vong, H.C. Lai and D. Rodger

Abstract—**A parameterization technique for use in optimizing electromagnetic devices is described. The method allows a rapid alteration of an initial template 2D or 3D finite element mesh of an electromagnetic device so that design studies or optimization can be conveniently carried out. Two case studies are described. The examples consist of the voltage generated by a wound rotor generator and the performance of a Fluxset magnetic field measuring device.**

Keywords— **Electromagnetic analysis, Finite Element Methods, Optimization methods.**

I. Introduction

THIS paper describes a new parameterization technique which allows alteration of an initial generic template mesh to be carried out while retaining the freedom to choose the type of elements and mesh density. The first step consists of setting up a 2D or 3D finite element model of the problem, with all the dimensions which are required to vary defined as input parameters. Once the template mesh is set up, new devices similar to the template can be modelled easily by altering the parameter input file. This simple design sheet contains a list of parameters which describe the basic dimensions of the device and names of the non linear material curves.

A few software packages address this problem via automatic meshing, perhaps also coupled with automatic refinement based on some error criterion. Often this results in very large meshes, usually due to the poor quality of elements which must be used in most automatic mesh generators, nearly always triangles for 2D and tetrahedrons for 3D.

In this paper two case studies are described. The examples consist of the voltage generated by a wound rotor generator and the performance of a Fluxset magnetic field measuring device.

II. The Template Mesh Technique

The technique allows the user to create a string of parameters in an auxiliary file [1]. These parameters may be simple geometric values or functions of other parameters. A monitor file is used to record all the actions which took place when the user creates the initial template mesh.

In creating the template the user enters the parameter name while describing the device dimensions instead of the usual numerical values. Once the parameters are altered and the program rerun, the monitor file will initiate the sequence of events in creating the new mesh. The optimization stage can be carried out either under human designer control, here the user observes the results of previous solutions and alters values in the parameter file, or it could be computer controlled, where the parameter file is altered by a program according to the requirements of an optimization algorithm.

Results produced by the manual method and one optimization method, the Nelder Mead Simplex algorithm [2], are compared.

Manuscript received June 6, 2000. The authors are with the Department of Electronic and Electrical Engineering, University of Bath, BATH. BA2 7AY UK. E-mail eeppkv@bath.ac.uk, d.rodger@bath.ac.uk, h.c.lai@bath.ac.uk

III. Parameterized templates for modelling a synchronous generator

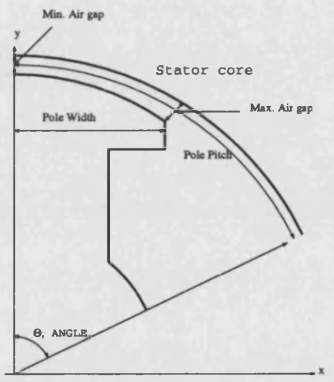

Fig. 1. Pole configuration.

During the template meshing process all the radii, pole/slot angles, tooth width, pole arc, pole pitch etc of the stator and rotor are parameterized to provide geometrical flexibility. A parameterized template with several parameter constraints is shown in Fig. 1. These parameterized values are contained in a simple ASCII file. They can either be defined by using simple geometric expressions or input values entered by the user. Some of the parameters involved are defined as expressions in terms of other parameters and constants.

For rotating electrical machinery problems, it is very convenient to use two separate meshes, one for the stationary stator, and the other for the moving rotor. The electromagnetic unknowns are coupled across a common interface in the air gap using Lagrange multipliers [3].

The rotor and stator templates would typically consist of half a pole/slot pitch or a periodic section of the entire machine. The complete machine is then created by appropriate duplication of the template mesh. The number

of rotor poles or stator slots required is itself a parameter and therefore can be altered easily. This enables the user to rapidly redesign the machine.

A. Human controlled design

The object of a good design includes maximizing the first harmonic voltage while also minimizing the amplitudes of all the other harmonics. A human designer soon becomes swamped if the number of variables in a design problem is high. Here we simplify the problem by using a classical design method [4] which uses experience and analytical techniques to describe the problem in terms of three variables.

In designing the synchronous generator, the pole shapes are constrained by the following three variables:

$$Var.X = \left[\frac{Pole\ \ Width}{Pole\ \ Pitch}\right] \qquad 0.50 \leq Var.X \leq 0.75$$

$$Var.Y = \left[\frac{Max.\ \ Air\ \ gap}{Min.\ \ Air\ \ gap}\right] \qquad 1.0 \leq Var.Y \leq 3.0$$

$$Var.Z = \left[\frac{Min.\ \ Air\ \ gap}{Pole\ \ Pitch}\right] \qquad 0.01 \leq Var.Z \leq 0.05$$

The pole surface is constrained to be of cylindrical shape, the dimensions of which are defined by the max. and min. air gaps shown on Fig. 1. For machines with a small air gap, $Var.Z$ can be fixed. We maintained $Var.Z$ at 0.015 throughout the investigation, as recommended in [5]. These three variables are parameterized and stored in the geometry monitor file. Changes in one of the ratios results in a new generator pole with the required pole pitch, pole arc and air gap size. Different pole shapes are generated easily for harmonic analysis of the induced voltage at no load.

The triplen harmonics {3rd harmonic and multiples of it} can be ignored since they virtually cancel each other out at the terminals of the 3-phase Y-connected generator. Since even harmonics do not exist and triplen harmonics are naturally cancelled, we are left with the 'belt harmonics' of 5th and 7th, and 'slot harmonics' of 11th and 13th. A fractional coil pitch design has greatly reduced the 5th and 7th harmonics. The slot harmonics of 11th and 13th cannot be suppressed by a coil short pitching and distribution method. Using pole surface shaping, we hope to suppress the slot harmonics and achieve a further reduction in the belt harmonics without having to rearrange the coil structure.

Twenty five designs were generated, with $Var.X$ and $Var.Y$ varying as shown in Figs. 2 - 6. The BH characteristics of the iron parts were non linear (standard lamination curves).

Fig. 2 shows the generated fundamental voltages while Fig. 3, Fig. 4, Fig. 5 and Fig. 6 show the harmonic voltages. A large reduction of harmonic voltages is achieved especially in the 11th harmonic when $Var.X = 0.71$. However, the magnitude of the fundamental voltages generated are lower. A trade off between harmonic reduction and fundamental magnitude of generated voltage has to be found.

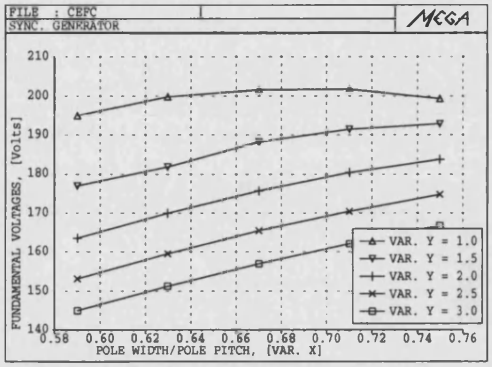

Fig. 2. Generated fundamental voltages.

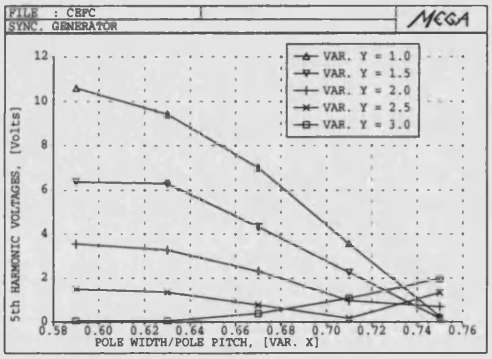

Fig. 3. Generated 5th harmonic voltages.

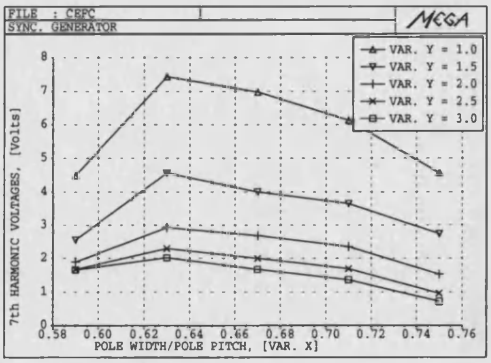

Fig. 4. Generated 7th harmonic voltages.

Table I shows the percentage of the Total Harmonic Distortion (**THD**) of the generated voltages. **% THD** is

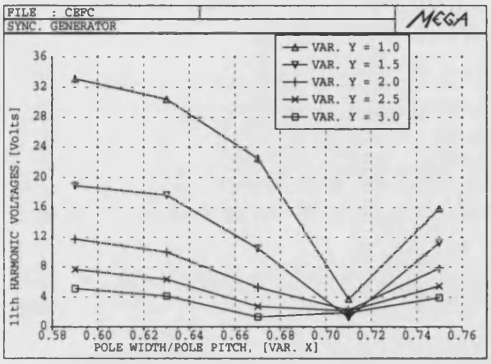

Fig. 5. Generated 11th harmonic voltages.

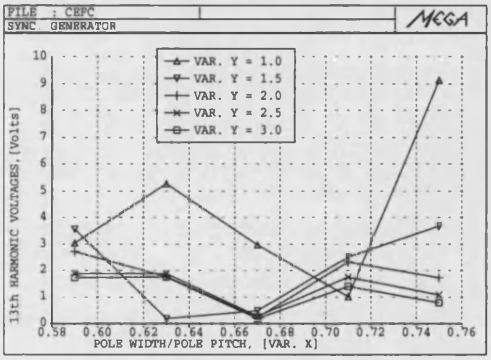

Fig. 6. Generated 13th harmonic voltages.

TABLE I
% TOTAL HARMONIC DISTORTION.

	Var.Y				
Var.X	1.0	1.5	2.0	2.5	3.0
0.59	18.1	11.5	7.8	5.4	3.9
0.63	16.6	10.6	6.5	4.5	3.3
0.67	12.3	6.4	3.6	2.1	1.4
0.71	4.0	2.7	2.3	1.9	1.8
0.75	9.5	6.3	4.5	3.3	2.7

defined as

$$\% \ \mathbf{THD} = \frac{1}{V_1}\left(\sqrt{\sum_{h\neq 1}^{\infty} {V_h}^2}\right) \times 100 \qquad (1)$$

where V_1 is the fundamental RMS value of voltage and V_h is the harmonic RMS values of voltage.

Using the information in Table I, a machine designer would probably choose values of $Var.X$ and $Var.Y$ around 0.71 and 3.0 respectively.

All the models so far are in 2D, for 3D modelling we used the 2D mesh as a base plane and extrude it into the required length. Fig. 7 shows the complete model with coils placed in the stator and rotor. Fig. 8 compares the generated voltages of the 2D and 3D finite element models for $Var.X = 0.71$ and $Var.Y = 3.0$. It may be observed that the finite length effects in the 3D model give rise to slightly different results from 2D, but that the effects are not large. The results suggest that a good design strategy would be to use 2D models to 'home in' close to an optimal design, and then use 3D to finish the study.

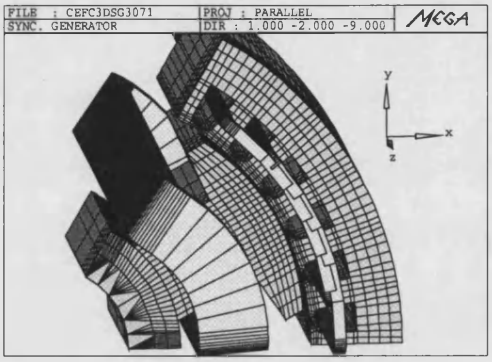

Fig. 7. Wound rotor generator.

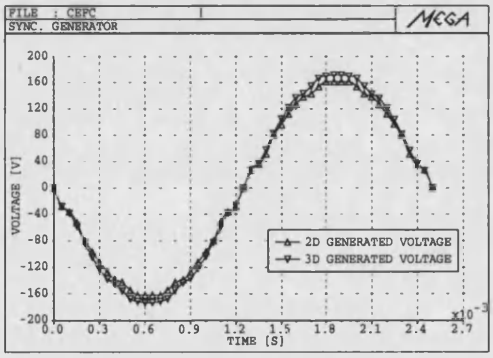

Fig. 8. Calculated induced voltages.

B. Computer controlled design

The variables $Var.X$ and $Var.Y$ were also optimized by a fully automated optimization technique using the Downhill Simplex algorithm [2]. The quantity to minimize is the **THD** in (1). Our finite element program is used to evaluate the objective function at the sampling point generated by the optimization program. This involves, for each step of the optimization, setting up a mesh according to the latest information, solving the problem, and post-processing the result using the interactive post-processing program. All of this is controlled by simple scripts and requires no

intervention once started.

Table(II) shows the initial value of **THD** at the corner of the starting simplex and also the final value.

TABLE II
SHOWING THE STARTING AND FINISHING SAMPLING POINTS.

	$Var.X$	$Var.Y$	THD
Starting corner 1	0.7	2.0	0.0367
Starting corner 2	0.72	1.8	0.0515
Starting corner 3	0.74	1.6	0.0701
Final	0.696	2.041	0.0322

Fig.(9) shows how the value of the objective function decreases with the optimization iterations.

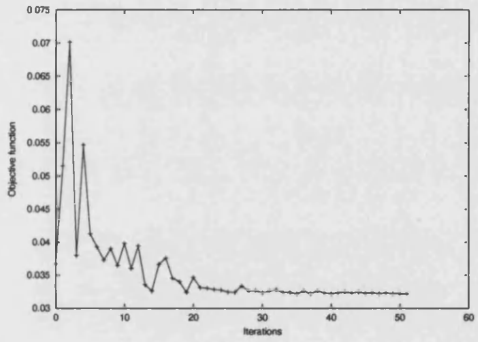

Fig. 9. Decrease of the objective function.

This shows that the automated system predicts an optimum in the same area as a machine designer would. The optimum is of course lower in the former case, since the 'human' optimum found in the previous section is based on a fairly coarse sweep of the available parameters.

Optimizing only the **THD** as in (1) resulted in a fairly low value of first harmonic, around 160-170 Volts. The optimization scheme was run again, allowing $Var.X$, $Var.Y$ and $Var.Z$ to vary. The objective was to minimize **THD** and also to maximize the fundamental component. This resulted in values of $Var.X$, $Var.Y$, $Var.Z$ and fundamental of voltage to be 0.51, 1.0, 0.01 and 208 respectively.

IV. Fluxset sensor

The Fluxset sensor is described in [6], it consists of a driving solenoid and pick up coil, concentric with a metallic glass core. The core in [7] has an approximately piecewise linear BH curve of $\mu_r = 85000$ for $|B| < 0.65$ T and $\mu_r = 1.0$ thereafter. The driving solenoid is fed with current with a triangular waveform, an external field produces more saturation in one direction along the ribbon than the other, hence a time shift in induced EMF which can be measured.

The device was modelled using the parameterized templates technique, while immersed in an axial external field of $200\mu T$. In optimizing the design, only the ribbon length is varied. Results for the average flux in the are shown in Fig 10. Since the pickup coil voltage depends on the time differential of this flux, it may be observed that more signal results from the longer core. Although a 3D mesh is required, the template method simplified this process greatly, as it only had to be generated once.

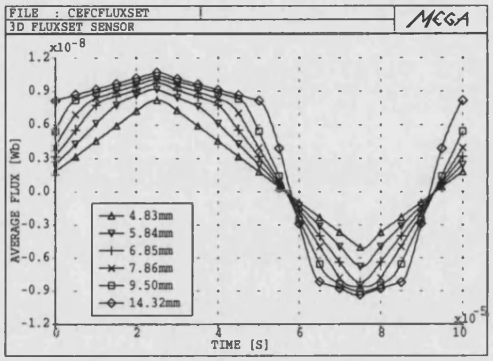

Fig. 10. Average flux in the pick up coil.

V. Conclusion

The finite element method has been used for many years for optimization. It is usually very easy to move a few nodes (particularly in 2D), but other changes can be very awkward. The method described here makes it easy to make global changes to a mesh, such as altering the number of teeth, pole pitch etc. It is therefore useful for electrical machine design, based on either computer controlled optimization or on design studies based on running many cases.

Acknowledgments

This work is partly supported by the INCO-COPERNICUS Project PL 964037 of the EC.

References

[1] D.Rodger, R.J.Hill-Cottingham and P.K.Vong, *Parameterized Template Meshes for 2D and 3D Finite Element Modelling*, IEEE Trans. Magn., vol.36, no.4, July 2000, pp.1610-1614.

[2] J.A.Nelder and R.Mead, *Computer Journal*, vol.7, 1965, pp.308-311.

[3] D.Rodger, H.C.Lai and P.J.Leonard, *Coupled Elements for Problems Involving Movement*, IEEE Trans. Magn., vol.26, no.2, March 1990, pp.548-550.

[4] D.Ginsberg, *Graphical Determination of Magnetic Fields*, AIEE Trans., vol.26, 1927, pp.141-154.

[5] D.Ginsberg, *Design Calculations for A-C Generators*, AIEE Trans., vol.69, 1950, pp.1274-1282.

[6] D.Daroczi, J.Szollosy, G.Vertesy, J.Pavo and K.Miya, *Electromagnetic NDT Material Testing by Magnetic Field Sensor*, Applied Electromagnetics and Mechanics 8, Nondestructive Testing of Materials, IOS Press, Amsterdam, 1995, pp.75-86.

[7] D.Rodger and P.K.Vong, *Some Finite Element Models of the FLUXSET Sensor*, Electromagnetic Nondestructive Evaluation (III), IOS Press, 1999, pp.182-187.

FINITE ELEMENT MODELS OF EDDY CURRENT BRAKES

D.Rodger H.C.Lai and P.K.Vong
Dept of Elec Eng, University of Bath, BA2 7AY U.K.

ABSTRACT

Permanent magnet eddy current brakes offer an economic method for bringing a moving object to rest. The performance of a decelerating eddy current brake can be modelled by a time transient finite element scheme. However, this may be time consuming, especially in the early stages of design. It is shown here how an adequate simulation is possible using a few steady state (Minkowski) finite element solutions.

FINITE ELEMENT EQUATIONS

Eddy current brakes usually comprise a set of stationary poles, excited with either DC or permanent magnets and a moving member. The finite element solver therefore has to be able to deal with moving conductors.

The non-conducting and conducting regions are modelled using the magnetic scalar potential, ψ, and the magnetic vector potential, $\mathbf{A}$, respectively.

Non Conducting Regions

Non conducting regions are modelled using magnetic scalar potentials, either the total scalar ψ ,defined as $\mathbf{H}_T = -\nabla\psi$, or the reduced scalar ϕ, defined as $\mathbf{H}_T = -\nabla\phi + \mathbf{H}_S$. Here $\mathbf{H}_T$ is the total magnetic field intensity and $\mathbf{H}_S$ is the field defined as $\nabla\times\mathbf{H}_S = \mathbf{J}_S$, where $\mathbf{J}_S$ is the source current density.

Both scalars give rise to a Laplacian type equation which has to be solved.

$$\nabla\cdot\mu\nabla\psi = 0 \tag{1}$$

Voltage forced conditions can be modelled using this technique [1].

Conducting Regions

Fields in conductors can be modelled using $\mathbf{A}$, the magnetic vector potential, and V, the electric scalar potential.

The formulations are different depending on whether the moving member is smooth in the direction of motion, ie whether the moving media cross section normal to the direction of motion is invariant as described below.

Smooth Moving Conductor Regions

If the moving conductors are smooth and the region moves at a constant velocity, the induced motional emf effect can be taken into account by including a velocity term $\mathbf{u}\times\mathbf{B}$, where $\mathbf{u}$ is the velocity (the Minkowski transformation).

Using $\mathbf{B} = \nabla\times\mathbf{A}$ and $\mathbf{E} = -\frac{\partial\mathbf{A}}{\partial t} - \nabla V + \mathbf{u}\times\nabla\times\mathbf{A}$, where $\mathbf{u}$ is the material velocity, Ampère's law and the divergenceless $\mathbf{J}$ condition are

$$\nabla\times\frac{1}{\mu}\nabla\times\mathbf{A} = \sigma\left(-\frac{\partial\mathbf{A}}{\partial t} + \mathbf{u}\times\nabla\times\mathbf{A} - \nabla V\right) \tag{2}$$

$$\nabla\cdot\sigma\left(\frac{\partial\mathbf{A}}{\partial t} - \mathbf{u}\times\nabla\times\mathbf{A} + \nabla V\right) = 0 \tag{3}$$

Where appropriate [2], it is possible to dispense with V from the above set of equations. Substituting $V = \mathbf{A}\cdot\mathbf{u}$ in Ampère's law yields

$$\nabla\times\frac{1}{\mu}\nabla\times\mathbf{A} = \sigma\left(-\frac{\partial\mathbf{A}}{\partial t} - (\mathbf{u}\cdot\nabla)\mathbf{A} - (\mathbf{A}\cdot\nabla)\mathbf{u} - \mathbf{A}\times(\nabla\times\mathbf{u})\right) \tag{4}$$

Now a solution of (4) involving only $\mathbf{A}$ is required, since V is specified in terms of $\mathbf{A}$.

Non Smooth Moving Conductor Regions

If the performance of decelerating objects such as eddy current brakes is required, a time transient solution must be carried out. This is also true even for constant velocity movement if the cross section of the moving object is not invariant in the direction of motion. The moving object is modelled by a mesh which slides relative to the stationary parts. The independent meshes can then be coupled at their common interface using Lagrange Multipliers. Stationary and moving parts can be meshed up independently and then brought together as shown in Fig. 1. The distribution and density of nodes on the interface need not be the same.

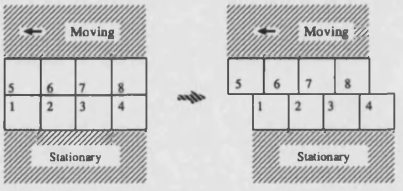

Figure 1: Both meshes remain undistorted

If we are required to make a functional $\Pi(\phi)$ stationary subject to the constraints

$C(\phi) = 0$ in Ω

We can introduce this constraint by forming a new functional

$$\Pi' = \Pi + \lambda C(\phi) \tag{5}$$

λ is a set of Lagrange Multipliers [3].

LINEAR EDDY CURRENT BRAKE

The simplest type of linear eddy current brake consists of a sheet of conductor fed into the airgap between a row of permanent magnets. A 3D computer model of such a device is shown on Figure 2, the magnetic circuit is 'U' shaped in cross section, only one side is shown for clarity. At this time the plate can be seen on the right hand side as it moves into the gap. The magnets can be observed on the left. The magnets shown are sintered NdFeB (54x31.25x8.75)mm, spacing 8.75mm and the 1.2m long plate is of 4mm thick aluminium.

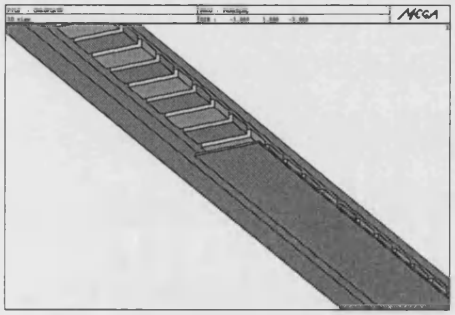

Figure 2: A double sided linear eddy current brake

Figure 3 shows a 2D view of the machine. A plate resistivity increase factor [4] is used to compensate for the finite plate width in the 2D models. All of the results discussed here refer to a braking system consisting of two double rows of magnets on either side of a moving vehicle.

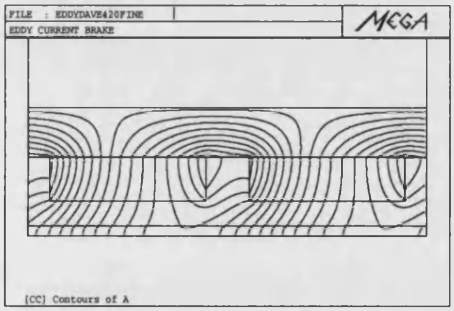

Figure 3: Showing part of an eddy current brake 2D

Figure 4 shows the force versus speed for the eddy current brake modelled using the 2D and 3D time transient and Minkowski 2D and 3D finite element schemes. Both the transient finite element schemes solve the rigid body equations of motion for the moving object as well as the electromagnetic equations at each instant of time.

The time transient models are more realistic in the sense that these include the effect of the plate being fed into the magnets (the initial curved ramp seen to the right of the curve) and the force ripple effect of the plate edges passing the magnets, it can be observed that these effects are absent from the Minkowski models which include an infinite plate without ends.

The Minkowski scheme returns the force at a speed specified by the user. It may be observed that apart from the initial transient at the right of the curve, and the force ripple effects, all of these methods agree quite well. The largest discrepancy is between 2D and 3D. The accuracy of the 2D models depends on the resistivity increase factor, this is derived from analytic solutions which depend on the pole pitch of the harmonic under consideration. Only one harmonic can be included in 2D finite element models, based on the machine pole pitch. This generally gives good results for reasonable well designed conventional round and linear induction machines but the harmonic content of the eddy current brake is quite high, so probably leading to higher errors in this case.

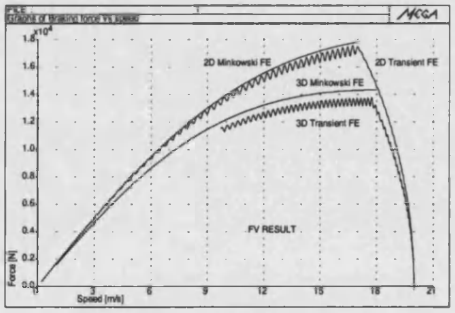

Figure 4: Force versus speed

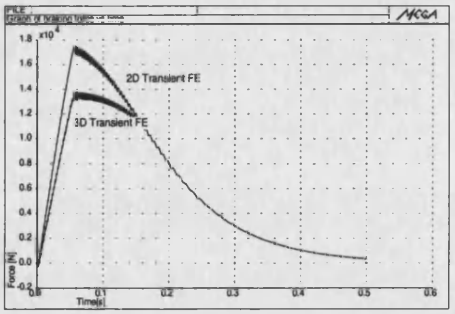

Figure 5: Force versus time

Figure 5 shows the force versus time for the 2D and 3D transient models.

Time transient behaviour of the machine is caused by the initial transient and plate end torque ripple, as well as

potentially due to the fact that the plate is decelerating. It appears that the deceleration is sufficiently slower than the electrical time constants so that at each instant of time after the initial transient the force produced at a given speed on the transient force versus velocity curve is similar to that at steady state.

This means that after all of the plate has been fed in, the device is essentially working in the steady state regime. The dynamics of the moving body may be solved very easily by using the variable force versus speed curve obtained from the steady state finite element solution (Minkowski) as input to the mechanical equation of motion. In this way we time step one equation rather than the thousands which are required in the finite element scheme. The result of this is shown on Figure 6.

The figure shows speed versus time for the decelerating system, calculated in 2D and 3D. The curves marked 'transient' are models of the entire machine and are therefore computationally expensive, The curves marked 'estimated' are calculated using either the 2D or 3D Minkowski results as input data for a time stepped solution to the mechanical equation only. Since only 20 Minkowski solutions were required for this process, compared with 5000 time transient solutions (0.1ms time steps for 0.5s) for the full time transient solution, this represents a considerable saving in computer time.

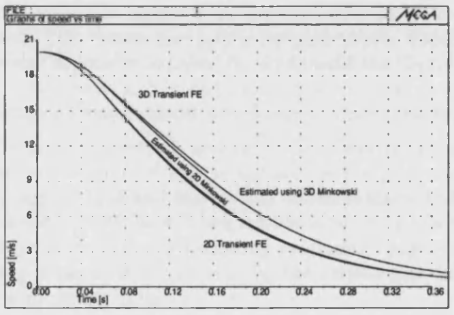

Figure 6: Velocity versus time

Figure 7 shows contours of modulus of current density in the plate at a time 0.03s after the plate enters the magnets.

CONCLUSIONS

The electrical time constants in a standard industrial eddy current brake are so much faster than the rate of change of mechanical parameters such as velocity that the device can be modelled using a steady state finite element scheme (Minkowski), providing that the moving member consists

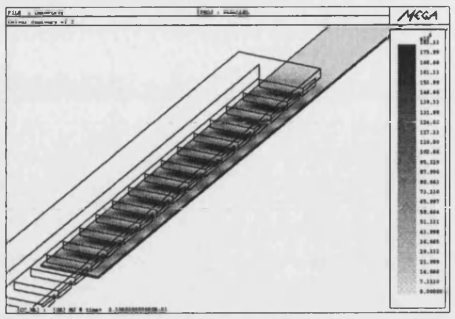

Figure 7: Showing contours of modulus of current density in the plate

of a smooth reaction plate.

References

[1] P.J.Leonard and D.Rodger. "Modelling voltage forced coils using the reduced scalar potential method". *IEEE Trans. Magn.*, 28(2):1615–1617, March 1992.

[2] D.Rodger, N.Allen, P.C.Coles, S.Street, P.J.Leonard, and J.F. Eastham. "Finite element calculation of forces on a DC magnet moving over an iron rail". *IEEE Trans. Magn.*, 30(6):pp4680–4682, November 1994.

[3] D. Rodger, H.C. Lai, and P.J. Leonard. "Coupled elements for problems involving movement". *IEEE Trans. Magn.*, 26(2):548–550, March 1990.

[4] R.L.Russel and K.H.Norsworthy. "Eddy currents and wall losses in screened rotor induction motors". *IEE Proc A.*, 105:163–175, 1958.

ON MODELLING WEAKLY COUPLED ELECTROMAGNETIC-THERMAL PROBLEMS WITH PRESCRIBED NON-LINEAR SURFACE HEAT TRANSFER

P K Vong, D Rodger P C Coles and H C Lai
Dept. of Electronic and Electrical Engineering, University of Bath, U.K.

***Abstract*—Finite Element modelling of coupled electromagnetic-thermal problems is described. The thermal sources can be eddy currents in conductors and winding I^2R losses. Since the thermal time constants are relatively very long the coupled electromagnetic-thermal problem is solved as a weakly coupled system, using time-harmonic and time- transient thermal methods. Non-linear surface convection and radiation terms are included in the thermal model. Results are compared with experimental measurements.**

INTRODUCTION

The analysis of coupled electromagnetic-thermal problems in current carrying conductors requires the solution of two parabolic differential equations coupled through the temperature dependent electrical conductivity. The thermal time constants are typically 10^4 times larger than the electrical time constant. This means that a fully coupled system would be very expensive to solve. Here we model the electrical problem as a time-harmonic system weakly coupled to a time-transient non-linear thermal system.

Non-linear convection and radiation boundary conditions are imposed on the surfaces of the conducting region. It is well-known that the convection and radiation coefficients $\hbar$ are functions of the surface temperature and the boundary is usually modelled using some form of curve fit to the known correlation empirical data.

$AV\psi$ - T FIELD REPRESENTATION

The consistency of Ampere's Law is enforced by solving:

$$\nabla \times \frac{1}{\mu}\nabla \times \mathbf{A} = -\sigma\left(\frac{\partial \mathbf{A}}{\partial t} + \nabla V\right)$$
$$\nabla \cdot \sigma\left(\frac{\partial \mathbf{A}}{\partial t} + \nabla V\right) = 0 \qquad (1)$$

For a moving conducting region, Ampere's Law with velocity is expressed in terms of **A** and V as

$$\nabla \times \frac{1}{\mu}\nabla \times \mathbf{A} = -\sigma\left[\frac{\partial \mathbf{A}}{\partial t} + \nabla V - \mathbf{u} \times (\nabla \times \mathbf{A})\right] \qquad (2)$$

The electric scalar potential V is required in modelling moving conducting regions but it can be set equal to $\boldsymbol{A} \cdot \boldsymbol{u}$, thus eliminating the need to solve for V directly. The voltage term ∇V is useful for modelling jumps in conductivity [1] or introducing sources into massive circuits [2],[3].

Equating $V = \boldsymbol{A} \cdot \boldsymbol{u}$ and using the vector identity $\nabla(\boldsymbol{A}\cdot\boldsymbol{u}) = (\boldsymbol{u}\cdot\nabla)\boldsymbol{A}+(\boldsymbol{A}\cdot\nabla)\boldsymbol{u}+\boldsymbol{u}\times\nabla\times\boldsymbol{A}+\boldsymbol{A}\times\nabla\times\boldsymbol{u}$, equation (2) is reduced to

$$\nabla \times \frac{1}{\mu}\nabla \times \boldsymbol{A} = -\sigma\left[\frac{\partial \boldsymbol{A}}{\partial t} + (\boldsymbol{u}\cdot\nabla)\boldsymbol{A} + (\boldsymbol{A}\cdot\nabla)\boldsymbol{u} + (\nabla \times \boldsymbol{u}) \times \boldsymbol{A}\right] \qquad (3)$$

For rotational velocity, the last two terms on the r.h.s of equation (3) are nonzero and with $\boldsymbol{u} = \mathbf{r} \times \boldsymbol{\omega}$, the equation can be expressed as

$$\nabla \times \frac{1}{\mu}\nabla \times \boldsymbol{A} = -\sigma\left[\frac{\partial \mathbf{A}}{\partial t} + (\boldsymbol{u}\cdot\nabla)\boldsymbol{A} + \boldsymbol{A} \times \boldsymbol{\omega}\right] \qquad (4)$$

with $\boldsymbol{\omega}$ as the angular velocity [4]. For translational velocity the angular velocity term is zero.

The time-transient method for solving fully coupled electromagnetic-thermal problems with large thermal time constants is expensive as the solution of the final set of equations is required at each time step [5].

In many cases however, a weakly coupled time-harmonic electromagnetic model is adequate. The time-harmonic magnetic vector potential **A** is described by

$$\begin{aligned} \boldsymbol{A} &= (\boldsymbol{A}_R + j\boldsymbol{A}_I)\, e^{j\omega t} \\ &= (\acute{\boldsymbol{A}})\, e^{j\omega t} \end{aligned} \qquad (5)$$

Thus, the time-harmonic eddy currents equation to solve for is

$$\nabla \times \frac{1}{\mu} \nabla \times \acute{A} = -\sigma[j\omega \acute{A} + (\boldsymbol{u} \cdot \nabla)\acute{A} + \acute{A} \times \omega] \quad (6)$$

The governing heat transfer equation for the conducting region is written as:

$$\rho C \left(\frac{\partial T}{\partial t} + \mathbf{u} \cdot \nabla T \right) - \nabla \cdot \kappa \nabla T - Q = 0, \quad (7)$$

where T, $\mathbf{u}$, κ, ρ and C are the unknown temperature function, velocity vector, thermal conductivity, material density and specific heat capacity respectively. Q is the internal volumetric heat generated, defined as $\mathbf{J}^2/\sigma$.

ALGORITHM

The algorithm to solve this weakly coupled problem is summarised below:

1. Initialise the electromagnetic unknowns $\mathbf{A} = \mathbf{A}_o$ with the given frequency and calculate the steady-state AC electromagnetic solution,

$$j\omega[\boldsymbol{C}]\mathbf{A} + [\boldsymbol{K}_a]\mathbf{A} = \boldsymbol{f}_a$$

2. Initialise the thermal unknowns $T = T_0$ for time $t = 0$. Set n=0 and the time step Δt.

3. Assemble the thermal system of equations for this position, x_n, $[\mathbf{K_n}]$.

4. Calculate the thermal heating using the steady-state AC electromagnetic result obtained previously.

5. Calculate the thermal solution, using backward differences,

$$\alpha_n = ([C] + \Delta t[\boldsymbol{K}_n])^{-1}\{\boldsymbol{f}_n - [\boldsymbol{K}_n][T_n]\}$$

$$T_{n+1} = T_n + \alpha_n \Delta t$$

6. Calculate the temperature dependent value of convection and radiation coefficients, and reassemble the matrix $[\boldsymbol{K}_n]$.

7. Set n=n+1 and repeat the algorithm from step 5.

During the iterative process, the electromagnetic problem can be solved again if there are significant changes in the media electrical conductivity due to temperature rise. The temperature dependent convection coefficient can be calculated from Churchill-Chu empirical correlations [6],[7]. The vertical surface and horizontal cylindrical surface convection coefficients are given respectively as;

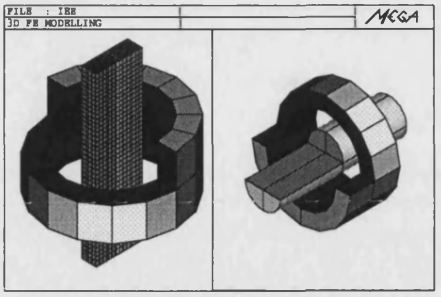

Fig. 1. Cut away view of 3D FE models of aluminium plate and cylinder.

$$\hbar = \frac{\kappa(T)}{\ell} \left\{ 0.825 + \frac{0.387[Ra(T)]^{\frac{1}{6}}}{[1 + [0.492/Pr(T)]^{\frac{9}{16}}]^{\frac{8}{27}}} \right\}^2$$

$$\hbar = \frac{\kappa(T)}{\ell} \left\{ 0.6 + \frac{0.387[Ra(T)]^{\frac{1}{6}}}{[1 + [0.559/Pr(T)]^{\frac{9}{16}}]^{\frac{8}{27}}} \right\}^2 \quad (8)$$

in which the thermal conductivity, $\kappa(T)$, Rayleigh number, Ra(T)and Prandtl number, Pr(T) are all functions of the surface temperature. Likewise the electrical conductivity can be temperature dependent and its resistivity ρ approximated linearly as

$$\rho(T) = \rho_o(T)[1 + \alpha(\Delta T)] \quad (9)$$

The aluminium electrical resistivity coefficient is measured as, $\alpha = 3.3 \times 10^{-3}\,^{\circ}C^{-1}$ while for copper the resistivity coefficient is, $\alpha = 3.93 \times 10^{-3}\,^{\circ}C^{-1}$.

VALIDATION

The weakly coupled electromagnetic-thermal code is validated by several experiments conducted in the laboratory. An aluminium plate and cylinder are placed separately into a massive coil shown in Fig. 1. The massive coil consists of 1600 turns of 1 mm diameter copper wire. The measured aluminium electrical conductivity is 2.9×10^7S/m.

Tests were performed on two flat plates with different length made up of either aluminium or copper. The short plates have dimensions of $70mm \times 16mm \times 50mm$ while the longer ones are $180mm \times 16mm \times 50mm$. The material thermal properties are shown in Table(I).

The simulated and measured results of the temperature rise at this surface for the long aluminium and copper plates are shown in Fig. 2 and Fig. 3. The frequency used is 50 Hz with coil excitation current at 2.0 A (rms) and 2.8 A (rms). At this excitation frequency the skin depth of the conductors according to skin depth effect is $\approx 14mm$ for aluminium

TABLE I
Material Thermal Properties.

Material properties	Aluminium	Copper
Thermal conductivity, $\kappa(W/m.K)$	204	399
Specific heat, $C_p(J/kgK)$	896	383
Density, $\rho(kg/m^3)$	2707	8933
relative permeability, μ_r	1.0	1.0

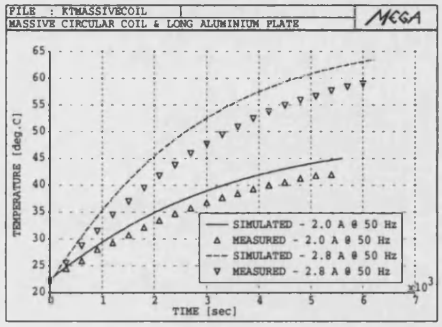

Fig. 2. Simulated and measured temperatures of the long aluminium plate with constant electrical conductivity.

and $\approx 10mm$ for copper, with $\mu = \mu_o\mu_r$ equal to $4\pi \times 10^{-7}$ H/m

The discrepancy is larger for the plate with an excitation current of 2.8 A in comparison with the one with excitation current of 2.0 A . This is due to the fact that both models are using constant electrical conductivities and at higher temperature level the heat dependency of the electrical conductivities cannot be ignored. This is further proven in the next set of experiments. The long metal plates are replaced with a shorter version of dimension $70mm \times 16mm \times 50mm$. The measured and computational results are shown in Fig. 4 and Fig. 5 for the short aluminium and copper plates. As the temperature started to climb the divergence of the simulated and measured curves become increasingly significant. The aluminium plate and copper plate FE models with 2.8 A @ 50Hz excitation current are rerun again with temperature dependent electrical conductivity. The results are shown in Fig. 6.

In the final experiment for heat transfer in non-moving media, a solid aluminium cylindrical drum is placed horizontally in to the massive coil. The measured and simulated results are shown in Fig. 7

In the final part of the validation exercise, the *MEGA* code is used to evaluate the thermal performance of an induction disk machine. The FE model of this machine is shown in Fig. 8. The induction machine consists of a 12 slots stator and a rotating conducting disk made up of aluminium. The iron

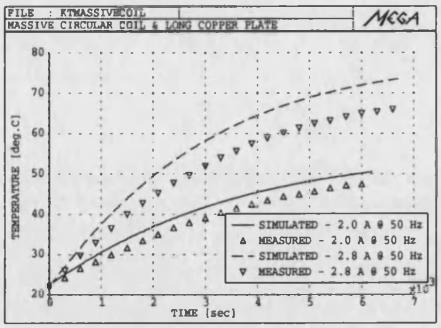

Fig. 3. Simulated and measured temperatures of the long copper plate with constant electrical conductivity.

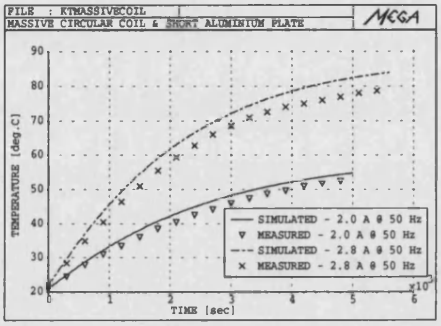

Fig. 4. Simulated and measured temperatures of the short aluminium plate with constant electrical conductivity.

core of the stator is made of thin lamination in order to reduce the eddy current losses. The stator has a total of 6 coils wound on the slots. Each coil has a 580 turns of 0.55 mm in diameter of copper wire. Each phase has two coils connected in parallel. Table(II) shows the dimensions of the machine.

TABLE II
Geometrical data of the disk induction machine.

	Machine Parameters	Dimensions in SI unit
1	Stator Height	39.0 mm
2	Stator Inner Diameter	71.0 mm
3	Stator Outer Diameter	128.0 mm
4	Tooth Height	27.0 mm
5	Slot Width	14.0 mm
6	Slot Opening Width	3.0 mm
7	Air Gap	1.0 mm
8	Aluminium Disk Diameter	184.0 mm
9	Shaft Diameter	32.0 mm

In general moving conductors are expensive to model using finite elements because a fully time-transient solution is required and the moving object must be

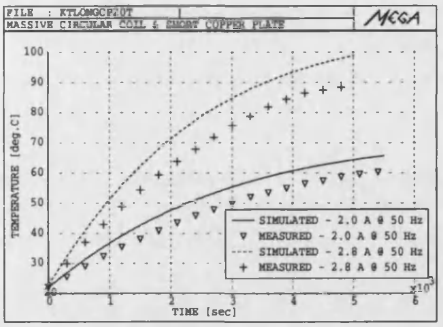

Fig. 5. Simulated and measured temperatures of the short copper plate with constant electrical conductivity.

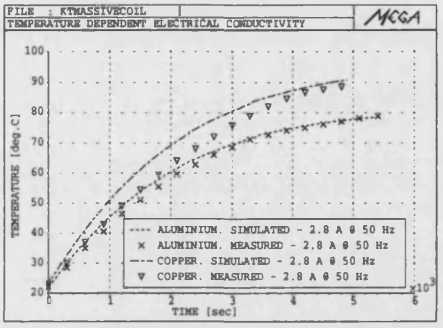

Fig. 6. Simulated and measured temperatures of the short aluminium and copper plates with variable electrical conductivity.

tracked through the mesh as time progresses. In modelling the moving conductor region (aluminium disk), the Minkowski transformation as explained earlier is used to formulate the eddy currents induced. The thermal equation is augmented by a convective term to model the influence of the specified velocity on the heat distribution in the rotating disk.

Heat transfer in the induction machine is a combination of conduction within the solid and laminated components of the machine and convection from the surfaces which are in contact with air. The dominant processes in heat transfer within a motor and to the environment are conduction and convection. Radiation is important only on the outer surfaces. Conduction is the first stage in the process of heat flow from the generation site to the outer surfaces after which convection takes over.

For surface cooled machines the heat transfer coefficients for free convection and radiation from the outer surface of the machine are the main parameters to which the accuracy of the predictions is most sensitive. This is one of the difficulties encountered when designing a thermal model. Another problem

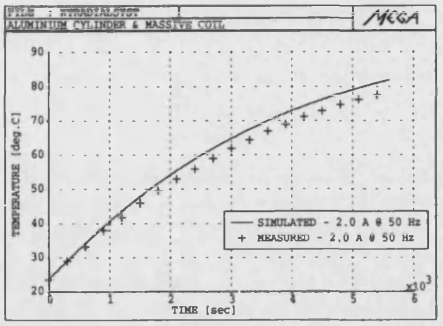

Fig. 7. Temperature rise in the aluminium cylinder.

is the separation of losses in the motor.

The convection coefficients $\hbar_\omega$ used for the moving component, specifically for rotating cylinder and disk are listed as below [8]:

- rotating cylindrical drum

$$\hbar_\omega = \frac{\kappa(T)}{D}\left[0.11(0.5Re^2 + GrPr)^{0.35}\right] \quad (10)$$

- rotating disk in laminar flow

$$\hbar_\omega = \frac{\kappa(T)}{D}\left[0.36\left(\frac{\omega r^2}{\nu}\right)^{0.5}\right] \quad (11)$$

$$\text{valid for } \frac{\omega r^2}{\nu} < 2 \times 10^5$$

- rotating disk in turbulent flow

$$\hbar_\omega = \frac{\kappa(T)}{D}\left[0.015\left(\frac{\omega r^2}{\nu}\right)^{0.8}\right] \quad (12)$$

where D is diameter of the cylinder/disk, r is the radius of the cylinder/disk, ω is the angular velocity and ν is the kinematic viscosity.

The induction machine is run with the aluminium disk rotating at 300 rpm at a load supplied by a DC brushless machine. The excitation current fed into the armature winding is 2.0 A and the resistance of each coil is 12.468 ohms. The main losses in the induction disk machine is the induced eddy currents in the rotating aluminium disk, the copper I^2R loss in the windings and the iron losses. The iron losses could be calculated very approximately using the normal empirical formula:

$$\begin{aligned} P_h &= k_h \hat{B}^m f \text{ for hysteresis losses} \\ P_e &= k_e \hat{B}^2 f^2 \text{ for eddy current losses} \end{aligned} \quad (13)$$

where k_h and k_e are the empirical constants, $\hat{B}$ is the peak magnetic field with m = 1.76 and f is the applied excitation frequency.

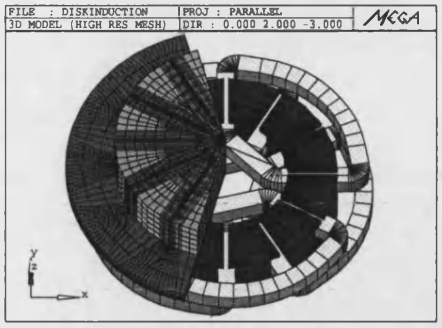

Fig. 8. Disk induction machine.

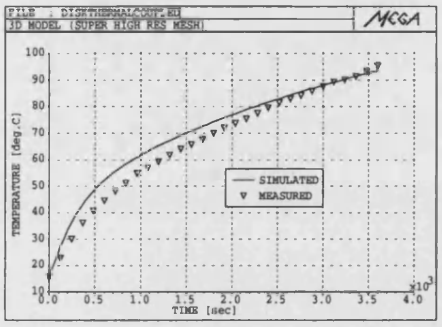

Fig. 9. Simulated and measured temperatures of the windings.

The simulated and measured results for the windings, stator teeth and rotating aluminium disk are shown in Figs. 9, 10 and 11. It can be seen that the predicted and measured results are in reasonable agreement.

CONCLUSION

The finite element technique of modelling eddy current losses in a thermo-electromagnetic coupled domain is described. Time-harmonic methods are used to solve the electromagnetic problem and then this is coupled to the time-transient thermal system. Nonlinear convection and radiation boundary conditions based on empirical equations are prescribed at the conductor surfaces.

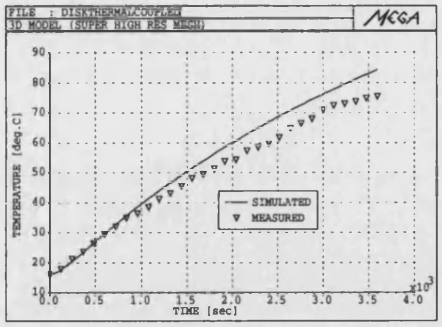

Fig. 10. Simulated and measured temperatures of the stator teeth.

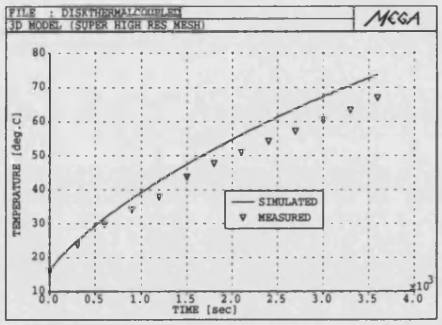

Fig. 11. Simulated and measured temperatures of the disk.

REFERENCES

[1] P.J.Leonard and D.Rodger, Mar., 1997 "Comparison of Methods for Modelling Jumps in Conductivity using Magnetic Vector Potential based Formulations". IEEE Trans. Magn., vol.33, no.2, pp.1295-1298.

[2] P.J.Leonard and D.Rodger, Sept., 1989, "A New Method for Cutting the Magnetic Scalar Potential in Multiply Connected Eddy Current Problems". IEEE Trans. Magn., vol.25, no.5, pp.4132-4134.

[3] P.J.Leonard and D.Rodger, Sept., 1990, "Modelling External Energy Sources in Massive Conductor Circuits using $A\psi$ Formulation with a Re-modified Vector Potential". IEEE Trans. Magn., vol.26, no.5, pp.2370-2372.

[4] N.Allen, H.C.Lai, P.J.Leonard and D.Rodger, Sept., 1998, "On the Validity of Two A -ψ Finite Element Formulations for Modelling Eddy Current Problems With Velocity", IEEE Trans. Magn., vol.34, no.5, pp.2535-2538.

[5] S.H.Le G.Bisson, P.J.Leonard and D.Rodger, Jan., 1993, "Finite Element Analysis of Transient Electromagnetic Heating Effects in Three Dimensions", IEEE Trans. Magn., vol.29, no.1, pp.1102-1106.

[6] S.W.Churchill and H.H.S.Chu, 1975, "Correlating Equations for Laminar and Turbulent Free Convection from a Horizontal Cylinder", Int. J. Heat Mass Transfer, vol.18, pp. 1049.

[7] S.W.Churchill and H.H.S.Chu, 1975, "Correlating Equations for Laminar and Turbulent Free Convection from a Vertical Plate", Int. J. Heat Mass Transfer, vol.18, pp. 1323.

[8] F.Kreith and M.S.Bohn, 1986,"Principles of Heat Transfer". Harper and Row, Fourth Edition.

Coupled Electromagnetic - Thermal Modelling of Electrical Machines

P.K. Vong and D. Rodger

Abstract—**This paper describes some modelling techniques used in computing the heat losses and temperature distribution in some electrical machines. The thermal sources can be eddy currents in conductors and winding I^2R losses. Since the thermal time constants are relatively very long the coupled electromagnetic-thermal problem is solved as a weakly coupled system, using time-harmonic and time-transient methods for the electromagnetic and thermal systems respectively. The electrical coil is modelled as a reduced scalar region coupled with the thermal equation. Results are compared with experimental measurements.**

Index Terms— **Coupled Electromagnetic-thermal analysis, Finite Element Methods, Reduced Scalar.**

I. Introduction

SOLVING a fully time-transient coupled electromagnetic-thermal problem is very expensive. Its thermal time constants could be 10^4 times larger than the electrical time constant. To circumvent this problem, we model the electrical problem as a time-harmonic system weakly coupled to a time-transient non-linear thermal system.

There are several approaches to modelling the electromagnetic behavior of moving conductors. If the moving region does not vary in cross section at the right angles to the direction of motion, "smooth", the *Minkowski transformation* can be used to introduce the effect of motion [1], [2].

The modelled 3D coils are independent of the finite element discretisation in the reduced magnetic scalar method. It is shown how the reduced magnetic scalar mesh may be used to model the source I^2R for the thermal model. These basic building meshes are known as fragments and are combined in groups to form coils. These coils are totally immersed in the reduced scalar regions.

II. Finite Element Modelling

A. Eddy Current Regions

In modelling "smooth" regions the *Minkowski* method is used. The velocity is taken care of by modifying the $\boldsymbol{E}$ field by adding a $\boldsymbol{u} \times \boldsymbol{B}$ term, where $\boldsymbol{u}$ is the velocity. Therefore, the governing equation is the usual

$$\nabla \times \frac{1}{\mu} \nabla \times \boldsymbol{A} = -\sigma \left(\frac{\partial \boldsymbol{A}}{\partial t} + \nabla V - \boldsymbol{u} \times \nabla \times \boldsymbol{A} \right) \quad (1)$$

$$\nabla \cdot \sigma \left(\frac{\partial \boldsymbol{A}}{\partial t} - \boldsymbol{u} \times \nabla \times \boldsymbol{A} + \nabla V \right) \quad (2)$$

Manuscript received June 16, 2002. The authors are with the Department of Electronic and Electrical Engineering, University of Bath, BATH. BA2 7AY UK. E-mail eespkv@bath.ac.uk, d.rodger@bath.ac.uk

The electric scalar potential V is required in modelling moving conducting regions but it can be set equal to $\boldsymbol{A} \cdot \boldsymbol{u}$, thus eliminating the need to solve for V directly. The voltage term ∇V is useful for modelling jumps in conductivity [3] or introducing sources into massive circuits [4].

Equating $V = \boldsymbol{A} \cdot \boldsymbol{u}$ and using the vector identity $\nabla(\boldsymbol{A} \cdot \boldsymbol{u}) = (\boldsymbol{u} \cdot \nabla)\boldsymbol{A} + (\boldsymbol{A} \cdot \nabla)\boldsymbol{u} + \boldsymbol{u} \times \nabla \times \boldsymbol{A} + \boldsymbol{A} \times \nabla \times \boldsymbol{u}$, equation (1) is reduced to

$$\nabla \times \frac{1}{\mu} \nabla \times \boldsymbol{A} = -\sigma \left[\frac{\partial \boldsymbol{A}}{\partial t} + (\boldsymbol{u} \cdot \nabla)\boldsymbol{A} + (\boldsymbol{A} \cdot \nabla)\boldsymbol{u} + (\nabla \times \boldsymbol{u}) \times \boldsymbol{A} \right] \quad (3)$$

For rotational velocity, the last two terms on the *r.h.s* of equation (3) are nonzero and with $\boldsymbol{u} = \boldsymbol{r} \times \boldsymbol{\omega}$, the equation can be expressed as

$$\nabla \times \frac{1}{\mu} \nabla \times \boldsymbol{A} = -\sigma \left[\frac{\partial \boldsymbol{A}}{\partial t} + (\boldsymbol{u} \cdot \nabla)\boldsymbol{A} + \boldsymbol{A} \times \boldsymbol{\omega} \right] \quad (4)$$

where $\boldsymbol{r}$ is the position vector relative to the axis of rotation and $\boldsymbol{\omega}$ is the angular velocity. For translational velocity the angular velocity term is zero.

B. Thermal Regions

The heat transfer region is governed by the usual Fourier's equation,

$$\nabla \cdot \kappa \nabla T + \dot{q} = \rho C \left(\frac{\partial T}{\partial t} + \boldsymbol{u} \cdot \nabla T \right) \quad (5)$$

in which κ is the thermal conductivity, T is the temperature, $\dot{q}$ is the heat source and ρC is the heat capacity.

C. Reduced Scalar Regions

In the regions which contain the known source currents, the $\nabla \times \boldsymbol{H}$ is non-zero. However, since the current is known, the magnetic field is divided into two parts. The field due to the source current is solved using the Biot-Savart law,

$$\boldsymbol{H}_s = -\frac{1}{4\pi} \int \boldsymbol{J}_s \times \nabla \left(\frac{1}{r} \right) \mathrm{d}\Omega_s \quad (6)$$

The actual magnetic field is the sum of the source field $\boldsymbol{H}_s$ and the gradient of a reduced scalar potential ϕ,

$$\boldsymbol{H} = -\nabla \phi + \boldsymbol{H}_s \quad (7)$$

Providing that the coils are totally immersed in a reduced scalar region, the reduced scalar potential region can be of any shape and the mesh can be independent of the coils. If however, we restrict the reduced scalar potential region so that it approximates the shape of each coil and assign each coils to its own reduced scalar potential region, then we can use these reduced scalar regions to conveniently approximate the I^2R loss for the thermal equation sources.

It should be noted that, for the usual type of coil with a hole in the middle, we are required to use cuts in the reduced scalar potential regions [5]. Fig. 1 shows a typical example.

To model the heat transfer due to the coils I^2R losses, the reduced scalar region is used as an approximation to the real coil and the heat source $\dot{q}$ can be calculated by dividing the I^2R losses by the volume integral of the reduced scalar region.

III. Galerkin Weighted Residual Formulations

The Galerkin procedure gives rise to the weak form of the governing equations. After the transformation:

1) Conducting regions

$$\int_{\Omega_{A_V}} \frac{1}{\mu}(\nabla \times \boldsymbol{N}) \cdot (\nabla \times \boldsymbol{A}) + \boldsymbol{N} \cdot \sigma \frac{\partial \boldsymbol{A}}{\partial t} \, \mathrm{d}\Omega = \oint_{\Gamma_{A_V}} \boldsymbol{N} \cdot \frac{1}{\mu} \nabla \times \boldsymbol{A} \times \mathrm{d}\Gamma \qquad (8)$$

2) Thermal regions

$$\int_{\Omega_T} \nabla N \cdot \kappa \nabla T \mathrm{d}\Omega + \int_{\Omega_T} N \rho C \frac{\partial T}{\partial t} \, \mathrm{d}\Omega - \int_{\Omega_T} N \frac{\boldsymbol{J}^2}{\sigma} \mathrm{d}\Omega = \oint_{\Gamma_T} N \, \kappa \nabla T \cdot \hat{\mathbf{n}} \, \mathrm{d}\Gamma \qquad (9)$$

3) Reduced scalar regions

$$\int_{\Omega_\phi} \mu \nabla N \cdot \nabla \phi \, \mathrm{d}\Omega = \oint_{\phi} N \, \mu \frac{\partial \phi}{\partial n} \, \mathrm{d}\Gamma \qquad (10)$$

IV. Validation

A series of test models consisting of coils, aluminium and copper plates were modelled for the validation exercise. The material thermal properties are shown in Table(I). The measured aluminium electrical conductivity is 2.9×10^7 S/m, while the copper used was measured to have an electrical conductivity of 5.4×10^7 S/m. The non-linear temperature dependent electrical conductivity σ could be approximated linearly as

$$\sigma = \frac{\sigma_o}{1 + \alpha(\Delta T)} \qquad (11)$$

where the aluminium electrical resistivity coefficient was measured as, $\alpha = 3.3 \times 10^{-3} \, ^\circ C^{-1}$ while for copper, the resistivity coefficient is, $\alpha = 3.93 \times 10^{-3} \, ^\circ C^{-1}$.

In the first experiment, two excitation currents of 1.5 A and 2.5 A at 50 Hz are fed into a 200 turn coil of 0.9 mm diameter wire. The copper coil itself is totally insulated with thermal insulating material to prevent any convection and radiation heat transfer to the ambient air. Fig. 1 shows a 3D finite element model of a 200 turn coil embedded in the reduced scalar region. The simulated and measured temperature rise results are shown in Fig. 2

In the second experiment, a copper coil of 800 turn with the wire diameter of 0.8 mm is used. Two plates of metal, aluminium and copper are used for validating the temperature rise caused by induction heating. The 3D FE model is shown in Fig. 3. The results of the temperature rise in the coil are shown in Fig. 4 for excitation currents of 2.5 A and 4.0 A respectively.

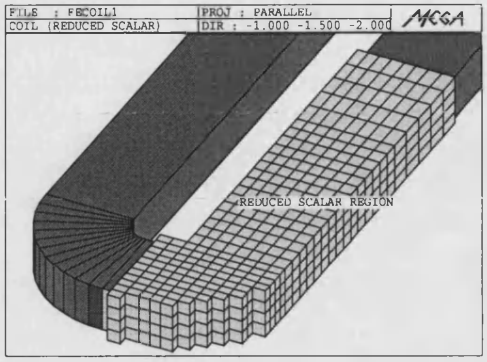

Fig. 1. 3D FE model of a simple coil and reduced scalar region.

TABLE I
Material Thermal Properties.

Material properties	Aluminium	Copper
Thermal conductivity, κ (W/m K)	204	399
Specific heat, C_p (J/kg K)	896	383
Density, ρ (kg/m^3)	2707	8933

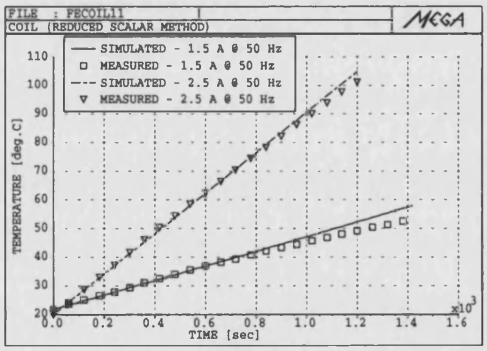

Fig. 2. Temperature rise in the 200 turn copper coil.

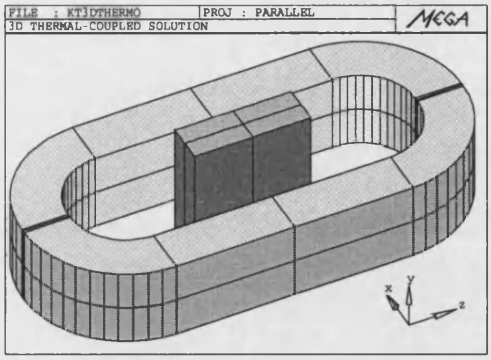

Fig. 3. Metal plate with 800 turn coil.

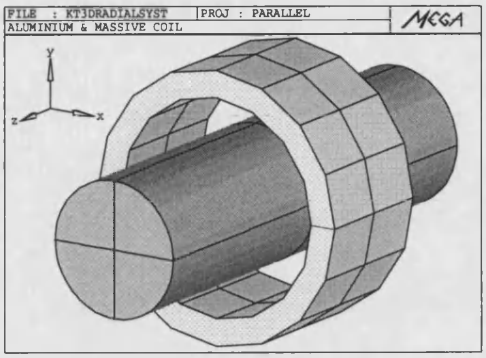

Fig. 6. Cylinder and massive coil

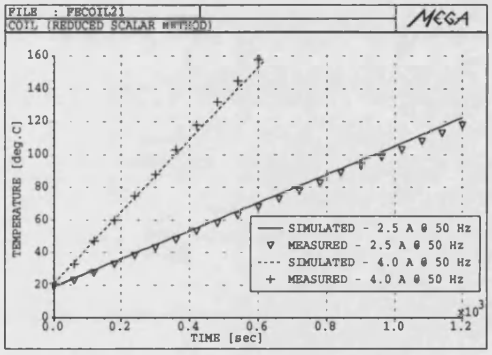

Fig. 4. Temperature rise in the 800 turn copper coil.

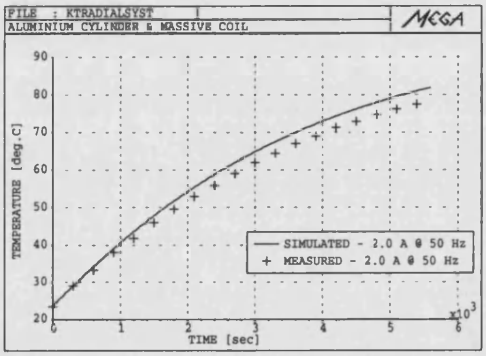

Fig. 7. Temperature rise in the aluminium cylinder.

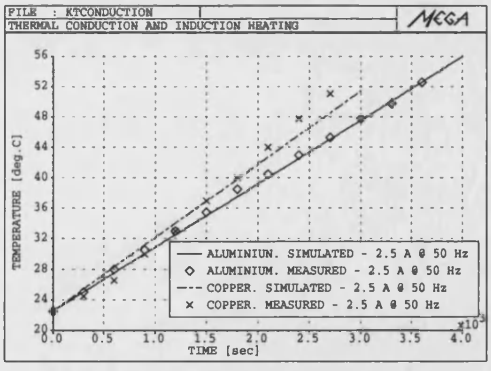

Fig. 5. Temperature rise in the insulated thick metal plate.

For the inductive heating experiment, the thick aluminium and copper plates are totally insulated to avoid any convection and radiation heat transfer at the material surface. The computational results for the inductive heating in the two metal plates are compared with the measured ones in Fig. 5.

In the subsequent experiment for heat transfer in non-moving media, a solid aluminium cylinder shown in Fig. 6 is placed horizontally into a 1600 turn coil. In this experiment, the surface of the cylinder is purposely exposed to the ambient air to take into account the effect of non-linear surface heat transfer. The heat transfer coefficients at the surface of the solid cylinder are based on the usual prescribed empirical correlation formulae [6]. The heat source in this case is due to the induced eddy currents in the cylinder. The measured and simulated temperatures at the surface of the cylinder are shown in Fig. 7.

In the final part of the validation exercise, the *MEGA* code is used to evaluate the thermal performance of a disk induction machine. The 3D FE model of this machine is shown in Fig. 8. The induction machine consists of a 12 slot stator and a rotating conducting disk made of aluminium. The iron core of the stator is made of thin laminations in order to reduce the eddy current losses. The stator has a total of 6 coils wound in the slots. Each coil has a 580 turn of 0.55 mm diameter of copper wire. Each phase has two coils connected in parallel and the resistance of each coil was measured to be 12.468 ohms. The windings and their reduced scalar regions are shown in Fig. 9. A full description of this machine is published in [6].

The induction machine is run with the aluminium disk rotating at 300 rpm at a load supplied by a DC brushless machine. A current of 2.0 A at 50 Hz excitation is fed into each of the

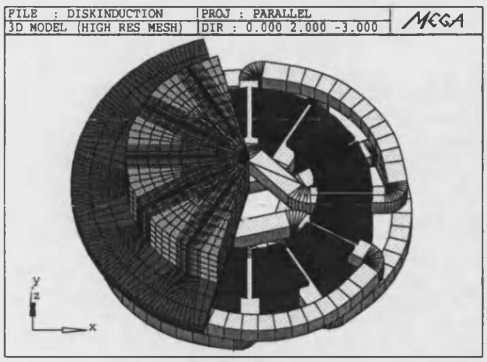

Fig. 8. Disk induction machine.

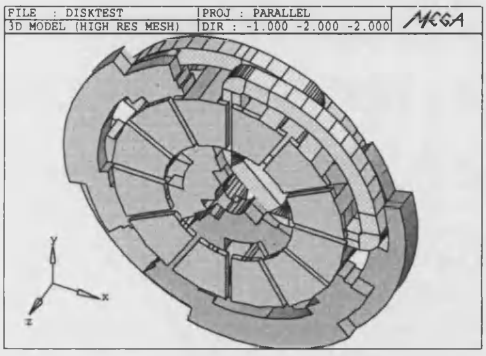

Fig. 9. Stator, windings and their reduced scalar regions.

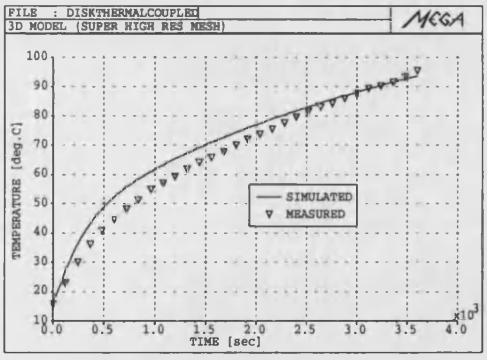

Fig. 10. Simulated and measured temperatures of the windings.

3-phase armature windings. The main losses in the induction disk machine are the induced eddy currents in the rotating aluminium disk, the copper I^2R loss in the windings and the iron losses. The simulated and measured results for the windings, stator teeth and rotating aluminium disk are shown in Figs. 10, 11 and 12. It can be seen that the predicted and measured results are in reasonable agreement.

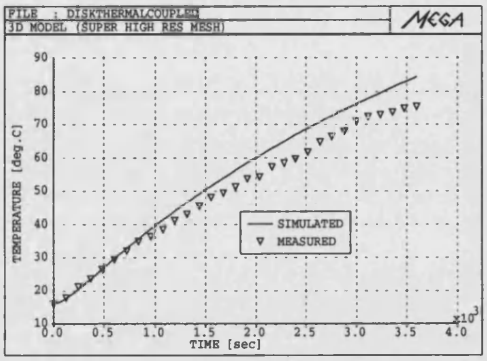

Fig. 11. Simulated and measured temperatures of the stator teeth.

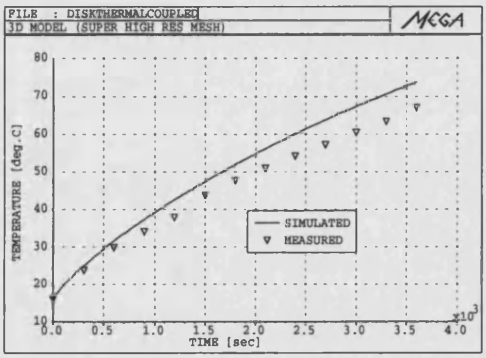

Fig. 12. Simulated and measured temperatures of the disk.

V. Conclusions

A scheme for modelling the heat source in coils and moving conductor regions is described. Time-harmonic methods are used to solve the electromagnetic problem and then this is coupled to the non-linear time-transient thermal system. The reduced scalar method is used to model the electrical coil to facilitate the thermal analysis of electrical machines.

References

[1] D.Rodger, T.Karaguler and P.J.Leonard, *A Formulation for 3D Moving Eddy Current Problems*, IEEE Trans. Magn., vol.25, no.5, September 1989, pp.4147-4149.

[2] N.Allen, H.C.Lai, D.Rodger and P.J.Leonard, *On the Validity of Two $\boldsymbol{A}$ - ψ Finite Element Formulations for Modelling Eddy Current Problems With Velocity*, IEEE Trans. Magn., vol.34, no.5, September 1998, pp.2535-2538.

[3] P.J.Leonard and D.Rodger, *Comparison of Methods for Modelling Jumps in Conductivity using Magnetic Vector Potential based Formulations*, IEEE Trans. Magn., vol.33, no.2, March 1997, pp.1295-1298.

[4] P.J.Leonard and D.Rodger, *Modelling External Energy Sources in Massive Conductor Circuits using $A\psi$ Formulation with a Re-modified Vector Potential*, IEEE Trans. Magn., vol.26, no.5, September, 1990, pp.2370-2372.

[5] P.J.Leonard and D.Rodger, *A New Method for Cutting the Magnetic Scalar Potential in Multiply Connected Eddy Current Problems*, IEEE Trans. Magn., vol.25, no.5, Sept., 1989, pp.4132-4134.

[6] P.K.Vong, D.Rodger, P.C.Coles and H.C.Lai, *On Modelling Weakly Coupled Electromagnetic-Thermal Problems with Prescribed Non-linear Surface Heat Transfer*, IEE PEMD Conf., vol.487, April 2002, pp.260-264.

References

[1] J.D. Kraus. 'Electromagnetics". *McGraw Hill International Edition*, 4th Edition, 1992.

[2] R.W.Clough."The Finite Element Method in Plane Stress Analysis". *Proc. 2nd ASCE Conf. on Electronic Computation*, Pittsburgh, Pa., September 8 1960.

[3] K.F.Riley. "Mathematical Methods for the Physical Sciences". *Cambridge University Press*, 1974.

[4] R.Courant. "Variational Method for the Solution of Problems of Equilibrium and Vibrations". *Bull. Am. Math. Soc.*, vol.49, 1943, pp.1-23.

[5] O.C.Zienkiewicz and R.L.Taylor. 'The Finite Element Method. Volume 1: Basic Formulation and Linear Problems". *McGraw Hill*, 4th Edition, 1989.

[6] P.P.Silvester and R.L.Ferrari. "Finite Elements for Electrical Engineers". *Cambridge University Press*, 2nd Edition, 1990.

[7] P.Hammond. "Applied Electromagnetism". *Pergamon Press*, 1971.

[8] D.Rodger. "Finite-element Method for Calculating Power Frequency 3 - Dimensional Electromagnetic Field Distributions". *IEE Proc., Part A*, vol.130, no.5, July 1983, pp.233-238.

[9] J.Simkin and C.W.Trowbridge. "On the use of the Total Scalar Potential in the Numerical Solution of Field Problems in Electromagnetics". *Int. J. Num. Meth. Eng.*, vol.14, 1979, pp.423-440.

[10] P.J.Leonard and D.Rodger. "Modelling Voltage Forced Coils using the Reduced Scalar Potential Method". *IEEE Trans. Magn.*, vol.28, no.2, March 1992, pp. 1615-1617.

[11] P.J.Leonard, D.Rodger and R.J.Hill-Cottingham. "Calculation of AC Losses in Current Forced Conductors using 3D Finite Elements and the AψV Method". *IEEE Trans. Magn.*, vol.26, no.2, March 1990, pp. 490-492.

[12] D.Rodger and J.F.Eastham. "A Formulation for Low Frequency Eddy Current Solutions". *IEEE Trans. Magn.*, vol.19, no.6, November 1983, pp.2443-2446.

[13] C.R.I.Emson and J.Simkin. "An Optimal Method for 3D Eddy Currents". *IEEE Trans. Magn.*, vol.19, no.6, November 1983, pp.2450-2452.

[14] D.Rodger. "Finite Element Analysis". *Fourth Year MEng. Course*, Dept of Electronic and Electrical Eng., University of Bath.

[15] M.V.K.Chari and P.P Silvester. "Finite Elements in Electrical and Magnetic Field Problems". *John Wiley & Sons*, 1984.

[16] W.L.Wood. "Practical Time Stepping Schemes". *Clarendon Press*, Oxford, 1990.

[17] T.Fujii and H.Imura. "Natural Convection Heat Transfer from a Plate with Arbitrary Inclination". *Int. J. Heat Mass Transfer*, vol.15, 1972, pp.755-767.

[18] S.W.Churchill and H.H.S.Chu. "Correlating Equations for Laminar and Turbulent Free Convection from a Horizontal Cylinder". *Int. J. Heat Mass Transfer*, vol.18, 1975, pp.1049-1053.

[19] S.W.Churchill and H.H.S.Chu. "Correlating Equations for Laminar and Turbulent Free Convection from a Vertical Plate". *Int. J. Heat Mass Transfer*, vol.18, 1975, pp.1323-1329.

[20] E.R.G Eckert and K.M.Drake. "Analysis of Heat and Mass Transfer". *McGraw Hill*, 1972.

[21] J.Gryzagoridis. "Natural Convection Correlations for Vertical Flat Plate in Low Grasnof Number Range". *Int. J. Heat Mass Transfer*, vol.14, 1971, pp.162-164.

[22] V.T.Morgan. "The Overall Convective Heat Transfer from Smooth Circular Cylinders". *Advances in Heat Transfer* , vol.11, 1975, Academic Press Inc., New York.

[23] J.P.Holman. "Heat Transfer". *McGraw Hill*, 8th Edition, 1997.

[24] F.Kreith and M.S.Bohn. "Principles of Heat Transfer". *Harper and Row*, 4th Edition, 1986.

[25] I.J.Perez and J.K.Kassakian. "A Stationary Thermal Model for Smooth Air Gap Rotating Electrical Machines". *Elec. Machines and Electromechanics*, vol.3, no.3-4, March 1979, pp.285-303.

[26] P.J.Leonard and D.Rodger. "A New Method for Cutting the Magnetic Scalar Potential in Multiply Connected Eddy Current Problems". *IEEE Trans. Magn.*, vol.25, no.5, September 1989, pp.4132-4134.

[27] P.J.Leonard and D.Rodger. "Modelling External Energy Sources in Massive Conductor Circuits using $A\psi$ Formulation with a Re-modified Vector Potential". *IEEE Trans. Magn.*, vol.26, no.5, September 1990, pp.2370-2372.

[28] K.T.Hsieh. "A Lagrangian Formulation for Mechanically, Thermally Coupled Electromagnetic Diffusive Processes with Moving Conductors". *IEEE Trans. Magn.*, vol.31, no.1, January 1995, pp.604-609.

[29] J.C.Heinrich, P.S.Huyakorn, O.C.Zienkiewicz and A.R.Mitchell. "An Upwind Finite Element Scheme for Two-Dimensional Convective Transport Equation". *Int. J. Num. Meth. Eng.*, vol.11, 1977, pp.131-143.

[30] T.J.R.Hughes. "A Simple Scheme for Developing Upwind Finite Elements". *Int. J. Num. Meth. Eng.*, vol.12, 1978, pp.1359-1365.

[31] S.H.Le G.Bisson, P.J.Leonard and D.Rodger. "Finite Element Analysis of Transient Electromagnetic Heating Effects in Three Dimensions". *IEEE Trans. Magn.*, vol.29, no.1, January 1993, pp.1102-1106.

[32] F.Kreith et al. "CRC Handbook of Thermal Engineering". *CRC and Springer*, 2000.

[33] T.M.Jahns and W.L.Soong. "Pulsating Torque Minimization Techniques for Permanent Magnet AC Motor Drives". *A Review, IEEE Trans. IE.*, vol.43, no.2, April 1996, pp.321-330.

[34] D.C.Hanselman. "Minimum Torque Ripple, Maximum Efficiency Excitation of Brushless Permanent Magnet Motors". *IEEE Trans. IE.*, vol.41, no.3, June 1994, pp.292-300.

[35] T.Z.Li and G.Slemon. "Reduction of Cogging Torque in Permanent Magnet Motors". *IEEE Trans. Magn.*, vol.24, no.6, November 1988, pp.2901-2903.

[36] T.Ishikawa and G.Slemon. "A Method of Reducing Ripple Torque in Permanent Magnet Motors without Skewing". *IEEE Trans. Magn.*, vol.29, no.2, March 1993, pp.2028-2031.

[37] Z.Q.Zhu and D.Howe. "Analytical Prediction of the Cogging Torque in Radial-Field Permanent Magnet Brushless Motors". *IEEE Trans. Magn.*, vol.28, no.2, March 1992, pp.1371-1374.

[38] J.Delaree and N.Boules. "Torque Production in Permanent Magnet Synchronous Motors". *IEEE Trans. IA.*, vol.25, no.1, January-February 1989, pp.107-112.

[39] R.P.Deodhar, D.A.Staton, T.M.Jahns and T.J.E.Miller. "Prediction of Cogging Torque using Flux-MMF Diagram Technique". *IEEE Trans. IA.*, vol.32, no.3, May-June 1996, pp.569-575.

[40] A.A.Abdel-Razek, J.L.Coulomb, M.Feliachi and J.C.Sabonnadiere. "Conception of an Airgap Element for the Dynamic Analysis of the Electromagnetic Field in Electrical Machines". *IEEE Trans. Magn.*, vol.18, no.2, March 1982, pp.665-659.

[41] D.Rodger, H.C.Lai and P.J.Leonard. "Coupled Elements for Problems Involving Movement". *IEEE Trans. Magn.*, vol.26, no.2, March 1990, pp.548-550.

[42] H.C.Lai, D.Rodger and P.J.Leonard. "Coupling Meshes in 3D Problems Involving Movement". *IEEE Trans. Magn.*, vol.28, no.2, March 1992, pp.1732-1734.

[43] F.Piriou and A.Razek. "A Model for Coupled Magnetic-Electric Circuits in Electric Machines with Skewed Slots". *IEEE Trans. Magn.*, vol.26, no.2, March 1990, pp.1096-1100.

[44] S.Williamson, T.J.Flack and A.F.Volschenk. "Representation of Skew in Time-Stepped Two-dimensional Finite-Element Models of Electrical Machines". *IEEE Trans. IA.*, vol.31, no.5, September 1995, pp.1009-1015.

[45] E.Favre, L.Cardoletti and M.Jufer. "Permanent Magnet Synchronous Motors - A Comprehensive Approach to Cogging Torque Suppression". *IEEE Trans. IA.*, vol.29, no.6, November-December 1993, pp.1141-1149.

[46] M.Jug, B.Hribernik, A.Hamler, M.Trlep and B.Kreca. "Investigation of Reluctance Torque of Brushless DC Motor". *Proc. Int. Conf. Elec. Machines*, 1990, pp.132-137.

[47] B.Ackermann, J.Janssen, R.Sottek and R.Van Steen. "New Technique for Reducing Cogging Torque in a Class of Brushless DC Motors". *IEE Proc.*, vol.139, no.4, July 1992, pp.315-320.

[48] T.Sebastion and V.Gangla. "Analysis of Induced EMF and Torque Waveforms in a Brushless Permanent Magnet Machine". *IEEE Rec. IA*, 1994, pp.240-246.

[49] A.Miraoui, L.De Fang and J.M.Kauffman. "Performance Analysis of Permanent Magnet Brushless DC Motor". *Proc. IEE Conf. Elec. Machines and Drives*, vol.29, no.2, September 1993, pp.371-375.

[50] D.C.Hanselman. "Effect of Skew, Pole Count and Slot Count on Brushless Motor Radial Force, Cogging Torque and Back EMF". *IEE Proc.*, vol.144, no.5, September 1997, pp.325-330.

[51] J.R.Hendershot JR and T.J.E.Miller. "Design of Brushless Permanent-Magnet Motors". *Magna Physics Publishing and Clarendon Press*, Oxford, 1994.

[52] M.Marinescu and N.Marinescu. "Numerical Computation of Torques in Permanent Magnet Motors by Maxwell Stress and Energy Method". *IEEE Trans. Magn.*, vol.24, no.1, January 1988, pp.463-466.

[53] K.Kondo. "Algebraic Method for Manipulation of Dimensional Relationships in Geometric Models". *Computer Aided Design*, vol.24, March 1992, pp.141-147.

[54] C.F.Parker, J.K.Sykulski and S.C.Taylor. "Parametric Environment for EM Computer Aided Design". *IEEE Trans. Magn.*, vol.32, no.3, May 1996, pp.1433-1436.

[55] D.Rodger, R.J.Hill-Cottingham and P.K.Vong. "Parameterized Template Meshes for 2D and 3D Finite Element Modelling". *IEEE Trans. Magn.*, vol.36, no.4, July 2000, pp.1610-1614.

[56] P.K.Vong, H.C.Lai and D.Rodger. "Optimization of Electromagnetic Devices using Parameterized Templates". *IEEE Trans. Magn.*, vol.37, no.5, September 2001, pp.3538-3541.

[57] J.A.Nelder and R.Mead. *Computer Journal*, vol.7, pp.308-311, 1965.

[58] W.H.Press, S.A.Teukolsky, W.T.Vetterling and B.P.Flannery. "Numerical Recipes: The Art of Scientific Computing". *Cambridge University Press*, 2nd Edition, 1989.

[59] D.Ginsberg. "Graphical Determination of Magnetic Fields". *AIEE Trans.*, vol.26, 1927, pp.141-154.

[60] D.Ginsberg. "Design Calculations for A-C Generators." *AIEE Trans.*, vol.69, 1950, pp.1274-1282.

[61] D.Daroczi, J.Szollosy, G.Vertesy, J.Pavo and K.Miya. "Electromagnetic NDT Material Testing by Magnetic Field Sensor," *Studies in Applied Electromagnetics and Mechanics 8, Nondestructive Testing of Materials*, Editors: R.Collins, W.D.Dover, J.R.Bowler and K.Miya, IOS Press, Amsterdam, 1995, pp.75-86.

[62] D.Rodger and P.K.Vong. "Some Finite Element Models of the FLUXSET Sensor". *Electromagnetic Nondestructive Evaluation (III)*, IOS Press, 1999, pp.182-187.

[63] S.A.Nasar and I.Boldea. "Linear Motion Electric Machines". *John Wiley and Sons*, 1976.

[64] D.Rodger, T.Karaguler and P.J.Leonard. "A Formulation for 3D Moving Conductor Eddy Current Problems". *IEEE Trans. Magn.*, vol.25, no.5, September 1989, pp.4147-4149.

[65] D.Rodger, P.J.Leonard and T.Karaguler. "An Optimal Formulation for 3D Moving Conductor Eddy Current Problems with Smooth Rotors". *IEEE Trans. Magn.*, vol.26, no.5, September 1990, pp.2359-2363.

[66] P.J.Leonard, H.C.Lai, G.Hainsworth, D.Rodger and J.F.Eastham. "Analysis of the Performance of Tubular Pulsed Coil Induction Launchers". *IEEE Trans. Magn.*, vol.29, no.1, January 1993, pp.686-690.

[67] D.Rodger and J.F.Eastham. "The Use of Transformations in Applying Boundary Conditions to 3D Vector Field Problems". *IEE Proc., Part A*, vol.132, no.4, July 1985, pp.165-170.

[68] "MEGA User Manual and Command Reference (Version 6.28)". *Applied Electromagnetics Research Centre*, Department of Electronic and Electrical Engineering, University of Bath, UK